



**HAL**  
open science

# Development of Magnetic Resonance Imaging (MRI) methods for in vivo quantification of lipids in preclinical models.

Roberto Salvati

► **To cite this version:**

Roberto Salvati. Development of Magnetic Resonance Imaging (MRI) methods for in vivo quantification of lipids in preclinical models.. Human health and pathology. Université de Rennes, 2015. English. NNT: 2015REN1B026 . tel-01308529

**HAL Id: tel-01308529**

**<https://theses.hal.science/tel-01308529v1>**

Submitted on 21 Oct 2016

**HAL** is a multi-disciplinary open access archive for the deposit and dissemination of scientific research documents, whether they are published or not. The documents may come from teaching and research institutions in France or abroad, or from public or private research centers.

L'archive ouverte pluridisciplinaire **HAL**, est destinée au dépôt et à la diffusion de documents scientifiques de niveau recherche, publiés ou non, émanant des établissements d'enseignement et de recherche français ou étrangers, des laboratoires publics ou privés.



**THÈSE / UNIVERSITÉ DE RENNES 1**  
*sous le sceau de l'Université Européenne de Bretagne*

pour le grade de  
**DOCTEUR DE L'UNIVERSITÉ DE RENNES 1**  
Mention: Génie Biologique et Médical

**Ecole doctorale Vie-Agro-Santé**

présentée par

**Roberto Salvati**

Préparée à l'unité de recherche LTSI - INSERM UMR1099  
Laboratoire du Traitement du Signal et de l'Image

---

**Development of Magnetic  
Resonance Imaging (MRI)  
methods for in vivo  
quantitation of lipids  
in preclinical models.**

**Thèse soutenue à Rennes  
le 15 Décembre 2015**

devant le jury composé de :

**Olivier BEUF**

Directeur de recherche CNRS Université  
Lyon 1 / *rapporteur*

**Florence FRANCONI**

IR PIAM Université d'Angers / *rapporteuse*

**Jérôme IDIER**

Directeur de recherche CNRS Université  
de Nantes / *examineur*

**Giulio GAMBAROTA**

PU Université Rennes 1 / *directeur de  
thèse*

**Eric HITTI**

MDC Université Rennes 1 / *co-directeur  
de thèse*



*Je remercie les rapporteurs Giulio Gambarota et Eric Hitti pour la grande disponibilité et courtoisie que m'ont montrées pendant ces trois ans.*

*Un gros merci est destiné aussi à Hervé Saint-Jalmes et Jean Jacques Bellanger pour tout l'aide que m'ont donné.*

*Je voudrai remercier encore tout l'équipe METRIQ qui m'a accueilli et supporté. Et, particulièrement mes collègues Amandine Coum et Caroline Le Ster qu'ont partagé le bureau avec moi et qui m'ont aidé en tout. Merci aussi Quentin Duché et Costanza Simoncini pour m'avoir accompagné pendant mon parcours académique.*





## **Résumé en français**



## **Introduction**

Au cours des dernières années il y a eu un intérêt croissant pour la quantification du métabolisme des graisses, dans les domaines de l'obésité, du diabète, de la nutrition, de la toxicologie et de la physiologie de l'effort, menant à la recherche de paramètres significatifs et mesurables aussi bien en routine clinique qu'en recherche clinique. L'obésité atteint actuellement des proportions épidémiques et, en 2005, à travers le monde, 1,6 milliard d'adultes étaient en surpoids dont 400 millions classés comme obèses [1]. Il est à noter qu'outre le manque d'exercice et l'augmentation de l'apport alimentaire, différents médicaments sont également en mesure de favoriser l'obésité chez un grand nombre de patients.

Ces niveaux d'obésité sont associés aux augmentations de la morbidité et de la mortalité liées à de nombreuses maladies, y compris le diabète de type 2, l'hypertension et des pathologies hépatiques menant à une surcharge lipidique d'origine non alcoolique. En particulier, une augmentation surprenante du diabète de type-2 est observée de nos jours, alimentée par l'augmentation de l'obésité: 190 millions de personnes touchées dans le monde, avec un nombre de patients qui devraient atteindre 300 millions en 2025 [2].

Par conséquent, il est essentiel de développer des outils permettant une évaluation précise et non invasive des quantités de graisse présentes dans certains organes, avec un intérêt particulier pour le foie et le muscle squelettique.

Le tissu musculaire contient de la graisse intracellulaire (lipide intramyocellulaires, IMCL) qui est stockée sous forme de gouttelettes sphériques dans les cellules musculaires et les lipides extramyocellulaires (EMCL), qui sont situés le long des fibres musculaires dans des longues cloisons grasses de forme laminaire [3], [4]. L'accumulation de l'un ou des deux types de matières grasses a été observée dans de nombreuses pathologies [5], [6]. Ainsi le tissu hépatique contient des lipides intra-hépatocellulaire (IHL) [7]. Une augmentation du niveau de IHL (i.e. stéatose) est associé à la résistance à l'insuline et au diabète de type 2. Bien que la stéatose hépatique soit une affection bénigne dans le court terme, elle peut dégénérer chez certains patients en une stéatohépatite (NASH) et même en une cirrhose après plusieurs années. Comme l'obésité, plusieurs médicaments tels que l'amiodarone, la tétracycline, le méthotrexate et l'acétaminophène sont des facteurs capables de favoriser l'accumulation de lipides dans le foie.

Il existe différentes méthodologies utilisées pour la quantification des matières grasses [8].

Pendant de nombreuses années, les analyses biochimiques et histochimiques de biopsies ont été les méthodes de références pour l'évaluation de la teneur en matières grasses dans le foie et les muscles. En outre, la mesure de rayon de gouttelettes (de l'ordre du micromètre) des IMCL peut aussi être réalisée en microscopie électronique en coupes ultraminesces (~0,1 micromètres) d'échantillons de biopsie. Cependant, ces biopsies sont invasives et, en plus de l'inconfort du patient, il existe toujours un risque de complications. Par conséquent, les biopsies ne sont pas bien adaptées dans le cas des études longitudinales, i.e. pour le suivi de la progression ou l'évaluation d'une efficacité thérapeutique.

La quantification *in vivo* de la graisse peut être réalisée par reconstruction tomographique de la carte d'absorption des rayons X (scanner X ou tomodensitométrie) dans les tissus. Les images générées par les différents tissus traduisent leurs caractéristiques d'absorption/atténuation, qui dépendent non seulement de la densité ces tissus mais également de leur composition chimique. Étant donné que l'atténuation est une fonction linéaire de la teneur en matières grasses, il est possible de mesurer cette teneur en graisse par la tomodensitométrie. Cependant, l'exposition aux radiations - bien que relativement faible - est toujours un facteur de risque et impose certaines limites dans les études longitudinales.

Dans les dernières années, les techniques de résonance magnétique, d'imagerie (IRM) et de spectroscopie (SRM), sont apparues comme les méthodes de choix pour l'évaluation non invasive de la teneur en graisse dans le foie et le muscle [9]–[13]. Les approches par résonance magnétique mesurent le signal émis par le spin de  $^1\text{H}$  dans l'eau et la graisse et permettent d'évaluer séparément la contribution de l'eau et de la graisse en exploitant leurs différences de fréquence de résonance.

Un état de l'art (chapitre 2) permet de dégager différentes méthodes d'imagerie par résonance magnétique pour la quantification de la graisse. L'objectif de la thèse a été de les adapter et de les tester pour un scanner IRM préclinique à 4,7 Tesla, tout d'abord en simulation par introduction de fantômes dits numériques, puis au moyen de fantômes physiques et enfin sur petit animal (souris).

De plus, dans cette thèse, on propose une nouvelle méthode de génération d'une image de référence sans l'aide d'objets physiques (Fat ViP MRI, Virtual Phantom Magnetic Resonance

Imaging). Plus particulièrement, l'objectif était ici de tester la faisabilité de la méthode ViP MRI pour générer en amplitude et en phase des images qui imitent les systèmes eau-graisse.

Cette thèse est structurée en 5 chapitres :

1. Dans le premier chapitre, les bases de l'IRM sont rappelées.
2. Dans le deuxième chapitre, deux méthodes de quantification du gras (Dixon et IDEAL) sont présentées et des simulations introduisant des fantômes numériques ont été réalisées pour analyser les performances d'IDEAL.
3. Dans le chapitre trois, les méthodes de quantification sont appliquées à des fantômes physiques.
4. Dans le chapitre quatre, les méthodes de quantification sont appliquées *in vivo* sur des souris.
5. Dans le chapitre cinq, on présente la méthode de génération d'un signal de référence (Fat ViP MRI).



## Résumé - Chapitre I

La résonance magnétique nucléaire (RMN) est une technique qui utilise le champ magnétique, généré par les noyaux en résonance quand un champ magnétique externe ( $B_0$ ) est utilisé. En RMN, les noyaux doivent présenter un moment magnétique intrinsèque (spin). Des exemples de noyaux de spin non nul, employés dans la RMN, sont  $^1\text{H}$ ,  $^{13}\text{C}$ ,  $^{15}\text{N}$ ,  $^{19}\text{F}$ ,  $^{23}\text{Na}$  et  $^{31}\text{P}$ . La plupart des scanners RMN utilisent le proton ( $^1\text{H}$ ), principalement contenu dans les molécules d'eau. Le champ magnétique  $B_0$  provoque la précession des moments magnétiques d'hydrogène à une fréquence déterminée à partir de l'équation de Larmor égale à :

$$\vec{\omega}_0 = -\gamma \vec{B}_0$$

où  $\gamma$  est le facteur gyromagnétique (42.58MHz/T pour le noyau d'hydrogène).

On appelle  $\vec{M}$  le vecteur d'aimantation, défini comme la somme de tous les moments magnétiques des noyaux. Le vecteur d'aimantation  $\vec{M}$  est parallèle à  $B_0$ , et est proportionnel au nombre total de noyaux, à l'intensité de champ magnétique  $B_0$  et à la température  $T$  du système des spins. La composante transversale (orthogonale à  $B_0$ ) de  $\vec{M}$  est nulle étant donné que les composantes du moment magnétique sur le plan  $xy$  ne sont pas en cohérence de phase.

Une impulsion de radiofréquence (l'impulsion RF ou impulsion d'excitation  $B_1$ ), appliquée perpendiculairement à  $B_0$ , est capable d'incliner le vecteur d'aimantation vers le plan  $xy$ . La composante d'aimantation transversale  $M_{xy}$  est alors générée par synchronisation des composantes transversales de moments magnétiques.

Dans  $^1\text{H}$ -IRM, le signal émis par les noyaux d'hydrogène est encodé spatialement permettant la construction d'une image qui permet d'avoir une idée de la répartition spatiale des noyaux d'hydrogène dans un tissu.

L'acquisition des images IRM nécessite :

- des impulsions d'excitation RF nécessaires à l'obtention de l'effet de résonance magnétique;
- trois gradients de champ magnétique pour le codage spatial : le gradient de coupe, le gradient de phase et le gradient de fréquence suivant les trois directions spatiales.



Comme indiqué précédemment, les atomes d'hydrogène sont contenus dans les molécules d'eau. Toutefois, ces atomes d'hydrogène sont également contenus dans les molécules de graisse. En outre, les atomes d'hydrogène dans les graisses ont des fréquences de précession différentes de celles des atomes d'hydrogène dans l'eau.

## **Résumé - Chapitre II**

Dans ce chapitre, deux méthodes de quantification de la graisse (Dixon [14] et IDEAL [15]) sont présentées et des simulations introduisant des fantômes numériques ont été réalisées pour analyser les performances d'IDEAL.

### **Les algorithmes de quantification**

La base des algorithmes de quantification de la graisse consiste à acquérir des images avec un décalage de phase adapté au déplacement chimique entre l'eau et la graisse [14].

La méthode de 2-points Dixon [14], le premier algorithme introduit pour la séparation de la graisse et de l'eau, a besoin de deux images, la première pour laquelle les signaux de l'eau et de la graisse sont en phase et l'autre où ils sont en opposition de phase. Cette méthode a été améliorée ensuite menant à la méthode 3-points Dixon [16] qui élimine une ambiguïté dans l'étiquetage eau/graisse non résolue dans la méthode 2-points.

Parallèlement aux améliorations de la méthode de Dixon [17]–[19], un algorithme nommé IDEAL [15] a été proposé par Reeder et al. en 2004. Contrairement aux méthodes de Dixon utilisant des images en phase et en opposition de phase, la méthode IDEAL utilise des images dont le signal de la graisse est dans des positions asymétriques par rapport au signal de l'eau. De plus on utilise au minimum trois images (complexes). L'algorithme IDEAL a été amélioré au cours des années avec l'addition de la correction de  $T2^*$  [20] ainsi que la prise en compte de la contribution des tous les pics de fréquences entrant dans la composition de la graisse [21].

### **Les fantômes numériques**

Des fantômes numériques ont été mis en œuvre dans Matlab avec deux objectifs :

- valider le programme IDEAL;
- analyser les performances de l'algorithme IDEAL en présence de bruit, de la carte de champ,...

Dans toutes les simulations, des images du fantôme numérique en écho de gradient ont été générées avec un premier TE à 1.5ms et un intervalle entre les échos de 2.5ms.

Pour la validation du programme IDEAL nous avons utilisé un fantôme numérique composé d'une matrice de disques, en faisant varier la valeur de la graisse de 0 à 100% suivant les

lignes et la valeur du  $T2^*$  de 2ms à 25ms suivant les colonnes. Nous avons constaté une bonne adéquation entre les résultats et les valeurs attendues.

Nous avons ensuite analysé les performances de l'algorithme **en fonction du niveau de bruit** sur les cartes de fraction de graisse et de  $T2^*$ . Pour cela :

- les fantômes numériques ont été générés avec une fraction de graisse de 10% et deux valeurs de  $T2^*$  (10 et 20ms) ;
- deux types de train d'échos (3 et 6 échos) ont été utilisés ;
- on a fait varier le rapport signal à bruit (SNR) de 125 à 20, sachant qu'il est approximativement égal à 40 dans la souris et à 100 dans les fantômes physiques, dans nos conditions expérimentales.

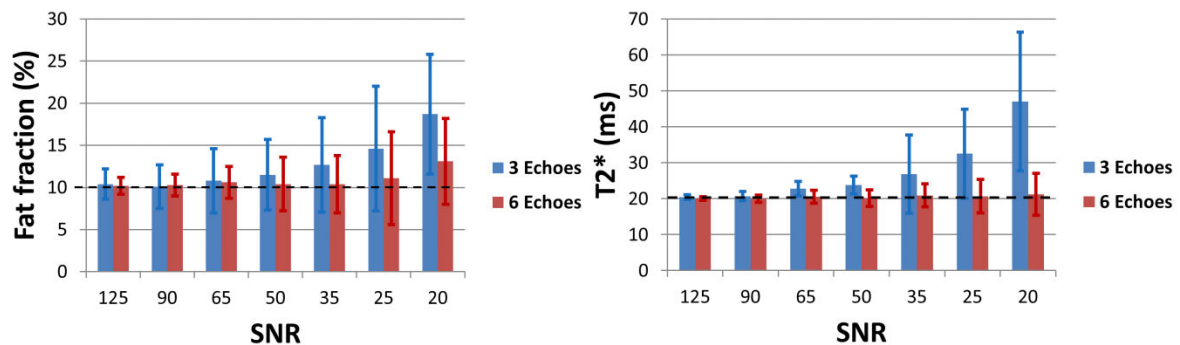


**Figure 1:** Résultats de la fraction de graisse et  $T2^*$  calculées par l'algorithme IDEAL. Les résultats pour les différents SNR sur le signal généré avec  $T2^* = 20ms$  sont présentés. La valeur nominale utilisé dans l'entrée pour la fraction de graisse et  $T2^*$  est marquée par une ligne noire (10% pour la fraction de matières grasses et 20ms pour  $T2^*$ )

On obtient sensiblement les mêmes résultats pour des valeurs de  $T2^*$  égales à 10ms et à 20ms. La diminution du SNR entraîne une augmentation des valeurs estimées de fraction lipidique et cette augmentation est plus importante pour un train de 3 échos. On observe le même effet pour l'estimation du  $T2^*$ . Il convient donc d'utiliser un train de 6 échos qui sera moins sensible à la diminution du SNR.

**Les effets de l'inhomogénéité de champ magnétique** (ou carte de champ) sur les estimations de la fraction de graisse et de  $T2^*$  par IDEAL ont été étudiés. L'algorithme IDEAL prend en compte cette inhomogénéité et en produit une estimation. Ceci nécessite une carte initiale qui, si trop différentes de la réalité, mène à des erreurs pour la fraction de graisse et  $T2^*$ . Afin d'éviter ces erreurs, trois solutions sont proposées:

- diminution de l'espacement d'écho;
- diminution du nombre d'échos;
- utilisation d'un algorithme de dépliage de la phase pour calculer une carte initiale de champ.

Nous avons ensuite étudié **l'influence de la température**. En effet les algorithmes sont basés sur la connaissance du décalage en fréquence entre l'eau et les pics de la graisse. Or ces décalages peuvent être altérés par des changements de températures. Nous avons généré un fantôme numérique simulant de tels décalages. On constate alors une diminution de la fraction de graisse estimée lorsque l'on augmente le nombre d'écho (de 3 à 10) tandis que l'estimation du  $T2^*$  est peu modifiée. Ainsi, appliquer l'algorithme IDEAL simultanément à différents objets ayant différentes températures risque d'entraîner un biais dans la mesure de la fraction de la graisse.

Enfin pour un même fantôme numérique incluant 6 pics pour représenter la graisse, nous avons testé l'algorithme IDEAL **en imposant dans IDEAL un nombre des pics à estimer variable**: 1 pic [20] (le pic primaire à 1.3ppm), 3 pics [21] (les trois pics avec surface relative la plus élevée) ou 6 pics [9]. Les images numériques ont été générées avec SNR égal à 50. En ce qui concerne la fraction de graisse, les modèles à 3 pics et 6 pics fournissent des valeurs compatibles avec la réalité. La fraction de graisse calculée en utilisant le modèle à un seul pic fournit des valeurs inférieures à la réalité mais compatible avec l'aire relative de ce pic principal.



### Résumé - Chapitre III

Après avoir testé IDEAL sur simulations dans le chapitre précédent, nous avons réalisé ici des acquisitions IRM sur des fantômes physiques comportant différentes fractions de la graisse. De plus, une comparaison entre IDEAL et les méthodes de Dixon à 2 et 3 points a été réalisée.

- Trois crèmes laitières ont été utilisées comme un modèle de mélange eau-graisse pour tester l'algorithme IDEAL (fluide-entière, fluide-légère et épaisse-légère).
- Pour les reconstructions de Dixon, trois séquences d'écho de gradient ont été utilisées. Les paramètres d'imagerie étaient: TR = 30ms, angle de basculement = 5°, taille de la matrice = 128x128, FOV = 4x4cm<sup>2</sup>, bande passante = 140kHz et 80 répétitions. Les séquences ont été acquises avec 1.45ms (première image en phase), 2.2ms (image en opposition de phase) et 2.9ms (deuxième image en phase).
- Pour la reconstruction IDEAL, des images RM ont été acquises avec une séquence de multi-écho de gradient. Les paramètres d'imagerie étaient: 10 échos, premier TE = 1.5ms, intervalle entre les échos = 2.5ms, TR = 30ms, angle de basculement = 5°, taille de la matrice = 128x128, FOV = 4x4cm<sup>2</sup>, bande passante = 140kHz et 80 répétitions.

Le script Matlab, utilisé dans les simulations, l'a été également pour le calcul des cartes de fraction de graisse et de T2\* en utilisant de 3 à 10 échos. Des statistiques sur des régions d'intérêt ont été effectuées pour les cartes de fraction de graisse et de T2\*.

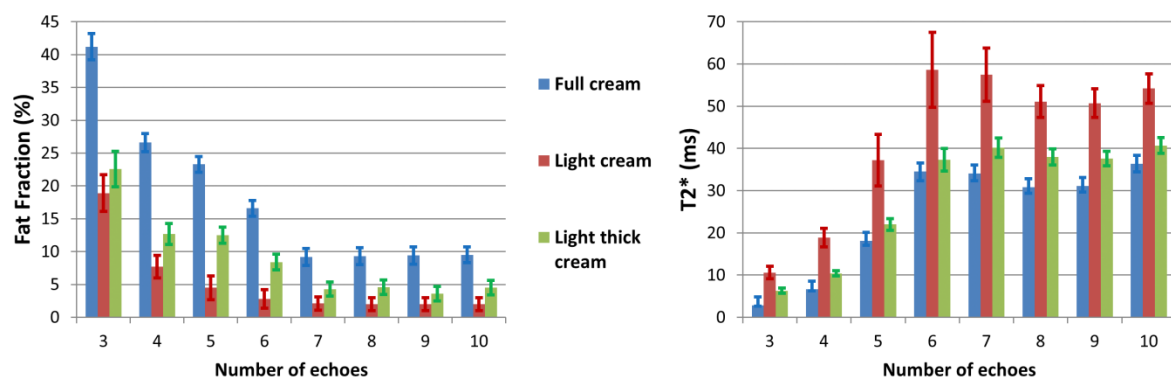


*Figure 2: Fraction de la graisse (gauche) et T2\* (droite) en fonction du nombre d'échos.*

Concernant la fraction de graisse, sa valeur diminue, pour toutes les crèmes, avec l'augmentation du nombre d'échos utilisés pour la reconstruction IDEAL. En ce qui concerne

l'estimation de  $T2^*$ , sa valeur augmente pour toutes les crèmes avec l'augmentation du nombre d'échos, atteignant finalement une valeur plateau. C'est avec 3 échos que l'on a obtenu des valeurs de fraction de la graisse similaires à celles obtenues avec 2 points Dixon et 3 points Dixon. La raison de la baisse de la fraction de graisse estimée pourrait être due au modèle de signal postulé dans l'algorithme IDEAL qui présuppose une valeur de  $T2^*$  commune à l'eau et à la graisse [20]. Or récemment, de nouveaux algorithmes introduisent des temps de relaxation pour la graisse et l'eau ( $T2^*_F$  et  $T2^*_W$ ) distincts, dans le but d'améliorer la quantification de la graisse. Les valeurs de  $T2^*_F$  et  $T2^*_W$  sont estimées par ces algorithmes, mais il n'y a pas de validation pour leur estimation finale, parce qu'il n'existe pas de vérité terrain pour ces quantités.

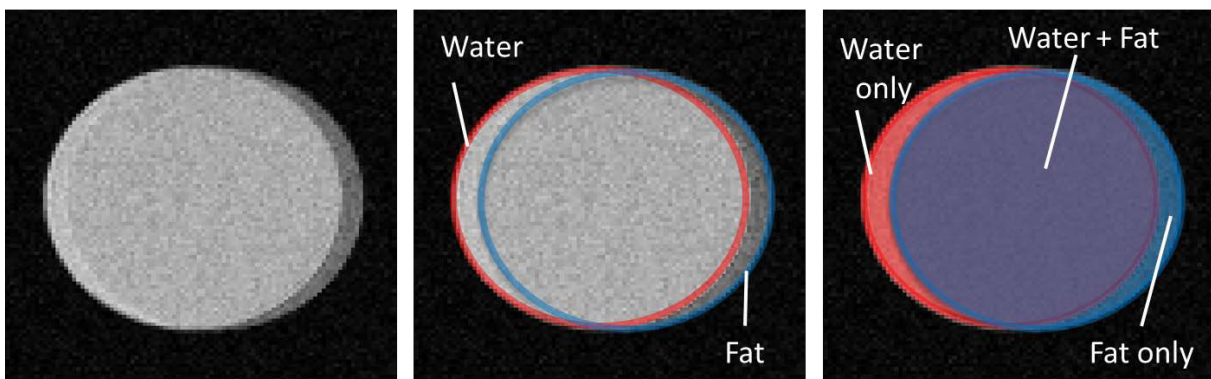


**Figure 3:** Fantôme contenant de la crème laitière entière acquise en utilisant une faible largeur de bande passante en réception. Dans le centre et le panneau de droite, deux cercles sont dessinés sur les images IRM afin de faciliter la visualisation du signal séparé des protons de l'eau et de la graisse.

Afin de dégager une vérité terrain pour  $T2^*_F$  et  $T2^*_W$ , on propose une méthode utilisant **une faible largeur de bande passante en réception**. Cette vérité terrain pourra être utilisée pour la validation et l'amélioration des algorithmes de quantification de la graisse.

Pour calculer les temps de relaxation par une mesure directe, les images IRM ont été acquises avec une faible bande passante du récepteur afin de séparer les signaux de l'eau et de la graisse selon la direction de codage de fréquence. Les temps de relaxation ont été obtenus dans l'eau seule, dans la graisse seule et dans le mélange eau + graisse. Les 3 fantômes à base de crèmes laitières ont été à nouveau utilisés. Pour les mesures de  $T2^*$ , 5 séquences d'écho de gradient décalés ont été combinés. Les paramètres d'acquisition étaient les suivants: 30 échos, 11.7ms d'intervalle d'écho, un premier TE = 6, 8, 10, 12 et 14ms pour chacune des 5 séquences. Toutes les images ont été acquises avec une taille de matrice = 256x256 et une bande passante de 25.2kHz.

Dans tous les fantômes, les valeurs de  $T2^*$  des protons de la graisse estimées étaient significativement inférieures aux valeurs de  $T2^*$  des protons de l'eau. De plus, les valeurs de  $T2^*$  des protons de l'eau dans la crème épaisse légère étaient nettement inférieures à celles trouvées dans les crèmes fluide-entière et fluide-légère. Les mêmes tendances ont été observées sur des fantômes réalisés à partir d'émulsions.

L'approche à faible bande passante en réception pour la mesure directe de  $T2^*_W$  et  $T2^*_F$ , où les protons de l'eau et de la graisse partagent le même microenvironnement, ne semble pas réalisable pour des mesures de tissus in vivo. Néanmoins, les valeurs de référence observées sur fantômes sont d'intérêt pour la validation des algorithmes ; de plus, la capacité de mesurer  $T2^*_W$  et  $T2^*_L$  sur fantômes représente certainement une étape importante vers le développement des algorithmes robustes qui utilisent la double correction  $T2^*$ .





## **Résumé - Chapitre IV**

Dans ce chapitre, les méthodes de quantification de la graisses et de T2\* ont été appliquées sur des souris.

Dans le cadre des modèles précliniques, seules quelques mesures quantitatives de lipides ont été rapportées dans la littérature, effectuées principalement par SRM. Un des inconvénients majeurs de l'approche SRM est son faible apport en information spatiale, limitée à un seul voxel d'intérêt. Comme avec la SRM, les approches d'IRM permettraient des mesures longitudinales sur les mêmes animaux, avec l'avantage cependant d'étendre l'estimation de la fraction lipidique à tout l'organe, voire au corps entier.

Contrairement aux fantômes physiques, les souris respirent et peuvent bouger au cours de l'acquisition, conduisant à la formation d'artefacts de mouvements.

Un paramètre de l'algorithme IDEAL est le nombre d'échos à déterminer pour une reconstruction optimale de la fraction de graisse et de T2\*. Selon Hines et al. [22], il existe par exemple une excellente corrélation entre la fraction de graisse calculée avec la reconstruction à 6 échos et la fraction de graisse calculée avec la reconstruction à 15 échos, chez la souris, imagée avec une machine à 3T.

Notre expérimentation a été réalisée sur des souris L-PK /c-myc, anesthésiées avec 2% d'isoflurane en oxygène (v /v). Pour la méthode de Dixon, trois séquences d'écho de gradient avec trois temps d'écho différents (1,45, 2,2 et 2,9 ms) ont été utilisées pour l'acquisition. En ce qui concerne l'algorithme IDEAL, trois séquences d'écho de gradient avec un premier temps d'écho égal à 1,37, 2,16 et 2,95ms, ont été acquises. L'intervalle entre les échos était égal à 2,37ms pour les trois séquences. Les images, acquises à partir de ces trois séquences, ont été combinées afin de créer une seule séquence (« la séquence effective ») avec espacement d'écho égal à 0.79ms.

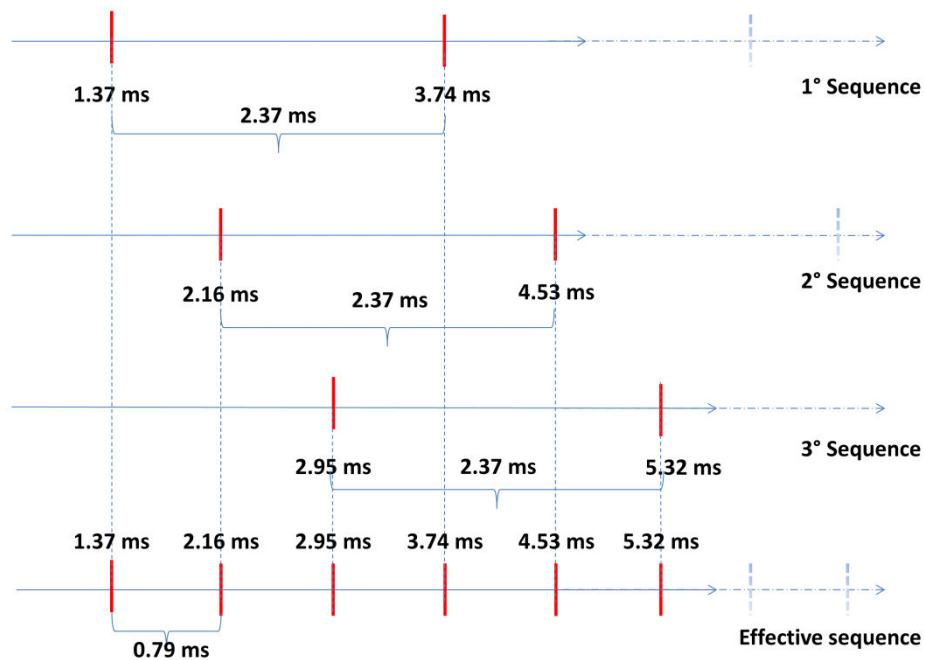


**Figure 4:** Schéma de la création de la 'séquence effective'. Les 3 séquences avec un intervalle d'échos de 2.37 ms sont combinées pour obtenir une séquence avec un intervalle d'échos de 0.79 ms.

Différentes analyses ont été effectuées afin d'étudier l'influence du nombre d'échos et de l'intervalle entre échos :

- en utilisant les images de la première séquence (1<sup>er</sup> TE = 1,37 ms, intervalle d'écho de 2,37 ms);
- en utilisant les images de la séquence effective (1<sup>er</sup> TE = 1,37 ms, intervalle d'écho de 0,79 ms);
- en comparant les résultats d'IDEAL obtenus en utilisant 3, 6 et 15 échos de la séquence effective;
- en comparant les valeurs du coefficient de variation ( $S/\sigma$ ) des estimations de la fraction de graisse et de  $T2^*$  obtenues avec les images de la séquence effective, en fonction du nombre d'échos;
- en comparant les valeurs de la fraction de graisse obtenues en utilisant la méthode à 3 points de Dixon et l'algorithme IDEAL avec la séquence simple et avec la séquence effective.

A partir de ROI positionnées sur les cartes des fractions de graisse et de  $T2^*$  dans le foie et dans les muscles, nous avons pu mettre en évidence les éléments rapportés dans ce qui suit.

Avec la séquence simple, nous avons constaté, dans les deux zones anatomiques, que la valeur de fraction de graisse augmente avec l'augmentation du nombre d'échos utilisés pour la reconstruction IDEAL et que les valeurs de T2\* convergent quand on utilise un nombre croissant d'échos.

Avec la séquence effective les valeurs estimées de la fraction de graisse et de T2\* sont presque constantes dans les deux zones anatomiques. À faible nombre d'échos, les valeurs trouvées dans le foie sont légèrement plus élevées, mais cette différence tend à disparaître avec les valeurs calculées avec un nombre élevé d'échos. Les valeurs obtenues en utilisant la séquence effective sont inférieures à celles trouvées avec la séquence simple. Dans les deux zones anatomiques, les valeurs moyennes (évaluées sur les ROI) de l'estimation de T2\* atteignent un plateau pour un nombre élevé d'échos. Les valeurs moyennes et les écart-types sont plus élevées pour un faible nombre d'échos.

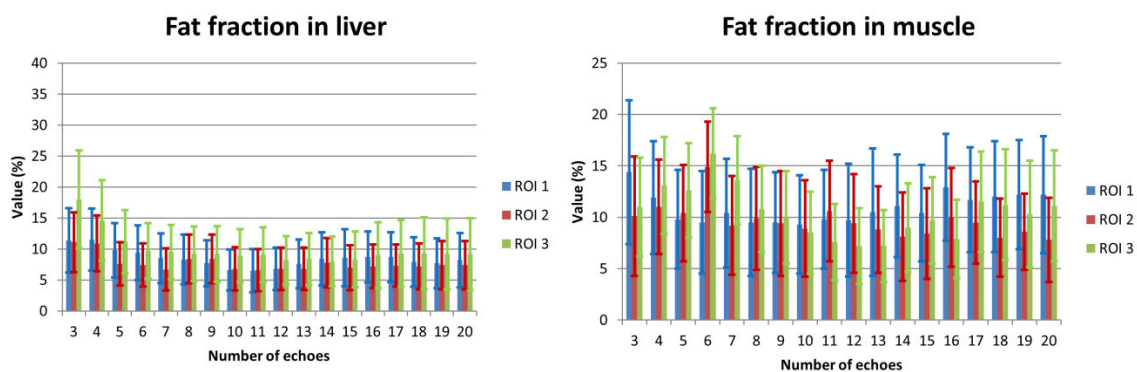


**Figure 5:** Fraction de graisse en fonction du nombre d'échos utilisés pour la reconstruction IDEAL, calculé dans le foie (gauche) et dans le muscle (droite)

Les reconstructions obtenues avec la séquence effective à 3, 6 et 15 échos ont été analysées plus en détail. Pour cela, des tests de Student ont été effectués pour les comparaisons des estimations de la fraction de graisse d'une part et de celles de la valeur du T2\* d'autre part, calculées en utilisant 3, 6 et 15 échos dans IDEAL. Dans le foie, les valeurs de fraction de graisse ne diffèrent pas significativement pour différents nombres d'échos. Dans le muscle seules les valeurs calculées avec 6 et 15 échos sont similaires. Les valeurs pour l'estimation avec 3 échos étaient plus élevées. En ce qui concerne le T2\*, les valeurs moyennes et les écart-types obtenus dans la reconstruction à 3 échos étaient trop élevés. Les valeurs T2\* calculées pour les reconstructions à 6 et 15 échos étaient similaires dans le foie et le muscle.

Pour les deux séquences (simple et effective) nous recommandons d'utiliser un train d'échos court uniquement pour le calcul de la fraction de graisse.

En effet, des erreurs dues à la différence de valeur entre  $T2^* W$  et  $T2^* F$  peuvent se produire en utilisant un nombre élevé d'échos.

*A contrario*, le choix d'utiliser un train écho long pour calculer les valeurs de  $T2^*$  est recommandé.

Le coefficient de variation a été calculé pour chaque ROI positionnée sur les cartes des fractions de graisse et de  $T2^*$ . Pour chaque nombre d'échos (utilisés pour la reconstruction IDEAL) et pour chaque souris, des coefficients de variation ont été calculés dans chaque ROI. Pour chaque région anatomique ont été calculés la moyenne des coefficients de variation et leur écart type. En ce qui concerne la fraction de graisse, aucune tendance n'a été observée dans le foie et dans le muscle. Les valeurs du  $T2^*$  dans le foie atteignent une valeur minimale entre 12 et 15 échos. De même les valeurs de  $T2^*$  dans le muscle diminuent avec l'augmentation du nombre d'échos.

Les valeurs de l'estimation de  $T2^*$  correspondant aux niveaux des plateaux pour les séquences simples (entre 6 et 12 échos) et effectives (entre 10 et 20 échos) ont été comparées avec un test de Student : on en a déduit que ces valeurs sont comparables.

En ce qui concerne la fraction de graisse, les valeurs calculées pour les deux séquences avec l'algorithme IDEAL (avec 3 échos) ont été comparées à celles obtenues avec la méthode à 3 points de Dixon. Dans le foie toutes les mesures de la fraction de graisse sont comparables. Dans le muscle, les valeurs de la fraction de graisse sont comparables à condition d'utiliser la séquence effective.





## Résumé - Chapitre V

Dans ce chapitre, on présente une méthode de génération d'un signal de référence (Fat ViP MRI). Le fantôme virtuel (VIP [23]) pour l'imagerie par résonance magnétique (IRM) est une méthode pour générer des signaux de référence, sans l'aide d'objets physiques. Cette méthode représente l'extension de la méthode ERETIC [24] (largement utilisé dans la spectroscopie) à l'IRM. ViP IRM fonctionne de la manière suivante: étant donné un fantôme numérique (spécifié dans l'espace k), un générateur de forme d'onde convertit les lignes de l'espace k en un signal radiofréquence (signal VIP) qui est transmis à l'appareil d'IRM par une bobine RF. Le scanner IRM enregistre simultanément le signal de ViP simultanément et le signal de l'objet d'intérêt. Dans l'article de Saint Jalmes et al., [23] il a été montré que le VIP IRM pourrait remplacer les fantômes de gel d'agar, en utilisant des images d'amplitude. L'objectif de l'étude est de tester la faisabilité de la méthode ViP IRM pour générer en amplitude et en phase des images qui simulent les systèmes eau-graisse. Nous avons réalisé des acquisitions IRM d'un fantôme physique (crème entière) couplé avec un fantôme virtuel puis elles ont été analysées avec l'algorithme IDEAL.

Un programme en Matlab qui permet de simuler des signaux MR a été élaboré : il permet de choisir le pourcentage de la fraction de graisse, le temps d'écho, le nombre d'échos et le temps de relaxation ( $T2^*$ ) pour chaque fantôme et de créer une carte de champ de forme arbitraire. Les images numériques ont été converties en leurs représentations dans l'espace k, transformées en amplitude et en phase RF pour être présentées en entrée du générateur de forme d'onde (Redstone Tecmag Inc. Houston TX, USA) et transmises au scanner IRM par une bobine RF. Les paramètres des images simulées étaient comme suit:  $T2^* = 20\text{ms}$ ;  $TE = 1.4, 3.8, 6.2$  et  $8.6\text{ms}$ .

Les images d'écho de gradient ont été acquises avec les mêmes TE que ceux des images numériques. Toutes les données numériques et expérimentales ont été traitées avec un codage en Matlab de l'algorithme IDEAL.

Différents fantômes ont été conçus:



1) un fantôme circulaire avec une fraction de graisse = 20% et  $T2^* = 20\text{ms}$  pour tester la faisabilité de la méthode ViP. Après traitement des images IRM on mesure un  $T2^*$  égale à  $23,7 \pm 0,5\text{ms}$  et une fraction de graisse égale à  $21,9 \pm 0,2\%$ .

2) Un fantôme circulaire avec deux formes pour les cartes de champ (une forme parabolique et une forme linéaire) pour tester la capacité de bien reproduire les cartes de phase. Les cartes de champs calculés à partir des données expérimentales étaient en bon accord avec celles qui étaient simulées.

3) Trois fantômes circulaires avec une fraction de graisse différente (10%, 20% et 30%) pour tester la faisabilité de la ViP IRM en présence d'un objet réel contenant de crème entière. Les valeurs obtenues dans les fantômes sont pour la fraction de graisse de  $10,5 \pm 1,9\%$ ,  $20,3 \pm 1,6\%$  et de  $30,4 \pm 1,2\%$ , et sur la carte de  $T2^*$ ,  $20,6 \pm 2,6\text{ms}$ ,  $26,5 \pm 4,1\text{ms}$  et  $21,2 \pm 1,2\text{ms}$ .

L'un des principaux résultats de cette étude est l'excellent accord entre les cartes de phase expérimentales et simulées. La capacité de générer des fantômes virtuels avec une phase donnée, afin de fournir une valeur de référence de phase sur une image RM, pourrait être d'intérêt, non seulement pour les techniques de décomposition graisse-eau, mais aussi pour d'autres techniques qui exploitent les informations de phase des images RM.

À ce jour, seul un nombre restreint d'études ont mis l'accent sur le développement de signaux de référence en IRM. La principale différence entre ViP IRM et les approches proposées précédemment est que dans ViP IRM il n'est besoin d'utiliser aucun composant du scanner RM pour générer le signal du fantôme virtuel. Ainsi la méthode ViP IRM peut être utilisée sur les appareils d'IRM de différents types.





## **Conclusions et perspectives**

Cette thèse est une contribution à la quantification de la fraction de graisse et à son optimisation pour des mesures in vivo. Les méthodes de Dixon et l'algorithme IDEAL, préalablement évaluées en simulation numérique, ont été utilisés pour les mesures des fractions de graisse et de  $T2^*$  sur des fantômes physiques et chez la souris in vivo. Les mesures IRM ont été effectuées sur un scanner RM pour petits animaux à 4.7T. Tout d'abord, concernant l'acquisition des données, les images RM des fantômes et des souris ont été acquises en 2D. L'idée est d'acquérir des images du corps entier en 3D pour le calcul de la fraction de graisse et  $T2^*$ . Ceci impliquera le développement et l'optimisation de séquences IRM spécifiques aux scanner à 4.7T. Ensuite, concernant le traitement des données, dans cette thèse il a été supposé que le signal généré suivait un modèle classique, avait une décroissance exponentielle dans le domaine temporel et une nature Lorentzienne dans le domaine fréquentiel. Cette modélisation pourrait être inadéquate en présence de grandes inhomogénéités de champ magnétique. Dans ce cas-là, un modèle Gaussien doit remplacer le modèle Lorentzien, comme cela a été montré dans des travaux récents sur le cerveau. Cet aspect n'a pas encore été abordé dans le cadre des mesures simultanées de la graisse et du  $T2^*$ . Enfin, des valeurs de référence sont nécessaires pour confirmer les résultats de la fraction de graisse et  $T2^*$  obtenus chez la souris dans le foie et dans le muscle. La biopsie sera un moyen direct pour mesurer la fraction de graisse. Une autre façon d'effectuer cette mesure peut être d'acquérir des spectres avec différents temps d'écho pour la rendre indépendante du temps de relaxation  $T2$ .



## Références

- [1] “WHO | Obesity and overweight.”
- [2] *Diabetes and Cardiovascular Disease: Integrating Science and Clinical Medicine*. Lippincott Williams & Wilkins, 2004.
- [3] G. Gambarota, R. L. Janiczek, R. V. Mulkern, and R. D. Newbould, “An NMR Phantom Mimicking Intramyocellular (IMCL) and Extramyocellular Lipids (EMCL),” *Appl. Magn. Reson.*, vol. 43, no. 3, pp. 451–457, 2012.
- [4] C. Boesch, J. Slotboom, H. Hoppeler, and R. Kreis, “In vivo determination of intramyocellular lipids in human muscle by means of localized  $^1\text{H}$ -MR-spectroscopy.,” *Magn. Reson. Med.*, vol. 37, no. 4, pp. 484–93, Apr. 1997.
- [5] A. Karatopis, O. Benekos, E. Efstathopoulos, Ioannis Kandarakis, and N. Kelekis, “ $^1\text{H}$  MRS and MRSI: analysis of acquisition parameters and improvement of various clinical applications,” in *2006 IEEE Nuclear Science Symposium Conference Record*, 2006, vol. 4, pp. 2025–2028.
- [6] Α. Καρατόπης, Ο. Μπενέκος, Ε. Π. Ευσταθόπουλος, Ι. Γ. Βαλαής, and Ι. Σ. Κανδαράκης, “Molecular imaging through  $^1\text{H}$  MRS and MRSI in everyday routine: improvements in various clinical applications and parameter optimization of spectroscopic imaging sequences,” Jan. 2015.
- [7] A. Hakkarainen, J. Lundbom, E. K. Tuominen, M.-R. Taskinen, K. H. Pietiläinen, and N. Lundbom, “Measuring short-term liver metabolism non-invasively: postprandial and post-exercise  $^1\text{H}$  and  $^{31}\text{P}$  MR spectroscopy.,” *MAGMA*, vol. 28, no. 1, pp. 57–66, Feb. 2015.
- [8] C. P. Bernard, G. P. Liney, D. J. Manton, L. W. Turnbull, and C. M. Langton, “Comparison of fat quantification methods: a phantom study at 3.0T.,” *J. Magn. Reson. Imaging*, vol. 27, no. 1, pp. 192–7, Jan. 2008.
- [9] S. B. Reeder and C. B. Sirlin, “Quantification of Liver Fat with Magnetic Resonance Imaging,” *Magn. Reson. Imaging Clin. N. Am.*, vol. 18, no. 3, pp. 337–357, Aug. 2010.
- [10] M. Nouredin, J. Lam, M. R. Peterson, M. Middleton, G. Hamilton, T.-A. Le, R. Bettencourt, C. Changchien, D. A. Brenner, C. Sirlin, and R. Loomba, “Utility of magnetic resonance imaging versus histology for quantifying changes in liver fat in nonalcoholic fatty liver disease trials.,” *Hepatology*, vol. 58, no. 6, pp. 1930–40, Dec. 2013.

- [11] N. F. Schwenzer, F. Springer, C. Schraml, N. Stefan, J. Machann, and F. Schick, “Non-invasive assessment and quantification of liver steatosis by ultrasound, computed tomography and magnetic resonance.,” *J. Hepatol.*, vol. 51, no. 3, pp. 433–45, Sep. 2009.
- [12] M. a Bernstein and Y. Ikezaki, “Comparison of phase-difference and complex-difference processing in phase-contrast MR angiography.,” *J. Magn. Reson. Imaging*, vol. 1, no. 2, pp. 725–729, 1991.
- [13] Y. H. Yoo, H.-S. Kim, Y. H. Lee, C.-S. Yoon, M. Y. Paek, H. Yoo, S. Kannengiesser, T.-S. Chung, H.-T. Song, J.-S. Suh, and S. Kim, “Comparison of Multi-Echo Dixon Methods with Volume Interpolated Breath-Hold Gradient Echo Magnetic Resonance Imaging in Fat-Signal Fraction Quantification of Paravertebral Muscle,” *Korean J. Radiol.*, vol. 16, no. 5, p. 1086, Jan. 2015.
- [14] W. T. Dixon, “Simple proton spectroscopic imaging.,” *Radiology*, vol. 153, no. 1, pp. 189–94, Oct. 1984.
- [15] S. B. Reeder, Z. Wen, H. Yu, A. R. Pineda, G. E. Gold, M. Markl, and N. J. Pelc, “Multicoil Dixon chemical species separation with an iterative least-squares estimation method,” *Magn. Reson. Med.*, vol. 51, no. 1, pp. 35–45, 2004.
- [16] G. H. Glover and E. Schneider, “Three-point Dixon technique for true water/fat decomposition with B<sub>0</sub> inhomogeneity correction.,” *Magn. Reson. Med.*, vol. 18, no. 2, pp. 371–383, 1991.
- [17] J. Berglund, H. Ahlström, L. Johansson, and J. Kullberg, “Two-point dixon method with flexible echo times,” *Magn. Reson. Med.*, vol. 65, no. 4, pp. 994–1004, Apr. 2011.
- [18] H. Eggers, B. Brendel, A. Duijndam, and G. Herigault, “Dual-echo Dixon imaging with flexible choice of echo times.,” *Magn. Reson. Med.*, vol. 65, no. 1, pp. 96–107, Jan. 2011.
- [19] T. Perkins, “Preliminary Clinical Experience with a Multiecho 2-Point DIXON ( mDIXON ) Sequence at 3T as an Efficient Alternative for Both the SAR-intensive Acquired In- and Out-of-Phase Chemical Shift Imaging as well as for 3D Fat-suppressed T1-weighted Sequences use,” *Proc. Int. Soc. Mag. Res. Med.*, vol. 194, no. 1984, p. 2705, 2009.
- [20] H. Yu, C. a. McKenzie, A. Shimakawa, A. T. Vu, A. C. S. Brau, P. J. Beatty, A. R. Pineda, J. H. Brittain, and S. B. Reeder, “Multiecho reconstruction for simultaneous water-fat decomposition and T<sub>2</sub>\* estimation,” *J. Magn. Reson. Imaging*, vol. 26, no. 4, pp. 1153–1161, 2007.

- [21] H. Yu, A. Shimakawa, C. a. McKenzie, E. Brodsky, J. H. Brittain, and S. B. Reeder, "Multiecho water-fat separation and simultaneous  $R_2^*$  estimation with multifrequency fat spectrum modeling," *Magn. Reson. Med.*, vol. 60, no. 5, pp. 1122–1134, 2008.
- [22] C. D. G. Hines, H. Yu, A. Shimakawa, C. A. McKenzie, T. F. Warner, J. H. Brittain, and S. B. Reeder, "Quantification of Hepatic Steatosis with 3-T MR Imaging: Validation in ob/ob Mice," *Radiology*, vol. 254, no. 1, pp. 119–128, Jan. 2010.
- [23] H. Saint-Jalmes, P.-A. Eliat, J. Bezy-Wendling, A. Bordelois, and G. Gambarota, "ViP MRI: virtual phantom magnetic resonance imaging," *Magn. Reson. Mater. Physics, Biol. Med.*, vol. 27, no. 5, pp. 419–424, 2014.
- [24] L. Barantin, A. Le Pape, and S. Akoka, "A new method for absolute quantitation of MRS metabolites," *Magn. Reson. Med.*, vol. 38, pp. 179–182, 1997.





# Index

Introduction .....	41
Chapter I.....	45
Introduction to Magnetic Resonance Imaging (MRI).....	45
1.1 Magnetic Resonance .....	45
1.2 The Bloch equation .....	48
1.3 MRI Pulse sequence .....	50
1.3.1 Slice selection gradient.....	51
1.3.2 Phase encoding gradient.....	51
1.3.3 Frequency encoding gradient .....	52
1.3.4 K-space.....	53
1.3.5 Spoiled gradient echo sequence .....	54
1.4 Fat signal .....	56
1.5 Choice of the repetition time TR, TE and flip angle.....	58
1.5.1 Weighted images .....	59
1.5.2 Ernst angle.....	61
1.6 Magnetic field inhomogeneity .....	61
1.6.1 Phase wrapping .....	62
1.7 Magnetic susceptibility .....	63
Chapter II .....	67
Water-fat separation with chemical shift imaging techniques .....	67
2.1 Introduction .....	67
2.2 Dixon's method .....	67
2.2.1 Introduction.....	67
2.2.2 2-point Dixon's method .....	68
2.2.3 3-point Dixon's method .....	70
2.2.4 Modifications on the 3-point Dixon's method .....	71
2.3 IDEAL .....	73
2.3.1 Introduction.....	73
2.3.2 IDEAL algorithm .....	73
2.4 Numerical phantom .....	76

2.4.1	Validation of the IDEAL script.....	77
2.4.2	Dependence on the noise.....	80
2.4.3	Dependence on spectral model: fat spectrum model and temperature....	82
2.4.3.1	Dependence on the temperature .....	82
3.4.3.2	Importance of the fat spectrum.....	84
2.4.4	Influence on the field map.....	85
Chapter III	.....	91
MRI measurements on physical phantoms	.....	91
3.1	Introduction .....	91
3.2	Materials and methods.....	92
3.3	Results.....	92
3.4	Discussion.....	96
3.5	Low receiver bandwidth .....	98
3.5.1	Introduction.....	98
3.5.2	Materials and Methods.....	99
3.5.2.1	Theory.....	99
3.5.2.2	Magnetic Resonance Imaging.....	99
3.5.2.3	Data Analysis.....	100
3.5.3	Results.....	100
3.5.4	Discussion .....	103
Chapter IV	.....	107
MRI measurements on mice liver and muscle	.....	107
4.1	Introduction .....	107
4.2	MRS and MRI.....	107
4.3	Review of the literature .....	108
4.4	Materials and methods .....	110
4.4.1	MRI experiment .....	110
4.4.2	Data analysis .....	110
4.5	Results.....	112
4.5.1	Results of IDEAL in mouse using one sequence .....	112
4.5.2	Results of IDEAL in mouse using the effective sequence .....	114
4.5.3	IDEAL results using 3, 6 and 15 echoes .....	116
4.5.4	Study on the coefficient of variation.....	119
		38

4.5.5 Comparison between IDEAL using single and effective sequences on $T_2^*$	120
4.5.6 Comparison between IDEAL (using single and effective sequences) and Dixon for the fat fraction	121
4.5.7 Spectrum acquired in literature vs spectrum acquired on a mouse	124
4.6 Misregistration	125
4.7 Problems with the brunch cut algorithm	128
4.7.1 Choice of the MR images to use	128
4.7.2 Choice of the pixel	130
4.8 Discussion	131
Chapter V	135
Fat Virtual Phantoms (Fat ViP) for Magnetic Resonance Imaging	135
5.1 Introduction	135
5.2 ERETIC method	135
5.3 ViP (Virtual Phantoms)	136
5.3.2 Introduction to ViP	136
5.4 Materials and methods	139
5.4.1 Numerical phantoms	139
5.4.2 MRI experiments	139
5.5 Results	140
5.6 Discussion	145
Conclusions	149
Bibliography	153
Appendix A - IDEAL equations	163
Appendix B – IDEAL dual $T_2^*$	167
Appendix C - Goldstein’s algorithm (branch-cut algorithm)	173
C.1 Explanation of the method	173
C.2 How to use the branch-cut algorithm in IDEAL algorithm	175
Appendix D – Article accepted in Magnetic Resonance Imaging	179
Appendix E – Article accepted in Applied Magnetic Resonance	199



# Introduction

In recent years there has been a growing interest in fat metabolism in the field of obesity, diabetes, food science, toxicology and exercise physiology, both in the clinical and research settings. Obesity is currently at epidemic proportions and in 2005, worldwide, 1.6 billion adults were overweight with 400 million being classified as obese [1]. It is noteworthy that besides the lack of exercise and increased food intake, different drugs are also able to favour obesity in a great number of patients.

These levels of obesity are associated with increasing morbidity and mortality connected with many diseases including type-2 diabetes, hypertension and non-alcoholic fatty liver disease (NAFLD). In particular, a dramatic increase of type-2 diabetes is observed nowadays, fuelled by the obesity increase: 190 million people affected worldwide, with the number of patients expected to reach 300 million in 2025 [2]

Therefore, it is essential to develop tools that would allow for precise and non-invasive assessment of fat. Specifically, of particular interest is the quantification of fat in liver and skeletal muscle.

Muscle tissue contains intracellular fat (intramyocellular lipid, IMCL) which are stored as spherical droplets in muscle cells, and extramyocellular lipids (EMCL), which are located in long fatty septa of laminar shape, along muscle fibers [3], [4]. Accumulation of both types of fat has been observed in many pathologies [5], [6]. Liver tissue contains intra-hepatocellular lipids (IHL) [7]. Increased levels of IHL (i.e. steatosis) are associated with insulin resistance and type-2 diabetes. Although hepatic steatosis is a benign condition in the short term, it can progress in some patients to steatohepatitis (NASH) and even cirrhosis after several years. Like obesity, several drugs such as amiodarone, tetracycline, methotrexate and acetaminophen are also able to favor fat accumulation in liver.

There are a number of methodologies employed for quantification of fat [8]. For many years, biochemical and histochemical analyses of biopsies have been the gold standard for the assessment of fat content in liver and muscle. Furthermore, measurements of droplet radius (~micrometers) of the IMCL can also be performed with electron microscopy in ultrathin slices (~0.1 $\mu$ m) of biopsy samples. However, biopsies are invasive and, in addition to patient discomfort, there is always a risk of complications. Therefore, biopsies are not well suited in

longitudinal studies, i.e. for monitoring of disease progression or assessment of therapy efficacy.

*In vivo* quantification of fat can be performed with Computerized Tomography (CT). CT is an imaging methodology that measures the absorption of x-rays in tissues. CT generates images where different tissues can be distinguished on the basis of their absorption/attenuation characteristics, which depend on tissue density and chemical composition. Since the decrease in attenuation is a linear function of increasing fat content, it is possible to measure fat content. However, the radiation exposure – although relatively low – is still a risk factor and represents a limiting factor in the longitudinal studies.

In recent years, Magnetic resonance (MR) techniques, <sup>1</sup>HMR spectroscopy and imaging, have emerged as the method of choice for non-invasive assessment of fat content in liver and muscle [9]–[13]. MR is a methodology that measures the signal emitted by the magnetic spin of <sup>1</sup>H in water and fat and it allows to assess separately the contribution of water and fat by exploiting their differences in resonance frequency.

The aim of the current thesis is to develop state-of-the-art Magnetic Resonance Imaging (MRI) methodology for fat quantitation on a preclinical 4.7 Tesla MRI scanner.

The thesis is structured in 5 chapters:

7. in the first chapter, the basis of Magnetic Resonance Imaging are introduced;
8. in the second chapter, two methods of fat quantification (Dixon's method and IDEAL algorithm) are presented. Moreover simulations were performed to study the IDEAL algorithm;
9. in the third chapter, the methods of fat quantification are applied to MR images of physical phantoms;
10. in the fourth chapter, the methods of quantification are applied to images acquired on mice;
11. in the fifth chapter, the method for generating reference signal for fat-water systems (Fat ViP MRI method) is presented.







# Chapter I

## Introduction to Magnetic Resonance Imaging (MRI)

### 1.1 Magnetic Resonance

The Nuclear Magnetic Resonance (known also as NMR) is a technique which makes use of the magnetic field, generated by nuclei in resonance when an external magnetic field is employed. For realizing this physical phenomenon, nuclei with an intrinsic magnetic moment are necessary: the spin. Examples of nuclei with non-zero spins employed in the NMR are  $^1\text{H}$ ,  $^{13}\text{C}$ ,  $^{15}\text{N}$ ,  $^{19}\text{F}$ ,  $^{23}\text{Na}$  and  $^{31}\text{P}$ . Most common NMR scanners make use of the proton ( $^1\text{H}$ ) magnetic resonance, principally contained in water molecules. From the quantum mechanics theory, the magnetic quantum number  $m_z$  that protons can have when an external magnetic field  $B_0$  (suppose in  $z$ -direction) is applied are  $1/2$  and  $-1/2$  hence, the  $z$ -components of the magnetic moment  $\vec{\mu}$  ( $\mu_z$ ) are

$$\mu_z = \frac{1}{2} \gamma \hbar \quad (\text{for spin-up nuclei})$$

$$\mu_z = -\frac{1}{2} \gamma \hbar \quad (\text{for spin-down nuclei})$$

where  $\gamma$  is gyromagnetic ratio (for hydrogen atoms is equal to 267.52MHz/T) and  $\hbar$  is the constant of Planck ( $h = 6.6 \times 10^{-34}$  J · s) divided by  $2\pi$ . The magnetic moments relative to the nuclei, which pointed in random direction before the application of  $B_0$ , align along the direction of  $B_0$ . Moreover, the external magnetic field  $B_0$  produces the rotation of all magnetic moment  $\vec{\mu}$  explained by the Larmor equation  $\vec{\omega}_0 = -\gamma \vec{B}_0 / 2\pi$  (**Figure 1.1**). For

better understanding the mechanism of an aggregate spin system let  $\vec{M}$  the bulk magnetization vector, defined as  $\vec{M} = \sum_{n=1}^{N_T} \mu_n$  where  $N_T$  is the total number of the spin. The bulk magnetization vector  $\vec{M}$  can be calculated from the Boltzmann relationship. Let  $\frac{N_\uparrow}{N_\downarrow} = \exp\left(\frac{\Delta E}{kT}\right)$  the Boltzmann relationship, where  $N_\uparrow$  represents the number of spin-up nuclei,  $N_\downarrow$  the number of spin-down nuclei,  $\Delta E$  the energy difference between the two spin systems ( $\Delta E = \gamma \hbar B_0$ ),  $k$  the Boltzmann's constant ( $1.38 \times 10^{-23}$  J/K) and  $T$  the temperature of the spin system.

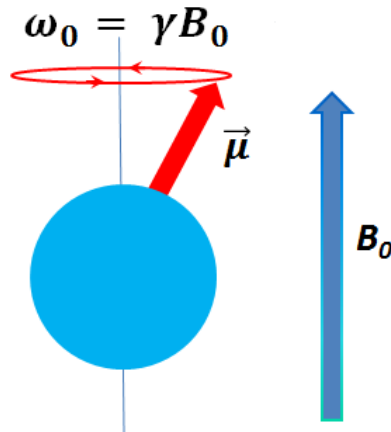


**Figure 1.1:** Precession of the magnetic moment of a proton under effect of an external magnetic field  $B_0$ .

Omitting the mathematical steps the magnitude of  $\vec{M}$  can be written as

$$|M| = \frac{\gamma^2 \hbar^2 B_0 N_T}{4kT} \quad (1.1)$$

The magnetization vector  $\vec{M}$  is parallel to  $B_0$ , and is proportional to the total number of nuclei  $N_T$  and the magnetic field strength  $B_0$ , and inversely proportional to the spin system temperature  $T$ . The transversal component of  $\vec{M}$  is zero since the magnetic moment components on the  $xy$  plane have not phase coherence. The fraction of nuclei which contributes to  $|M|$  is low in fact, using  $B_0 = 1\text{T}$  and  $T = 25^\circ\text{C}$  the fraction is 3 in a million.

A radiofrequency pulse (the  $B_1$  RF pulse or excitation pulse), applied perpendicularly to the  $B_0$  magnetic field, is able to tip the bulk magnetization toward the  $xy$  plane. The bulk magnetization transversal component  $M_{xy}$  is generated, phasing the transversal components of magnetic moments [14] (**Figure 1.2**).

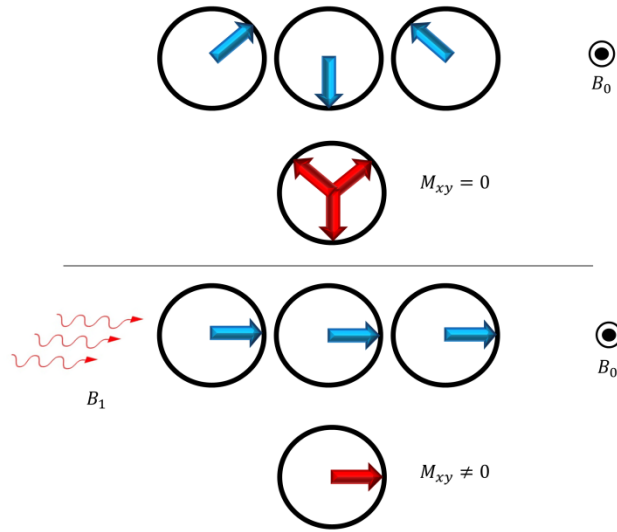


**Figure 1.2:** (Top) Hydrogen nuclei system under effect of an external magnetic field  $B_0$ . The transversal component of  $\vec{M}$  is zero since the magnetic moment components on the  $xy$  plane have not phase coherence. When the excitation pulse is applied on the hydrogen nuclei system, their magnetic moments are aligned, creating a transverse bulk magnetization  $M_{xy}$ .

The angle between the bulk magnetization and the magnetic field  $B_0$  (i.e. in the  $z$ -direction) is named flip angle  $\alpha$  (**Figure 1.3a**). The flip angle is function of the duration, shape and magnitude of the pulse and is given by

$$\alpha = \int_0^t \gamma B_1(t) dt = \int_0^t \omega_{B_1}(t) dt \quad (1.2)$$

where  $t$  is the duration of the pulse. An excitation pulse with sinc shape corresponds in the Fourier transform to a rectangular function (**Figure 1.3b**). If  $B_1$  has a rectangular shape, the resulting flip angle is equal to

$$\alpha = \gamma B_1 t = \gamma \omega_{B_1} \quad (1.3)$$

The evolution of the bulk magnetization is described by the Bloch equation, explained in the next paragraph.

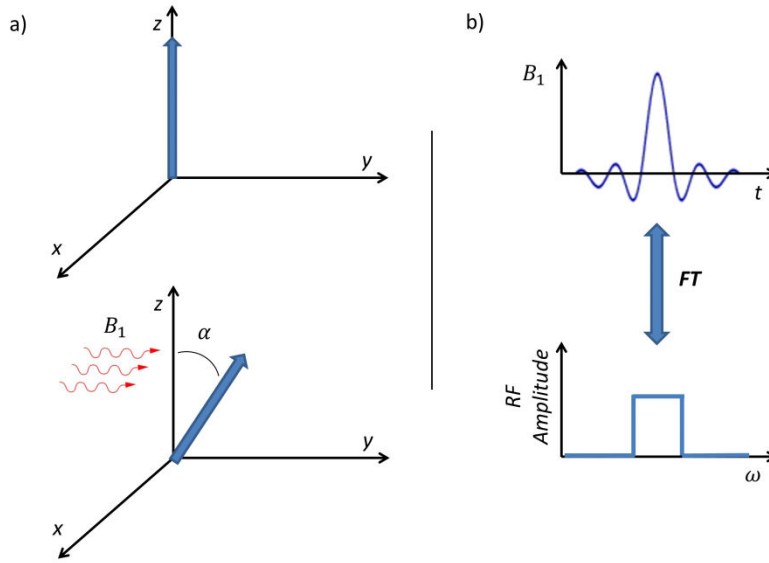


**Figure 1.3:** a) The magnetization vector is tipped toward the x-y plane in presence of the excitation pulse. b) A  $B_1$  RF pulse with sinc shape corresponds in the Fourier transform to a rectangular function

## 1.2 The Bloch equation

The excitation pulse makes turn the bulk magnetization  $\vec{M}$  in the transversal plane, it rotates in this plane while it comes back to its equilibrium in the longitudinal direction. The time-depending equation which describes the bulk magnetization motion after the excitation is described with the following equation by Felix Bloch [15]:

$$\frac{d\vec{M}(t)}{dt} = \gamma \vec{M}(t) \times \vec{B}(t) - \frac{M_x(t)\vec{i} + M_y(t)\vec{j}}{T_2^*} - \frac{(M_z(t) - M_z^0)\vec{k}}{T_1} \quad (1.4)$$

where  $M_z^0$  is the value of  $\vec{M}$  in presence of the  $B_0$  only and  $T_2^*$  and  $T_1$  are named spin-spin and spin-lattice relaxation times, respectively. The Bloch equation could be divided in 3 components:

$$\begin{cases} \frac{dM_x}{dt} = (\gamma \vec{M}(t) \times \vec{B}(t))_x - \frac{M_x(t)}{T_2^*} \\ \frac{dM_y}{dt} = (\gamma \vec{M}(t) \times \vec{B}(t))_y - \frac{M_y(t)}{T_2^*} \\ \frac{dM_z}{dt} = (\gamma \vec{M}(t) \times \vec{B}(t))_z - \frac{(M_z(t) - M_z^0)\vec{k}}{T_1} \end{cases} \quad (1.5)$$

and define

$$M_{xy} = M_x + iM_y. \quad (1.6)$$

It is possible to demonstrate that, in the Larmor frequency rotating frame, the term:

$$(\gamma \overline{M}(t) \times \overline{B}(t)) = 0. \quad (1.7)$$

So, calling  $x'$ ,  $y'$  and  $z'$  the axis in the rotating frame and grouping the first 2 equations of the system equations, it could be written in the following form:

$$\begin{cases} \frac{dM_{x'y'}(t)}{dt} = -\frac{M_{x'y'}(t)}{T_2^*} \\ \frac{dM_{z'}}{dt} = -\frac{(M_z(t) - M_z^0)\vec{k}}{T_1}. \end{cases} \quad (1.8)$$

The solutions of these two first-order differential equations are respectively:

$$M_{x'y'}(t) = M_{x'y'}(0)e^{-t/T_2^*} \quad (1.9)$$

$$M_{z'}(t) = M_{z'}(0)e^{-t/T_1} + M_z^0(1 - e^{-t/T_1}) \quad (1.10)$$

where  $M_{z'}(0)$  represents the value of the longitudinal magnetization immediately after the RF pulse. Hence  $T_2$  represents the time necessary to  $M_{x'y'}$  to reach the 33% of the initial transverse magnetization value  $M_{x'y'}(0)$ . Simultaneously,  $T_1$  represents the time necessary to  $M_{z'}$  to recover the 66% of the longitudinal magnetization value at equilibrium  $M_z^0$ . The  $T_1$  and  $T_2^*$  relaxation times depend on several factors:

- Structure and composition of the tissue or object to study;
- $B_0$  magnetic field;
- Surrounding structures.

In **Figure 1.4**, the trajectory of the magnetization  $\vec{M}$  is illustrated.

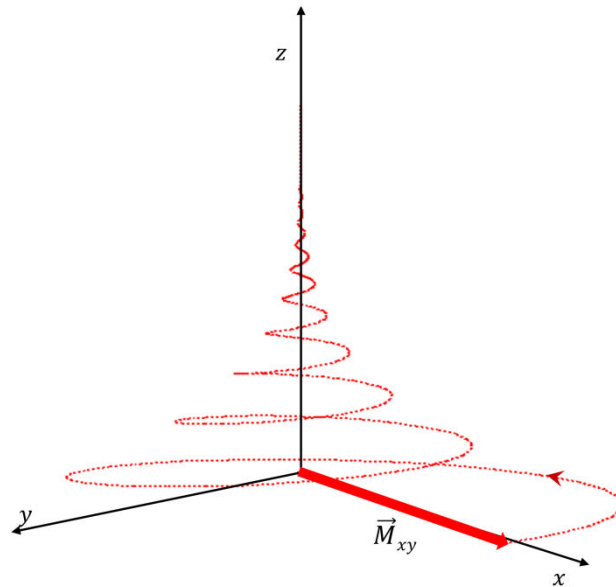


**Figure 1.4:** Trajectory performed by the bulk magnetization after having tipped toward the x-y plane. The bulk magnetization returns to the equilibrium along the z-axis, rotating in the xy plane.

The equations can be written in the laboratory frame

$$M_{xy}(t) = M_{xy}(0)e^{-t/T_2^*} e^{-i\omega t} \quad (1.11)$$

$$M_z(t) = M_z(0)e^{-t/T_1} + M_z^0 \left(1 - e^{-t/T_1}\right) \quad (1.12)$$

where the factor  $e^{-i\omega t}$  takes in account of the rotation of the magnetization vector in the transverse plane. So  $\vec{M}$  rotates at Larmor frequency, losing the  $M_{xy}$  component and recovering the longitudinal magnetization  $M_z$ .

### 1.3 MRI Pulse sequence

The MRI pulse sequence is a scheme which summarizes all the pulses and gradients used for acquiring the MR images. The pulse sequence is composed by 2 parts:

- The RF excitation pulses, which are necessary for obtaining the magnetic resonance effect;
- The spatial encoding gradients, which are necessary for selecting the interested area to acquire. The spatial information is given by the inverse Fourier transform of the k-space, built using phase and frequency encoding gradient.

The information about the shapes and durations of the pulses and gradients employed for acquiring the MR images are represented in the MRI pulse sequence. There exist three types of gradients and they will be explained in the current section.

### 1.3.1 Slice selection gradient

The RF pulse excites the interested area to analyze. The slice thickness  $\Delta z$  of the area to analyze is connected with the bandwidth of the RF pulse  $\Delta\omega$  and the gradient strength from the relation

$$\Delta z = \frac{\Delta\omega}{\gamma G_z} \quad (1.13)$$

where  $\gamma$  is the gyromagnetic factor (267.58MHz/T for hydrogen atom) and  $G_z$  the gradient strength in the z direction (the one orthogonal to the slice of interest). In **Figure 1.5** a scheme of this mechanism is illustrated.

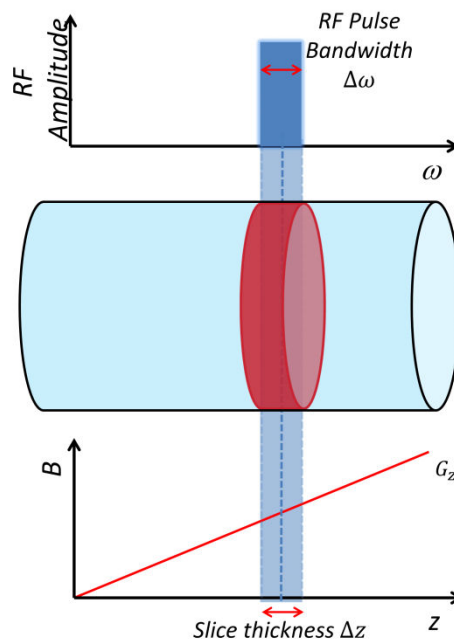


**Figure 1.5:** Scheme of the mechanism for selecting the slide to analyze. The object, under effect of a gradient  $G_z$  is excited by the excitation pulse. The slice thickness depends on the bandwidth  $\Delta\omega$  of the pulse and on the gradient strength.

### 1.3.2 Phase encoding gradient

After the excitation due to the RF pulse, the phase encoding gradient is applied along a direction orthogonal to  $G_z$  (i.e.  $G_y$ ). With the phase encoding gradient  $G_y$ , the phases of the magnetization vectors (aligned after the action of the excitation pulse) along the y axis are



linearly varied (**Figure 1.6**). In this way for each  $y$  position a phase is associated. The process is repeated for each repetition time depending on the chosen  $y$  matrix size.

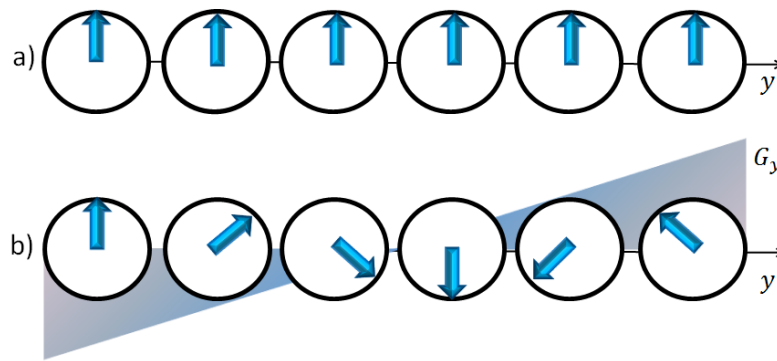


**Figure 1.6:** The phases of the magnetization vectors along the  $y$ -direction are linearly varied under effect of the phase encoding gradient  $G_y$

The phase  $\phi(t)$  accumulated by the magnetization vector along the  $y$ -direction is given by the following equation

$$\phi(t) = \gamma y G_y t \quad (1.14)$$

where  $y$  is the position,  $t$  the time and  $G_y$  the gradient along the  $y$ -direction.

### 1.3.3 Frequency encoding gradient

The frequency encoding gradient is applied on the third dimension ( $x$ -direction) for allowing the spatial localization of the signal. It is called readout gradient as well, in fact the gradient  $G_x$  is active when the signal is collected. Similarly to the phase encoding gradient, the frequency encoding gradient is applied along the  $x$  axis to linearly vary the frequency (**Figure 1.7**). Thus, for each  $x$  position a frequency  $\omega$  is associated (**Figure 1.7**). Along the  $x$  direction, the frequency  $\omega$  is equal to

$$\omega(x) = \omega_0 + \gamma G_x x \quad (1.15)$$

and the magnetic field

$$B = B_0 + G_x x \quad (1.16)$$

The scheme of the three gradients applied for the spatial localization is illustrated in **Figure 1.8**.

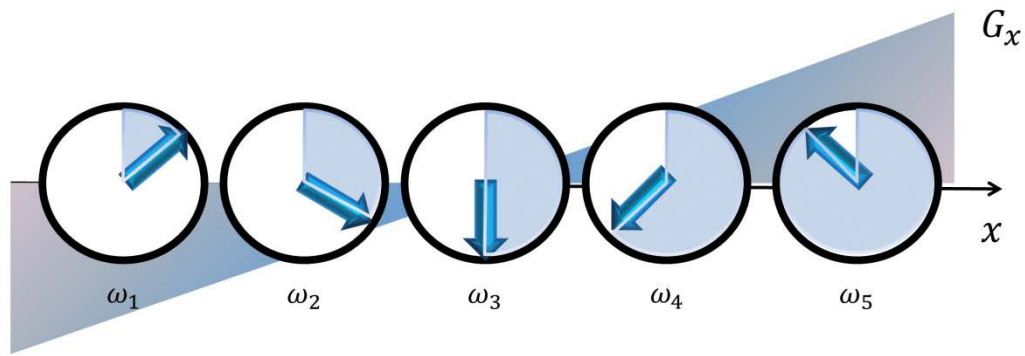


**Figure 1.7:** Similarly to the phase encoding gradient, the frequency encoding gradient  $G_x$  varies the magnetization vectors along the  $x$ -direction. The blue areas within the circles indicate the area covered by each magnetization vector in the unit time. The areas increase along the  $x$ -direction.

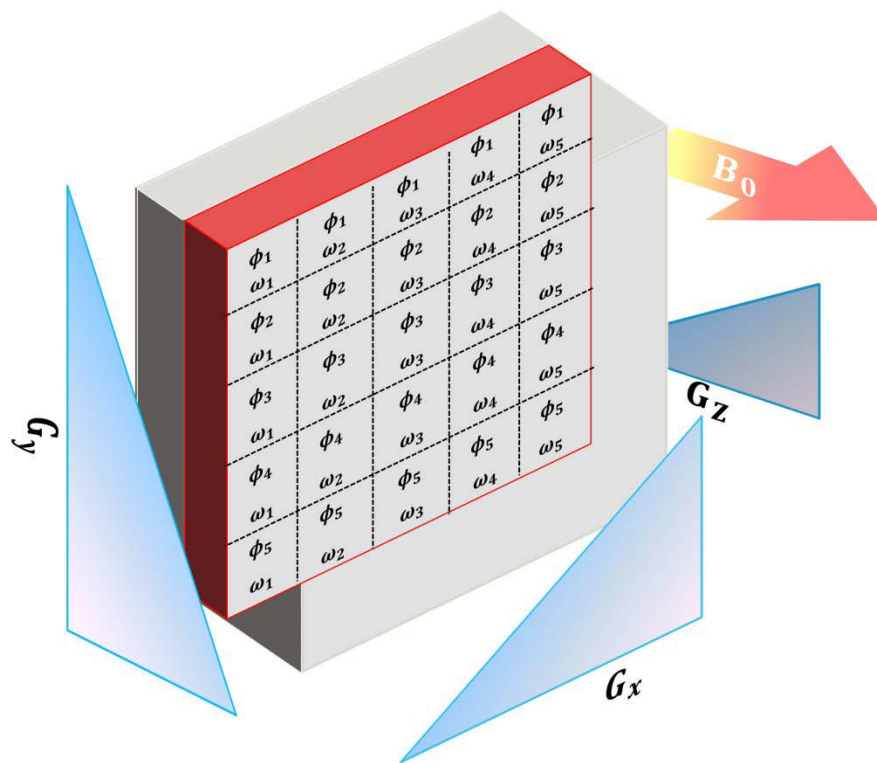


**Figure 1.8:** Scheme of the action of the three gradients along the three directions.  $G_z$  determines the slice thickness (with the bandwidth of the B1 RF pulse),  $G_y$  the dephasing  $\phi_n$  along the  $y$ -direction,  $G_x$  the new Larmor frequencies  $\omega_n$  along the  $x$ -direction.

### 1.3.4 K-space

The signals with the phase and frequency information are used for filling the  $k$ -space matrix.

The element  $(k_x, k_y)$  of this matrix are calculated as

$$\begin{cases} k_x = \gamma G_x \tau / 2\pi \\ k_y = \gamma G_y t / 2\pi \end{cases} \quad (1.17)$$

where  $\tau$  is the dwell time ( $1/BW$ , where  $BW$  is the receiver bandwidth) and  $t$  the duration of the phase encoding gradient. For acquiring more k-space lines, the excitation pulse and the gradients are repeated  $N_{ph}$  times where  $N_{ph}$  is the sample number in the phase encoding direction. The time between two excitation pulses is called repetition time (TR). Thus after a TR a k-space line is acquired. The time between the excitation pulse and the frequency encoding gradient is the echo time (TE). The elements on the frequency encoding direction are acquired at each dwell time at the opening of the analog-to-digital converter (ADC). The ADC window is opened when the frequency encoding gradient is active. In **Figure 1.9** an image representing the acquisition of the k-space is shown.

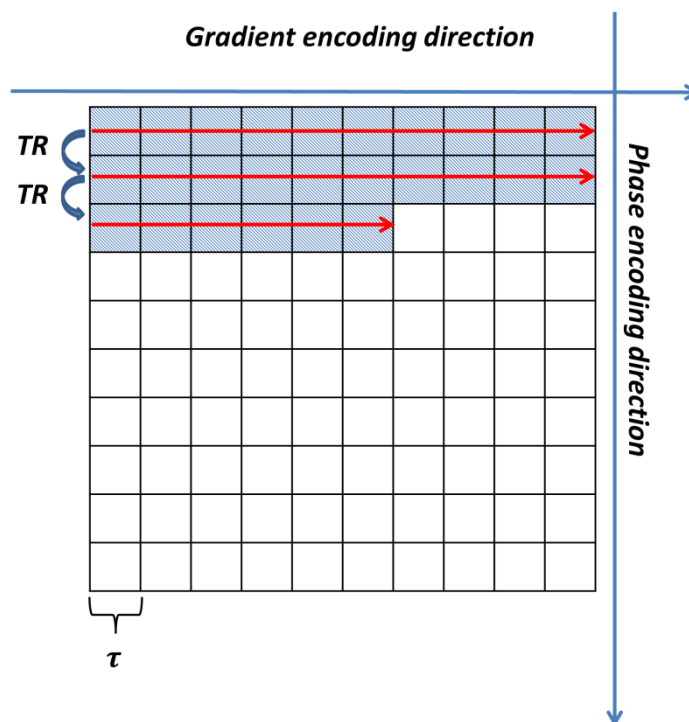


**Figure 1.9:** K-space acquisition. Each line is acquired in a repetition time TR, when the ADC window is opened. The ADC is opened when the frequency encoding works. Each pixel will contain the signal sampled in a dwell time  $\tau$ . This procedure is repeated depending on the sample number in the phase encoding direction.

At the end of the k-space acquisition, the 2-D fast Fourier transform is calculated for converting the image from the frequency domain to the spatial domain.

### 1.3.5 Spoiled gradient echo sequence

The spoiled gradient echo sequence allows to acquire images in rapid procedure. Differently from the spin echo sequences, the gradient echo sequence allows to use flip angle lower than  $90^\circ$  reducing the repetition time TR and, hence, the acquisition time ( $= N_{ph} * TR * N_{av}$

where  $N_{av}$  is the number of averages, used for increasing the signal-to-noise ratio). The gradient echo is originated by switching the frequency encoding gradient which, firstly dephases the magnetization vectors, then it changes the polarity for refocusing the magnetization vectors. In **Figure 1.10** the scheme of the formation of the gradient echo is represented. From the time 0 to  $\tau$  the frequency encoding gradient is turned on for dephasing the magnetization vectors. At time  $\tau$  there is the maximum dephasing between the magnetization vectors. From time  $\tau$  and  $3\tau$  the frequency encoding gradient reverses the polarity keeping the same amplitude and makes rephase the magnetization vectors. At instant  $2\tau$ , the magnetization vectors are realigned: at this instant the signal is maximum. After the instant  $2\tau$  the magnetization vectors continue dephasing until arriving to instant  $3\tau$  where the spins reach the maximum dephasing. The analog-to digital converter (ADC) is open from the instant  $\tau$  to  $3\tau$ .

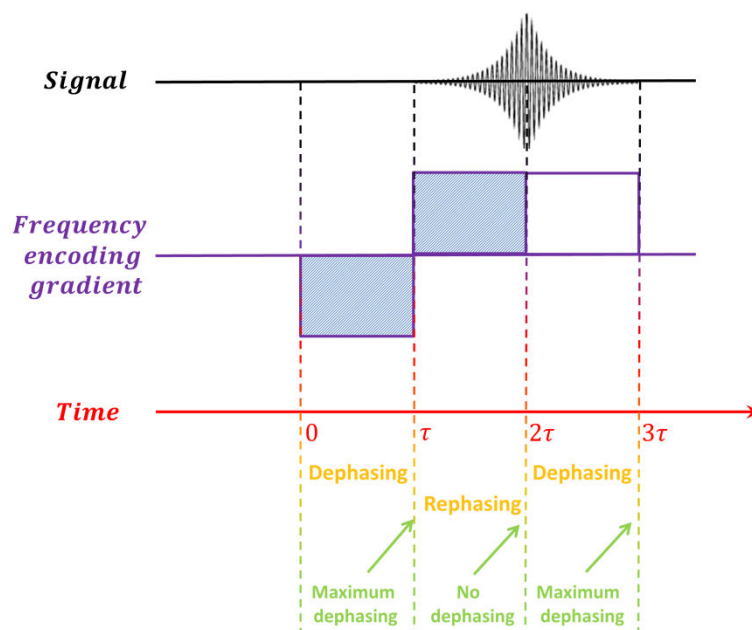


**Figure 1.10:** Formation of the gradient echo. The frequency encoding gradient firstly dephases the transverse magnetization vectors, and then the gradient reverses the polarity. When the frequency encoding reverses the polarity, the ADC window is opened and begins to acquire the signal.

At last a spoiled gradient destroys the remaining transverse magnetization. After having explained the principle of the formation of the echo in gradient echo sequences, the chronogram in **Figure 1.11** could be shown. Multiple lines are represented for examining the shape and the duration, slice, phase and frequency encoding gradients and the excitation pulse.

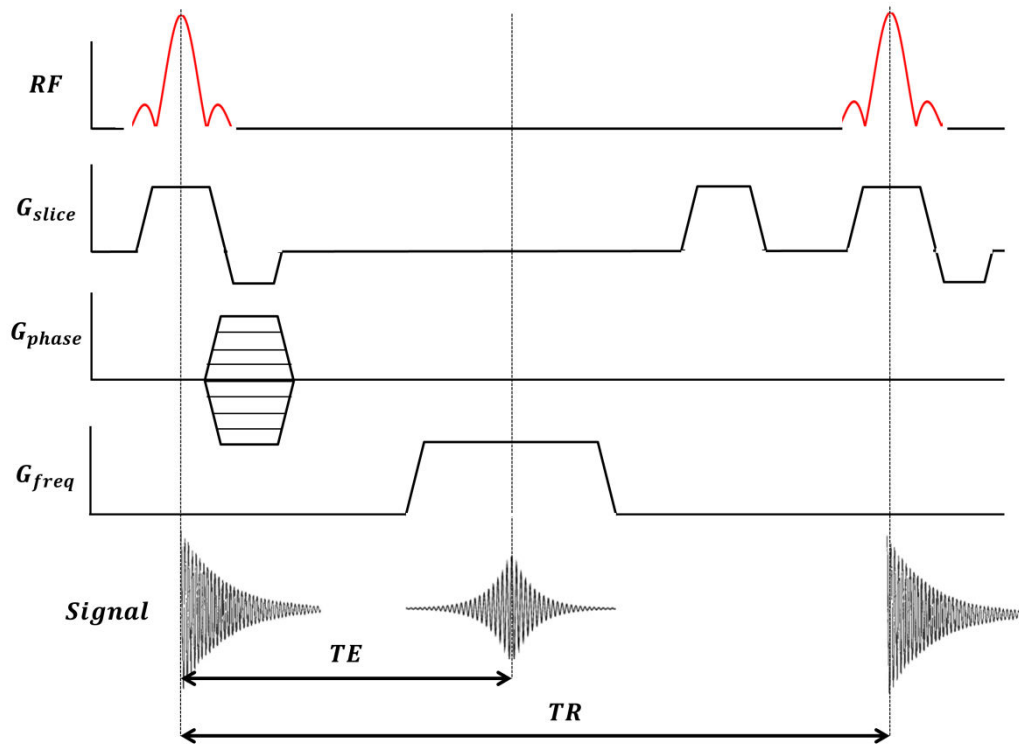


**Figure 1.11:** Spoiled gradient echo sequence. The shape and duration of the gradients and excitation pulses are indicated here.

In gradient echo sequence, the signal equation ( $S$ ) is

$$S(TR, \alpha, TE) = K\rho_0 \sin(\alpha) e^{-TE/T_2^*} \frac{(1 - e^{-TR/T_1})}{(1 - \cos(\alpha)e^{-TR/T_1})} \quad (1.18)$$

where  $K$  is a constant depending on the sensitivity of the receiver,  $\rho_0$  the amplitude of the signal,  $\alpha$  the flip angle,  $TE$  the echo time,  $T_2^*$  the spin-spin relaxation time,  $TR$  the repetition time and  $T_1$  the spin-lattice relaxation time.  $T_1$  and  $T_2^*$  depend on the MR properties of the object to examine, whereas  $TR$ ,  $\alpha$  and  $TE$  are the sequence parameters chosen by the user.

#### 1.4 Fat signal

Thanks to the use of the  $^1\text{H}$  magnetic resonance imaging, the signal deriving from the hydrogen atoms is mapped. This technique allows to have an idea of the distribution of water molecules in subjects. An external magnetic field causes the rotation of the hydrogen magnetic moments with a frequency determined from the Larmor equation. Nevertheless, hydrogen atoms are largely contained in fat molecules as well. In **Figure 1.12** (top), the

triglyceride molecule is illustrated: it is composed by carbon, oxygen and hydrogen atoms. However, fat hydrogen atoms have different precession respect to the water hydrogen atoms. The reason of the different precession is due to the different chemical species (i.e. water and fat) which have different Larmor frequencies. Moreover, the Larmor frequency changes for different assignments of the fat chain (**Fig. 1.12**, below), which have different amounts of electron shielding.

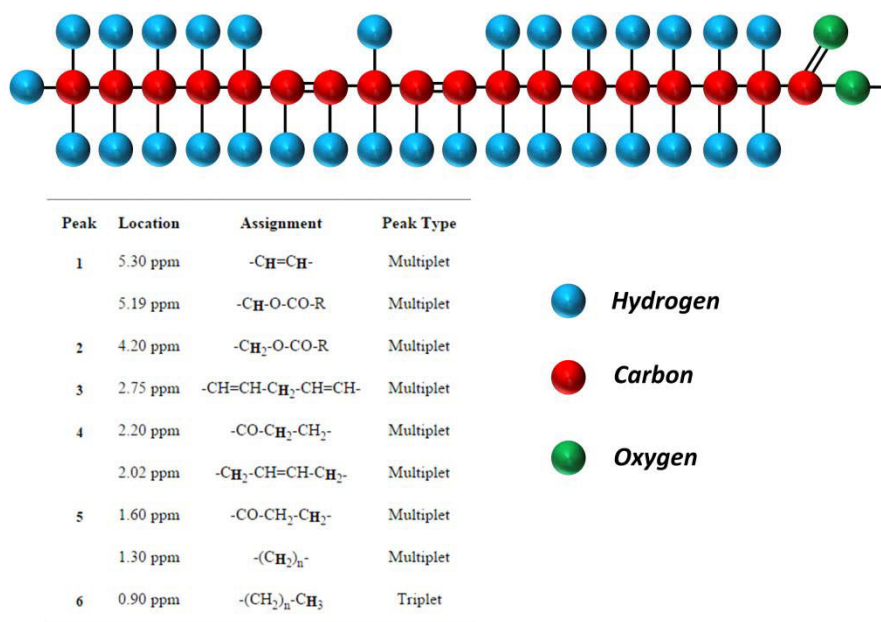


**Figure 1.12:** (Top) Structure of the triglyceride molecule, composed by carbon, oxygen and hydrogen. Depending on the different assignments of the fat chain, the Larmor frequencies for the hydrogen nuclei are different. The localization of each fat peak is illustrated in the table below.

In **Figure 1.13** a spectrum of a cream containing water and fat is illustrated. At 4.7ppm the peak relative to the water hydrogen signal is located. The fat spectrum is composed by multiple peaks principally situated on right (at lower ppm) respect to the “water peak”. The primary fat peak is off from the water peak of 3.4ppm (at 4.7T about 700Hz and include in it about the 70% of the fat signal).



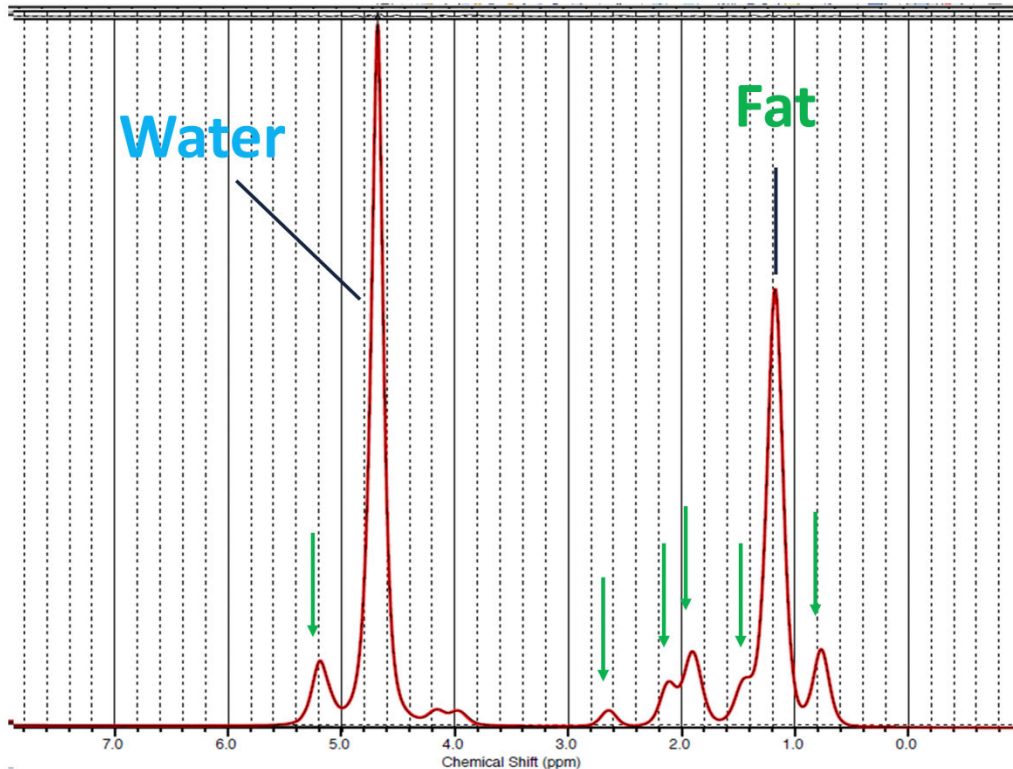


**Figure 1.13:** Spectrum of the water and fat (triglycerides). The water peak is positioned at 4.7ppm. The primary fat peak is off from the water peak of 3.4ppm (at 4.7T about 700Hz). The fat spectrum is composed by other smaller peaks which resonate at different frequencies. The positions of these last peaks are indicated with green arrows

### 1.5 Choice of the repetition time TR, TE and flip angle in the MRI acquisition

The repetition time TR and flip angle  $\alpha$  influences the signal intensity of the images to acquire. Morphological and physiological information, useful for clinicians and researcher, depend on the combination of TR and flip angle. For studying the effects of these two parameters, it is necessary to analyze the form of the signal equation. In the gradient echo sequence, the signal  $S$  is described by **Equation 1.18**. This equation is valid for a single chemical specie: instead, in case of multiple chemical species (for example water and fat) the equation should take in account of multiple  $T_1$  and  $T_2^*$  values. In this scenario, water and fat signals are separately calculated with the **Equation 1.18** (with the respective values), and then the total signal is summed using the respective values. Reminding the constraint  $TE < TR$ , the MR sequence parameters shown in the **Equation 1.18** ( $TR, \alpha, TE$ ) are chosen in function of the type of study to effectuate. In the next paragraph the different kind of images are explained in detail.

### 1.5.1 Weighted images

Considering the complete knowledge of the MR properties of the object to examine, clinicians and researcher investigate on 3 types of images containing the signal information described in the aforementioned equation:

- $T_1$  weighted images: the user chooses a TR and flip angle values in way to exploit the terms  $e^{-TR/T_1}$ ,  $\sin(\alpha)$  and  $\cos(\alpha)$ . In this acquisition, the longitudinal magnetization is not totally recovered and the chemical species having shorter  $T_1$  (fat) has a higher signal than the one having longer  $T_1$  (water). In fat-only zones, the fat results brighter respect to water in water-only zones.
- $T_2^*$  weighted images: the user chooses long TR and TE values in way to exploit the terms  $e^{-TE/T_2^*}$ . In this acquisition, the chemical species having shorter  $T_2^*$  has a higher signal than the one having longer  $T_2^*$ .
- Proton density images: in this acquisition, the longitudinal magnetization is completely recovered and the images show the no weighted signal coming from the sum of different chemical species. For having this kind of images, a combination of short TR and low flip angle, or long TR are used. Hence the real relationship between fat and water is only achieved with this configuration.

For fat fraction measurements, different types of images could be acquired: if proton density images and  $T_2^*$  weighted images are acquired for calculating fat fraction, this last is called proton density fat fraction (if the algorithm which use this kind of images take in account of the  $T_2^*$  relaxation effect). Instead, the  $T_1$  weighted images transfer a  $T_1$  bias on the fat fraction measurement, due to the  $T_1$  value of fat shorter than the water one. It means that in presence of  $T_1$  bias the fat fraction is overestimated and it depends on the amount of fat content. For minimizing the  $T_1$  bias, two solutions are proposed: the first one consists to choose a long TR in way to recover the longitudinal magnetization, the second one focus on taking a combination of short TR and small flip angle. An example of  $T_1$  and  $T_2^*$  weighted images could be better explained looking at plots in **Figure 1.14**, respectively. Water and fat have different  $T_1$  and  $T_2^*$  values and the choice of the repetition time and echo time to acquire the image is essential. On the left of **Figure 1.14**, a plot representing the recovery of the longitudinal signal for fat (green curve) and water (blue curve) after the excitation pulse versus the time is shown. After the excitation pulse, the water and fat longitudinal signals, starting from 0, increase with  $(1 - e^{-TR/T_1})$ . Since  $T_1$  of fat is shorter than the water one, the



longitudinal signal of fat increase faster until it arrives at plateau before the water signal. Hence, considering the water and fat content equal, the green curve, relative to fat signal is always on top: at any moment the image is acquired, the fat-only zones are always brighter (without considering the  $T_2^*$  effect) than the water ones. For avoiding the  $T_1$  bias, the image is acquired at short TR (and low flip angle, before the separation of the two curves) or at high TR (when the longitudinal signal is completely recovered, or almost, for both chemical species). Obviously, for improving the signal-to-noise ratio, it is necessary to increase the number of averages. Another solution could be to take the image with a certain TR and flip angle such that the longitudinal signals are recovered. On the right of **Figure 1.14**, a plot representing the loss of transversal signal for fat (green curve) and water (blue curve) after the excitation pulse versus the time is shown.

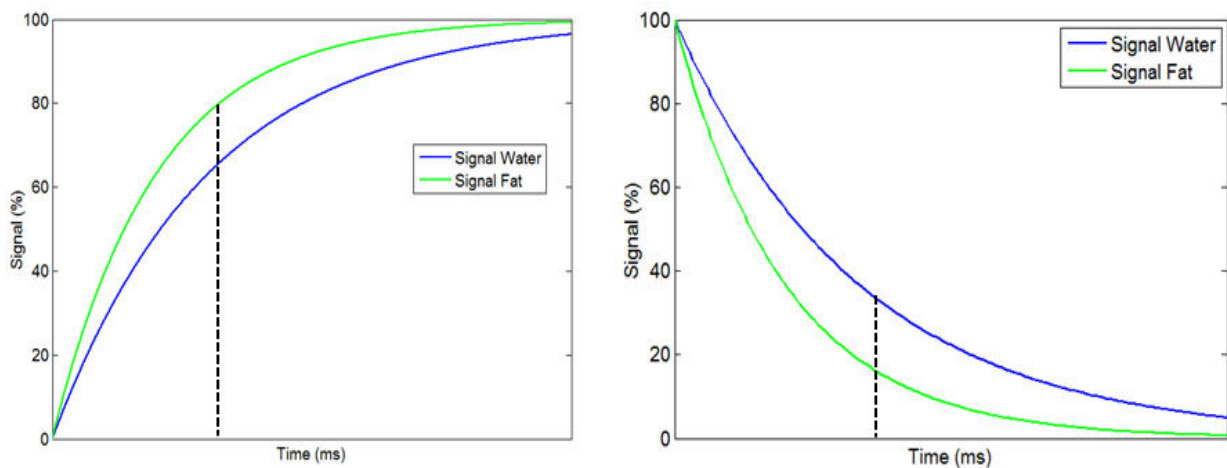


**Fig.1.14:** (Left) Plot of the longitudinal magnetization versus the time. The longitudinal magnetization is recovered with the increasing of time depending on the  $T_1$ . In this plot the water (blue curve) and fat (green curve) longitudinal magnetizations are represented. (Right) Plot of the transversal magnetization versus the time. The transversal magnetization is lost with the increasing of time depending on the  $T_2^*$ . In this plot the water (blue curve) and fat (green curve) transversal magnetizations are represented.

After the excitation pulse, the water transversal signals, starting from their maximum signals, decrease with  $e^{-TE/T_2^*}$ . If there are the same fat and water content but different  $T_2^*$  values (considering  $T_2^*$  for fat shorter than the water one) the fat curve is always below the water one. For avoiding the  $T_2^*$  bias, the image is acquired at short echo time. Theoretically, the image could be acquired at high echo time as well but the signals are really smaller respect to the first case. The solution could be to acquire more averages to increase the SNR but the acquisition time increases too much, without bringing any advantage respect to the first case.

### 1.5.2 Ernst angle

Researchers acquire  $T_1$  weighted images in order to improve the SNR, and the  $T_1$  bias is corrected *a posteriori* knowing the  $T_1$  of fat and water. For increasing the SNR, a solution commonly used in literature is to employ the Ernst angle. The Ernst angle represents the angle in relation of a specific TR in which the SNR of an image MR is maximum. Considering the **Equation 1.18** and calculating the angle for which the signal is maximum, the equation is derived for  $\alpha$  and the result is the following relation

$$\alpha = \arccos\left(e^{-TR/T_1}\right) \quad (1.19)$$

Hence, the only request for knowing the Ernst angle is to know the  $T_1$  of the chemical species to analyze. The image acquired with the Ernst angle is  $T_1$  weighted if

$$TR < 3 * T_1 \quad (1.20)$$

i.e. it does not recover over the 95% of the longitudinal signal.

## 1.6 Magnetic field inhomogeneity

Magnetic moments  $\vec{\mu}$  under effect of an external magnetic field  $B_0$  rotate with frequency  $\vec{\omega}_0 = -\gamma\vec{B}_0$ . Vendors offer MR scanners at different magnetic field and the most common are 1.5 and 3T. However when an object is inserted in the scanner bore, the magnetic field lines are deflected. These deflections cause an inhomogeneity in the magnetic field. The magnetic field inhomogeneity smoothly changes the Larmor frequency at different spatial locations. After the action of the excitation pulse, the magnetic field inhomogeneity causes the rotation of the bulk magnetization in different way on each area; only along the isopotential lines (the lines where the magnetic field inhomogeneity are equivalent) the Larmor frequencies are equal. After a time  $t$  from the excitation pulse, on each area, a phase between the magnetization vector (with the new Larmor frequency) and the magnetization vector with 0 magnetic field inhomogeneity (with the Larmor frequency relative to the magnetic field of the scanner) is accumulated. The phase information is transparent in magnitude images but the complex data, constituted by real and imaginary information, are not. In **Figure 1.15** (left) an example of magnetic field inhomogeneity map (or field map) calculated treating in appropriate way the phase or, similarly, the complex images. Multi-

gradient-echo images were acquired with a scanner with 4.7T magnetic field. In **Figure 1.15** right, the values in Hz along a vertical profile drawn on the field map are plotted. The range of values of the field map is about [-100Hz, 400Hz], hence 500Hz in difference between maximum and minimum values.

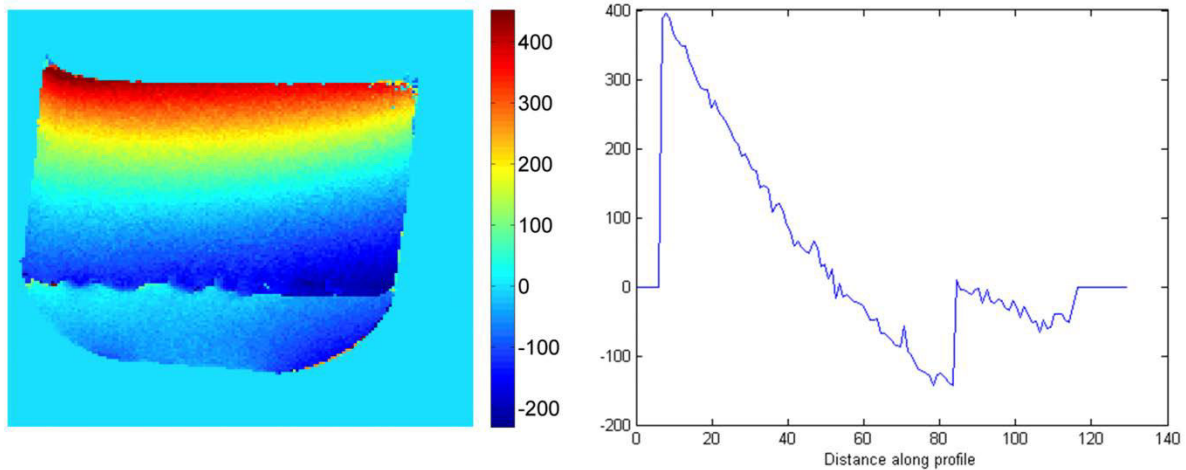


**Figure 1.15:** (Left) Field map calculated using the phase information. (Right) Vertical profile of the values drawn on the field map.

Now we calculate the magnetic field necessary to obtain 200Hz of value in the field map. The magnetic field employed was 4.7T and the Larmor frequency associated is 200MHz, whereas the magnetic field associated to 200Hz is  $4.7 \times 10^{-7}$ T. Thus for generating a value of 200Hz, using a scanner at 4.7T, an additional magnetic field of strength  $4.7 \times 10^{-7}$ T is required. In order of magnitude, the magnetic field inhomogeneity is 7 times smaller than the magnetic field  $B_0$ .

In the next paragraph, the effect of the magnetic field inhomogeneity on the phase maps, the phase wrapping, is discussed.

### 1.6.1 Phase wrapping

The range of values of a phase map is  $[-\pi; \pi]$  and their values smoothly change. However, if in a region, the phase exceeds one of these values, the problem of phase wrapping comes out. In other terms, between two adjacent regions, a phase discontinuity equal to  $2\pi$  exists. Thus the continuity of the values in this scenario is lost. In **Figure 1.16** an example of phase wrapping on the same image illustrated in **Figure 1.15** is shown. The values on the profile

drawn on the image illustrated the jump between two regions in proximity of each wrap. In this case, the phase map needs to be corrected with phase unwrapping algorithms to be used.

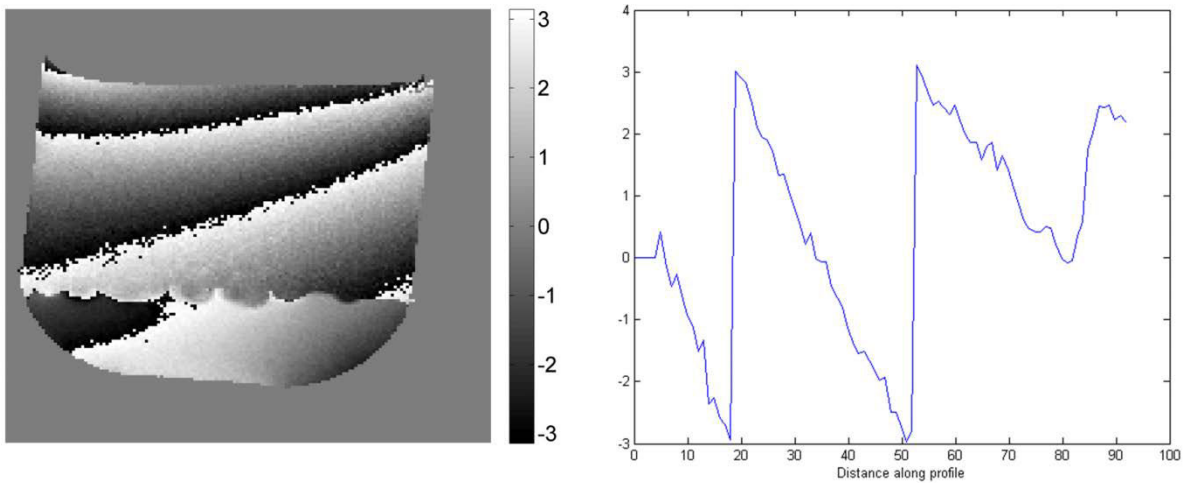


**Figure 1.16:** (Left) Phase map relative to the MR image acquired: the map is not smooth in fact the vertical profile of the values drawn on the map shows discontinuity in proximity of each wrap.

## 1.7 Magnetic susceptibility

Experimentally, there exists a linear relation between the magnetization vector  $\vec{M}$  and the magnetic field  $\vec{B}_0$ . The constant between these two physical quantities depends on the magnetic properties of the substance. The relation is

$$\vec{M} = (1 + \chi_m)\vec{B}_0 \quad (1.21)$$

where  $\chi_m$  is the magnetic susceptibility of the substance. In according to the values that  $\chi_m$  could have, 4 types of substances with different magnetic behavior occur:

- Diamagnetic behavior: these substances are characterized by a negative value of  $\chi_m$ . The order of magnitude reached by  $\chi_m$  is  $10^{-6}$ ;
- Paramagnetic behavior:  $\chi_m$  is positive and in the order of magnitude  $10^{-5}$ ;
- Ferromagnetic behavior:  $\chi_m$  is positive and achieves large values, normally higher than  $10^2$ ;
- Superparamagnetic behavior: the small ferromagnetic particles are part of an intermediate class which exists between the paramagnetic and ferromagnetic behaviors.

The effect of two different magnetic susceptibilities is visible in the field map as well. In **Figure 1.17** the same plot shown in **Figure 1.15** is illustrated more in detail. The object contained water and vinegar and, the profile of the values show a jump in the proximity of the separation between water and oil.

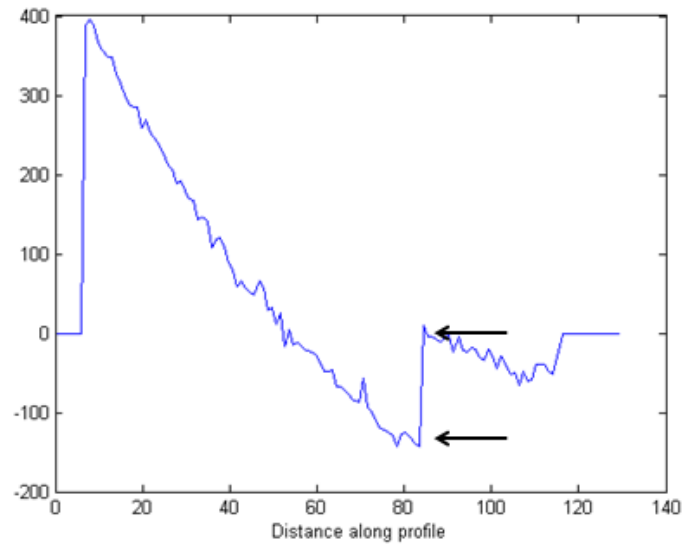


**Figure 1.17:** Profile of the values shown in **Figure 1.15**. The arrows show the jump of values passing from the oil to the water.





## Chapter II

# Water-fat separation with chemical shift imaging techniques

### 2.1 Introduction

MRI methods for fat quantification are based on the principle of chemical shift imaging [16]. In the  $H^1$ -MRI, the hydrogen nuclei are mapped and the most of the signal derives from the water and fat molecules. MRI exploits the fact that water protons precesses at a different frequency than fat protons, the difference (i.e., the chemical shift) being 3.4ppm. Thus, in gradient echo sequences, the water and fat protons are in phase with each other at certain echo times ( $TE = 0, 1.45, 2.9ms$  at 4.7T, for example), whereas at other TEs ( $TE = 0.7, 2.1, 3.5ms$  at 4.7T) the water and fat protons are  $180^\circ$  out of phase with each other. In one of the first methods proposed for fat quantification (the Dixon's method [16]) the fat content was obtained using the “in-phase” and “out-of-phase” MR images. In the last decade, a similar method has been proposed for fat quantification (IDEAL [17], *Iterative Decomposition of water and fat with Echo Asymmetry and Least-squares estimation*), capable to work using asymmetric phases as well.

In this chapter, an overview of these two methods for fat quantification is presented. The method IDEAL, which is the main topic of this thesis, will be analyzed in detail with the use of simulations.

### 2.2 Dixon's method

#### 2.2.1 Introduction

All algorithms for fat/water quantification are based on the knowledge of the chemical shift difference between fat and water spins. After the excitation pulse, the fat and water spins rotate with different rotational speed, depending on the proton resonance of different chemical species and on the magnetic field of the MR scanner. As previously said, the water peak (placed at 4.7ppm) is off from the principal fat peak of 3.4 ppm, hence, at 4.7T, the difference in frequency is about 700 Hz. This means that, after 1.45ms, the fat spins have completed one rotation around the water spins (**Figure 2.1**).



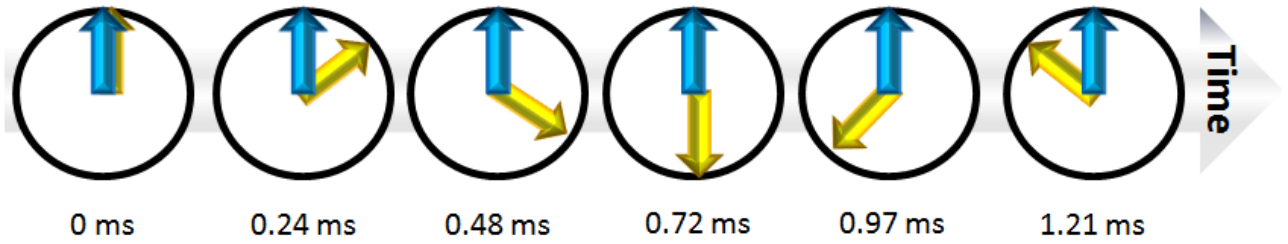


**Figure 2.1:** Scheme of the precession of the fat spins (yellow arrow) as a function of time in the water rotating frame. The water spins (blue arrow) are considered fixed in this frame. The period of the fat spins respect to the water spins lasts 1.45ms.

The first of these algorithms was developed by Dixon in 1984 and takes the name of “Dixon’s method” [16]. It requires the acquisition of two MR images: a first image, where the fat spins are in phase with the water spins, and a second image where fat and water spins are in opposition of phase (**Figure 2.2**). After its introduction, the Dixon’s method has been constantly improved [18]–[20] and the latest version is the mDixon algorithm [21], where multiple images at different echo times are acquired to calculate fat fraction and  $T_2^*$  maps. In the following paragraph the 2 and 3-point Dixon’s method will be analyzed more in detail.

### 2.2.2 2-point Dixon’s method

Using the in-phase and out-of-phase magnitude images, with simple mathematical steps, it is possible to determine the water and fat maps. The in phase  $IP(x, y)$  and out of phase  $OP(x, y)$  images can be written as:

$$\begin{cases} IP(x, y) = W(x, y) + F(x, y) \\ OP(x, y) = W(x, y) - F(x, y) \end{cases} \quad (2.1)$$

where  $W(x, y)$  and  $F(x, y)$  are respectively the water and fat signal in the pixel  $(x, y)$  (**Figure 2.2**). Solving the system of **Equations 2.1**:

$$\begin{cases} W(x, y) = \frac{IP(x, y) + OP(x, y)}{2} \\ F(x, y) = \frac{IP(x, y) - OP(x, y)}{2} \end{cases} \quad (2.2)$$

we obtain the  $W(x, y)$  and  $F(x, y)$  as function of  $IP(x, y)$  and  $OP(x, y)$  The fat fraction ( $FF$ ) is calculated as:

$$FF(x, y) = \frac{F(x, y)}{W(x, y) + F(x, y)} * 100 = \frac{IP(x, y) - OP(x, y)}{2 * IP(x, y)} * 100 \quad (2.3)$$

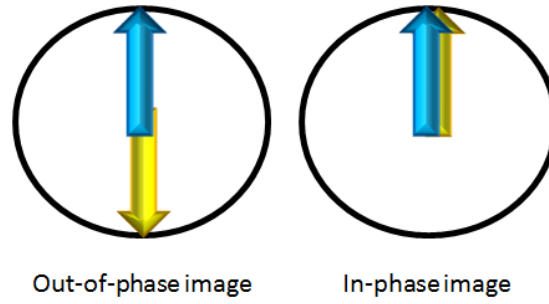


**Figure 2.2:** Scheme of the water and fat spins positions in the images acquired in the Dixon's method. In the out-of-phase image (left), the water and fat spins are antiparallel, in the in-phase image (right) the spins are parallel. In the rotational frame the water spins (in blue) are stationary. No magnetic field inhomogeneity is considered in this scheme.

The first Dixon's method, also called two-point Dixon's method, does not take into account of the possibility that the fat signal could be higher than the water one. Actually, for including this scenario, the equation relative to the out of phase image should be rewritten:

$$OP(x, y) = |W(x, y) - F(x, y)| \quad (2.4)$$

using the absolute value. Due to the nature of the magnitude images,  $OP(x, y)$  cannot reach negative values and, hence, the absolute bracket are necessary. If  $F(x, y) < W(x, y)$  the equation remains in the same form, otherwise

$$OP(x, y) = F(x, y) - W(x, y) \quad (2.5)$$

$OP(x, y)$  should be rewritten changing the sign inside the absolute bracket. However, *a priori*, it is not possible to determine the right sign for each pixel. Moreover, if the system of **Equations 2.1** is used for determining the fat fraction, a complication could emerge. In fact the pixel in the fat fraction map, which should contain more fat than water, actually displays less than 50% of fat fraction. In the worst scenario of 100% fat fraction, the fat fraction map will reveal 0%. For better understanding the problem behind the 2-point Dixon's method, the equations can be written as:

$$\begin{cases} IP(x, y) = (W(x, y) + F(x, y))e^{i\phi_0(x, y)} \\ OP(x, y) = (W(x, y) - F(x, y))e^{i[\phi(x, y) + \phi_0(x, y)]} \end{cases} \quad (2.6)$$

where  $\phi(x, y)$  represents the phase accumulated because of the magnetic field inhomogeneity in the pixel  $(x, y)$  and  $\phi_0$  the phase errors due to the system imperfections, both expressed in Hz. If the absolute values are applied to these equations they turn into the system of **Equations 2.1**. The phase information is completely transparent in magnitude data, but it could be helpful to quantify fat fraction higher than 50%, without falling in the water-fat

calculus ambiguity. However, the system of equations cannot be solved with two equations (two images). For calculating the fat and water maps, it is necessary to know  $\phi_0(x, y)$  and  $\phi(x, y)$ . To sum up, the real problem of using this method is the coexistence of a double solution, the first one where  $W > F$  and the other one where  $F > W$ ; for eliminating this ambiguity, the phase accumulated  $\phi(x, y)$  and the phase errors  $\phi_0(x, y)$  need to be calculated. In the 3-point Dixon's method, another image is acquired to calculate  $\phi(x, y)$  and  $\phi_0(x, y)$ .

### 2.2.3 3-point Dixon's method

For eliminating the fat-water ambiguity, the 3-point Dixon's method [18] was proposed by Glover in 1991. Consider the generalized equations of the 2-point Dixon's method:

$$\begin{cases} IP(x, y) = (W(x, y) + F(x, y))e^{i\phi_0(x, y)} \\ OP(x, y) = (W(x, y) - F(x, y))e^{i[\phi(x, y) + \phi_0(x, y)]} \end{cases} \quad (2.7)$$

In these equations, 4 unknowns have to be calculated for solving the system of equations (the water signal  $W$ , the fat signal  $F$ , the phase accumulated  $\phi$  and the phase offset  $\phi_0$ , for each pixel). In this section, a different solution, given by Wang et al. [22]–[24] is explained. For solving the system of equations, three equations are necessary for having a unique solution: another image is acquired when the water and fat signal are in phase:

$$\begin{cases} IP_1(x, y) = (W(x, y) + F(x, y))e^{i[\phi_0(x, y)]} \\ OP(x, y) = (W(x, y) - F(x, y))e^{i[\phi_0(x, y) + \phi(x, y)]} \\ IP_2(x, y) = (W(x, y) + F(x, y))e^{i[\phi_0(x, y) + 2\phi(x, y)]} \end{cases} \quad (2.8)$$

The term  $e^{i[\phi_0(x, y)]}$  is brought to the left part of the equations:

$$\begin{cases} IP_1(x, y)e^{-i\phi_0(x, y)} = (W(x, y) + F(x, y)) \\ OP(x, y)e^{-i\phi_0(x, y)} = (W(x, y) - F(x, y))e^{i[\phi(x, y)]} \\ IP_2(x, y)e^{-i\phi_0(x, y)} = (W(x, y) + F(x, y))e^{2i[\phi(x, y)]} \end{cases} \quad (2.9)$$

The phase errors  $\phi_0(x, y)$  can be calculated from the first equation. Then the equations can be rewritten using the first equation and considering that the term in the first equation can be substituted with the magnitude value:

$$\begin{cases} |IP_1(x, y)| = (W(x, y) + F(x, y)) \\ OP(x, y) \frac{IP_1^*(x, y)}{|IP_1(x, y)|} = (W(x, y) - F(x, y))e^{i[\phi(x, y)]} \\ IP_2(x, y) \frac{IP_1^*(x, y)}{|IP_1(x, y)|} = (W(x, y) + F(x, y))e^{2i[\phi(x, y)]} \end{cases} \quad (2.10)$$

The term  $\phi(x, y)$  is calculated using the first and third equation. Once  $\phi(x, y)$  is calculated, the absolute value is applied to the third equation:

$$\begin{cases} |IP_1(x, y)| = (W(x, y) + F(x, y)) \\ OP(x, y) \frac{IP_1^*(x, y)}{|IP_1(x, y)|} = (W(x, y) - F(x, y))e^{i[\phi(x, y)]} \\ |IP_2(x, y)| = (W(x, y) + F(x, y)) \end{cases} \quad (2.11)$$

Using the first and third equation, the sum between the water and fat signal can be written in one of the two following forms:

$$W(x, y) + F(x, y) = \sqrt{|IP_1(x, y)||IP_2(x, y)|} \quad (2.12)$$

$$W(x, y) + F(x, y) = \frac{|IP_1(x, y)| + |IP_2(x, y)|}{2} \quad (2.13)$$

for increasing the SNR. Using the variable  $p$  defined as:

$$p(x, y) = \cos\left(\angle\left(OP(x, y) \frac{IP_1^*(x, y)}{|IP_1(x, y)|} e^{-i[\phi(x, y)]}\right)\right) \quad (2.14)$$

The water and fat signal can be obtained as:

$$\begin{cases} W(x, y) = \frac{1}{2}\left(\sqrt{|IP_1(x, y)||IP_2(x, y)|} + p(x, y)|OP(x, y)|\right) \\ F(x, y) = \frac{1}{2}\left(\sqrt{|IP_1(x, y)||IP_2(x, y)|} - p(x, y)|OP(x, y)|\right) \end{cases} \quad (2.15)$$

The sign of  $p$  allow to know when  $W(x, y) > F(x, y)$  or vice versa. Hence, the fat-water ambiguity is eliminated using the 3-point Dixon's method.

#### 2.2.4 Modifications on the 3-point Dixon's method

Some modifications on the 3-point Dixon's method were proposed. The modifications concern the calculus of the field map. The first and third images, both acquired when the water and fat are in phase, are used for calculating the field map, with the following equation:

$$\psi(x, y) = \frac{\phi_{IP_1}(x, y) - \phi_{IP_2}(x, y)}{2\pi\Delta TE} \quad (2.16)$$

where  $\phi_{IP1}$  and  $\phi_{IP2}$  represent the phase image at first and second (in phase) image, respectively, and  $\Delta TE$  is the difference between the echo times ( $TE_3 - TE_j$ ). The system of equations can be written as:

$$\begin{cases} IP(x, y) = (W(x, y) + F(x, y))e^{i2\pi\psi(x,y)TE_1}e^{i\phi_0(x,y)} \\ OP(x, y) = (W(x, y) - F(x, y))e^{i2\pi\psi(x,y)TE_2}e^{i\phi_0(x,y)}. \end{cases} \quad (2.17)$$

The exponential terms are brought to the other side:

$$\begin{cases} W(x, y) + F(x, y) = IP(x, y)e^{-i2\pi\psi(x,y)TE_1}e^{-i\phi_0(x,y)} \\ W(x, y) - F(x, y) = OP(x, y)e^{-i2\pi\psi(x,y)TE_2}e^{-i\phi_0(x,y)} \end{cases} \quad (2.18)$$

and the two equations are summed:

$$\begin{cases} F(x, y) = e^{-i\phi_0(x,y)} \frac{IP(x, y)e^{-i2\pi\psi(x,y)TE_1} - OP(x, y)e^{-i2\pi\psi(x,y)TE_2}}{2} \\ W(x, y) + F(x, y) = IP(x, y)e^{-i2\pi\psi(x,y)TE_1}e^{-i\phi_0(x,y)}. \end{cases} \quad (2.19)$$

When the fat map  $F$  (or water map  $W$ ) is calculated, it is substituted into the second equation for calculating the second unknown. The fat and water map are explicated as:

$$\begin{cases} F(x, y) = e^{-i\phi_0(x,y)} \frac{IP(x, y)e^{-i2\pi\psi(x,y)TE_1} - OP(x, y)e^{-i2\pi\psi(x,y)TE_2}}{2} \\ W(x, y) = e^{-i\phi_0(x,y)} \left( IP(x, y)e^{-i2\pi\psi(x,y)TE_1} - \frac{IP(x, y)e^{-i2\pi\psi(x,y)TE_1} - OP(x, y)e^{-i2\pi\psi(x,y)TE_2}}{2} \right) \end{cases} \quad (2.20)$$

the absolute brackets are applied to both equations:

$$\begin{cases} |F(x, y)| = \left| \frac{IP(x, y)e^{-i2\pi\psi(x,y)TE_1} - OP(x, y)e^{-i2\pi\psi(x,y)TE_2}}{2} \right| \\ |W(x, y)| = \left| \frac{IP(x, y)e^{-i2\pi\psi(x,y)TE_1} + OP(x, y)e^{-i2\pi\psi(x,y)TE_2}}{2} \right| \end{cases} \quad (2.21)$$

and the fat fraction can be calculated.

The form of the system of **Equations 2.21** is equal to the one of the system of **Equations 2.2**. Thus, the third image (the second one “in phase”) is acquired only for the field map calculation. The exponentials inside the absolute brackets allow to avoid the fat-water swapping. However, if the magnetic field inhomogeneity is too high, this algorithm could

give problems since the phase could wrap and cause incorrect results. In order to avoid the miscalculation, algorithms which help to unwrap the phase are necessary. Moreover, the 3-point Dixon's method does not take into account of the  $T_2^*$  relaxation time. Recently, a novel Dixon's method (mDixon [21]) has been proposed for calculating the  $T_2^*$  maps, in addition to the fat fraction maps.

To summarize, the 2-point Dixon's method uses magnitude images and can be applied to scenario where the fat-water ambiguity is not a problem (for instance, in tissue like liver, where the fat percentage is always lower than 50%). Fat-water ambiguity might occur in tissues like skeletal muscle where large portion of subcutaneous fat or fat fasciae between different muscles are present. To solve the fat-water ambiguity, the 3-point Dixon's method, which uses complex images, is necessary.

## 2.3 IDEAL

### 2.3.1 Introduction

The 3-point Dixon's method partially solves the problem of fat-water ambiguity calculating the phase map. However, when a high magnetic field inhomogeneity occurs, phase wrapping could appear in the calculus of the phase map. In this case, the 3-point Dixon's method miscalculates the fat fraction and it needs an additional algorithm which unwraps the phase. In 2004, Reeder et al. [17] proposed a new algorithm, based on the acquisition of minimum 3 images, for calculating fat fraction without the use of phase-unwrapping algorithm. The fat-water separation algorithm, improved during the years and employed by the General Electric Company, required in input complex data, that is magnitude and phase images. The algorithm takes the name of IDEAL [17], [25]. In contrast to Dixon's methods, this method uses images taken when the fat signal is in asymmetric positions respect to the water signal. In the next paragraphs, the IDEAL algorithm will be explained and, in the appendix A, the IDEAL equations are described in detail.

### 2.3.2 IDEAL algorithm

The first version of the algorithm did not consider the multi-peak nature of the fat spectrum, but only the primary peak, positioned at 1.3ppm. Furthermore,  $T_2^*$  relaxation effects were neglected [17]. Thus, the signal equation was:

$$S(t_n) = (W + F e^{i2\pi\Delta f t_n}) e^{i2\pi\psi t_n} \quad (2.22)$$

where  $S$  is the signal acquired at echo time  $t_n$  (TE),  $W$  and  $F$  the water and fat component, respectively,  $\Delta f$  the chemical shift frequency of the fat peak respect to the water one and  $\psi$  ( $\psi = \phi/2\pi t$ ) the magnetic field inhomogeneity (or field map). The IDEAL algorithm requires complex images to estimate the field map  $\psi$  and the fat fraction. The algorithm works following the steps described in **Figure 2.3**.

It's possible to verify that, taking in-phase and out-of-phase images, the equations are equivalent to the ones of the Dixon's method. Reeder et al. in [25] found for the IDEAL algorithm the best combination of TEs for maximizing the SNR in the estimation of water and fat images. Considering the rotating frame (where the water signal is fixed and the fat signal rotates), the best positions of fat signal respect to the water one, for acquiring the images and obtaining the best noise performance with 3 images, are

$$\begin{cases} 1^\circ \text{ Echo} = -\frac{\pi}{6} + k\pi \\ 2^\circ \text{ Echo} = \frac{\pi}{2} + k\pi \\ 3^\circ \text{ Echo} = \frac{4}{3}\pi + k\pi \end{cases} \quad (2.23)$$

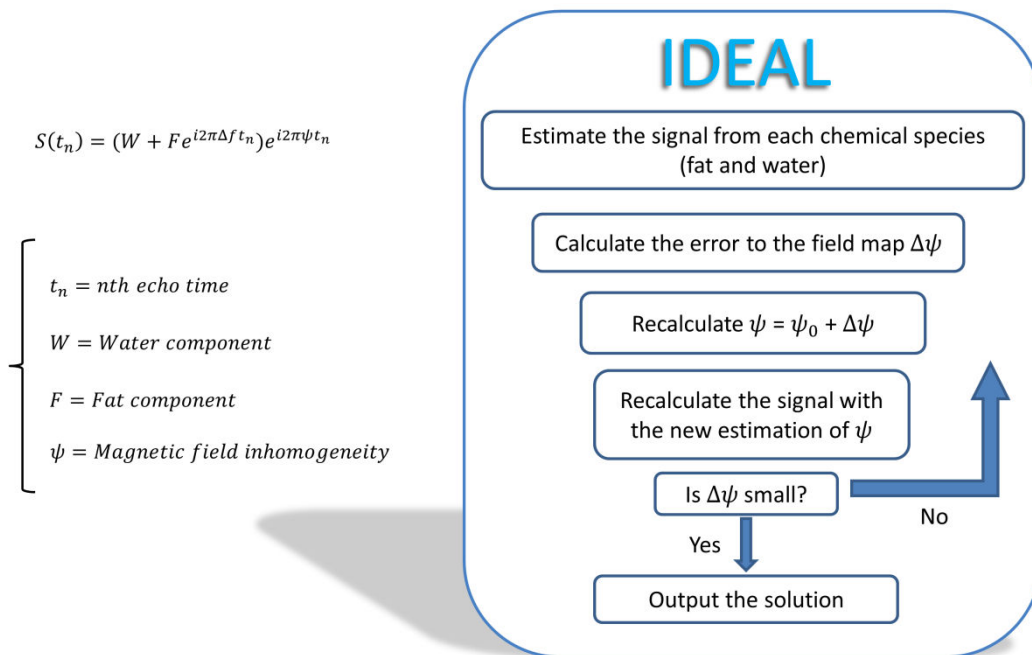


**Figure 2.3:** Scheme of the IDEAL algorithm. It is an iterative algorithm which stops when the error on the magnetic field inhomogeneity is small (e.g. <1Hz). The output of IDEAL algorithm (in the first version) are the fat fraction and field map.

In **Figure 2.4**, the positions of the fat signal respect to the water signal are illustrated. The positions assumed by the fat signal are spaced of  $\frac{2}{3}\pi$ , the maximal angle between the 3 fat signals in  $2\pi$  radians.

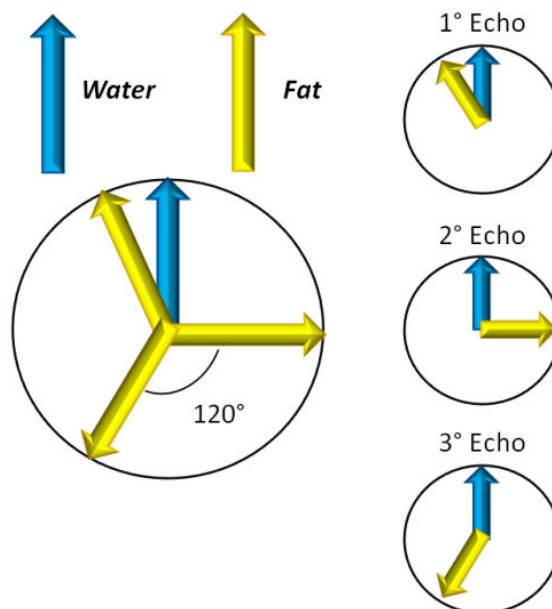


**Figure 2.4:** Scheme of the positions of fat spins (yellow) respect to the water spins (blue), in the rotating frame. The magnetic field inhomogeneity is not considered in this scheme.

However, in this article [17], Reeder et al. suggest to the reader to use short echo times for avoiding the relaxation effects. In fact, no  $T_2^*$  correction was proposed in [17] so, long echo times and/or high iron concentration could alter the results. This last factor is very important in clinical scenarios, since liver with iron overload could be found in some diseases. The  $T_2^*$  correction in IDEAL algorithm is shown for the first time in the article of Yu et al. [26]. The form of the IDEAL equation turns into the following

$$S(t_n) = (W + F e^{i2\pi\Delta f t_n}) e^{i2\pi\psi t_n} e^{-t_n/T_2^*} \quad (2.24)$$

where  $\Delta f$  the chemical shift frequency of the fat peak respect to the water one, and the factor  $e^{-t_n/T_2^*}$  takes into account the spin-spin relaxation effect due to  $T_2^*$ . In this article [26], the resolution of the problem is achieved including the exponentials external to the bracket. They proposed to use a complex field map  $\hat{\psi}$ , connected to  $\psi$  by the following relation

$$\hat{\psi} = \psi - \frac{i}{2\pi T_2^*} \quad (2.25)$$

The steps for calculating the output are basically the same: at the end, the real part of the complex map is the phase map and the imaginary part, opportunely multiplied by a constant,



offers the  $T_2^*$ . Hence, IDEAL algorithm yielded another output over the field map and the fat fraction map: the  $T_2^*$  map.

The early versions of the IDEAL method, presented before, do not consider the complexity of the fat signal. The multi-peak nature of the fat spectrum is well known in literature [27]. For considering this problem, in 2008 Yu et al. [28] showed their improvements on IDEAL algorithm, adding to the equations the term which includes the multiple frequencies relative to the fat signal. In this work [28], Yu et al. employed 3 fat peaks for the water-fat separation, then in [9] the same research group utilized 6 peaks. Hence the signal model changes in

$$s(t_n) = \left( W + F \sum_{i=1}^6 \alpha_i e^{i2\pi\Delta f_i t_n} \right) e^{i2\pi\psi t_n} e^{-t_n/T_2^*} \quad (2.26)$$

where  $\alpha_i$  is the relative area underlying the  $i$ -th fat peak ( $\sum_{i=1}^6 \alpha_i = 1$ ) and  $\Delta f_i$  the frequency shift of the  $i$ -th fat peak respect to the water one.

Two main scripts in Matlab were developed in this thesis:

- one script which implements the IDEAL algorithm (the “IDEAL script”) described above. This script was used to analyze all the *in vitro* and *in vivo* data shown in this thesis;
- one script which allows to generate numerical phantoms. This script is described in detail in the next paragraph.

## 2.4 Numerical phantom

As said above, a script to generate numerical phantoms was implemented in Matlab. This script was used for two purposes:

- to validate the IDEAL script: this validation was necessary to ensure that no errors were present in the IDEAL script;
- to investigate the performances of the IDEAL algorithm (as a function of SNR, field map...).

The numerical phantom was generated with the following signal model

$$S(t_n, \vec{r}) = \left[ W(\vec{r}) + F(\vec{r}) \sum_{i=1}^6 \alpha_i e^{i2\pi\Delta f_i t_n} \right] e^{i2\pi\psi(\vec{r})t_n} e^{-t_n/T_2^*(\vec{r})} \quad (2.27)$$

where  $S$  is the signal,  $t_n$  represents the  $n$ -th echo time,  $\vec{r}$  the spatial position (seven fat peaks are noticeable at 4.7T). In this equation we can distinguish the parameters which depend on tissue proprieties ( $T_2^*$ , fat fraction and fat spectral model), MRI acquisition parameters (echo

times, number of echoes) and experimental parameters (field map). This last equation is equivalent to the **Equation 2.26**. This script allows to generate complex images of disk-shaped phantoms with a given fat fraction,  $T_2^*$  and field map. In addition, the script allows the user to choose the echo times and the number of echoes.

**2.4.1 Validation of the IDEAL script**

The validation of the IDEAL script was performed using images of numerical phantoms. To this purpose, we generated a numerical phantom (**Figure 2.5**) which consisted of multiple disks positioned in columns and rows. The fat fraction values were changed for each row and the  $T_2^*$  for each column. The values of fat fraction ranged from 0 up to 100% with steps of 10%. Moreover, the value of 5% fat fraction was added since it represents the cut-off value between healthy liver and fatty liver. The  $T_2^*$  values were changed from 25 to 5ms with steps of 5ms. A short  $T_2^*$  value of 2ms was added for simulating the scenario of iron overload in liver. In **Figure 2.5**, a scheme of the phantoms is shown.

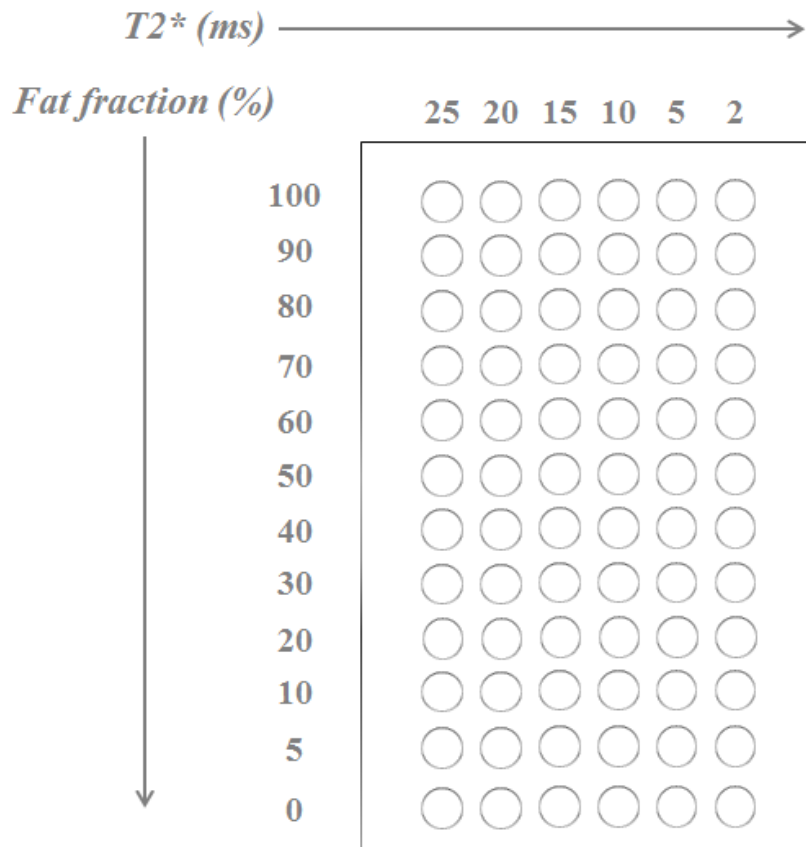


**Figure 2.5:** Scheme of the numerical phantoms used for the validation of the IDEAL script. Twelve values of fat fraction and six values of  $T_2^*$  were employed for testing the IDEAL script. For this purpose seventy-two phantoms were created at 3 echo times (1.5, 4 and 6.5ms).

At last, the images were used for the IDEAL algorithm for calculating fat fraction and  $T_2^*$  values for each phantom.

The other parameters used for the numerical signal were:  $1^\circ$  TE = 1.5ms, echo spacing = 2.5ms. The field map was not considered in this study. The numerical images had matrix size 585x315. A low level of noise (0.5%) was added to the signal in way to not have an infinite SNR. Three echoes were used for calculating fat fraction and  $T_2^*$  maps. The output of IDEAL was compared with the fat fraction and  $T_2^*$  maps used in input for generating the signal. The numerical and experimental (the one calculated with the IDEAL reconstruction) fat fraction maps are illustrated in **Figure 2.6**. The numerical and experimental  $T_2^*$  maps are displayed as well in **Figure 2.7**. The maps relative to the numerical images are similar to the experimental ones.

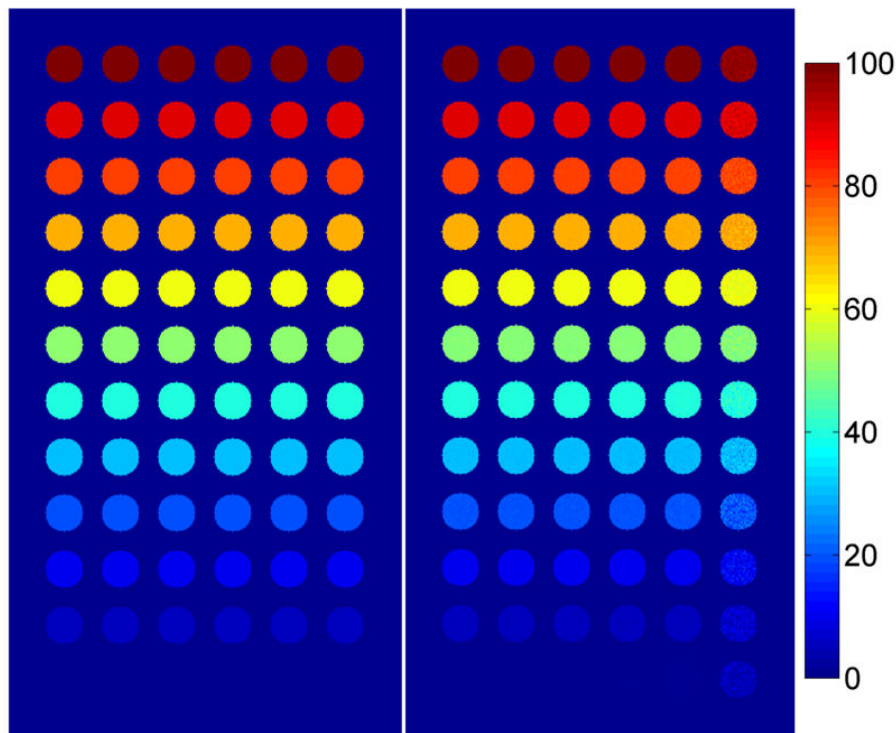


**Figure 2.6:** Numerical (left) and experimental (right) fat fraction maps. The values of fat fraction are well calculated by IDEAL algorithm.

The mean values of fat fractions and  $T_2^*$ s for each phantom were calculated with 14-pixel radius ROIs. The numerical and experimental mean values of fat fraction and  $T_2^*$  are plotted in **Figure 2.8**.

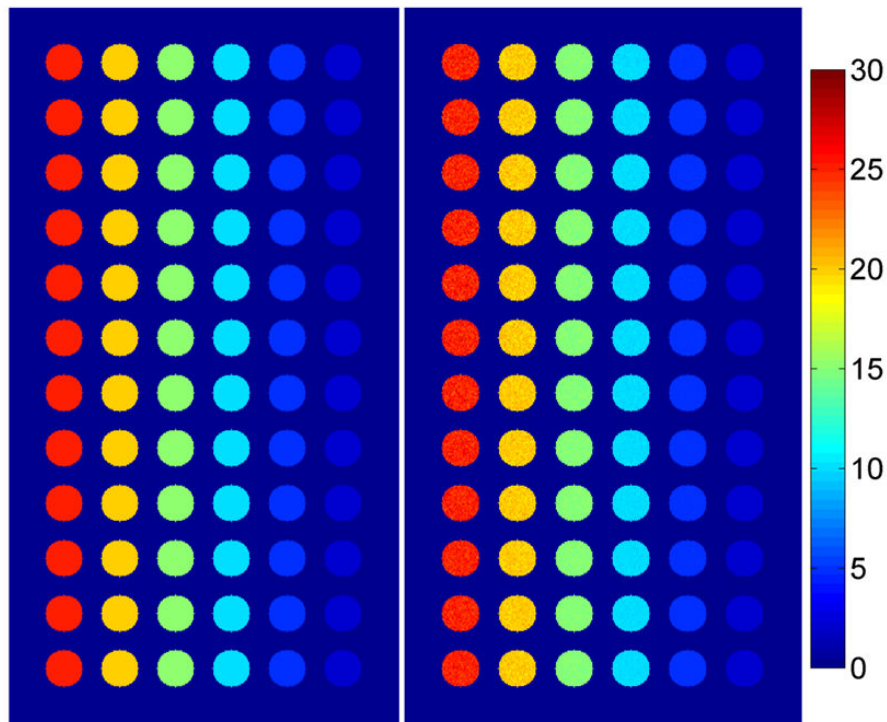


**Figure 2.7:** Numerical (left) and experimental (right)  $T_2^*$  maps. The values of  $T_2^*$  as well are well calculated by IDEAL algorithm.

The equation in each plot represents the equation of the linear data fitting. Excellent correlations exist between the numerical and experimental fat fraction and  $T_2^*$  values. According to these results, the IDEAL script could be validated.

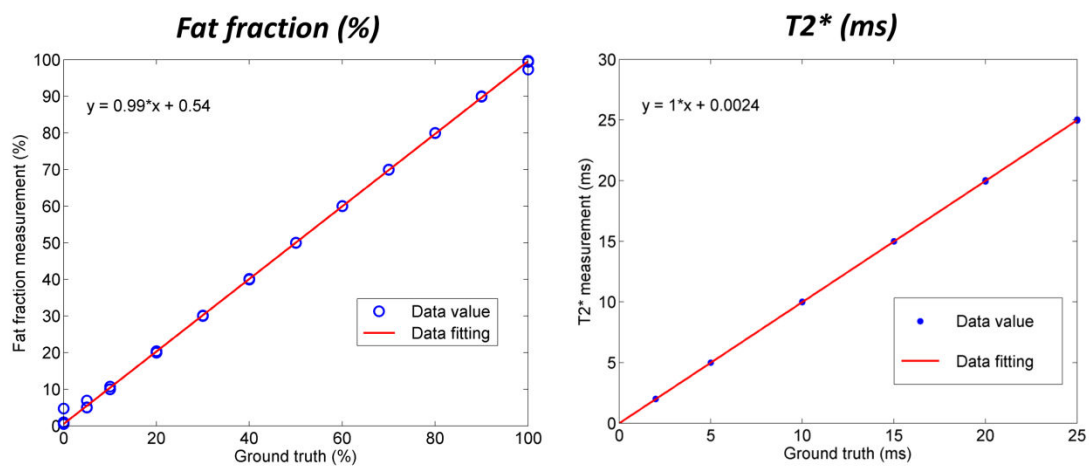


**Figure 2.8:** Numerical versus experimental fat fraction (left) and  $T_2^*$  (right) plots. Excellent correlation between the numerical and experimental values can be verified from the linear data fitting. The equation of the linear data fitting is displayed on each plot.

### 2.4.2 Dependence on the noise

In this paragraph, we investigate the effect of the noise on the IDEAL output. The noise in MR magnitude images is governed by a Rician distribution [29]. Each component of the complex images (i.e. real and imaginary images) is affected by Gaussian noise [30]. So, Gaussian noise was added to the **Equation 2.26**. The parameter which describes the noise level in MR images is the SNR. The SNR depends on many acquisition and experimental parameters, such as number of averages, receiver bandwidth, type of coil, etc. The SNR is defined as  $S/\sigma$ , where  $S$  is the signal and  $\sigma$  the standard deviation of the noise.

The numerical phantoms were generated with the following parameters:

- tissue parameters: fat fraction = 10% and  $T_2^*$  equal to 20 and 10ms. These  $T_2^*$  values represent two values found in muscle and liver, in preliminary measurements on mice at 4.7T;
- MR sequence parameters: gradient echo sequence with first TE = 1.5ms, echo spacing = 2.5ms, number of echoes equal to 3 and 6 echoes. The images were simulated using a 128x128 matrix size;
- experimental parameters: SNR values from 125 to 20. This range was chosen since preliminary measurements of SNR yielded values equal to approximately 40 in mice and 100 in MR phantoms. The field map was not considered in this study.

Here, we explain in more detail the choice of the MR acquisition parameters. With respect to the choice of the echo times (first TE = 1.5ms, echo spacing = 2.5ms), these values were chosen since preliminary MR acquisition and optimization indicated that these were the shortest values allowed on our scanner (with a chosen spatial resolution, receiver bandwidth, etc). It should be noted that the original 3-point IDEAL would yield echo times of 1.5, 2.0 and 2.5ms. However, these values cannot be achieved without heavily compromising image spatial resolution. With respect to the number of echoes, we generated numerical phantoms with 3 and 6 echoes. The 6-point IDEAL was introduced to calculate the  $T_2^*$  in addition to the fat fraction [26]. A comparison between the 3 and 6-echo reconstruction was performed. ROI measurements on  $T_2^*$  and fat fraction maps in all reconstructions were used. The signals (with fat fraction equal to 10%) generated with  $T_2^*$  20ms (in blue) and 10ms (in green) and the echo times (in red) are represented in **Figure 2.9**.

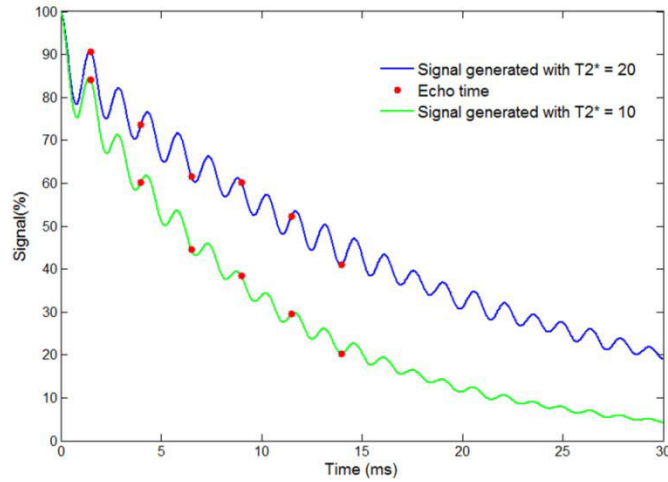


**Figure 2.10:** Signals generated with  $T_2^* = 20\text{ms}$  (in blue) and  $10\text{ms}$  (in green). The 6 echo times used in this simulation (in red) on both curves are represented. For the 3-echo reconstruction, the shorter 3 echo times were selected.

Means and standard deviations, calculated with ROIs in both reconstructions, were determined. In **Figure 2.10**, the results of fat fraction and  $T_2^*$  on the signal generated with  $T_2^* = 20\text{ms}$  for different SNRs are illustrated.

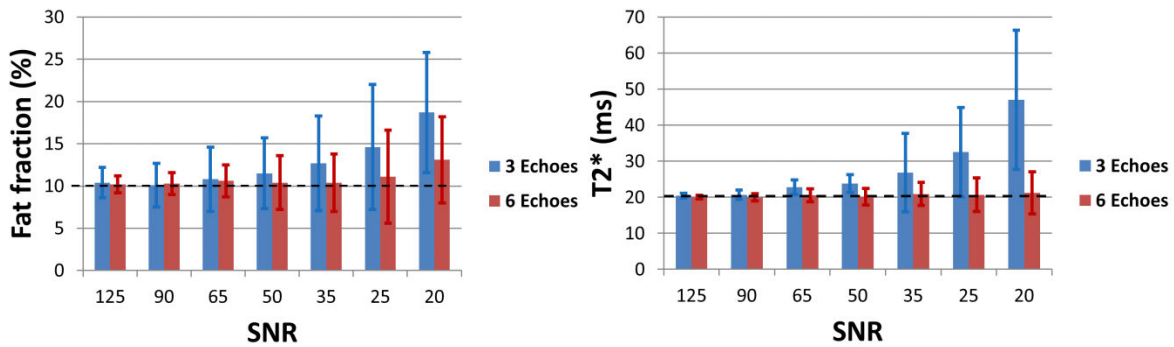


**Figure 2.10:** Results of fat fraction and  $T_2^*$  calculated by the IDEAL algorithm. The results for different SNRs on the signal generated with  $T_2^* = 20\text{ms}$  are shown. The nominal value used in input for fat fraction and  $T_2^*$  is marked with a dot black line (10% for fat fraction and  $20\text{ms}$  for  $T_2^*$ ).

In both reconstructions, when the SNR decreases, the standard deviations increase for both fat fraction and  $T_2^*$  values. The mean values relative to the 3-echo reconstruction in both plots increase with the decreasing of the SNR. In the  $T_2^*$  plot, the mean values for the 6-echo reconstruction are almost equal to the numerical value ( $20\text{ms}$ ). In **Figure 2.11**, the results of IDEAL for the signal generated with  $T_2^* = 10\text{ms}$  are shown. For the fat fraction values, the values of fat fraction relative to both reconstructions are the same. In the  $T_2^*$  plot the increasing of the mean values in the 3-echo reconstruction is lower than the ones in **Fig. 2.10**. In this plot as well, the mean values for the 6-echo reconstruction are almost the same. Thus,

given a sequence with multiple echo times, the IDEAL reconstruction effectuated using the first 6 echoes gives better results than the reconstruction done using the first 3 echoes. The benefits of using more echoes are observed on the  $T_2^*$  estimated values which are closer to the numerical ones.

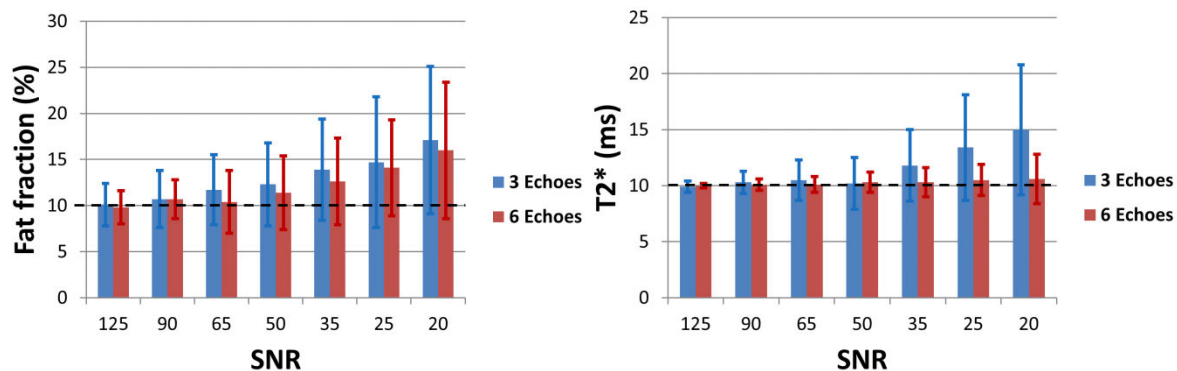


**Figure 2.11:** Results of fat fraction and  $T_2^*$  calculated by the IDEAL algorithm. The results for different SNRs on the signal generated with  $T_2^* = 10\text{ms}$  are shown. The nominal value used in input for fat fraction and  $T_2^*$  is marked with a dot black line (10% for fat fraction and 10ms for  $T_2^*$ )

### 2.4.3 Dependence on spectral model: fat spectrum model and temperature

#### 2.4.3.1 Dependence on the temperature

The Dixon's method and the IDEAL algorithm are based on the knowledge of the frequency shift between the water and the fat peaks. However, this shift could be altered by the change of temperature: in fact the water proton resonant frequency is sensible to it. In particular, the frequency shift rate is equal to  $0.01\text{ppm}/^\circ\text{C}$  [31]–[33] which, at 4.7T, is above  $2\text{Hz}/^\circ\text{C}$ . A decrease in temperature corresponds to an increasing of the frequency shift between the water and the primary fat peak. Likewise, an increasing in temperature makes decrease this frequency shift. In the case where multiple objects with different temperature are positioned inside the scanner (i.e. a mouse with a smaller phantom) the user has to consider the temperature shift. In **Figure 2.12**, two spectra, one taken on a mouse (top) and another one taken on phantom (bottom) having a different temperature (both inserted in the scanner bore), are represented. The water peak is positioned at 4.7ppm in both spectra, but the fat peaks are shifted. In particular, the fat peaks in the spectra acquired on phantom appear shifted toward the right respect to the positions found in mouse (the black dot lines help the reader to observe this difference in frequency). Actually, when the temperature changes, the fat peaks are fixed and the water peak changes position; in particular, when the temperature decreases the water peak is shifted toward left, thus the frequency offset between the water peak and the primary



fat peak increases. In **Figure 2.13**, the spectrum taken in phantom is adjusted respect to the one taken on mouse. In fact, the fat peak positions are now in the right position and the water peak, relative to the phantom, is shifted toward left respect to the one relative to the mouse.

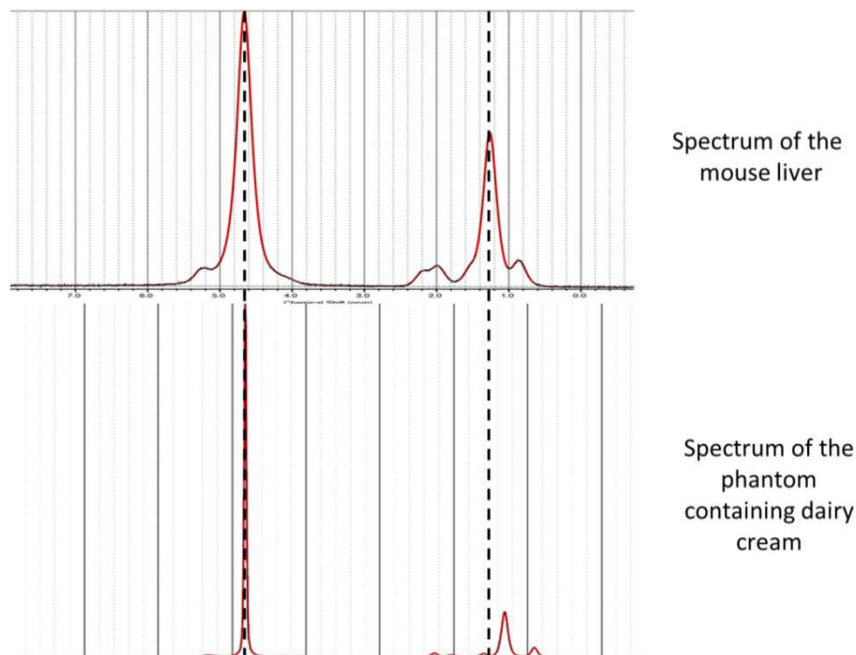


**Figure 2.12:** Two spectra acquired on mouse (top) and a phantom containing dairy cream (bottom). The water peaks in the two spectra are both positioned at 4.7ppm but the fat peaks are shifted.

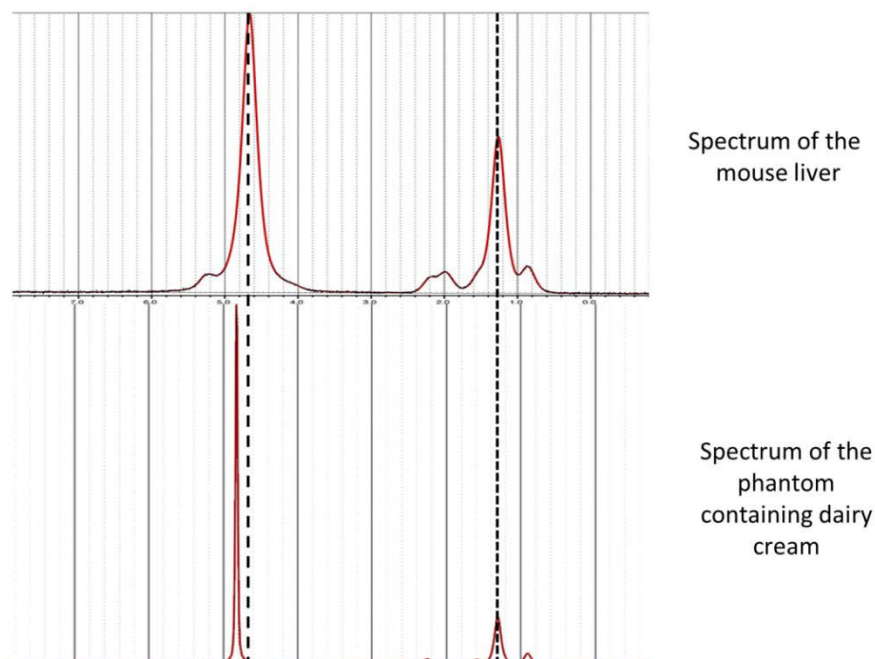


**Figure 2.13:** Two spectra acquired on mouse (top) and a phantom containing dairy cream (bottom) (the same of the ones shown in Figure 2.12). A correction due to the difference in temperature is necessary. The fat peak positions do not change with the temperature but the water peak does. Hence in this spectrum, the primary fat peak is fixed at 1.3ppm with the resulting shift toward left of the water peak.



Simulations were done, considering a bigger phantom at 36°C (the temperature found in healthy mice) and a smaller one at 20°C (the temperature inside the room). The numerical signal had the following parameters:  $1^\circ \text{TE} = 1.5\text{ms}$ , echo spacing 2.5ms. The field map and the noise were not considered in this study. The phantoms had 10% fat fraction and  $T_2^* = 10\text{ms}$ . The fat spectrum was considered equal for both phantoms; therefore, the only difference was the water peak shift between these two spectra, equal to 0.16ppm (32Hz at 4.7T). In **Figure 2.14**, the plots relative to the values of fat fraction and  $T_2^*$  in function of the number of echoes, are represented. The mean values of fat fraction, calculated by IDEAL, decrease with the increasing of the number of echoes. The  $T_2^*$  mean values are almost constant and equal to the nominal value (10ms).

In conclusion, the IDEAL algorithm, applied on MR images of several objects at different temperature, could lead to bias in fat fraction measurements. The difference in temperature was assumed for simulating the water peak shift.

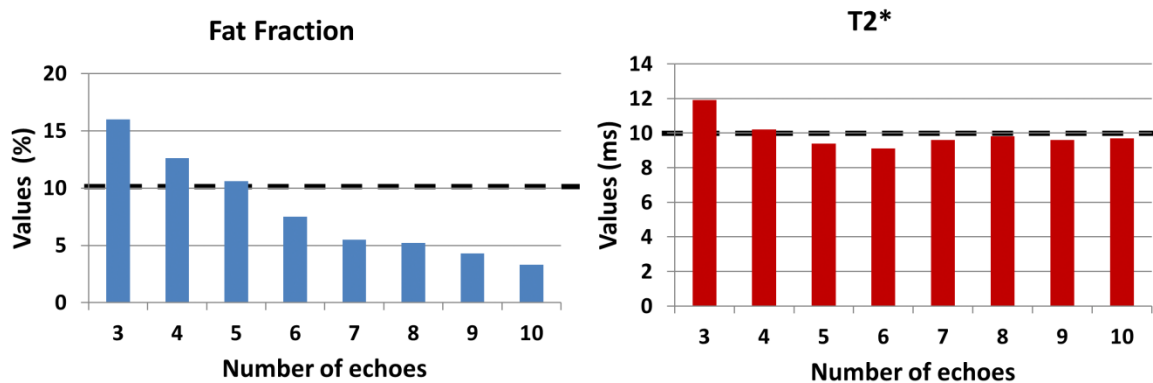


**Figure 2.14:** Fat fraction and  $T_2^*$  values calculated in the phantom with the shifted water peak. The values of fat fraction (left) decrease with the increasing of the number of echoes used for the IDEAL reconstruction. Differently, the  $T_2^*$  values are approximately equal to the nominal value of 10ms.

### 3.4.3.2 Importance of the fat spectrum

The actual version of the IDEAL algorithm uses the knowledge of the multiple fat peak frequencies and their relative areas. In the first version of this algorithm, Reeder et al. used only the information relative to the position of the primary fat peak. In 2008 Yu et al. [26] used 3 fat peaks for calculating the fat fraction, using the relative area for each peak. At last, the same research group began to use 6 peaks for the fat quantification [9]. The questions which arise are: 1) Do the positions or the relative areas change for each subject? 2) Is it necessary to acquire a spectrum for knowing the position and the relative area of each fat peak? In the work of Hamilton et al. [27], they calculated spectra on healthy mice and they

found no significant differences between all the spectra. And what about the number of the fat peaks to consider? In the current paragraph, simulations were effectuated for studying the fat fraction and  $T_2^*$  values, calculated with the IDEAL algorithm using 1, 3 and 6 peaks, separately. The numerical phantom was generated using the information of 6 fat peaks. The parameters of the signal models were:  $1^\circ\text{TE} = 1.5\text{ms}$ , echo spacing =  $2.5\text{ms}$ . A signal coming from the liver with fat fraction = 10% and  $T_2^* = 10\text{ms}$  was simulated. Images, with SNR equal to 50 on the images at first echo time, were simulated. The results of fat fraction and  $T_2^*$  versus the number of echoes are represented in **Figure 2.15**. The fat fraction mean values are 7.2% for the reconstruction done using 1 peak (in input the relative area of the primary peak was 0.63), 9.2% for the reconstruction done using 3 peaks (the sum of the relative areas of the three peaks were 0.81) and, for 6 peaks, 10.7% (the sum of the relative areas of all peaks were 1). The values of  $T_2^*$  are equal to the nominal value for all 3 reconstruction (10ms).

The benefit of using several peaks instead of the only primary peak is straightforward in literature. However, the use of the primary peak only is a good way to quantify fat fraction for some research group. In fact, knowing the relative area of the primary peak, it is possible to calculate the fat fraction and divide the result for its relative area. Otherwise, if in literature a spectrum of the mouse in healthy condition was already analyzed, it could be used. In both ways, the acquisition of the spectrum could be avoided by the user, reducing the total scan time.

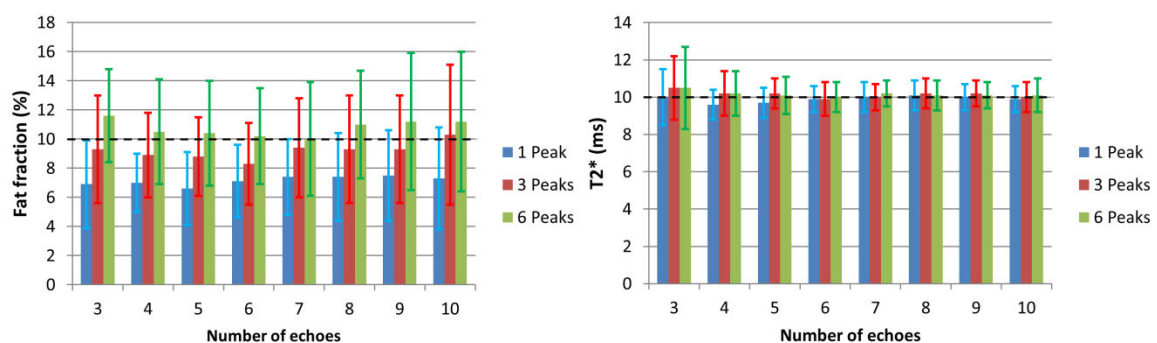


**Figure 2.15:** Fat fraction and  $T_2^*$  values reconstructed by IDEAL using 1 (blue), 3 (red) and 6 (green) peaks. The black dot lines indicate the nominal values (10% for fat fraction and 10ms for  $T_2^*$ )

#### 2.4.4 Influence on the field map

The IDEAL algorithm requires in input complex images. The complex images are influenced by the magnetic field inhomogeneity  $\psi$  (field map), present in the signal model. The reconstructions done with IDEAL depend on the experimental field map and on the initial

field map, used as input for the algorithm. An example of IDEAL output, where the initial field map used in IDEAL does not fit well with the experimental one, is illustrated in **Figure 2.16**. The fat fraction and the  $T_2^*$  map are partially miscalculated because of a wrong initial field map.

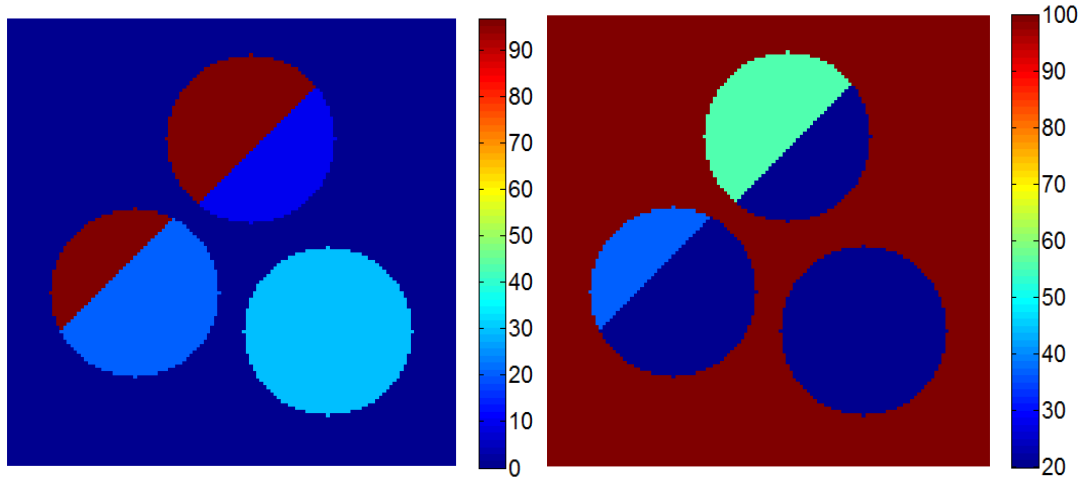


**Figure 2.16:** Fat fraction (left) and  $T_2^*$  (right) maps calculated by IDEAL. The maps are partially miscalculated because of the initial field map not adapt.

In fact, the values of fat fraction and  $T_2^*$  are well calculated only in the areas where the initial field map fits well. The field map  $\psi$  is a function of the echo spacing and first echo time, by reducing these two values, the difference between the real field map and the initial field map (which IDEAL needs) is smaller. Simulations were performed and the images had the following parameters:  $1^\circ\text{TE} = 1.5\text{ms}$ , echo spacing  $2.5\text{ms}$ ,  $T_2^* = 10\text{ms}$ . A magnetic field inhomogeneity, which had the shape of a plane, was generated and included into the signal. In **Figure 2.17** an example of field map used for creating the signal is shown: the pixel in position (1,1) has a value of 50Hz and the value of the slope (the direction of the slope is along the line which connects the pixel (1,1) with (128,128)) is equal to 1Hz/pixel. The initial field map for IDEAL algorithm was a matrix with values equal to 0. Two different slopes of values 1 and 3Hz/pixel were adopted and the two results of fat fraction calculated by IDEAL using 3 echoes are shown in **Figure 2.18**.

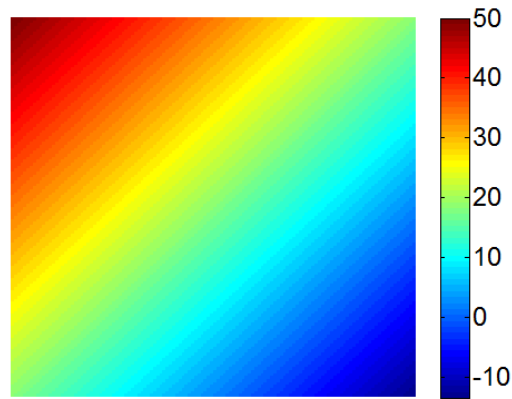


**Figure 2.17:** Example of field map used for generating the signal. In this case, the value of the pixel in position (1,1) is equal to 50Hz and the slope is 1Hz/pixel. The slope is along the line which connects the pixel (1,1) and (128,128).

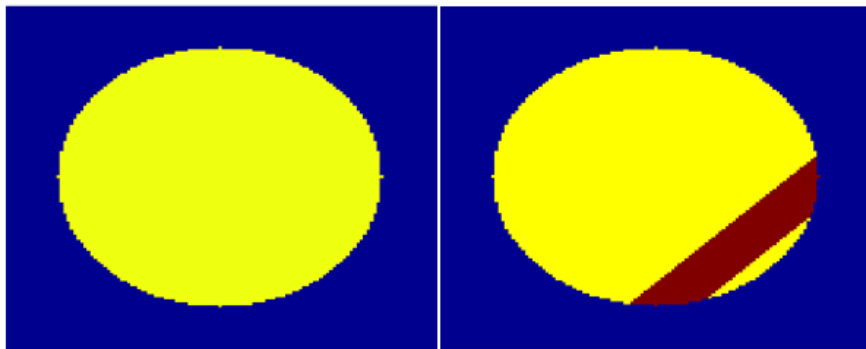


**Figure 2.18:** Fat fraction maps generated with the two different field maps. Both maps were reconstructed using 3 echoes. In the fat fraction map calculated on the signal having the field map with slope equal to 1Hz/pixel (left), no miscalculations are present in the image. In contrast, the second fat fraction map (right), calculated using the second field map (the one with 3Hz/pixel slope) is partially miscalculated.

The fat fraction map on the left is calculated on the signal which had the minor slope (1Hz/pixel). The map is well calculated, and in each pixel, the nominal value (10%) is found (**Figure 2.18**, left). Differently from the first map, the second one, calculated on the signal having a field map of slope (3Hz/pixel), is partially miscalculated (**Figure 2.18**, right). On the  $T_2^*$  images, analogous results are found. On the estimation of the field map calculated by IDEAL, the phase is wrapped on the area where the fat fraction is miscalculated. For avoiding or solving this problem, three solutions are proposed:

- Decreasing the echo spacing: in the signal model, the term  $e^{i2\pi\psi t_n}$  depends on the product of field map with the echo spacing. Reducing the echo spacing, the effect of

phase wrapping on IDEAL algorithm will be reduced (in other words, for re-obtaining the phase wrap in the solution of IDEAL algorithm the field inhomogeneity must be higher);

- Decreasing the number of echoes: the possibility to have phase wrapping in the image in output is reduced, since the evolution of the phase is limited;
- To use an algorithm of phase unwrapping or region growing for calculating an initial field map which fits well with the real one.

In conclusion, IDEAL is a multi-parametric algorithm which calculates fat fraction and  $T_2^*$ . The outcomes depend on the initial field map put in IDEAL and from the noise. To reduce the possibility of miscalculation due to an incorrect initial field map, it is necessary to use short echo times and/or a minor number of points. For improving the quality  $T_2^*$  maps, long echo times are mandatory. In absence of noise, the IDEAL algorithm provides perfect fat fraction and  $T_2^*$  maps for whichever echo time and number of echoes adopted.





# Chapter III

## MRI measurements on physical phantoms

### 3.1 Introduction

MRI has become nowadays an essential bio-imaging technique and the development of novel acquisition schemes (i.e., MR pulse sequences) and/or novel quantification methods is a very active domain of research. The early phase of optimization of MR pulse sequences is typically performed on phantoms, which are objects mimicking tissue properties such as the  $T_1$ ,  $T_2$  and  $T_2^*$  relaxation time, the magnetization transfer and the diffusion coefficient. The main advantage of using phantoms is that, in the time-consuming steps of sequence optimization, they provide a reference value for the parameter under measurement and can be repeatedly measured. Many MRI phantoms have been developed in the last two decades. One of the most commonly employed phantoms is a gel based on agarose and water (agar gel) [34]–[36]. By changing the concentration of agarose, it is possible to achieve  $T_2^*$  values that are similar to the  $T_2^*$  values of most tissues. In general, some of the MRI phantoms proposed in the literature can be prepared exclusively with laboratory equipment and material. Emulsions that have been generated in a well-controlled environment, can provide insight into the relaxation mechanisms and/or structural properties of water-fat mixtures. On the other hand, it should be noted that, throughout the years, MR scientists have also investigated the MR properties of substances commonly encountered in everyday life. These products include water-fat mixtures consisting of oil droplets dispersed in an aqueous phase (so-called oil-in-water food emulsion: milk [37], dairy cream [3], [38]–[40], mayonnaise [41], [42]...) and water-fat mixtures consisting of water droplets dispersed in an oil phase (so-called water-in-oil food emulsion: butter [40], [43], margarine...). For instance, dairy cream has been used as a model of biexponential relaxation decay or as a model of water-fat mixture to test and optimize novel pulse sequences. One advantage of these phantoms is that they are readily available and inexpensive. In the current paragraph, MR phantoms, composed by dairy creams, are employed as water-fat systems. The images acquired with multi-gradient-echo sequences were processed with 2-point and 3-point Dixon's method and IDEAL algorithm.



### 3.2 Materials and methods

MRI experiments were performed on a 4.7T horizontal-bore MR scanner (47/40 Biospec, Bruker, Wissembourg, France) using a volume coil (72 mm inner-diameter) as a transmitter/receiver. Three phantoms were prepared with dairy creams (full, light and light thick cream) that were bought at a local grocery shop. Each dairy cream was poured into a 15ml tube. A second phantom, an homemade emulsion with above 30% fat fraction, was used as well. For Dixon's reconstructions, three gradient echo sequences were used. Imaging parameters were: TR= 30ms, flip angle = 5°, matrix size = 128x128, FOV = 4x4cm<sup>2</sup>, BW = 140kHz and 80 averages. The sequences were acquired with 1.45ms (first in-phase image), 2.2ms (out-of-phase image) and 2.9ms (second in-phase image) echo times, respectively. Two scripts in Matlab which reproduces the 2-point and 3-point Dixon's methods were used for calculating the respective fat fractions. For the IDEAL reconstruction, MR images were acquired with a multi-gradient-echo sequence. Imaging parameters were: 10 echoes, first TE = 1.5ms, echo spacing = 2.5ms, TR= 30ms, flip angle = 5°, matrix size = 128x128, FOV = 4x4cm<sup>2</sup>, BW = 140kHz and 80 averages. The homemade script in Matlab used in simulations as well was employed for calculating the fat fraction and  $T_2^*$  map using 3 up to 10 echoes.

### 3.3 Results

In **Figure 3.1**, a multi-gradient-echo image of the physical phantoms is shown. The contents are displayed on the image as well.

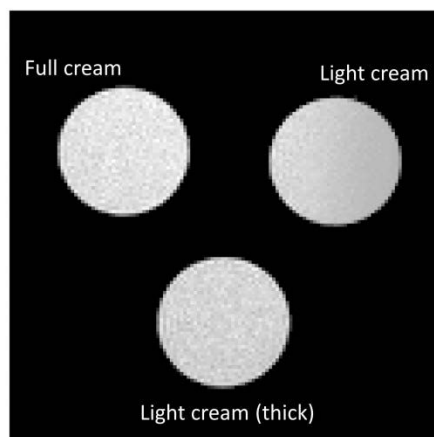


**Figure 3.1:** MR gradient-echo image of the three water-fat phantoms: full dairy cream (left), light dairy cream (right) and thick light dairy cream (bottom).

In **Figure 3.2**, the fat fraction maps relative to dairy creams, calculated using 2-point and 3-point Dixon's method, are illustrated.

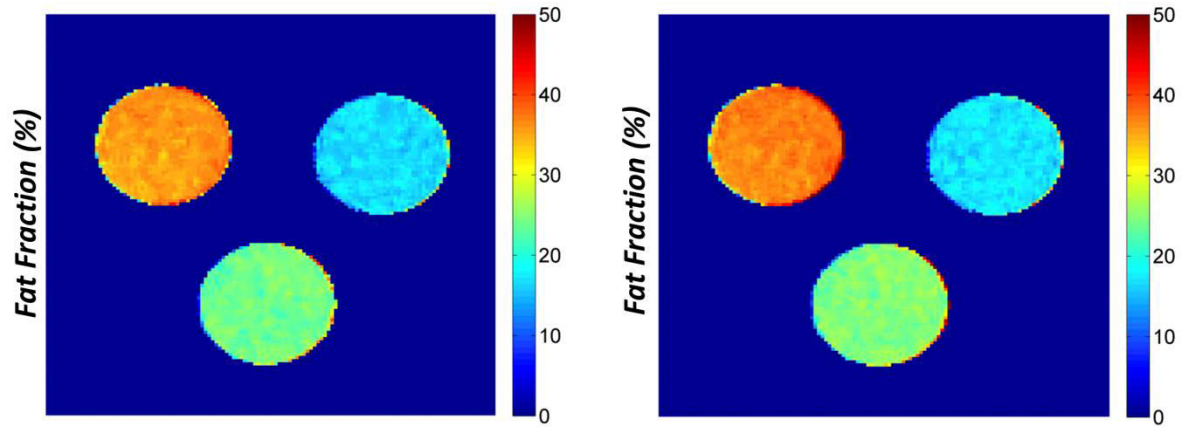


**Figure 3.2:** Fat fraction maps of dairy creams reconstructed with the 2-point (left) and 3-point (right) Dixon's method.

No significant differences in values are found between the two reconstructions.

In **Figure 3.3**, the fat fraction and  $T_2^*$  maps relative to dairy creams, generated by IDEAL algorithm using 3 echoes, are shown.

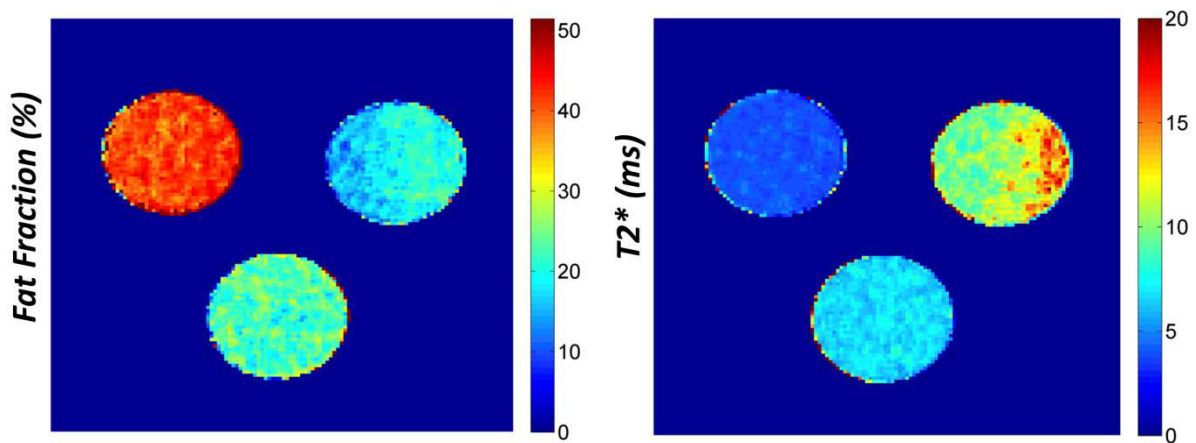


**Figure 3.3:** Fat fraction and  $T_2^*$  maps of dairy creams reconstructed with IDEAL algorithm using 3 echoes.

In **Figure 3.4**, the mean and standard deviation values of fat fraction and  $T_2^*$  for each dairy cream, calculated by IDEAL algorithm, are plotted as a function of the number of echoes. The values of fat fraction and  $T_2^*$  for each phantom are calculated with 15-pixel radius ROIs. It is noticeable, for each phantom employed, a decreasing of values with the increasing of the number of echoes. The 3-point IDEAL yields fat fraction values closer to the ones obtained with Dixon's methods.

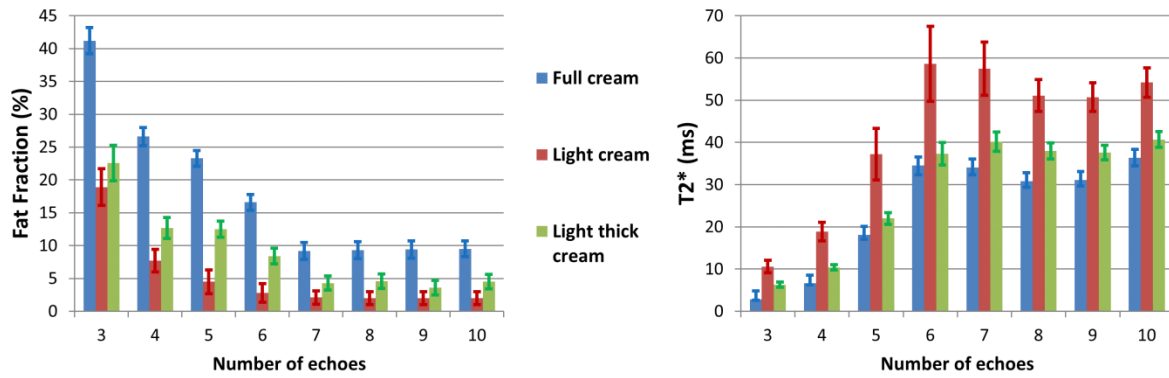


Figure 3.4: Fat fraction (left) and  $T_2^*$  values vs the number of echoes for dairy creams.

The mean and standard deviation value of fat fraction calculated with the 3-point IDEAL are included in **Table 3.1** with the values obtained with Dixon’s methods. From the values of fat fractions shown in the **Table 3.1**, it is evident that the Dixon’s methods represent more robust algorithms for calculating the fat fraction (the standard deviation relative to the values of fat fraction calculated with the IDEAL algorithm are higher than those of the Dixon’s methods).

<i>Phantom</i>	<i>2-point Dixon</i>	<i>3-point Dixon</i>	<i>3-point IDEAL</i>
Full cream	$35.7 \pm 0.8$	$36.9 \pm 0.8$	$41.2 \pm 2.0$
Light cream	$16.7 \pm 0.9$	$17.2 \pm 0.9$	$18.9 \pm 2.8$
Light cream (thick)	$24.0 \pm 0.8$	$24.9 \pm 0.8$	$22.6 \pm 2.7$

Table 3.1: Mean and standard deviation values of fat fraction for full, light and light thick cream. The values are calculated with 15-pixel radius ROIs on each phantom.

The fat fraction mean values, calculated with the Dixon’s methods and IDEAL, were compared in ratio (i.e. fat fraction calculated on full cream/ fat fraction calculated on light cream....). The purpose of this study was to understand if the ratio between the values is conserved. In **Table 3.2**, the ratio of the fat fraction values for each reconstruction is shown. In this table, the ratio relative to the values in weight written on packs (full cream =30%, light cream = 12%, light thick cream = 18%) were inserted as well. The calculated ratios for 2 and

3-point Dixon's methods are equivalent. The ratio values relative to the IDEAL algorithm are closer than the Dixon's methods values to the ratio values relative to the confectons.

<i>Fat fraction ratio</i>	<i>Packs</i>	<i>2-point Dixon</i>	<i>3-point Dixon</i>	<i>3-point IDEAL</i>
Full cream/Light cream	2.5	2.1	2.1	2.2
Full cream/Light thick cream	1.7	1.5	1.5	1.8
Light thick cream/ Light cream	1.5	1.4	1.4	1.2

**Table 3.2:** Values of the ratio between the fat fraction values written in **Tab 3.1**.

However, even if the ratios are close between them, the fat fraction values written on the confectons are significantly different respect to the fat fraction values calculated with the Dixon's methods and IDEAL algorithm.

With respect to  $T_2^*$ , the mean values increase using a low number of echoes (number of echoes  $< 6$ ) and then (number of echoes  $\geq 6$ ) the values reach a value of plateau for each phantom. The  $T_2^*$  map calculated using 10-echo IDEAL reconstruction was obtained. With respect to the results obtained, it is noteworthy that the values of  $T_2^*$  calculated by the IDEAL algorithm decrease with the increasing of cream thickness ( $T_2^*$  light cream =  $54.2 \pm 3.5$ ms vs  $T_2^*$  of light thick cream =  $40.7 \pm 1.9$ ms) and fat fraction ( $T_2^*$  light cream =  $54.2 \pm 3.5$ ms vs  $T_2^*$  of full cream =  $36.4 \pm 1.6$ ms). The fat fraction (left) and  $T_2^*$  (right) maps calculated by IDEAL algorithm using 3 and 6 echoes, respectively, are illustrated in **Figure 3.5**.

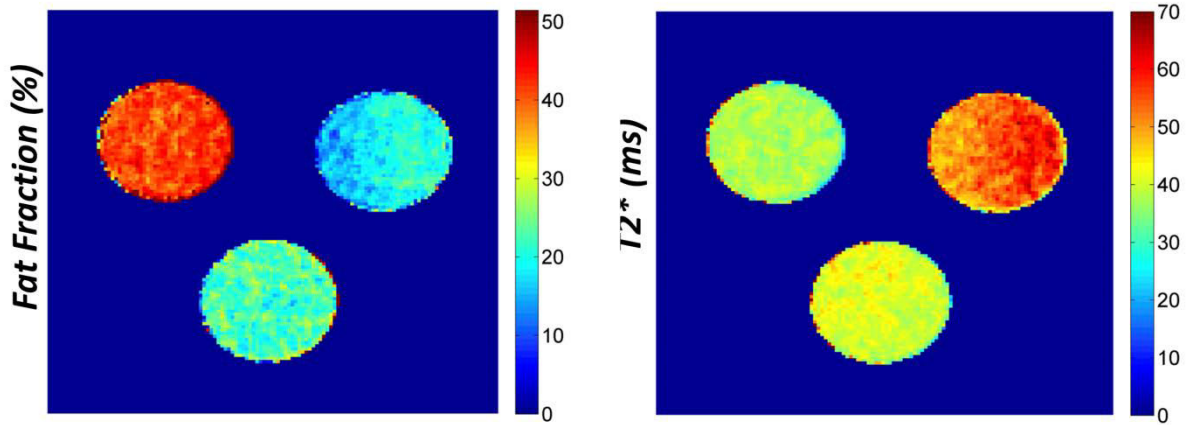


**Figure 3.5:** IDEAL reconstruction output for the full dairy cream (left), light dairy cream (right) and thick light dairy cream (bottom). The pixel-by-pixel maps of fat fraction (left) and  $T_2^*$  values (right) are shown.

These trend for fat fraction and  $T_2^*$  values were found in the emulsion as well. In **Figure 3.6**, the fat fraction and  $T_2^*$  values calculated with 15-pixel radius ROIs are plotted in function of the number of echoes. Hence, even in emulsions, the straightforward values of fat fraction are obtained with the 3-point IDEAL. The  $T_2^*$  values are better calculated using a higher number of echoes (more than 6).

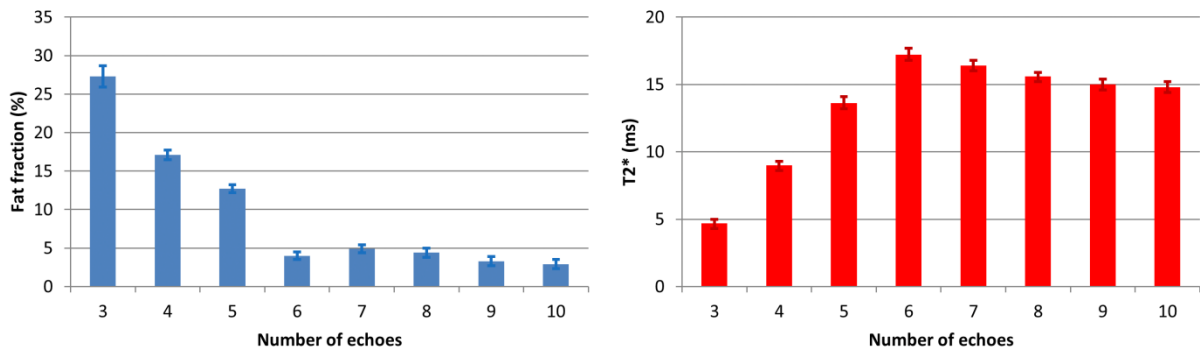


**Figure 3.6:** Fat fraction (left) and  $T_2^*$  values (right) vs the number of echoes for the emulsion. The results are in agreement with the one found in dairy creams.

### 3.4 Discussion

Dixon's methods and IDEAL algorithm are continually compared in literature. Several studies on animals, human and phantoms are operated using these chemical shift algorithms at different magnetic fields. Dixon's methods represent an easier way to calculate fat fraction. On the other hand they do not correct for  $T_2^*$  decay and for the multi-peak nature of fat as IDEAL algorithm does. It makes use of complex data. Thus, they depend on the magnetic

field inhomogeneity as well, differently from the magnitude images used for the 2-point Dixon's method. A wrong estimation of the field map can lead to the miscalculation of fat fraction. An example of miscalculation of fat fraction due to a wrong estimation of the field map is shown in **Figure 3.7**. In each image two phantoms, composed by tubes filled with full (left) and light (right) cream on the sagittal plane, are displayed. The fat fraction calculated with the 2-point Dixon's method (left) does not have artifacts. Instead, the fat fractions calculated with the 3-point Dixon's method (center) and IDEAL algorithm (right) are miscalculated, since the estimation of the field map is not appropriate. The 3-point Dixon's method well calculates the fat fraction values in the central part of the tubes. The IDEAL algorithm completely miscalculates the fat fraction relative to the tube containing full cream and partially miscalculates the fat fraction of the light cream.

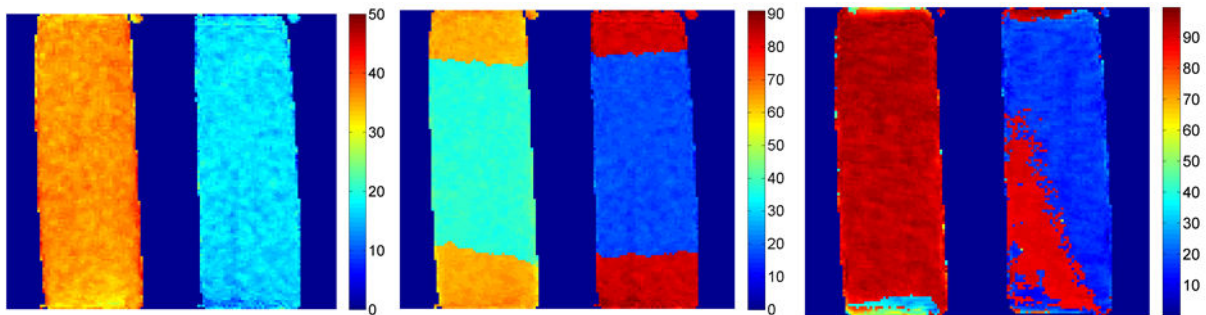


**Figure 3.7:** Fat fraction maps calculated with the 2-point (left), 3-point (center) Dixon's method and IDEAL algorithm (right)

However, with an appropriate field map, the 3-point Dixon's method and IDEAL algorithm can well calculate the fat fraction in this last scenario.

With respect to the results obtained on phantoms study, the outcome of IDEAL algorithm were not in agreement with the results obtained in Chapter II. The fat fraction calculated in phantoms decreased with the increasing of the number of echoes.

Returning to the results on dairy creams, the values of fat fractions calculated with IDEAL algorithm are higher than the values calculated with Dixon's method and this result is in agreement with the literature values [44].

About the ratio in **Table 3.2**, the values were similar. Nevertheless, even if the ratios are close between them, the fat fraction values written on packs are significantly different respect to the fat fraction values calculated with the Dixon's methods and IDEAL algorithm. This overestimation is explained with the molecular structures of the fat (triglyceride chain) and water. The MR scanner calculates the signal coming from the hydrogen atoms of fat and water molecules. Nevertheless, fat and water are composed of other elements as well. The

water molecules are also composed of oxygen (atomic mass = 16Da), whereas fat especially from the  $(\text{CH}_2)_n$  groups on the chain (carbon = 12Da, hydrogen = 1Da). Hence, the fat fractions in weight written on confectons are not equivalent to the “fat hydrogen fraction” calculated with chemical shift algorithms. However, the ratio between the fat fractions displayed in **Table 3.2** does not take into account of the fat fraction in weight and the “fat hydrogen fraction” calculated by chemical shift algorithms.

For explaining the decreasing of the fat fraction with the increasing of the number of echoes, the “low receiver bandwidth” method was developed. The current method is explained in the next paragraph.

### 3.5 Low receiver bandwidth

#### 3.5.1 Introduction

MRI methods for fat quantification have been steadily improved over the years to yield a more accurate measurement of fat content, with hundreds of studies performed worldwide. With the aim of correcting the measure of the fat content for  $T_2^*$  decay, a number of algorithms were introduced over the years. Nevertheless these algorithms assumed that the  $T_2^*$  of the water protons is the same as the  $T_2^*$  of fat protons; thus these methods are typically referred to as ‘single  $T_2^*$ ’ correction methods [26]. It should be noted that these correction methods also allow for the quantification of  $T_2^*$ , and thus they provide an additional biomarker of interest in clinical settings. Specifically, the knowledge of  $T_2^*$  is important in the case of liver pathologies, for assessing liver iron overload [45].

Very recently, a handful of studies has proposed a further refinement of the model for fat quantification [44], [46]–[49]. The main idea is the following: since the  $T_2^*$  of the water protons might differ from the  $T_2^*$  of fat protons, a more appropriate correction algorithm should include two separate  $T_2^*$  values, one for the water protons ( $T_{2w}^*$ ) and the other for the fat protons ( $T_{2F}^*$ ). These methods are typically referred to as ‘dual  $T_2^*$ ’ correction methods (Appendix B). However, as pointed out by the same authors, the performance of dual  $T_2^*$  models “remains controversial”, since it increases the model instability related to the higher number of degrees of freedom [48], [49].

Furthermore, the problem with dual  $T_2^*$  methods is exacerbated by the fact that there are no reference values for the  $T_2^*$  of water protons and  $T_2^*$  of fat protons. In other words, dual  $T_2^*$  methods provide in output: i) the value of fat content, which can be compared with a reference value obtained by other techniques, and ii) the value of  $T_{2w}^*$  and  $T_{2F}^*$ , which however cannot

be compared to any reference value. It is of course straightforward to measure with a gradient echo sequence the  $T_2^*$  of a single chemical species (water in tissue, for instance), when no other chemical species (that give a MRI-visible signal) are present. However, when two chemical species (water and fat, for instance) co-exist in the same pixel, as in the case of liver tissue, a basic multi gradient-echo approach does not allow for measuring the  $T_2^*$  of each chemical species. As a consequence, no ground truth value is available to test and validate the dual  $T_2^*$  correction methods.

Motivated by these recent developments of dual  $T_2^*$  methods and by the challenges involved in validating these methods, we sought a direct measure of  $T_{2w}^*$  and  $T_{2F}^*$ , with the aim of providing ground truth values in phantoms. These measurements may be of importance for developing, optimizing and testing dual  $T_2^*$  methods for quantification of fat content and  $T_2^*$  values.

### 3.5.2 Materials and Methods

#### 3.5.2.1 Theory

The MR signal of a water-fat system in IDEAL algorithm is given by **Equation 2.26**

$$S(t_n) = \left( W + F \sum_{i=1}^7 \alpha_i e^{i2\pi\Delta f_i t_n} \right) e^{i2\pi\psi t_n} e^{-t_n/T_2^*} \quad (2.26)$$

It should be noted that  $W$ ,  $F$ ,  $T_2^*$  and  $\psi$  are functions of the spatial position, i.e., may have a different value in different pixels of the image. This model represents a ‘single  $T_2^*$ ’ correction model since a common value of  $T_2^*$  for water and fat is considered. In more recent studies, a more sophisticated model, where the  $T_2^*$  of water and fat protons have different values, has been proposed:

$$S(t_n) = \left[ W e^{-t_n/T_{2w}^*} + F e^{-t_n/T_{2F}^*} \sum_{i=1}^7 \alpha_i e^{i2\pi\Delta f_i t_n} \right] e^{i2\pi\psi t_n} \quad (3.1)$$

where  $T_{2w}^*$  and  $T_{2F}^*$  are the transverse relaxation time of the water and fat signal, respectively.

#### 3.5.2.2 Magnetic Resonance Imaging

MRI experiments were performed on a 4.7T horizontal-bore MR scanner (47/40 Biospec, Bruker, Wissembourg, France) using a volume coil (72mm inner-diameter) as a transmitter/receiver. Three phantoms containing dairy creams and an oil-in-water emulsion



were employed. To calculate the  $T_2^*$  of water protons and  $T_2^*$  of fat protons by a direct measurement, MR images were acquired with a low receiver bandwidth/pixel to separate water and fat signals along frequency encoding direction. Four multi-gradient echo sequences were acquired with the following parameters: 10 echoes, echo spacing = 13.3ms, repetition time (TR) = 280ms, flip angle =  $25^\circ$ , matrix size = 256x256, field of view (FOV) =  $4.3 \times 4.3 \text{cm}^2$  and receiver bandwidth (BW) = 35kHz. Each sequence was acquired with a different value of the first echo time (TE = 6.1, 8.1, 10.1 and 12.1ms, respectively). This would result into an off-set of the sampling echoes, i.e., four shifted multi gradient-echo sequences. The data were combined together to generate a single relaxation decay curve. The goal of combining the data from four shifted multi gradient-echo sequences was to obtain a finer sampling of the relaxation decay curve, in order to improve the  $T_2^*$  measurement.

### 3.5.2.3 Data Analysis

The curve fitting of data acquired with a low receiver bandwidth was performed to obtain the  $T_2^*$  of water protons and  $T_2^*$  of fat protons. For each phantom, three regions of interest (ROIs) were drawn to include separately the signal from water, fat and water+fat. The  $T_2^*$  relaxation time values of water, fat and water+fat were calculated by fitting the signal from magnitude images at 40 TEs to a monoexponential function. The curve fitting routine of Matlab (Mathworks, Natick, MA, USA) was employed. Mean and standard deviation values of  $T_2^*$  were obtained in water-only, fat-only and water+fat regions of interest. For each curve fitting, the coefficient of determination  $r^2$  was also calculated to assess the goodness of the data fitting.

### 3.5.3 Results

In **Figure 3.8**, the MR image of the three phantoms containing dairy creams acquired at the first echo (6.1ms) of a multi-gradient-echo sequence is shown.

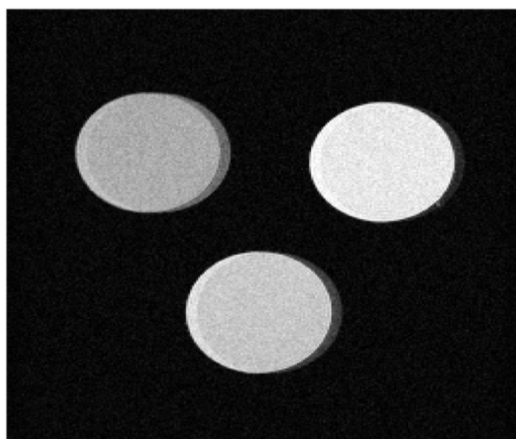


**Figure 3.8:** MR gradient-echo image of the three water-fat phantoms: full dairy cream (left), light dairy cream (right) and thick light dairy cream (bottom). A chemical shift artifact can be observed along the left-right frequency encoding direction. The receiver bandwidth value was purposely chosen to generate this artifact, in order to detect separately the signal of water and fat protons.

A shift of five pixels between the water and fat signals along the frequency encoding direction is noticeable. This shift can be ascribed to the low receiver bandwidth/pixel and the measured value of five pixels is in agreement with the expected theoretical value of 5.1. In **Figure 3.9**, a detail of **Figure 3.8** is displayed.

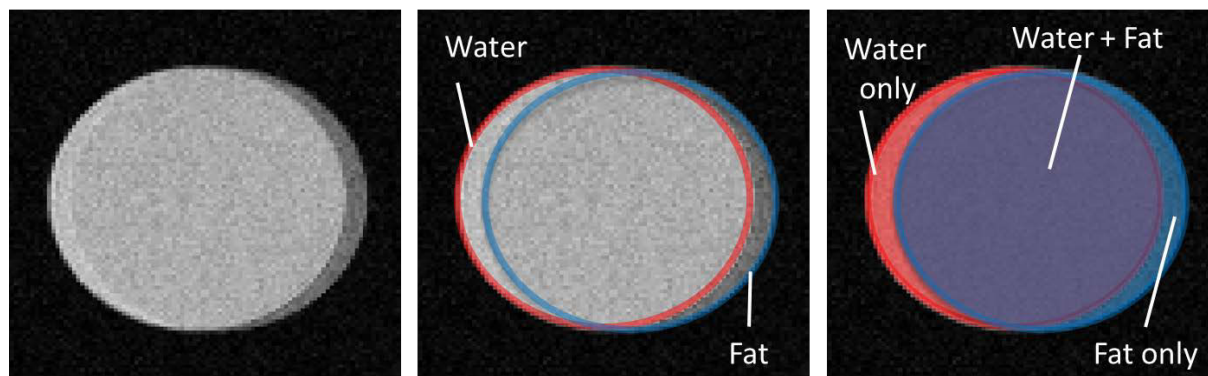


**Figure 3.9:** A zoom-in of the full dairy cream phantom, which was shown in **Figure 3.8**. In the center and right panel, two circles are drawn on the MR images in order to aid visualization of the separate signal of water and fat protons.

Specifically, the MR image of the phantom containing full cream is illustrated. To help the visualization of the separate signals two circles - one for highlighting the water signal (in red) and the second for the fat signal (in blue) - are drawn. The intersection between these two circles represents the signal originating from water+fat protons (in purple). The values of the signal calculated in water-only and fat-only areas of the full cream are plotted as a function of the echo time in **Figure 3.10**.

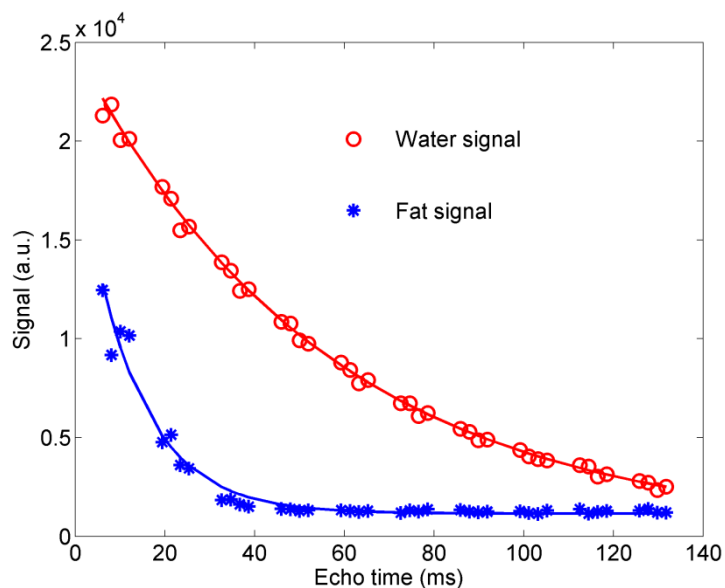


**Figure 3.10:**  $T_2^*$  relaxation decay of water (symbol ‘O’) and fat (symbol ‘\*’) protons in full cream. The continuous lines indicate the curve fitting calculated on the water and fat signals using the monoexponential function. The water signal ( $T_{2w}^* = 57.1 \pm 1.0\text{ms}$ ) decays slower than the fat signal ( $T_{2F}^* = 10.7 \pm 0.8\text{ms}$ ).

Phantom	Water $T_2^*$ (ms)	Fat $T_2^*$ (ms)	Water + Fat $T_2^*$ (ms)
Full Cream	$57.1 \pm 1.0$ [0.998]	$10.7 \pm 0.8$ [0.992]	$56.7 \pm 6.6$ [0.924]
Light Cream	$57.4 \pm 0.9$ [0.998]	$7.6 \pm 0.9$ [0.984]	$54.5 \pm 0.8$ [0.999]
Light Cream (thick)	$48.9 \pm 0.7$ [0.999]	$10.3 \pm 1.5$ [0.966]	$47.1 \pm 0.9$ [0.998]
Emulsion	$14.1 \pm 0.4$ [0.994]	$8.0 \pm 0.3$ [0.988]	$13.6 \pm 0.8$ [0.977]

**Table 3.3:** Values of  $T_2^*$  (mean  $\pm$  standard deviation) measured in water-only, fat-only and water+fat regions selected on the three phantoms. Below each value of  $T_2^*$ , the coefficient of determination of the curve fitting is indicated in square brackets.

In **Table 3.3**, the results of  $T_2^*$  measurements for full, light, light thick cream and emulsion are shown. In all phantoms, the  $T_2^*$ s of fat protons were significantly lower than the  $T_2^*$ s of water protons. The value of  $T_2^*$  of water protons in light thick cream was significantly lower than those found in full and light cream. The coefficients of determination relative to the data fitting of the water signal were equal or higher than 0.994. Lower coefficients of determination were found for the fat signal. The values calculated on the emulsion are significantly lower than those relative to dairy creams.

It can be noticed that the fat signal decays faster than the water signal. The values of  $T_2^*$  found in fat-only and water-only regions were  $10.7 \pm 0.8\text{ms}$  and  $57.1 \pm 1.0\text{ms}$ , respectively. The values of the signal calculated in the water+fat area of the full cream are plotted as a function of the echo time in **Figure 3.11**.

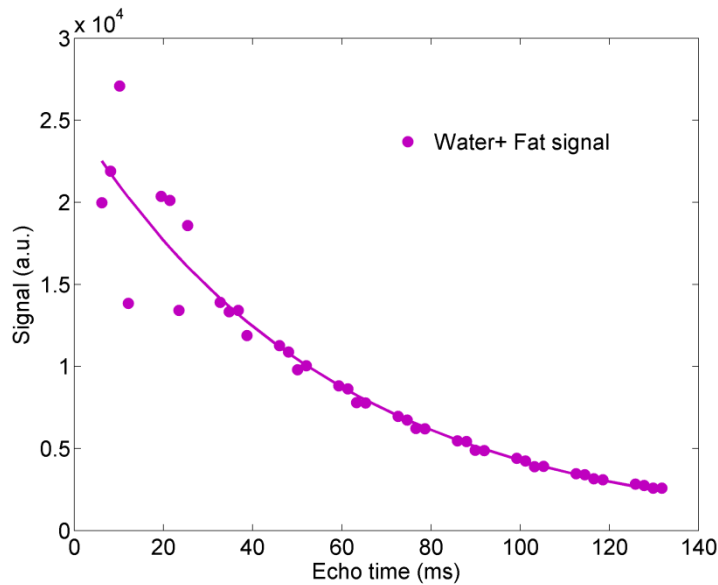


**Figure 3.11:**  $T_2^*$  relaxation decay of water+fat signal in full cream. The continuous lines indicate the curve fitting calculated on the water+fat signal using the monoexponential function. At short TEs the monoexponential model poorly reproduces the experimental data.

At short TEs a scatter of the data points around the curve fitting is noticeable. At longer TEs, this scatter virtually disappears. The value of  $T_2^*$  found in the water+fat region was  $57.7 \pm 6.6\text{ms}$ . The values of  $T_2^*$  of full, light and light thick cream were  $36.4 \pm 2.0\text{ms}$ ,  $54.2 \pm 3.5\text{ms}$  and  $40.7 \pm 1.9\text{ms}$ , respectively.

### 3.5.4 Discussion

In the current study, a direct measure of the  $T_2^*$  of water protons and the  $T_2^*$  of fat protons was achieved in dairy cream phantoms, which were chosen here as a model of water-fat mixtures

[3], [50]. Thus, the low receiver bandwidth approach -as proposed in the current study- represents a fast and effective method for an unequivocal measurement of  $T_{2w}^*$  and  $T_{2F}^*$ .

The knowledge of  $T_{2w}^*$  and  $T_{2F}^*$  may prove of value for developing, testing and optimizing fat quantification algorithms. As a matter of fact, novel algorithms for fat quantification have been recently proposed with a dual  $T_2^*$  correction model. However, while the value of the fat content (obtained by these algorithms) can be compared to a reference value obtained with other techniques, this is not the case for  $T_{2w}^*$  and  $T_{2F}^*$ . In other words, the value of  $T_{2w}^*$  and  $T_{2F}^*$  obtained by these algorithms cannot be compared to any reference value. In the current study, we propose the low receiver bandwidth approach to directly measure  $T_{2w}^*$  and  $T_{2F}^*$  in phantoms so to provide the ground truth values of  $T_{2w}^*$  and  $T_{2F}^*$ . As a result,  $T_{2w}^*$  and  $T_{2F}^*$  values obtained by the algorithms can be validated versus ground truth values.

To the best of our knowledge, no reference values exist for  $T_{2w}^*$  and  $T_{2F}^*$  in tissues (such as liver for example) where the water and fat proton pools share the same microenvironment. It is needless to say that it is straightforward to perform measurements of  $T_{2w}^*$  and  $T_{2F}^*$  in tissues such as subcutaneous adipose tissue and gray/white matter, where only one of these two proton pools is present. At this stage, the low receiver bandwidth approach for direct measure of  $T_{2w}^*$  and  $T_{2F}^*$ , where the water and fat proton pools share the same microenvironment, does not appear feasible for tissue measurements *in vivo*. Nevertheless, the reference values observed in phantoms are of interest for algorithm validation and the ability to measure  $T_{2w}^*$  and  $T_{2F}^*$  in phantoms certainly represents an important step towards the development of robust dual  $T_2^*$  algorithms. Indeed, as indicated also in the literature, current dual  $T_2^*$  algorithms methods still suffer from instability and poor noise performances [47]–[49]. The values of  $T_2^*$  (of water and water+fat) obtained by the low receiver bandwidth approach decrease with the increasing of cream thickness (**Table 3.3**). Overall, the  $T_2^*$  values determined with the low receiver bandwidth approach show that in all phantoms the  $T_2^*$  relaxation time of the fat protons is significantly shorter than that of water protons (**Table 3.3**). In light cream, the value of  $T_2^*$  found by the low receiver bandwidth approach in the water+fat region is in excellent agreement with the value of  $T_2^*$  calculated by IDEAL algorithm.

Within the context of fat quantification *in vivo*, it represents an important burden to the economy and the health care system. Because of the high clinical interest of fat quantification, MRI vendors have installed on the MRI scanners novel algorithms that allow for a real-time calculation of the fat content [17], [48], [49]. So, at the end of the MRI examination, physicians have access to images of fat content, that is, pixel-by-pixel maps of fat content in a

chosen anatomical area. Thus, a paradigm shift is currently taking place: for investigations of certain pathologies, the relevant output of an MRI examination is not anymore a  $T_1$ - or  $T_2^*$ -weighted image, but a quantitative map of a biomarker. The physicians at the end of the MRI acquisition will base their diagnosis on these quantitative maps. For instance, liver is one of the main organs of interest for fat quantification: fat content greater than 5% is indicative of liver steatosis and the  $T_2^*$  values can be used to determine liver iron overload. An example of pixel-by-pixel maps of fat content and  $T_2^*$  values, similar to those generated on clinical MRI scanners, was obtained in the current study using the single  $T_2^*$  IDEAL algorithm.

The water-fat mixture models are of interest to a wide range of scientific disciplines, e.g. clinical research, colloid science, food industry [51]–[53]. In this context, the application of MR techniques to investigations of water-fat mixtures is not novel. Many NMR studies have been performed on water-fat mixtures [51]–[53], but less attention has been paid to quantitative MRI [54]–[56]. The ability to directly measure the  $T_2^*$  relaxation time of the water proton pool and the  $T_2^*$  relaxation time of the fat proton pool may prove of value also for investigating the basic relaxation mechanisms in water-fat mixtures. For instance, in emulsion that have been generated in a well-controlled environment, detailed measurements of  $T_2^*$  as a function of the fat content can provide insight into the relaxation mechanisms and/or structural properties of water-fat mixtures.

To conclude, direct  $T_2^*$  measurements of water and fat protons are of interest as they provide reference values for  $T_2^*$ . In the current study, we showed that the low receiver bandwidth approach represents a fast and effective method for direct measurements of  $T_{2w}^*$  and  $T_{2F}^*$ . Within the context of the fat quantification *in vivo*, these reference values of  $T_{2w}^*$  and  $T_{2F}^*$  may be of interest for development, validation and optimization of fat quantification methods based on dual  $T_2^*$  correction.



# Chapter IV

## MRI measurements on mice liver and muscle

### 4.1 Introduction

In the Chapter II, the Dixon's methods and the IDEAL algorithm were presented. Moreover, the IDEAL algorithm was analyzed with simulations (Chapter II) and then with MR physical phantoms (Chapter III). Both types of measurements were used for better understanding how to employ this multiparametric algorithm (IDEAL), for optimizing the *in vivo* measurements of fat fraction and  $T_2^*$  on mice. Very little has been done for development/optimization of *in vivo* non-invasive fat quantitation in preclinical models. Differently from the MR phantoms, the mice breathe and can move during the MR acquisitions, leading to the formation of motion artifacts.

Magnetic resonance signal is influenced by the spin-spin relaxation time  $T_2^*$  which causes the decreasing of the signal in time. The  $T_2^*$  shortening and signal dephasing are connected to the presence of iron in tissue. In condition of iron overload the  $T_2^*$  could reach the order of few milliseconds [57]. IDEAL algorithm allows the joint estimation of both fat fraction and  $T_2^*$  maps. IDEAL algorithm requires at least of 3 images for allowing the joint estimation of both fat fraction and  $T_2^*$  maps. The number of echoes to be acquired for an optimal reconstruction of the output (fat fraction and  $T_2^*$ ) represents an important parameter of IDEAL. In Chapter III, we have observed a decreasing of fat fraction values with the increasing of the number of echoes. Nevertheless, in according to Hines et al. [58], there exists an excellent correlation between fat fraction calculated with 6-echo and 15-echo reconstructions in mice using a 3T clinical scanner.

### 4.2 MRS and MRI

As previously said, magnetic resonance spectroscopy (MRS) and magnetic resonance imaging (MRI) are powerful methods for calculating fat fraction. They represent two non-invasive ways for calculating the fat fraction without using ionizing radiation. With the MRS, spectra, which provide information about fat composition, are acquired. Differently from MRI, MRS does not give spatial information; the only information the user has, is that the signal derives



from the voxel positioned by him. The data acquired from the voxel of few  $\text{cm}^3$  are then converted in a mono dimensional spectrum. On the other hand, MRI provides images of the object to study and can cover large portion of it. Thus MRI offers the spatial information from 2D (in whatever direction) or 3D acquisition. In MRI, the images are composed by pixels (or voxel if we consider the slice thickness as well) which display the sum of the signals deriving from all protons. No information about the fat fraction or the composition of fat is displayed from a single image. Hence, MRI and MRS represent two complementary tools for calculating fat fraction. Research groups had studied the possible correlation between the results of fat fraction calculated with MRS and MRI. Good correlations and agreements were found for hepatic fat fraction in some works [59]–[63]. However, confounding parameters, like spectral modeling of fat, relaxation times ( $T_1$ ,  $T_2$  and  $T_2^*$ ) and noise, could play a role in the fat fraction miscalculation. Agreement was not reached in other works [64], where the primary peak only and/or the transverse relaxation decay was not considered [59], [61], [62]. In conclusion, good correlation and agreement exists between the measurements of fat fractions done with MRS and MRI, when all fat components and transverse relaxation decay are considered.

### 4.3 Review of the literature

In **Table 4.1**, a list of works effectuated on mice is illustrated. On this table only MRI methods for separating fat and water are listed [65]–[76].

The MR acquisition parameters and the types of reconstructions are listed, as well. The majority of the research groups prefers to acquire multi-gradient-echo images for fat-water separation. This choice allows to use short TR for reducing the  $T_1$  bias and scan time. The majority of the works employs the IDEAL algorithm and Dixon's methods. Nevertheless, VARPRO [77], [78] as well, is a valid algorithm for calculating fat fraction and  $T_2^*$  values. The majority of these works were performed with clinical scanners, operating at 1.5 and 3T. The preclinical scanners, used in the other works, operate at higher magnetic fields.

CHAPTER IV. MRI MEASUREMENTS ON MICE LIVER AND MUSCLE

<i>Article</i>	<i>Mice</i>	<i>Area</i>	<i>Magnetic field</i>	<i>Sequence</i>	<i>Algorithm</i>	<i>Acquisition time</i>
[65]	Obese and lean	Liver	3T	3D spoiled GE	IDEAL	7min 24s
[66]	Obese	Liver	7T (preclinical)	Spoiled GE	2-point Dixon	Not specified
[67]	Obese and lean	Liver	7T (preclinical)	2D T1w aRARE	IDEAL	Not specified
[68]	Obese and lean	Liver	3T	3D Spoiled GE	IDEAL	10min 13s
[69]	Obese and lean	Liver	3T	3D Spoiled GE	IDEAL	6min
[70]	Obese and lean	Liver	1.5T	Spoiled GE	2-point Dixon	44s
[71]	Lean	Liver	1.5T	3D Spoiled GE	[76]	1min 46s
[72]	Lean	Liver	1.5T	Spoiled GE	VARPRO	Not specified
[73]	Obese and lean	Liver	3T	mDixon 3D	mDixon	Not specified
[74]	Lean	Liver and inters. brown adipose	9.4 (preclinical)	2D Spoiled GE	IDEAL	30min
[75]	Obese and lean	Brown/white adipose tissue	3T	3D Spoiled GE	IDEAL	10min
	<i>Flip angle</i>	<i>N° echoes</i>	<i>TR</i>	<i>1° TE</i>	<i>Echo spacing</i>	<i>Voxel size</i>
[65]	5°	15	30ms	2.1ms	3.7ms	0.5x0.5x0.8mm <sup>3</sup>
[66]	40°	2	500ms	1.47ms	0.5ms	0.1x0.1x2.0mm <sup>3</sup>
[67]	90°	4	1087ms	9.1ms	318μs	0.2x0.2x1.0mm <sup>3</sup>
[68]	5°	15	41.4ms	2.6ms	1.4ms	0.5x0.3x0.8mm <sup>3</sup>
[69]	5°	15 (5x3)	24.4ms	2.2ms - 3.4ms - 4.6ms	1.2ms (3.6ms/3)	0.6x0.6x0.8mm <sup>3</sup>
[70]	13°	2	6.9ms	2.4ms	2.4ms	Not specified
[71]	35°	32	55ms	1.6ms	1.3ms	1.2x1.2x1.2mm <sup>3</sup>
[72]	75°	12 (4x3)	1000ms	2.46ms - 3.36ms - 4.26ms	0.9ms (2.7ms/3)	Not specified
[73]	Not specified	4	Not specified	Not specified	Not specified	Not specified
[74]	10°	3	295ms	2.8ms	1ms	0.5x0.3x0.8mm <sup>3</sup>
[75]	5°	6	41.4ms	2.6ms	1.4ms	0.5x0.3x0.8mm <sup>3</sup>

**Table 4.1:** List of publications on mice. In this table, the MR sequence parameters, the magnetic fields, the analyzed areas, the type of mouse and the reconstructions for calculating the fat fractions are listed.

## 4.4 Materials and methods

### 4.4.1 MRI experiment

Mice L-PK/c-myc (n=9) were used for *in-vivo* experiments. They were anesthetized with 2% isoflurane-oxygen (v/v) and the respiration was monitored. MRI measurements were performed at 4.7T with a scanner dedicated to small animal imaging (47/40 Biospec, Bruker, Wissembourg, France), using a BGA06 gradient system (maximum strength equal to 950mT/m). A linear volume coil was used as transmitter and receiver.

Gradient-echo sequences were acquired to perform Dixon and IDEAL reconstruction.

With respect to Dixon's method, three separate gradient-echo sequences at three different echo times (1.45, 2.2 and 2.9ms, respectively) were acquired. The other parameters were: FOV = 3.2x3.2cm<sup>2</sup>, repetition time = 280ms, flip angle = 30°, slice thickness = 1mm, interslice distance = 1.5mm, 8 averages and 15 slices.

With respect to the IDEAL method, three separate multi-gradient-echo sequences with first echo time equal to 1.37, 2.16 and 2.95ms, respectively, were acquired. The echo spacing was for all of the three sequences equal to 2.37ms. The images, acquired from these three sequences, were combined in order to create a single data set with effective echo spacing 0.79ms (**Figure 4.3**).

A first set of IDEAL data was acquired with 12 echoes and 8 slices. The TR was set to the minimal value (380ms) to reduce the scan time. Three multi-gradient-echo (MGE) sequences were acquired with these parameters: 12 echoes, repetition time = 380ms, flip angle = 50°, field of view = 3.2x3.2cm<sup>2</sup>, slice thickness 1.2mm, 8 slices, interslice distance = 1.5mm, matrix size = 160x160, bandwidth = 2x10<sup>5</sup> Hz and 4 averages. A second set of IDEAL data was acquired with the modified parameters following the analysis of the first IDEAL data set: in particular it was observed that, for each multi-gradient-echo sequence, the useful number of echoes could be reduced to six echoes. Thus, the TR could be shortened to 280ms. The flip angle was chosen to 30° in order to minimize the  $T_1$  bias. The other parameters were: slice thickness = 1 mm, 6 echoes and 8 averages (effective sequence, **Figure 4.1**).

### 4.4.2 Data analysis

With respect to the IDEAL method, different analyses were performed to study the effects of different number of echoes and echo spacing on the IDEAL output (fat fraction and  $T_2^*$  value):

- IDEAL reconstruction was applied to the images acquired with single multi-gradient-echo sequence (1° Sequence, **Figure 4.1**). Fat fraction and  $T_2^*$  maps were reconstructed using 3, 4, 5...12 echoes;

- IDEAL reconstruction was applied to the images obtained with the three multi-gradient-echo sequences (**Figure 4.1**). Fat fraction and  $T_2^*$  maps were reconstructed using 3, 4, 5...20 echoes.

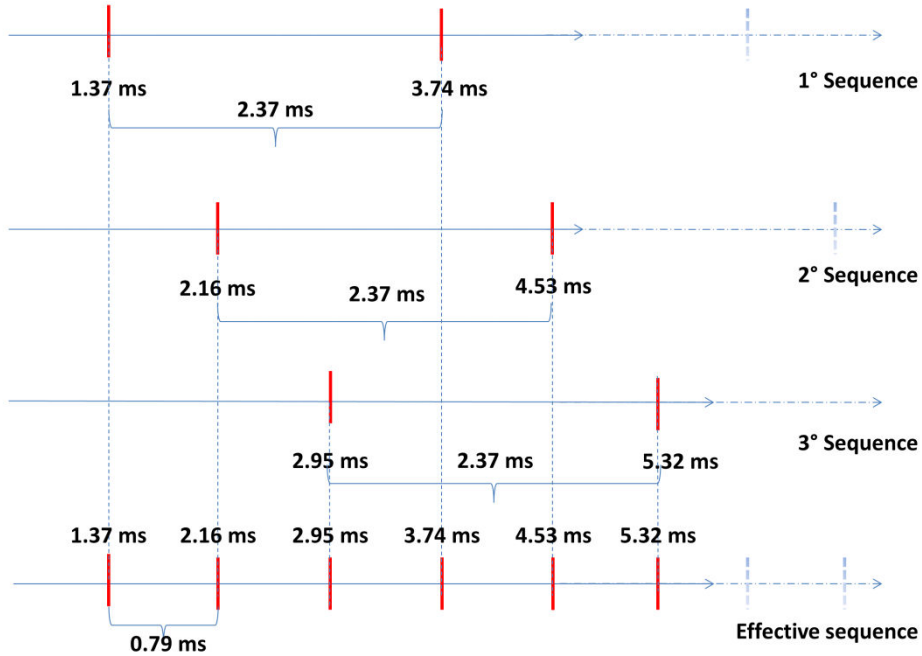


**Figure 4.1:** Scheme of the creation of the “effective sequence”. The 3 sequences with echo spacing 2.37ms were combined to have a sequence with 0.79ms echo spacing.

Comparison between IDEAL at different number of echoes was performed.

- ROI measurements were performed in liver and muscle. For each ROI, chosen as 10-pixel (liver) and 5-pixel (muscle) radius, the mean and standard deviation of fat fraction and  $T_2^*$  was calculated;
- the coefficient of variation (CV), defined as standard deviation divided by the mean value, was calculated for each ROI of 5-pixel radius. The fat fraction and  $T_2^*$  obtained at different number of echoes were compared. As a metrics of the quality of fat fraction and  $T_2^*$  maps, the CV was used;
- further analyses were performed to compare the specific scenario of 6 and 15 echoes since in the literature this was subject of interest [65]. Moreover the 3-echo reconstruction was added to the comparison. Student’s t-test was performed on the values of fat fraction of  $T_2^*$ ;
- comparison between the single and effective sequence was performed on  $T_2^*$  and fat fraction values;

Furthermore, a comparison between Dixon and IDEAL was performed on fat fraction values.

At last, in a mouse, a spectrum was acquired for comparing the results obtained with IDEAL algorithm, using the calculated spectrum, and the results obtained using the spectrum proposed by Hamilton et al. [27].

For avoiding phase unwrapping problems, the brunch-cut algorithm [79] was used. It was performed on phase images for generating the initial field map (Appendix C).

All images (**Figure 4.1**) were processed with homemade scripts in Matlab which reproduces the IDEAL algorithm and 3-point Dixon's method.

## 4.5 Results

### 4.5.1 Results of IDEAL in mouse using one sequence

In **Figure 4.2**, the  $T_2^*$  and fat fraction maps reconstructed by IDEAL algorithm using 3 echoes are shown. With the output of IDEAL algorithm, a multi-gradient-echo image is illustrated as well.

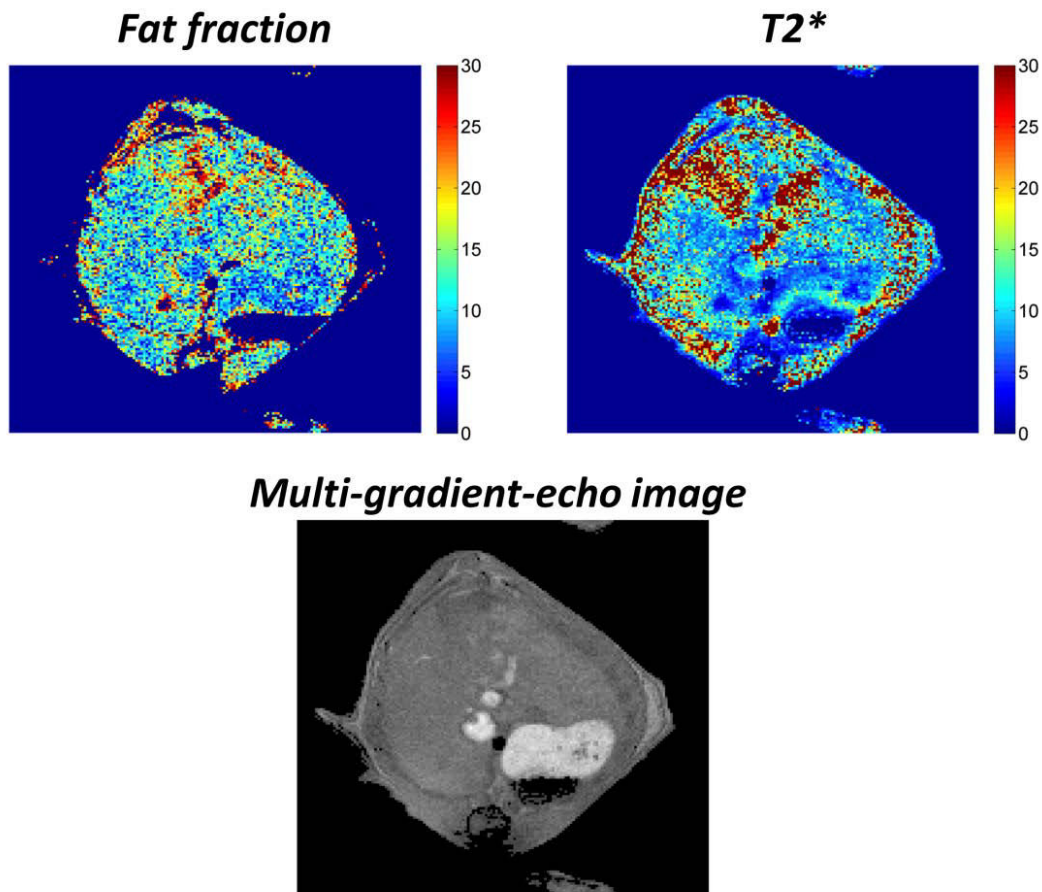


**Figure 4.2:** On top the output of the 3-echo IDEAL reconstruction: fat fraction (left) and  $T_2^*$  (right) maps. The results are relative to the MR images acquired on a mouse. On bottom a multi-gradient-echo image of the mouse used.

IDEAL reconstructions, using different number of echoes, were obtained. ROI measurements were achieved on the obtained fat fraction and  $T_2^*$  maps in liver and muscle. For each mouse, three ROIs were positioned in liver and muscles, where no visible artifacts were present. The mean and standard deviation values of fat fraction found in a mouse are represented in the plots in **Figure 4.3**. The fat fraction mean values in liver and muscle increase with the increasing of the number of echoes used for IDEAL reconstruction. **In Figure 4.4**, the mean and standard deviation values of  $T_2^*$  are represented.

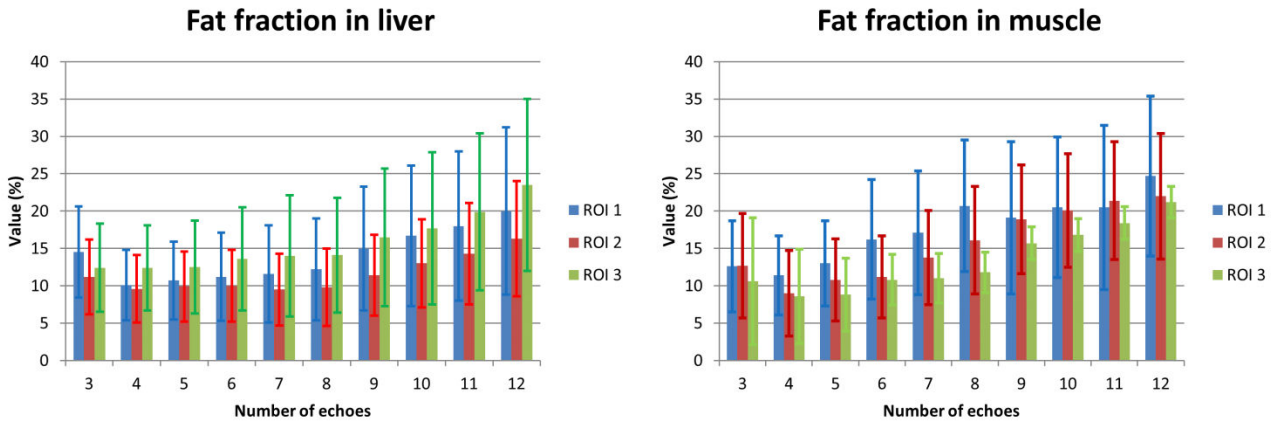


**Figure 4.3:** IDEAL reconstruction relative to the images acquired with the single multi-gradient-echo sequence ( $1^\circ$  Sequence, **Figure 4.1**). Fat fraction values as a function of the number of echoes used for IDEAL reconstruction. The values were calculated in liver (left) and muscle (right)

The values of  $T_2^*$  in liver and muscle converge using a high number of echoes. The standard deviation values in muscle decrease using more than 3 echoes. For the fat fraction estimation, it is appropriate to use a low number of echoes for avoiding the increasing of the values and/or any bias due to eventual differences between the  $T_{2W}^*$  and  $T_{2F}^*$ .

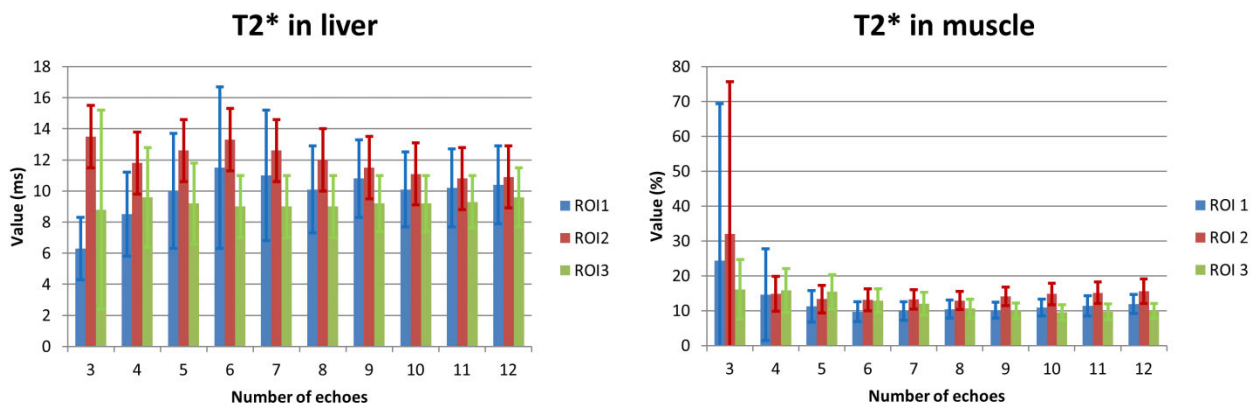


**Figure 4.4:**  $T_2^*$  values as a function of the number of echoes used for IDEAL reconstruction. The values were calculated in liver (left) and muscle (right)

In **Figure 4.5** the fat fraction and  $T_2^*$  map reconstructed by IDEAL algorithm using 3 (for the fat fraction) and 6 echoes (for the  $T_2^*$ ) are shown.

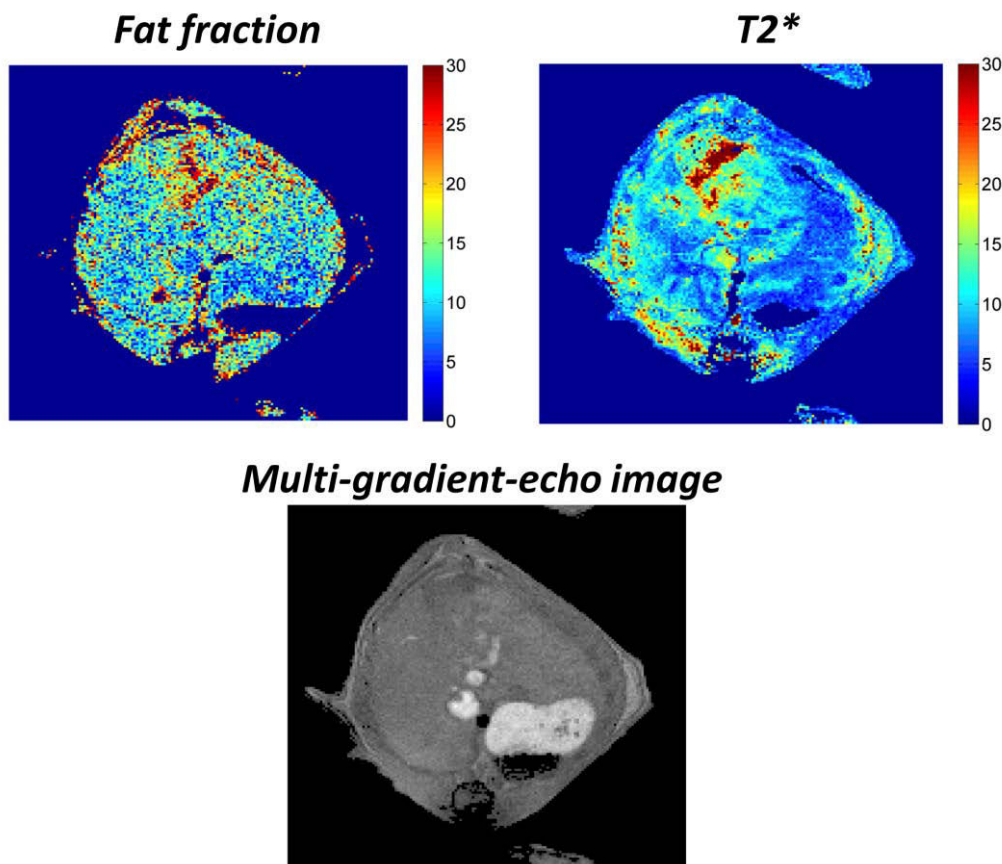


**Figure 4.5:** Output of IDEAL algorithm. On top the fat fraction (left) and  $T_2^*$  (right) map reconstructed using 3 echoes (for the fat fraction) and 6 echoes (for the  $T_2^*$ ). The 6-echo reconstruction provides a  $T_2^*$  map less noisy than the 3-echo reconstruction. The results are relative to the multi-gradient-echo image illustrated on bottom.

#### 4.5.2 Results of IDEAL in mouse using the effective sequence

IDEAL reconstructions were obtained at different number of echoes for the images of the effective sequence. ROI measurements were achieved on the obtained fat fraction and  $T_2^*$  maps in liver and muscle. For each mouse, three ROIs were positioned in liver and muscles where no visible artifacts were present. The mean and standard deviation values of fat fraction found in a mouse are represented in the plots in **Figure 4.6**.

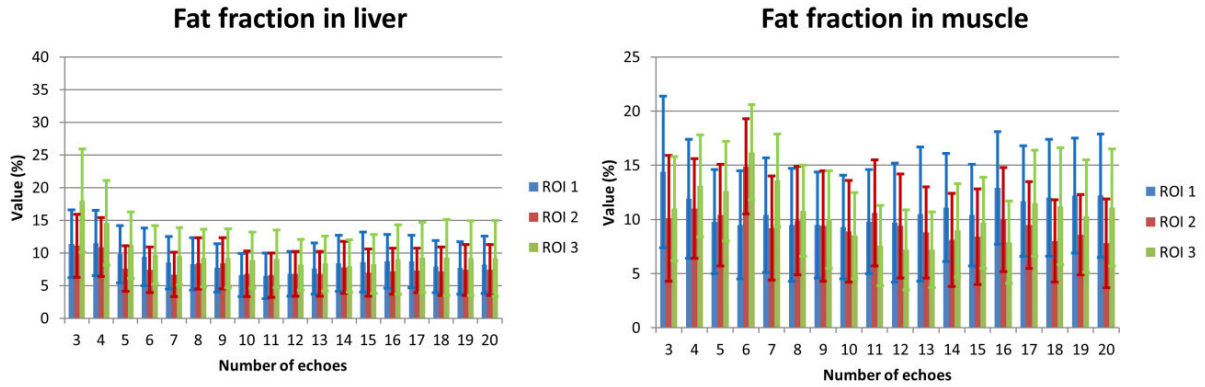


Figure 4.6: Fat fraction values in function of the number of echoes used for IDEAL reconstruction. The values were calculated in liver (left) and muscle (right)

The values of fat fraction are almost constant in both anatomical areas. At low number of echoes, the values found in liver are slightly higher, but consistent with the values calculated at high number of echoes. The values found using the effective sequence are lower than the ones found for the single sequence. In Figure 4.7, the  $T_2^*$  mean and standard deviation values, relative to the images of the effective sequence, are represented.

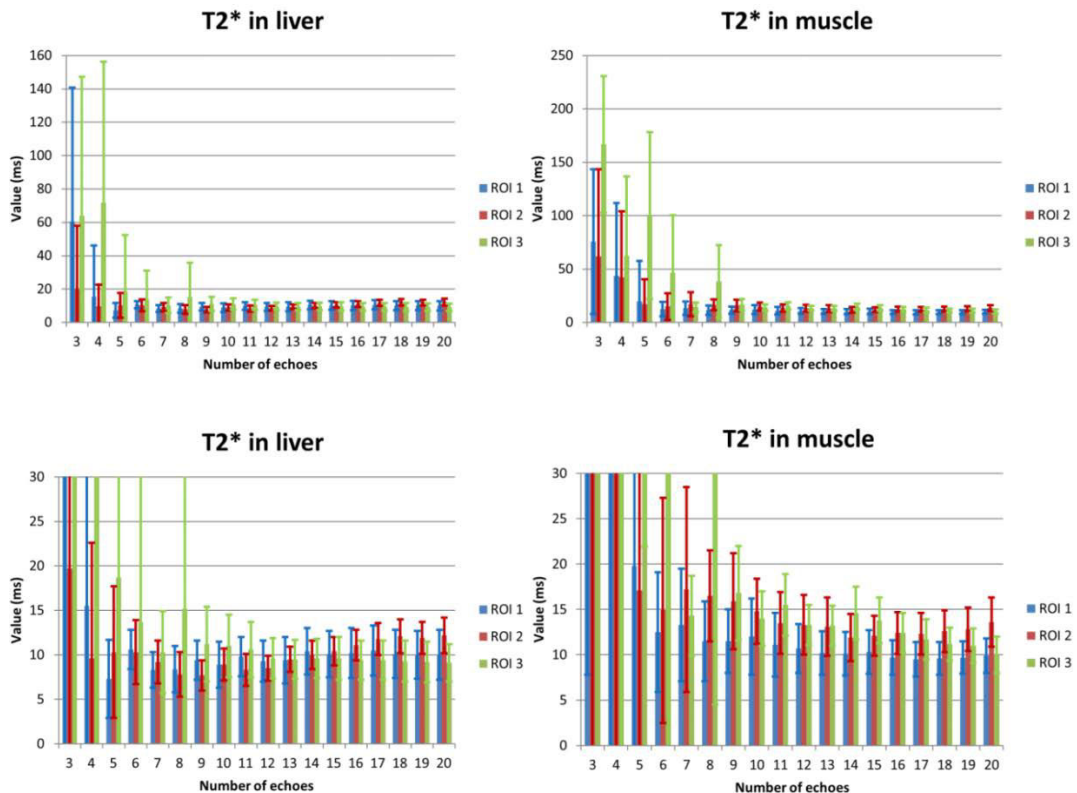
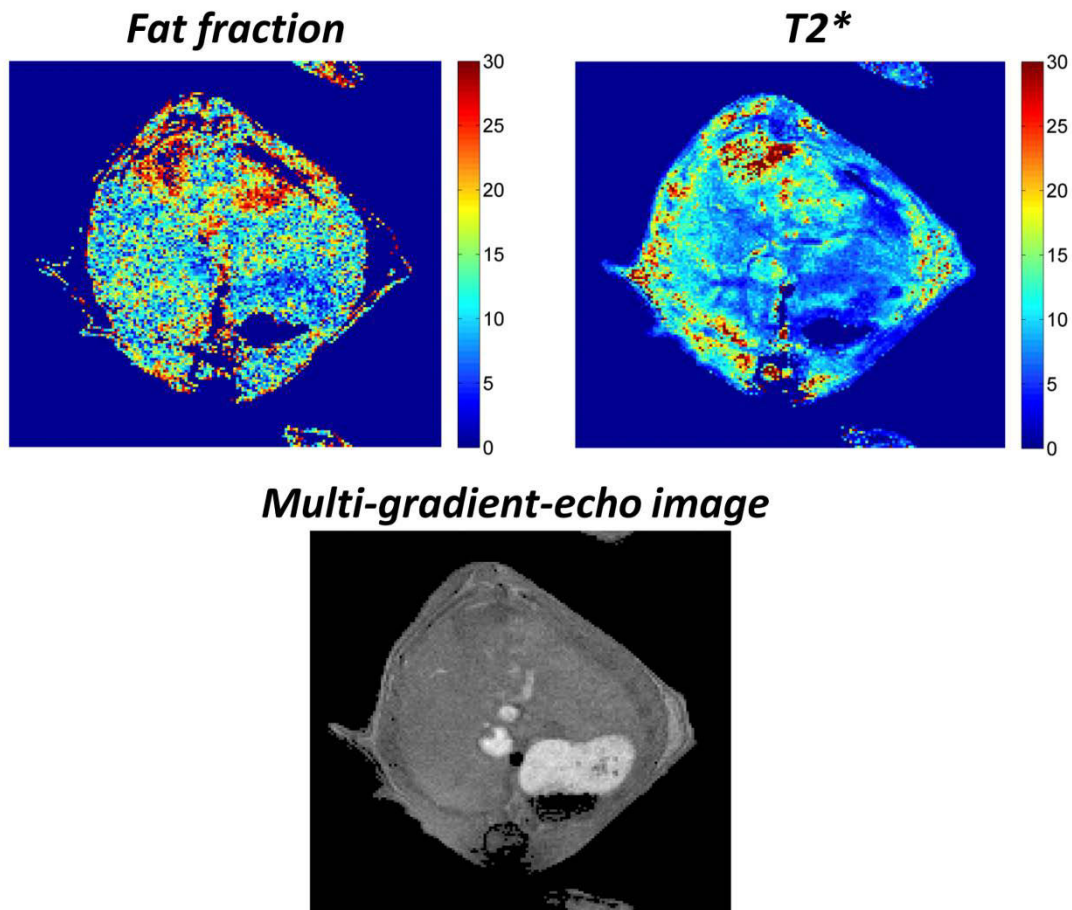


Figure 4.7:  $T_2^*$  values in function of the number of echoes used for IDEAL reconstruction. The values were calculated in liver (left) and muscle (right). On bottom, the same plots illustrated on top are shown for a better visualization of the plateau.



The  $T_2^*$  means reach the values of plateau at high number of echoes in both anatomical areas. The mean and standard deviation values are higher at low number of echoes. In **Figure 4.8**, the fat fraction and  $T_2^*$  map reconstructed by IDEAL algorithm using 3 and 10 echoes, respectively, are illustrated.



**Figure 4.8:** Output of IDEAL algorithm. On top the fat fraction (left, reconstructed using 3 echoes) and  $T_2^*$  (right, reconstructed using 10 echoes) map. The results are relative to the multi-gradient-echo image illustrated on bottom.

#### 4.5.3 IDEAL results using 3, 6 and 15 echoes

The results of fat fraction and  $T_2^*$ , obtained on the images of the effective sequence and shown in the previous paragraph, were further analyzed, with the focus on the outputs of IDEAL at 3, 6 and 15 echoes. The fat fraction values are represented in Bland-Altman plots (on the x-axis the mean value of 2 measurements is represented, whereas, on the y-axis, the difference between these two measurements is expressed), in **Figure 4.9**, for comparing the results of the three reconstructions. Three plots were necessary for comparing the results (3-echo vs 6-echo, 3-echo vs 15-echo and 6-

echo vs 15-echo). About the comparison between the 3-echo and 6-echo reconstructions (top, left), the values relative to the muscle with the 3-echo reconstruction are higher than the ones in the 6-echo reconstruction. About the comparison between the 3-echo and 15-echo reconstructions (bottom), the values for liver are around the 0 value in difference. For the muscle, the same consideration done in the previous plot can be concluded.

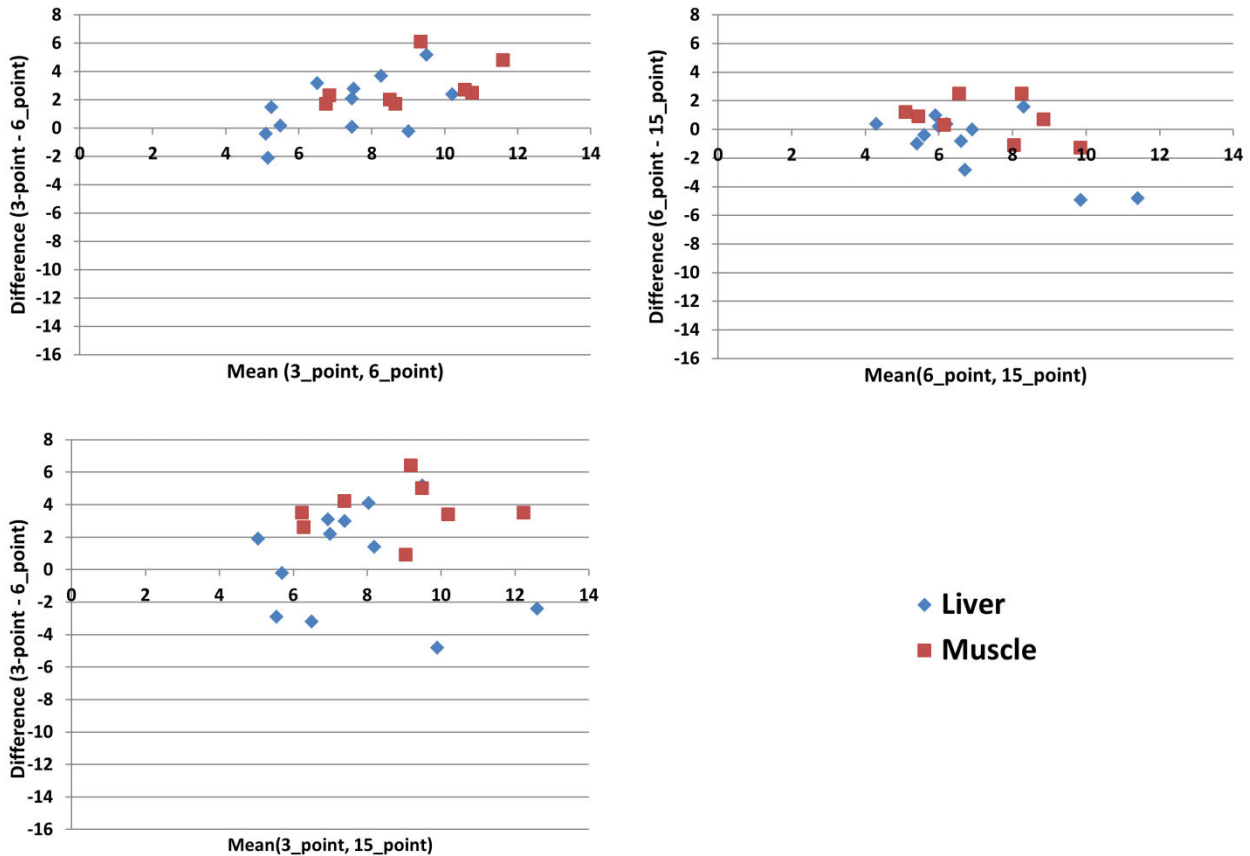


**Figure 4.9:** Bland-Altman plots relative to the fat fraction mean values. On the x-axis and y-axis the mean values of two measurements and their differences are respectively represented. The fat fraction mean values were calculated on the maps generated by the 3-echo, 6-echo and 15-echo reconstructions.

The last comparison was performed between the 6-echo and 15-echo reconstructions (top, right). The values, calculated in liver and muscle, show a spread around the 0 value in difference.

The Student’s t-test analyses were performed for the comparison between the three reconstructions on the fat fraction and  $T_2^*$  values. For the Student’s t-test analyses, the two-tail distribution values, using a risk factor equal to 0.05, were considered. The statistical t and the two-tail critical values for each comparison are reported in **Table 4.2** (for fat fraction) and **Table 4.3** (for  $T_2^*$ ).

<i>Area</i>	<i>3-echo vs 6-echo</i>		<i>3-echo vs 15-echo</i>		<i>6-echo vs 15-echo</i>	
	<i>Stat. t</i>	<i>Crit. t</i>	<i>Stat. t</i>	<i>Crit. t</i>	<i>Stat. t</i>	<i>Crit. t</i>
Liver	1.5	2.1	0.2	2.1	1.0	2.1
Muscle	2.4	2.2	2.7	2.2	0.7	2.2

**Table 4.2:** T-test statistic performed on the fat fraction values relative to IDEAL reconstruction liver and muscle. The 3-echo, 6-echo and 15-echo fat fraction reconstruction, calculated in four mice, were compared.

<i>Area</i>	<i>6-echo vs 15-echo</i>	
	<i>Statistical t</i>	<i>Critical t</i>
<b>Liver</b>	0.5	2.1
<b>Muscle</b>	1.2	2.1

**Table 4.3:** T-test statistic effectuated on the  $T_2^*$  values of IDEAL algorithm in liver and muscle, and considering the set constituted by the values of both anatomical areas. The 6-echo and 15-echo  $T_2^*$  values, calculated in four mice, were compared.

In liver, the measurements are consistent in the three comparisons. Instead, in muscle the values are consistent only in the comparison between the 6 and 15-echo reconstructions. However, short echo trains are suggested to be used for avoiding any bias due to differences between  $T_{2W}^*$  and  $T_{2F}^*$ .

With respect to the  $T_2^*$  values, only the t-test between the 6-echo and 15-echo reconstructions is displayed, since the  $T_2^*$  standard deviation values found for the 3-echo reconstruction were generally too high. The values of  $T_2^*$  found in the 6-echo and 15-echo reconstruction are consistent for both anatomical area. In summary, from the plots and Student's t-test analyses:

- In muscle, the 3-echo reconstruction provides higher values than in the other two reconstructions;
- In liver, the three reconstructions yield consistent values;
- The  $T_2^*$  values, found in the 6-echo and 15-echo reconstruction, are consistent.

All these considerations are done for ROI measurements, performed where no visible artifacts were present.

**4.5.4 Study on the coefficient of variation**

IDEAL reconstruction was performed at different number of echoes (from 3 to 21 for the first set of mice and 3 to 18 for one of the second set) and ROI measurements on  $T_2^*$  and fat fraction maps were performed in liver and muscle. Means and standard deviations were determined and the coefficients of variation (CV) were calculated for each ROI, reconstruction and mouse. For each number of echoes and mouse, the coefficients of variation were regrouped for both anatomical areas. These coefficients of variation were used for calculating the mean values of the coefficients of variation for fat fraction and  $T_2^*$  values. At last, these values were plotted in function of the number of echoes for liver and muscle (**Figure 4.10**). Each error bars, displayed in the histogram plots of **Figure 4.10**, was calculated as the standard deviation of the coefficient of variation mean. For both plots relative to the fat fraction, no trend was observed. In the plots relative to  $T_2^*$  in liver, the values achieve their minimum at 12-15 number of echoes. In the plots relative to  $T_2^*$  in muscle, the coefficient of variation means decrease with the increasing of the number of echoes. These results on  $T_2^*$  represent a further confirm of the advantage to calculate the  $T_2^*$  maps using long echo trains.

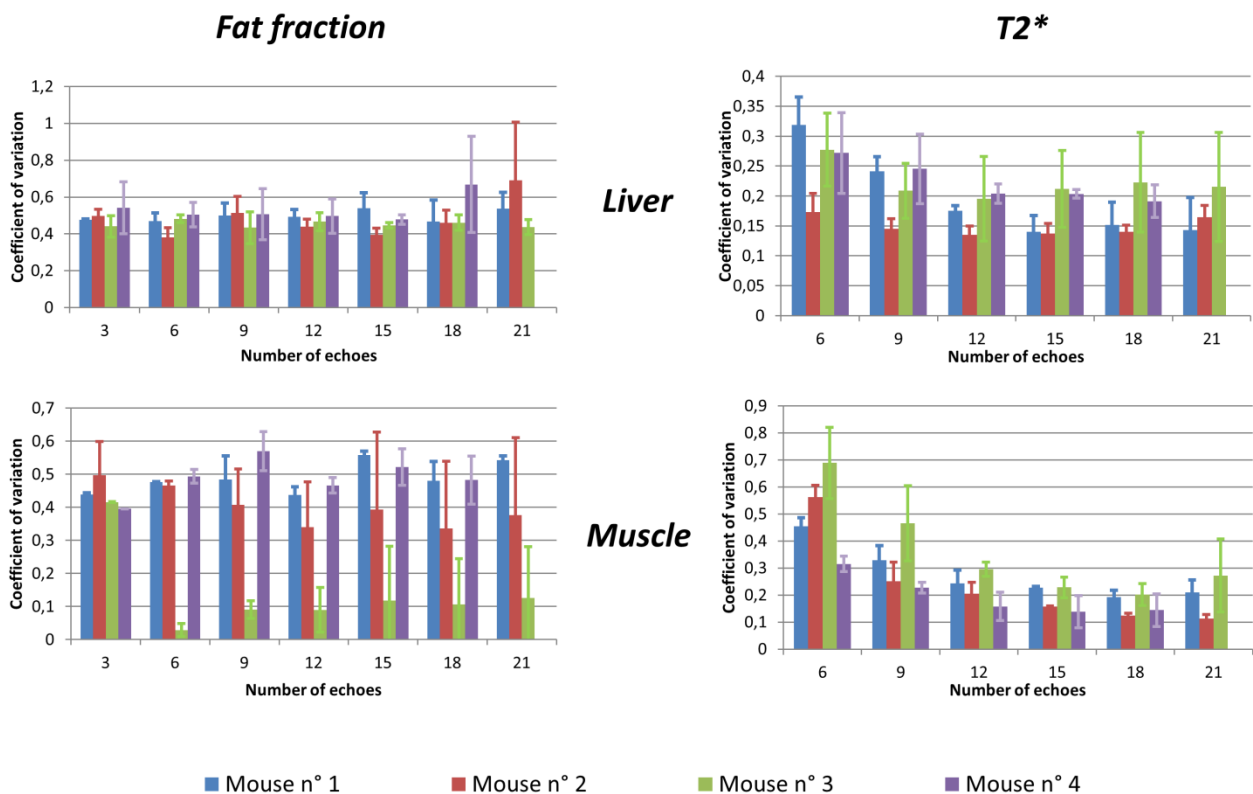


**Figure 4.10:** Coefficient of variation versus number of echoes plots. On left the plots relative to the fat fraction CV and, on right, relative to the  $T_2^*$  ones. The values, calculated in liver and muscle are determined for the four mice. The error bars are calculated as the standard deviation of the standard error means.

**4.5.5 Comparison between IDEAL using single and effective sequences on  $T_2^*$**

The  $T_2^*$  maps, calculated by IDEAL using the single and effective sequences, were compared. For understanding if it is necessary to acquire 3 sequences for calculating the  $T_2^*$  (with the parameters indicated in materials and methods) or if it is sufficient to use a single sequence, the values at plateau were analyzed. The  $T_2^*$  mean values calculated with ROIs from 6 to 12 echoes (for the single sequence) and from 10 to 20 echoes (for the effective sequence) were averaged. The mean values in liver and muscle for the single and effective sequences were compared with the Student's t test. In **Table 4.4**, the statistical t and two-tail critical values are shown.

<i>Area</i>	<i>Single vs Effective</i>	
	<i>Statistical t</i>	<i>Critical t</i>
<b>Liver</b>	0.6	2.3
<b>Muscle</b>	0.7	2.4

**Table 4.4:** T-test statistic calculated on the values at plateau found for the single and effective sequences. The values were taken in liver and muscle.

The values of plateau calculated from the two sequences in liver and muscle, are consistent. In **Figure 4.11**, the  $T_2^*$  maps calculated using 7 echoes of the single sequence and 19 echoes of the effective sequence, respectively, are displayed. The reason why we use 7 echoes and 19 echoes, respectively, derives from the creation of the effective sequence. Using 7 and 19 echoes, the last echo time (15.6ms) for both sequences is the same (this is not the singular combination, however using these number of echoes for the two sequences the  $T_2^*$  mean values reach the plateaus). The values in both maps are similar, but the advantage of using the effective sequence is the creation of smoother maps. However, also the single sequence provides good  $T_2^*$  maps when more than 6 echoes are used.

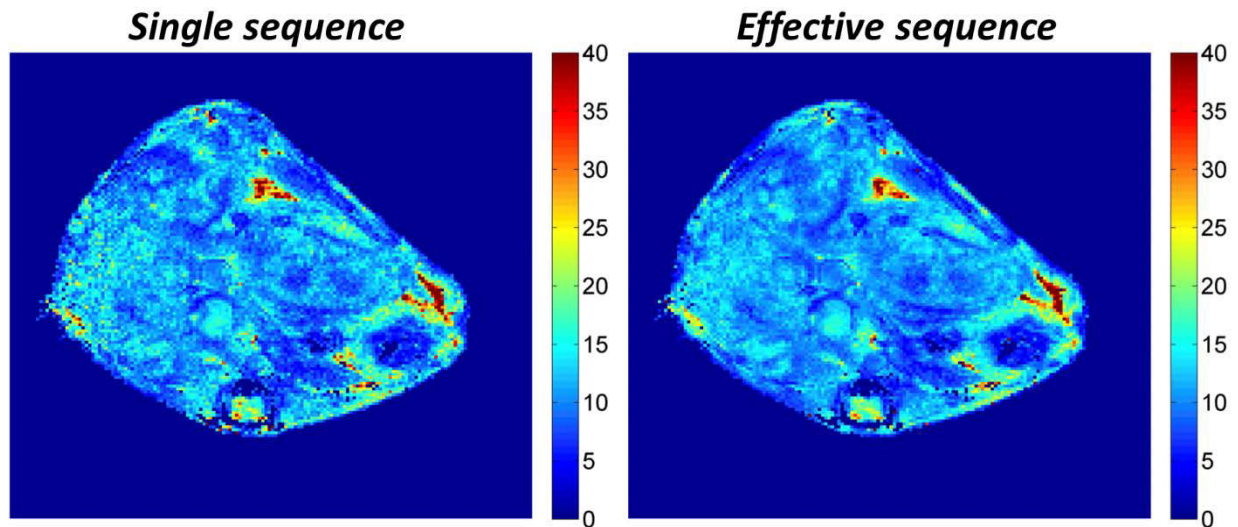


**Figure 4.11:**  $T_2^*$  maps calculated using the single sequence (left) and the effective sequence (right). For the single sequence, 7 echoes were used, whereas, for the effective sequence, 19 echoes.

#### 4.5.6 Comparison between IDEAL (using single and effective sequences) and Dixon for the fat fraction

A comparison between the results of fat fraction obtained with IDEAL, using the single and effective sequences, was performed. The 3-echo IDEAL reconstructions, using the single and effective sequences, were compared with the 3-point Dixon's method. The fat fraction mean and standard deviation values, obtained with ROIs, were calculated. The fat fraction values, relative to the 3-point Dixon's method, were corrected since the 3-point Dixon's method provided single-peak estimations. Each value was divided for 0.7, approximately the area under the fat peak at 1.3ppm [73]. The mean values were used for creating Bland-Altman plots, illustrated in **Figure 4.12**. The values in liver and muscle are almost around the 0 value in all three plots.

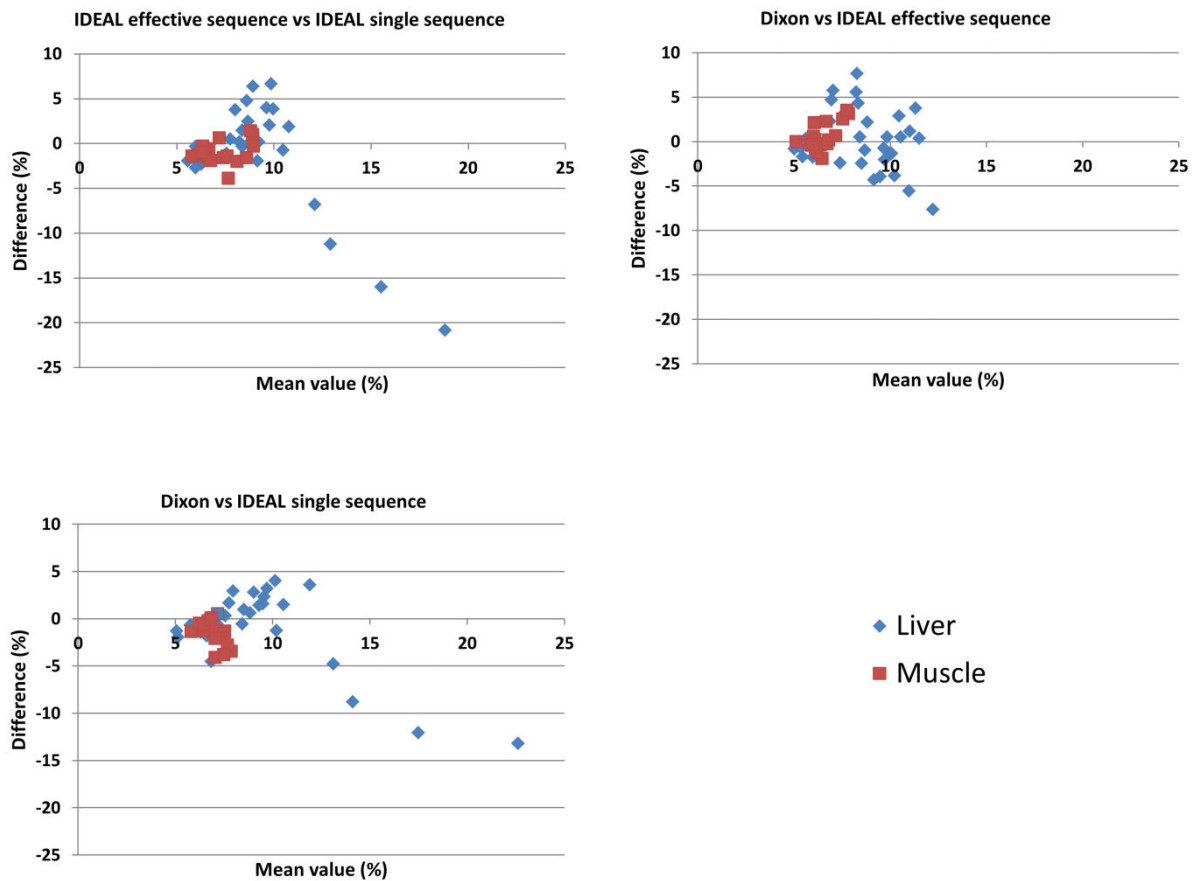


**Figure 4.12:** Bland-Altman plot with the fat fraction mean values calculated with the IDEAL algorithm (using single sequence and effective sequences) and 3-point Dixon’s method

The Student’s t-test analyses were performed for the fat fraction values acquired in both anatomical areas for the three reconstructions. The values of the statistical t and two-tail critical values are shown in **Table 4.5**.

Area	IDEAL (single) vs IDEAL (effective)		Dixon vs IDEAL (single)		Dixon vs IDEAL (effective)	
	Stat. t	Crit. t	Stat. t	Crit. t	Stat. t	Crit. T
Liver	0.9	2.0	1.0	2.0	0.2	2.0
Muscle	2.5	2.0	5.3	2.0	1.4	2.0

**Table 4.5:** T-test statistic effectuated on the values of 3-echo IDEAL algorithm and 3-point Dixon’s method. The values were taken in liver and muscle

The fat fraction values calculated in liver are consistent for the three reconstructions. In muscle the values calculated using IDEAL single sequence are not consistent with the ones calculated with the



other two reconstructions. Hence, in normal cases, the three methods are equivalent for calculating the fat fraction in liver but not in muscle. However, attention to areas with very short  $T_2^*$  was paid. In slices close to lungs, the magnetic field inhomogeneity was higher than in the slices on bottom. As a consequence, the magnetic field inhomogeneity critically reduced the  $T_2^*$  value to less than 5 ms. In this case, neither in liver the fat fraction estimation was equivalent for the three reconstructions. In **Figure 4.13**, fat fraction estimations achieved with the three reconstructions in a slice close to lungs are shown. On bottom, the  $T_2^*$  map calculated using 10 echoes of the effective sequence and a multi-gradient-echo image are displayed. In the area with short  $T_2^*$ , the fat fraction map is overestimated using IDEAL single sequence (top, left) and the 3-point Dixon's method (top, right). The IDEAL reconstruction performed using three sequences yields more realistic fat fraction values in the areas with short  $T_2^*$  value. Hence, the advantage to use three sequences for IDEAL reconstruction is evident in this case.

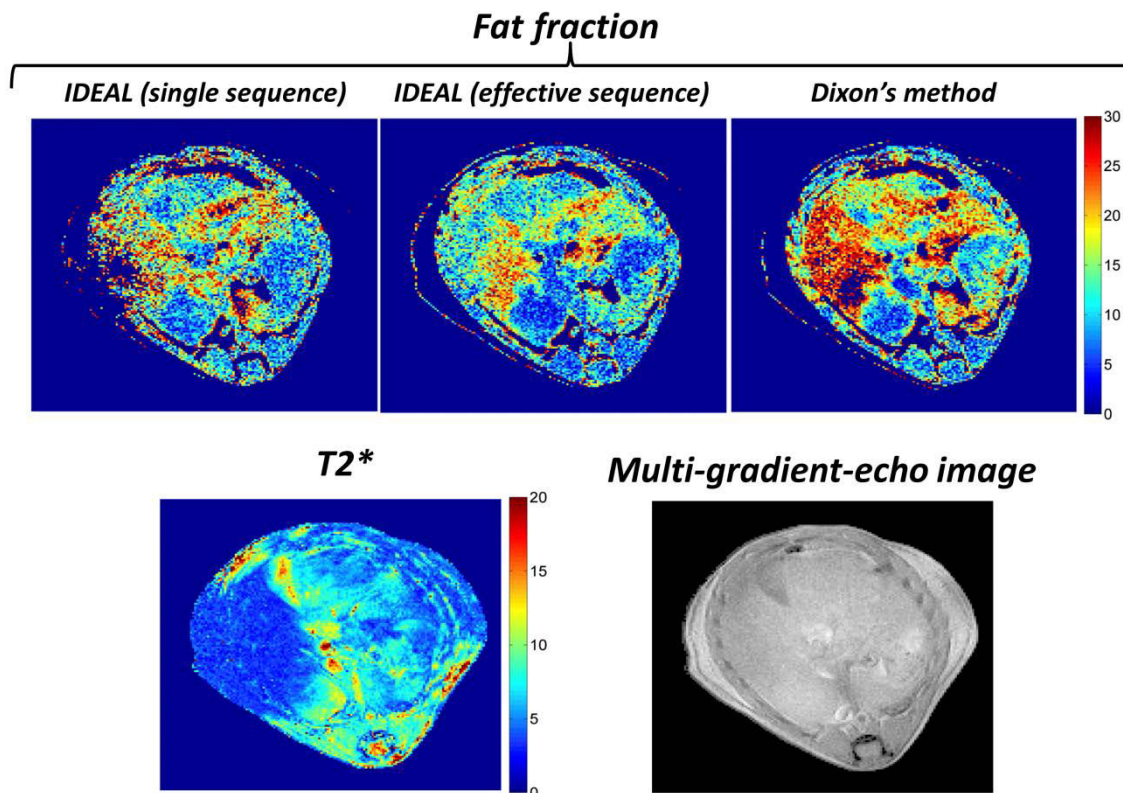


**Figure 4.13:** Fat fraction maps (top) calculated with IDEAL algorithm (using the single and effective sequence) and 3-point Dixon's method. On bottom, the  $T_2^*$  map (calculated by IDEAL algorithm using 10 echoes of the effective sequence) and a gradient echo image are shown for further information on the morphologic and physiologic structure



**4.5.7 Spectrum acquired in literature vs spectrum acquired on a mouse**

The spectrum acquired in a mouse liver was employed in IDEAL algorithm for calculating the fat fraction maps. These maps were compared with the maps obtained using a spectrum taken from literature [27]. The difference between the fat fraction maps (the difference is between the fat fraction map with the spectrum of a mouse liver found in literature and the fat fraction map with the spectrum calculated on the mouse) is shown in **Figure 4.14**. In addition, the difference between the field maps reconstructed by IDEAL and a multi-gradient-echo image are shown. The differences are especially on the edges and in subcutaneous fat. These differences are located where high values occur in the “field map difference” (**Figure 4.14**, top right). A profile was drawn on the fat fraction difference map in liver (**Figure 4.15**, left). The values along the profile are shown in **Figure 4.15**. In liver, the “fat fraction difference” provides values around 0.6% in mean. The values in muscle are consistent with this mean. Hence, in the light of the current results, the two spectra have the same action on the fat fraction maps, calculated by IDEAL algorithm.

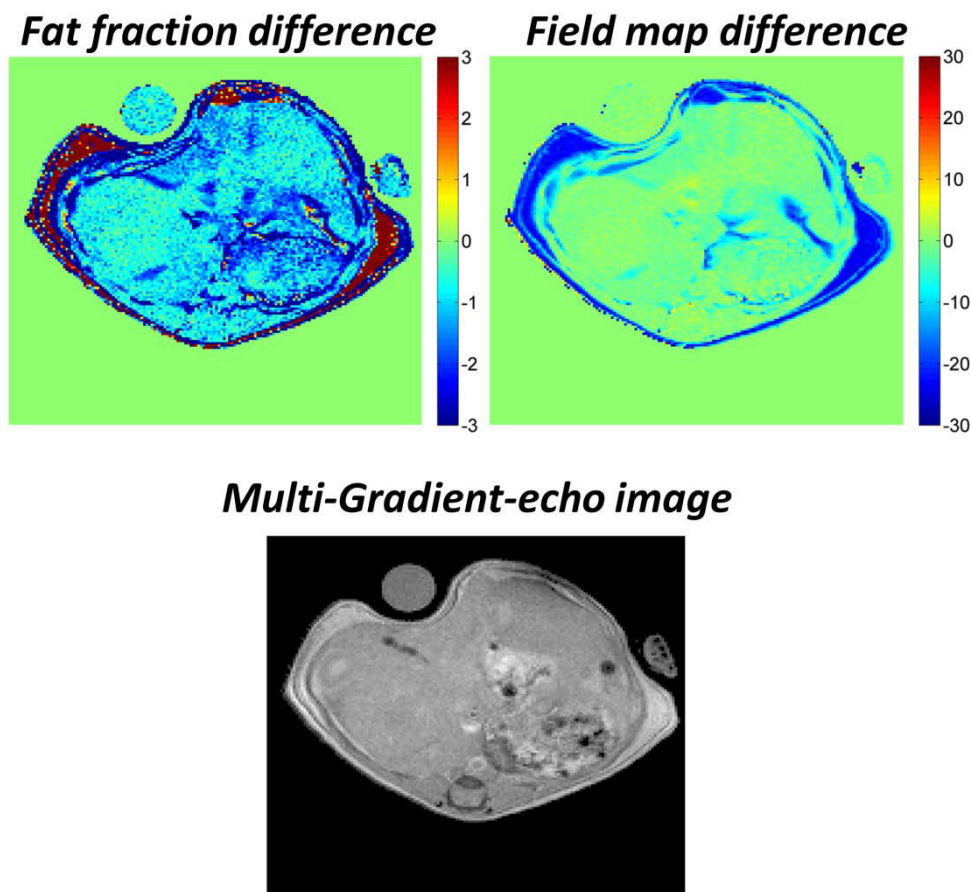


**Figure 4.14:** Comparison between the fat fraction calculated using a spectrum acquired on a mouse and the ones calculated using the literature spectrum. The fat fraction and field maps calculated with each spectrum using IDEAL algorithm were subtracted. The results of the fat fraction map difference map and field map difference are illustrated on top. On bottom a multi-gradient-echo image is illustrated.

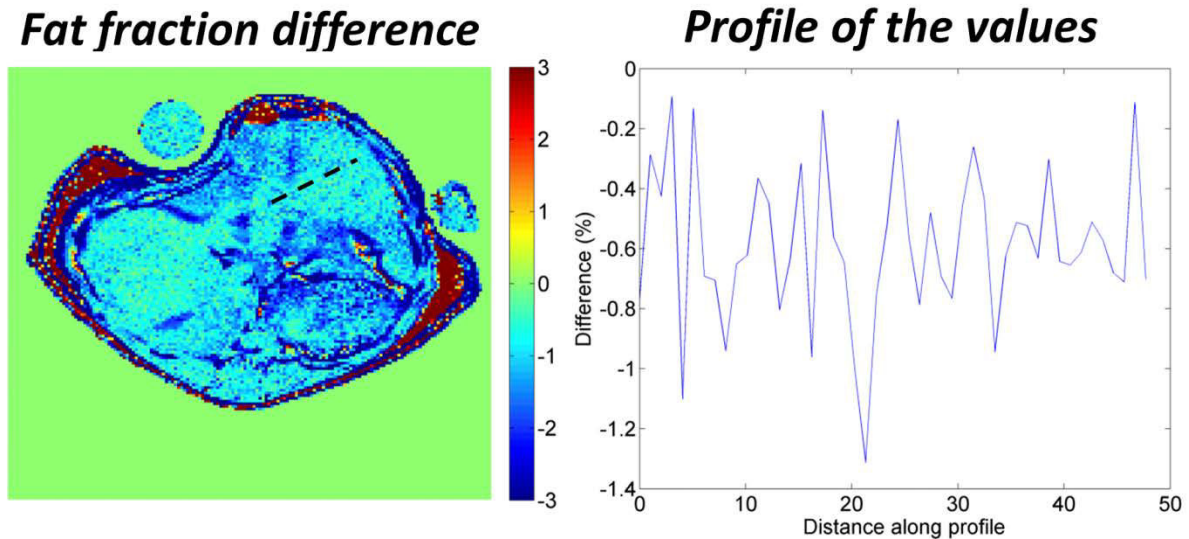


**Figure 4.15:** (Left) Difference between the two fat fraction maps calculated using two different spectra. On right the profile of the values relative to the fat fraction maps. The mean value is about 0.6% in difference.

#### 4.6 Misregistration

For fat-water acquisitions on mice, the choice of using 3 sequences, opportunely spaced in time, was operated. The three sequences were put together to create a thicker sequence (the effective sequence) of echo spacing shorter than in the single sequences. For using this approach, it was assumed that the mice did not move during the sequence acquisitions. The assumption could be erroneous and it needs to be proved, so additional analyses were performed with the use of Imagej [80]. For the comparison, the images acquired at first time echo of each sequence were selected and examined with the StackReg plugin [81], [82] for analyzing the presence of misregistration artifacts. In **Figure 4.16**, the images at first time echo for the three sequences ( $S_1$ ,  $S_2$  and  $S_3$ , respectively) are illustrated: the images were put in a stack ( $S_n$ ) for the application of the plugin. The plugin considers four types of transformations: rigid body, translation, rotation and affine. It works as follow: once created the image stack and chosen the type of transformation to study, the plugin analyzes all images and align them respect to the first one. In output, a stack ( $S'_n$ ) composed by the transformed images (three images in this case) is created. For this study, the rigid body transformation was considered, supposing that the mice could rotate and translate only limiting to the axial plane (the same of the image). For a direct measurement of the effect of the transformations, the difference ( $S'_n - S_n$ ) was calculated and normalized for  $S_n$ . Since the image  $S_1$  is not transformed (the transformation respect to itself is 0), the only images necessary to be analyzed are  $S_2$  and  $S_3$ . Hence, the  $(S'_2 - S_2)/S_2$  and  $(S'_3 - S_3)/S_3$  maps were calculated and in **Figure 4.17** are shown.

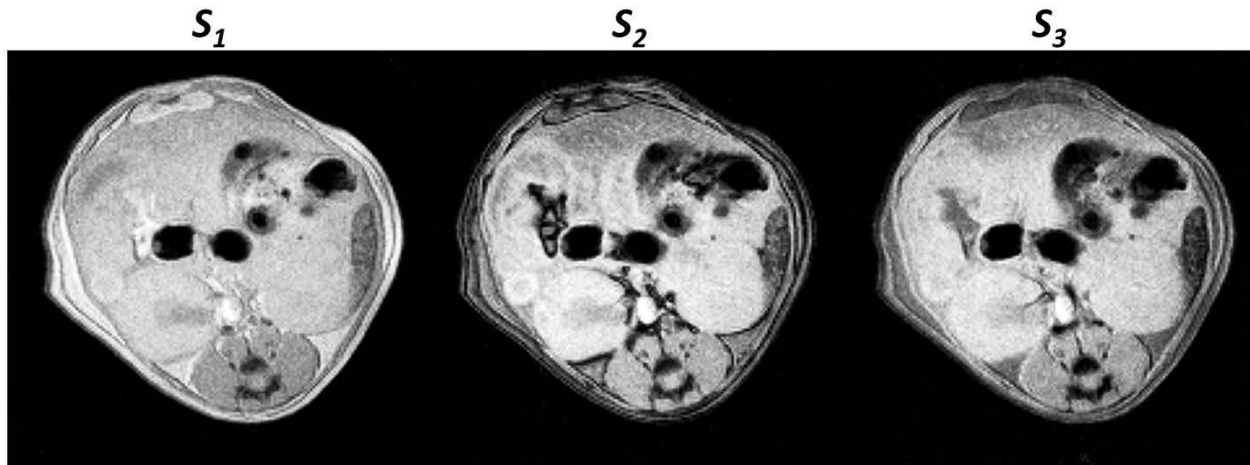


**Figure 4.16:** Images at first time echo for the three multi-gradient-echo sequences. These images were compared for studying the presence of misregistration artifacts

In the images in **Figure 4.17**, the edges of the external and internal structures are visible: in these zones, the differences are higher than in the other areas. At first glance no artifacts are visible on these images. The plots below the images represent the profile of the values on the yellow lines. The profiles show mean values equal to 0. For confirming the results, the same process was applied between the first and second echo images of the first sequence. The results for the last process are shown in **Figure 4.18**. The external and internal structures of the mouse are visible as previously observed in **Figure 4.17**. The profile of the values on the yellow line yields values around 0. No artifacts are visible in the current image. Since the same results are found for both the images of the effective sequence and the first sequence, the technique of putting together the three sequences seems valid for these mice. Moreover, on the IDEAL results, the structures like the spinal cord are noticeable and no visible artifacts are present.

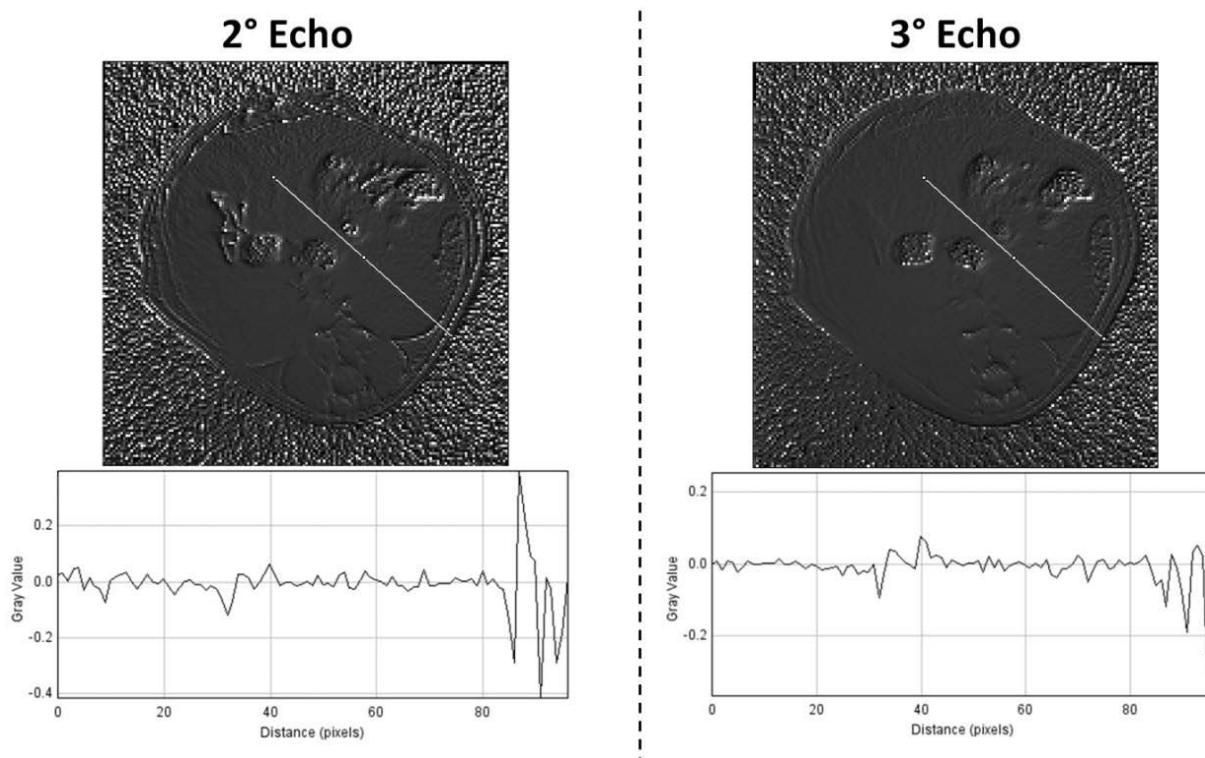


**Figure 4.17:** Results for the study on the misregistration. The images (relative to the effective sequence) of the second and third echo are compared with the image acquired at first echo with the StackReg plugin. Thus the images were subtracted to the not modified images of second and third echoes, respectively. At last they were normalized respect to their not modified images. The values taken along the yellow profiles indicate the values on the current images.

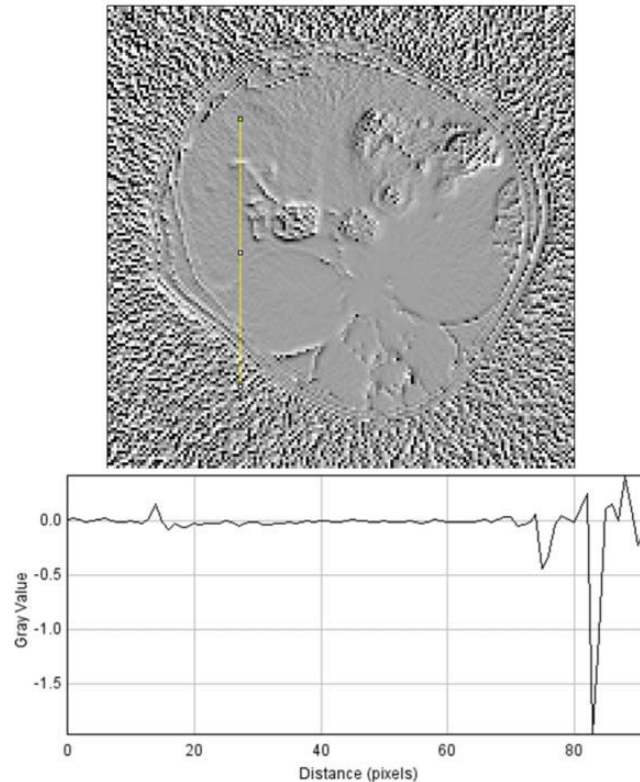


**Figure 4.18:** Results for the study on the misregistration. The image (relative to the first sequence) at second echo time is compared with the image acquired at first echo with the StackReg plugin. Thus the images were subtracted to the not modified images of first and second echoes, respectively. At last they were normalized respect to their not modified images. The values taken along the yellow profile indicates the values on the current image.

## 4.7 Problems with the brunch cut algorithm

Each initial field map, used as input for IDEAL algorithm, was calculated using the phases of two MR images, acquired at different echo times. Then, the branch cut algorithm was used on the phase map difference to, eventually, unwrap the phase. The image with no phase wrapping was used as input for IDEAL algorithm. However, the outcome of the branch cut algorithm can differ from the real one. In fact, the evolution of the phase and the choice of the initial pixel can play a role in the final result. In the current paragraph, some scenarios where the branch cut algorithm bring to the miscalculation of the fat fraction map calculated by IDEAL algorithm, are shown.

### 4.7.1 Choice of the MR images to use

In **Figure 4.19**, the phase maps of the same slice from first to third echo are displayed. Two different initial field maps were calculated and used as input for IDEAL algorithm.



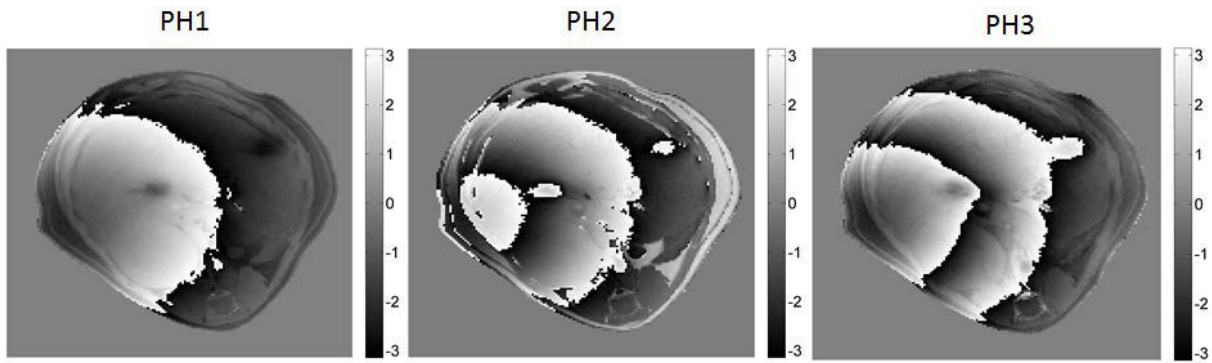


**Figure 4.19:** Phase maps relative to the MR image acquired at first (left) second (center) and third echo time (right).

Calling  $PH1$ ,  $PH2$  and  $PH3$  the phases relative to the MR images at first, second and third echo time, respectively, the two initial field maps were calculated, using the differences  $PH2-PH1$  and  $PH3-PH1$ . The branch cut algorithm was applied to these differences and opportunely transformed in field maps. The unwrapped field maps and the respective fat fraction calculated by IDEAL algorithm are illustrated in **Figure 4.20**.

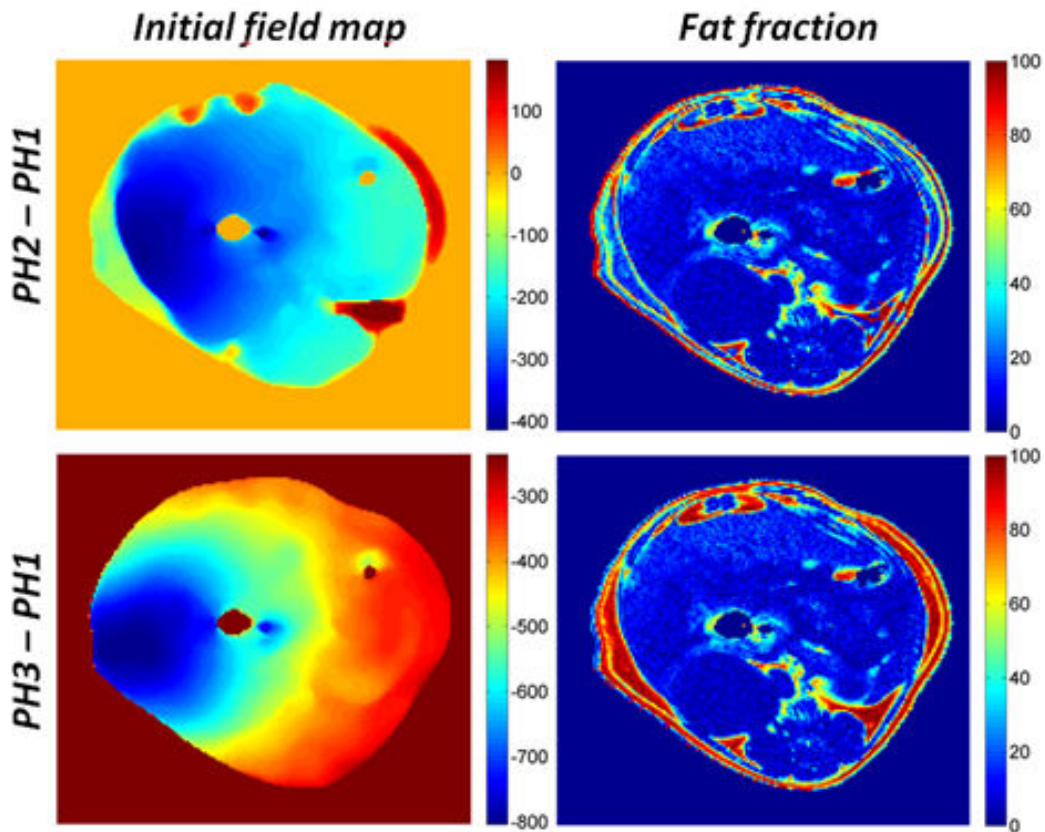


**Figure 4.20:** Initial field map created using different phase maps combinations. The associated fat fraction map calculated by IDEAL could be different. In this figure, the subcutaneous fat is not calculated using the initial field map calculated by the combination of the first and second phase map

The initial field maps differ in both shape and values. The fat fraction maps are not reconstructed in the same way in subcutaneous fat. In other words, the fat fraction map, calculated using the field map relative to  $PH2 - PH1$ , is not determined in the appropriate way. The miscalculation concerns the calculus in subcutaneous fat, which is composed of almost 100% fat. Moreover, the field map on top is not smooth everywhere.

In conclusion, the choice of the phase images, to use for calculating the initial field map, is important for a correct fat fraction reconstruction.

#### 4.7.2 Choice of the pixel

The second scenario, where the fat fraction is miscalculated by IDEAL algorithm, concerns the choice of the initial pixel from where the branch cut algorithm begins to work. The difference  $PH3 - PH1$  and the choice of two different pixels for unwrapping the phase are operated. In **Figure 4.21** the unwrapped field maps (calculated starting from different pixels) and the respective fat fraction, calculated by IDEAL algorithm, are illustrated.

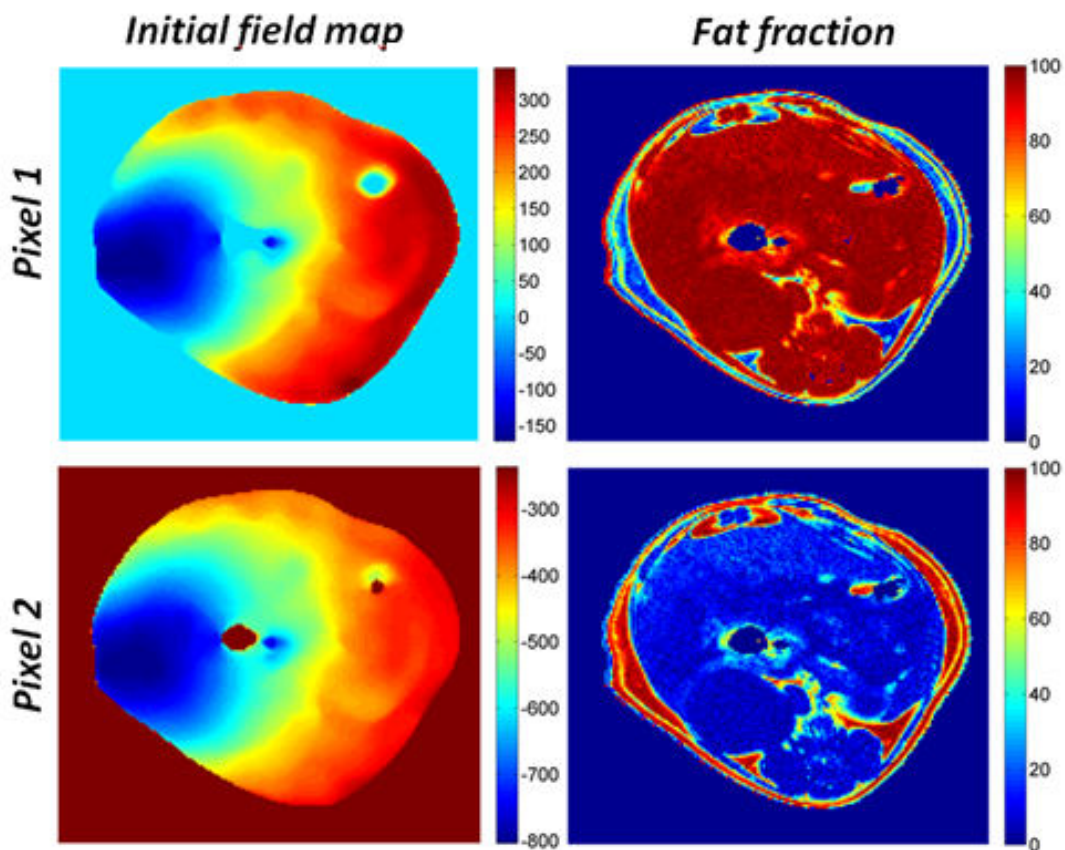


**Figure 4.21:** Initial field map created choosing different pixels. The associated fat fraction map calculated by IDEAL could be different. In this figure, the water and fat are swapped in the fat fraction map illustrated on top.

The calculated field map has the same shape but different values. The fat fraction maps obtained from these field maps are inverted. In other words, in the fat fraction map on top, the values in subcutaneous fat are very low, whereas in muscle and liver are very high: IDEAL algorithm swaps the fat with the water. No complications are found in the fat fraction map on bottom.

In conclusion, the application of the branch cut algorithm cannot be done automatically. Manual attempts are mandatory for obtaining successful fat fraction maps.

## 4.8 Discussion

In the current work, gradient-echo images of mice were acquired. The fat fraction and  $T_2^*$  maps were reconstructed with the IDEAL algorithm using one and three sequences. The fat fraction values, calculated with ROIs, were compared with the ones obtained using the 3-point Dixon's method. The mice used in the current work did not have fat fraction values too high in liver and muscle, and only in subcutaneous fat, the fat fraction exceeded the 20% in value. A linear regression (as the one present in the article of Hines et al. [65]) with the fat fraction values found in mice using 3, 6 and 15 echoes would have yielded weak results. Hence, this procedure represents a limitation of this work for proving the correlation between the values of fat fractions found using 3, 6 and 15 echoes in IDEAL algorithm. A comparison between the values of fat fractions in the three reconstructions and their eventual consistencies with the Student's t test could be only shown. No reference values from MRS or biopsy were obtained to validate the results on fat fraction achieved with the IDEAL algorithm and 3-point Dixon's method. Further analyses are necessary for validating our results.

The fat fraction overestimation in muscle in the 3-echo reconstruction is probably related to the  $T_2^*$ , slightly longer than in liver, and SNR. In simulations, the fat fraction bias in the 3-echo reconstruction was higher than in the 6-echo reconstruction when the SNR decreased.

Regarding the values of fat fraction calculated in mice muscle and liver, the use of the 3-point Dixon's method did not provide any advantages respect to the 2-point Dixon's method since no fat fraction higher than 50% were achieved. However, to avoid *a priori* the water-fat swapping the 3-point Dixon's method, is preferred to be used. Moreover, it can reconstruct the subcutaneous fat areas as well.

The results, obtained with the 3-point Dixon's method and IDEAL algorithm, depend on the initial field map. Each field map was calculated with the use of two phase maps acquired at different echo times. To better follow the evolution over time of the phase maps, it is straightforward to use sequences with short echo spacing. Since the magnetic field inhomogeneity increases getting closer to lungs it could be hard to well-calculate the initial field map when large echo spacing are used.



The use of the three sequences for generating the effective sequences allows to well follow the phase evolution. Moreover the user benefits of images with short echo spacing without decreasing the spatial resolution at the price of the total acquisition time which increases.





## Chapter V

# Fat Virtual Phantoms (Fat ViP) for Magnetic Resonance Imaging

### 5.1 Introduction

In Chapter III, IDEAL reconstructions and Dixon's methods were performed on physical phantoms. These phantoms, made by homemade emulsions and dairy creams, were employed for simulating fat-water systems. However, the physical phantoms provide semi-unknown MR properties and no ground truth exists. This is a contradiction, since phantoms are commonly used in clinical scenario as a reference.

In 1997, a method called ERETIC [87] was introduced for generating reference signals. The ERETIC signal has all the MR properties chosen by the user. Moreover, the ERETIC method uses an electronically synthesized signal as a reference, hence, no physical phantoms are necessary when this method is performed. In the current chapter, an introduction on the ERETIC method, and its evolution, the ViP MRI method, is discussed.

### 5.2 ERETIC method

In 1997, Barantin et al. [87] proposed to use an electronically synthesized signal as a reference. The ERETIC method (*Electronic Reference To access In vivo Concentration*), principally used in MRS, works with the use of an external apparatus. This apparatus is connected to the second RF channel of the spectrometer, not tuned at the Larmor frequency. All parameters regarding the signal are completely controlled from the spectrometer console. The ERETIC FID is transmitted inside the scanner bore with the use of an antenna. The scanner records the signal coming from ERETIC and from the object of interest in the scanner bore. In output, a spectrum with the ERETIC reference peak is generated. The ERETIC method yields a stable signal of any frequency and shape without using a physical reference.

ERETIC method was performed in several works regarding *in vitro* [84]–[87] and *in vivo* [[83], [88][89]] MRS studies, however, ERETIC has found some application in MRI as well [90], [91]. In the work of Franconi et al. [90] the ERETIC signal was generated by the second transmitter of the MRI scanner. It acquires the ERETIC signal simultaneously with the signal from the object of

interest. At last an image was creating with both ERETIC signal and the signal coming from the real object. For creating the ERETIC signal, sinc pulses were used as k-space lines. The operator could determine the broadening of the sinc pulses changing the ERETIC pulse duration. If the ERETIC pulse is sent at Larmor frequency and if the phase is equal for each k-space line, the ERETIC signal is generated at the center of the image. For changing the position of the ERETIC signal along the frequency encoding direction, the frequency (respect to the Larmor frequency) was changed. For changing the position along the phase encoding, a phase increment was applied for each lines.

The ERETIC method can be applied to whatever MR scanner that has a second RF channel for simultaneous measurements. Otherwise, for non-simultaneous measurements, the single RF channel could be used.

### **5.3 ViP (Virtual Phantoms)**

Virtual Phantom Magnetic Resonance Imaging (ViP MRI) is a method to generate reference signals on MR images, without using physical objects [92]. This method represents the extension of the ERETIC method, largely used in spectroscopy [84]–[88], to MRI.

#### **5.3.2 Introduction to ViP**

ViP MRI works as follows: first, a numerical MRI phantom is designed and its k-space representation is calculated; then, the k-space lines are entered into a waveform generator that converts the k-space lines into radiofrequency (RF) signals (the ViP signal); lastly, the ViP signal is transmitted to the MRI scanner by an RF coil (the ViP coil). The MRI scanner acquires the ViP signal simultaneously with the signal from the object of interest and, as a result, an MR image of the object of interest and the virtual phantom is obtained.

As a first validation of the ViP MRI method, an analysis of the MR magnitude images of virtual phantoms was performed, in order to test ViP signal reliability and stability [92]. On the other hand, MR images are intrinsically complex data with a real and imaginary part or, equivalently, with a magnitude and phase. In the study that introduced the ViP MRI method, no investigation concerning the MR phase images originating from the virtual phantom was conducted. As the phase information is often exploited in many MR methods, the question then arises: is it possible with the ViP MRI method to generate an MR image with a given magnitude as well as with a given phase? In other words, can the ViP MRI method be used to generate reference signals with both a known magnitude and phase?

One of the most commonly used MRI methods that exploit both the magnitude and phase information of the MR images is the IDEAL (Iterative Decomposition with Echo Asymmetry and Least squares estimation) method [17]. Specifically, IDEAL decomposes the water and fat signals in order to quantify the fat fraction. To apply the ViP MRI method to fat quantification (Fat ViP MRI), it is necessary to generate a ViP signal that represents multiple chemical species, with each species being characterized by an amplitude, a chemical shift and a  $T_2^*$  relaxation time. In the previous work on the ViP MRI method, only signals of one chemical species (water) were tested, in order to generate reference signals mimicking agar gel signals. In the current work, we sought to employ the ViP MRI method to generate reference signals similar to those of physical phantoms, such as fat emulsions, that contain two chemical species (water and fat).

Thus, the overall aim of the current study was to apply the ViP MRI method to water-fat decomposition algorithms that are based on complex-data image analysis. To this aim, it was necessary to assess the feasibility of generating: i) reference signals with both a known magnitude and phase and ii) reference signals from two chemical species, each with a given chemical shift, amplitude and  $T_2^*$  relaxation time, so to mimic a water-fat system.

MRI experiments were performed using a multi-gradient-echo sequence on virtual and physical phantoms. Decomposition of the water and fat signals was conducted using the magnitude and phase images in combination with the IDEAL algorithm.

### **5.3.3 ViP MRI method**

The scheme of the Fat ViP MRI method is illustrated in **Figure 5.1**. The script in Matlab for generating numerical phantom was employed. As indicated in the scheme of **Figure 5.1**, the numerical phantom is then converted to its k-space representation, with the k-space center normalized to the value of 1. The k-space representation (amplitude and phase) is used as input to the waveform generator (Redstone, Tecmag Inc., Houston TX, USA).

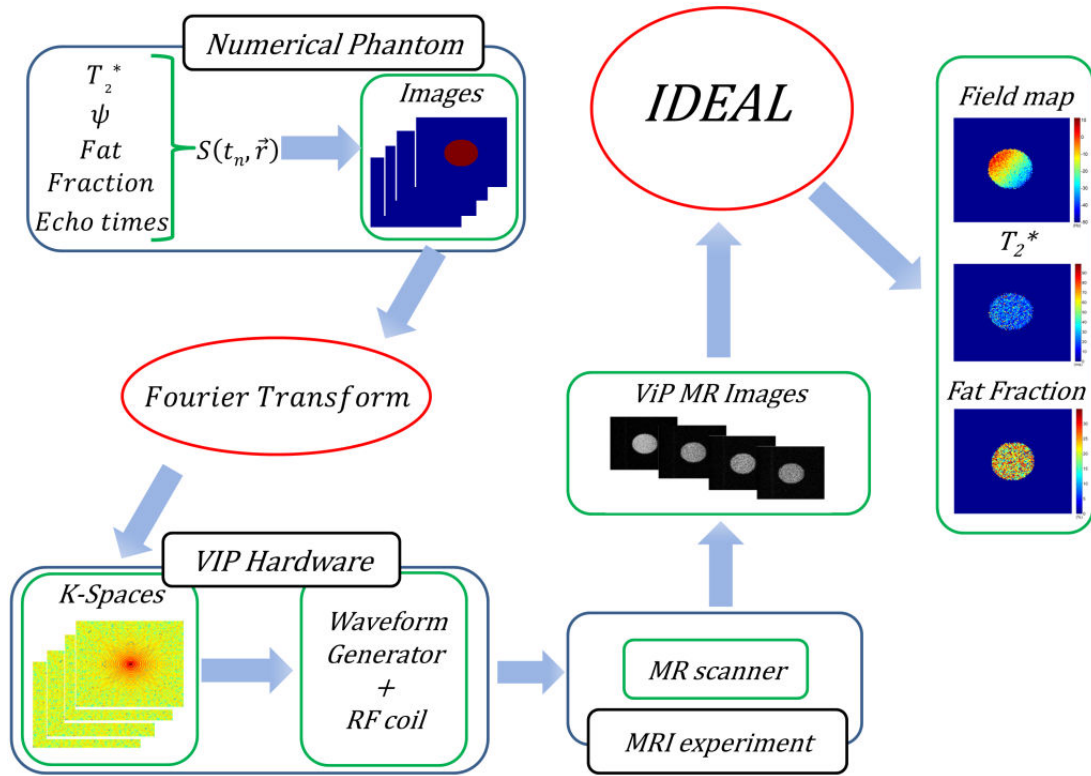


**Figure 5.1:** Scheme of the Virtual Phantom (ViP) MRI method applied to the IDEAL (Iterative Decomposition with Echo Asymmetry and Least squares estimation) water-fat decomposition algorithm.

A home-made 15mm diameter RF coil (the ViP coil) was connected to the waveform generator and positioned inside the scanner bore. The waveform generator and the ViP RF coil constituted the ViP hardware (**Figure 5.1**).

The k-space lines, in form of a radiofrequency signal (ViP signal), were transmitted to the MR scanner by the ViP coil to generate MR images of the virtual phantom. The RF unblanking signal from the MR scanner was used to synchronize the waveform generator with the analog-to-digital converter of the MR scanner. In each experiment, the waveform transmitter gain was adjusted to obtain a range of values of the ViP signal intensity similar to that obtained from physical phantoms. The MR scanner receiver coil recorded the ViP k-space signal, played line-by-line, simultaneously with the signal from the physical phantom. The ViP signal was sent to the scanner bore with the same carrier frequency of the MR scanner (200MHz).

## 5.4 Materials and methods

### 5.4.1 Numerical phantoms

Four different scenarios were investigated. In all cases, four multi-echo images ( $t_n = 1.5, 4, 6.5$  and  $9\text{ms}$ ) of matrix size equal to  $128 \times 128$  were generated, with a  $T_2^*$  relaxation time of water and fat equal to  $20\text{ms}$ . For each scenario, specific numerical phantoms were created and served as an input to the ViP hardware.

In the first study, a disk-shaped numerical phantom of 24-pixel radius, with a fat fraction equal to 20% was generated. In the signal equation of this numerical phantom, a field map in the form of a plane with slope of  $45^\circ$  was considered. This numerical phantom was used to investigate the overall aim of the current work, that is, to test the feasibility of the ViP MRI method to generate complex-data images of phantoms mimicking water-fat systems.

In the second study, a phantom with a radius (48-pixels) larger than the first phantom was generated in order to achieve a better visualization of the field map. The 48-pixel radius phantom covered most of the field of view (FOV) of the  $128 \times 128$  image. This phantom was used to test the feasibility of reproducing field maps of different shapes. In particular, two field maps were simulated: a field map in the form of a plane (slope equal to  $45^\circ$ ) and a field map in the form of a 2D parabola with vertex in the center of the matrix.

In the third study, the numerical phantom consisted of three small disk-shaped phantoms. These three phantoms were located at the borders of the FOV so that they could be used in a real case scenario, where the object of interest is typically located in the center of the image and the reference phantom at the borders of the FOV. These three phantoms were generated with different fat fractions (10%, 20% and 30%). In this third experiment, a physical phantom (dairy cream) was also positioned in the scanner bore and MR images of the virtual and physical phantom were simultaneously acquired.

In the fourth study, two disk-shaped phantoms of different size (60 and 24-pixel radius) were simulated with all other parameters being identical. Following the k-space theory, the integral of the signal in the image domain is directly proportional to the value of the signal at the k-space center (in the k-space domain), regardless of the shape or dimension of the phantom. This fourth scenario was investigated to test the consistency of the ViP MRI method, using the aforementioned well-known property of the k-space.

### 5.4.2 MRI experiments

MRI experiments were performed on a 4.7T MR scanner (47/40 Biospec, Bruker, Wissembourg, France) using an RF volume coil (72mm inner-diameter) as a transmitter/receiver. In all



measurements, a multi-gradient-echo sequence was used with dwell time =  $6.6\mu\text{s}$ , matrix size =  $128 \times 128$ , repetition time (TR) = 100ms and the same echo times used for generating the numerical phantoms (TE = 1.5, 4, 6.5 and 9ms). In one experiment (the third scenario) a physical phantom was positioned in the MRI scanner bore and the following pulse-sequence parameters were modified: TR = 500ms, FOV = 4cm, slice thickness = 4mm and flip angle =  $40^\circ$ . The physical phantom was a 15-ml cylindrical tube filled with dairy cream, a readily accessible substance that was used here as reference of a water/fat system.

Data analysis was performed with a homemade script in Matlab, which implements the IDEAL algorithm for decomposition of the water and fat signals using complex images. The images of the numerical phantom (that is, the images generated by the program in Matlab that allows for simulating MR signals) and the images the virtual and physical phantoms (that is, the MR images acquired with the MRI scanner) were processed with IDEAL to obtain pixel-by-pixel maps of fat fraction,  $T_2^*$  and field map.

## 5.5 Results

Multi-gradient-echo magnitude images of a virtual phantom (24-pixel radius) acquired at four echo times are shown in **Figure 5.2**.

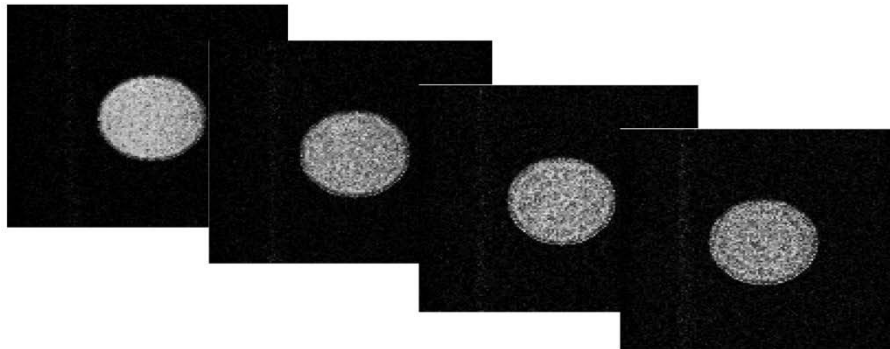


**Figure 5.2:** Multi-gradient-echo images of a disk-shaped virtual phantom acquired at 4 echo times (1.5, 4, 6.5 and 9ms). This virtual phantom was designed to mimic a water-fat system, with a fat fraction equal to 20% and a  $T_2^* = 20\text{ms}$ .

This virtual phantom was designed to mimic two chemical species (water and 20% fat), with a value of  $T_2^* = 20\text{ms}$  and a planar field map. Complex images were analyzed with the IDEAL algorithm. In **Figure 5.3**, the output of the IDEAL reconstruction of the numerical and virtual phantom is shown.

The IDEAL data processing of the numerical phantom (top row) yielded a value of  $T_2^*$  and fat fraction equal to 20ms and 20%, respectively, and a planar field map. Data processing of the MR images of the virtual phantom (bottom row) yielded a value of  $T_2^*$  and fat fraction equal to  $23.7 \pm 0.5$ ms and  $21.9 \pm 0.2\%$ , respectively. The IDEAL reconstruction of the virtual phantom well reproduced the plane-like shape of the numerical field map.

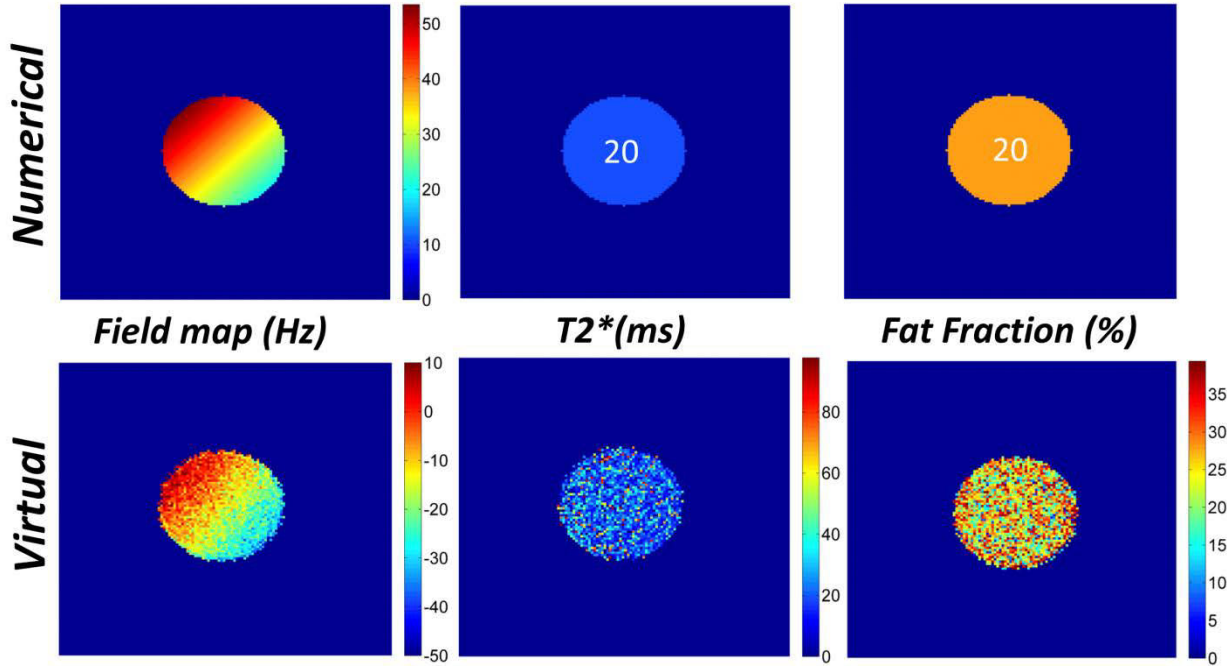


**Figure 5.3:** The IDEAL reconstruction output of a numerical (top row) and virtual (bottom row) phantom. The virtual phantom shown here is the same as the one of Figure 2. The IDEAL reconstruction of its corresponding numerical phantom is illustrated here as a reference. The planar field map (first column) of the numerical phantom is well reproduced by the virtual phantom. A good agreement between the  $T_2^*$  (second column) and fat fraction (third column) maps of the numerical and virtual phantom is also noticeable.

In order to achieve a better visualization of the field maps, a large disk-shaped phantom (48-pixel radius) was generated and two experiments were performed, with field maps of two different shapes (planar and parabolic). The planar field map of the virtual phantom (**Figure 5.4**, bottom row, left) was similar to that of the numerical phantom (**Figure 5.4**, top row, left).

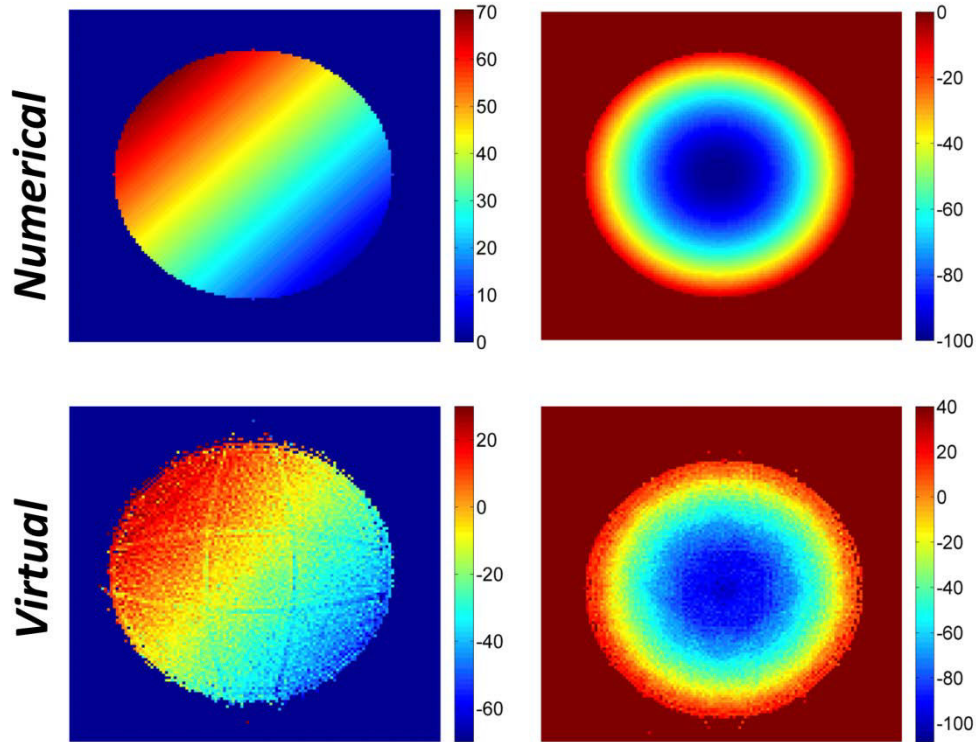


**Figure 5.4:** Example of two field maps (planar, left column; parabolic, right column) obtained with the ViP MRI method. As a reference, the field maps of the numerical phantom are also illustrated (top row). The field maps calculated from the MR images of the virtual phantom (bottom row) are in good agreement with those of the corresponding numerical phantom (top row).

The values of the virtual phantom field map, evaluated along the direction of the steepest descent of the plane, displayed an excellent linearity (coefficient of determination  $r^2 = 0.990$ ). The slope coefficient was  $1.096 \pm 0.014\text{Hz/pixel}$  vs  $1\text{Hz/pixel}$  for the numerical phantom. The range of field values was  $\sim 70\text{Hz}$  vs  $67\text{Hz}$  for the numerical phantom. A good agreement was also observed between the parabolic field map of the virtual phantom (**Figure 5.4**, bottom row, right) and that of the numerical phantom (**Figure 5.4**, top row, right). The field map values were evaluated along an image profile corresponding to the intersection with a plane that contains the axis of symmetry of the parabola. The quadratic fit applied to the virtual phantom data yielded the quadratic coefficient value of  $0.049 \pm 0.001\text{ Hz/pixel}$  vs  $0.05\text{Hz/pixel}$  in the numerical phantom, with coefficient of determination  $r^2 = 0.986$ . The range of field map values in the virtual phantom was  $\sim 120\text{Hz}$  vs  $115\text{Hz}$  in the numerical phantom.

**Figure 5.5** shows the results of the experiment performed on a physical phantom containing dairy cream and three virtual phantoms.

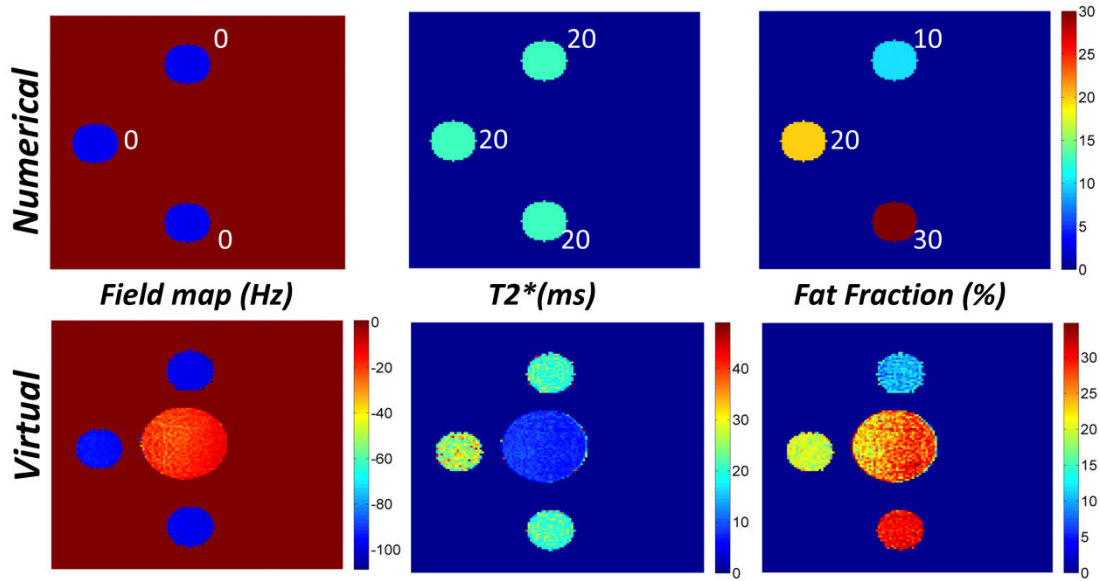


**Figure 5.5:** The output of the IDEAL reconstruction of the numerical (top row) and virtual + physical phantoms (bottom row). The physical phantom is a 15-ml cylindrical tube filled with dairy cream, positioned in the center of the field of view. The three virtual phantoms, located around the physical phantom, are designed with a  $T_2^* = 20\text{ms}$  and different fat fractions (10%, 20% and 30%). A good agreement between the numerical and virtual phantom is observable.

Similarly to the previous experiments, the IDEAL reconstruction algorithm was applied to multi-gradient-echo images acquired at four TEs. In the numerical phantom, the IDEAL reconstruction yielded a value of  $T_2^* = 20\text{ms}$ , fat fraction equal to 10, 20 and 30% and a constant-value field map (**Figure 5.5**, top row). Similar values were obtained for the  $T_2^*$ , fat fraction and field maps of the virtual phantoms (**Figure 5.5**, bottom row). In Table 1, the values of  $T_2^*$  and fat fraction relative to the physical and virtual phantoms are shown. Overall, an excellent agreement between the fat fraction values of the virtual and numerical phantoms was observed. The  $T_2^*$  values of the virtual phantoms were similar to that of the numerical phantom ( $T_2^* = 20\text{ms}$ ), with the exception of the 20% fat-fraction virtual phantom.

In **Figure 5.6**, the MR magnitude images of two virtual phantoms of different size (24-pixel and 60-pixel radius) are shown.

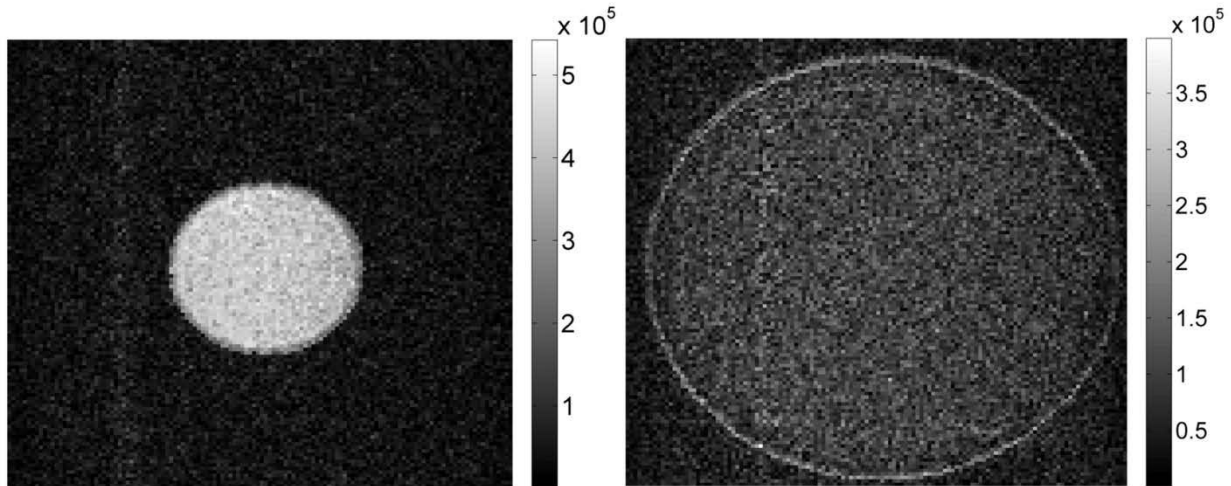


**Figure 5.6:** MR magnitude images of two virtual phantoms of different size. MR images are acquired with the same sequence and sequence parameters. The signal intensity of the smaller phantom is higher than that of the larger phantom. On the other hand, the total signal intensity (that is, the sum of the signal for all pixels in the image) is the same in both phantoms (see Results).

Images were acquired using the same multi-gradient-echo sequence, with identical sequence parameters. The total signal (defined as the sum of the signal for all pixels in the image) was calculated for both virtual phantoms. The ratio between the total signal of the 24-pixel radius phantom and the 60-pixel radius phantom was 1.04 vs the expected theoretical value of 1. The same ratio value was observed in all four echoes.

To determine the origin of the artifacts observed in **Figure 5.4**, where four lines crossing the field maps were noticeable, an additional investigation was performed. The results of the MR experiments and simulations are illustrated with magnitude images in **Figure 5.7**. A large disk-shaped phantom was designed. As in all previous experiments, the numerical phantom was generated in 32 bits (**Figure 5.7**, left). A ViP MRI experiment was performed using this numerical phantom and artifacts similar to those of the field maps of **Figure 5.4** were observed (**Figure 5.7**, center). The k-space of the numerical phantom was then discretized to different bit values and, for each discretization value, a simulated image was generated by Fourier transform of this k-space. When the k-space of the numerical phantom was discretized to 7 bits, the corresponding image (**Figure 5.7**, right) displayed artifacts similar to those of the ViP MR image acquired on the scanner (**Figure 5.7**, center).

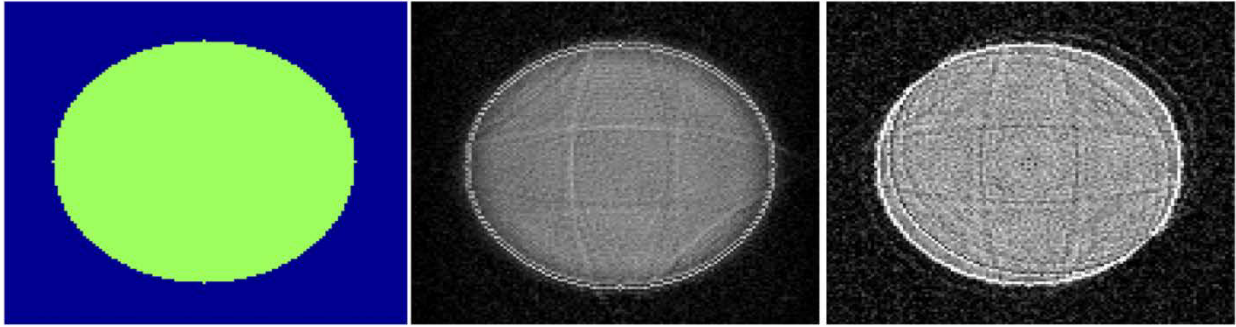


**Figure 5.7:** The effect of the  $k$ -space discretization on magnitude images in a large disk-shaped phantom. The 32-bit numerical phantom (left), the ViP MR image of the numerical phantom (center) and the simulated image generated by a 7-bit discretization of the  $k$ -space (right) are shown. The discretization of the  $k$ -space yields the same artifacts as those observed in the ViP MR image.

It should be noted that this artifact was not observed in the phantom shown in **Figure 5.6** (right) due to the low signal intensity of the phantom, which mitigated the  $k$ -space discretization.

## 5.6 Discussion

The application of the ViP MRI method to water-fat signal decomposition using complex images was here investigated. First, the results of the current study indicate that ViP MRI allows for generating reference signals (i.e., imaging phantoms) with a well-defined magnitude and phase. It should be noted that in the previous validation study of the ViP MRI method only the magnitude of the signal was investigated [34]. In the current study, different phase-map patterns were tested and an excellent agreement between the simulated and experimental phase maps was observed.

Secondly, it was shown here the ViP MRI method is not restricted to mimicking a single chemical species: various virtual phantoms were designed to mimic phantoms such as fat emulsions, which contain two chemical species (water and fat). MR images of virtual phantoms with different fat percentages were acquired. A good agreement was observed between the simulated and experimental fat fraction values, that is, between the fat fraction values of the numerical and virtual phantoms. In a previous study, the ViP MRI method was employed to mimic agar gel signals. Since the beginning of MRI, agar gels have been extensively investigated (and then used over the years) to provide reference signals in MR experiments [34], [35]. On the other hand, agar gels cannot reproduce signals originating from tissues containing both water and fat components, so other phantoms are employed for mimicking this scenario. Emulsions composed of oil and water [93], [94] and dairy creams [38], [39], [95] are among the most commonly-employed reference phantoms

for mimicking water/fat systems or, in general, two-compartment models. The Fat ViP MRI method could be of interest for replacing these physical phantoms when performing an MR experiment.

Given the growing interest in the simultaneous measurement of fat content and  $T_2^*$  relaxation time, the transverse relaxation decay was also included into the signal model [96]. As matter of fact, both fat content and  $T_2^*$  are useful biomarkers, in particular with respect to liver pathologies: a fat content greater than 5% is indicative of liver steatosis [97] and  $T_2^*$  values can be used to determine liver iron overload [45]. As a result, in the last decade there has been a substantial development of MR quantitative approaches for simultaneous fat and  $T_2^*$  quantification. In this context, reference phantoms that simulate water-fat systems, including  $T_2^*$  relaxation effects, could be useful for development, testing and improvement of novel signal decomposition algorithms [44], [46], [49].

All MRI experiments were performed using a multi-gradient-echo sequence and data analysis was conducted with the IDEAL algorithm. In particular, numerical phantoms were generated at four echo-time values, four multi-gradient-echo images were acquired on the MR scanner and the 4-point IDEAL method was applied to the ViP MR images. However it should be noted that the Fat ViP MRI method as proposed here has no limitation with respect to the number of echoes, that is, it can be directly extended to include a higher number of echoes. With an increased number of echoes, for instance, the estimation of  $T_2^*$  can be also improved [96].

Virtual phantoms that covered a large part of the FOV were generated to aid in the visualization and quantification of the phase maps. These ViP MR images displayed an unusual and unexpected artifact. Different hypotheses were considered. The most appropriate one was that the origin of this artifact was related to the discretization of the k-space signal, occurring in the waveform generator. To test the validity of this hypothesis, a numerical phantom was generated in 32 bits and its k-space was converted to lower number-of-bit representations. The image obtained by the Fourier transform of the 7-bit k-space displayed the same artifact as the image of the virtual phantom acquired by the MR scanner. In phantom of smaller size (such as the single disk-shaped phantom show in **Figure 5.3**), this artifact was not present, as the total signal did not reach the levels that would result in this k-space discretization problem. Thus, this type of artifact would not occur in a typical application of the ViP MRI method, since usually the dimensions of the reference phantoms are much smaller than the FOV of the image.

One of the main results of the current study is the excellent agreement between the simulated and experimental phase maps (**Figure 5.4**). The ability to generate virtual phantoms with a given phase, so to provide a phase reference value on an MR image, might be of interest not only to the water-fat

decomposition techniques, but also to other techniques that exploit the phase information of the MR images [12], [98]–[100].

To date, only a handful of studies have been focused on the development of reference signals in imaging [90]–[92]. The main difference between ViP MRI [92] and previously proposed approaches [90], [91] is that in ViP MRI no hardware or software components of the MR scanner (with the exception of a trigger signal) are used for generating the signal of the virtual phantom. Thus ViP MRI can be performed on MRI scanners of different types and vendors, since the ViP hardware/software is a self-contained unit, independent of the MRI scanner hardware/software.





# Conclusions

In this thesis, the problems, related to the fat fraction quantification and the optimization of *in vivo* measurements, have been discussed. The Dixon's methods and IDEAL algorithm were used for fat fraction and  $T_2^*$  measurements on MR phantoms and mice. The MR measurements were performed on a dedicated small-animal, horizontal-bore 4.7 MR scanner, located in the lab of the host institution.

However, further studies are necessary to investigate as well encountered issues or topics, not treated in the current thesis.

First of all, the images of MR phantoms and mice were acquired in 2D. The idea is to acquire 3D whole body images for calculating the fat fraction and  $T_2^*$  with the IDEAL algorithm and Dixon's method. This implies the development and optimization of specific sequences at 4.7T MRI scanner.

Second, it was assumed that the signal generated from water-fat systems had an exponential decay. This type of decay comes out from the Fourier transform of a Lorentzian lineshape in the frequency domain. This assumption could be wrong in the moment in which large magnetic field inhomogeneities occur. In this case, the Lorentzian lineshape turns into a Gaussian lineshape and, in the time domain, the exponential decay turns into a Gaussian decay. The methods which use the exponential model like IDEAL need of corrections. In literature the signal model used in this last case is

$$s(t_n) = \left( W e^{-t_n/T_{2,W}^*} + F e^{-t_n/T_{2,F}^*} \sum_{i=1}^7 \alpha_i e^{i2\pi\Delta f_i t_n} \right) e^{i2\pi\psi t_n \Delta z} \text{sinc} \left( \frac{\gamma G \Delta z t_n}{2\pi} \right)$$

Hence, the "classical" signal model is multiplied for the factor  $\Delta z \text{sinc} \left( \frac{\gamma G \Delta z t_n}{2\pi} \right)$ , where  $G$  is the field gradient and  $\Delta z$  the slice thickness. In the work of Mulkern et al. [101], the lorentzian and Gaussian distributions are considered for rewriting the signal in the time domain using the GESFIDE sequence [102]. The new forms of signals are calculated using the frequency distributions (lorentzian or Gaussian) in the Bloch equation. The signal models that they found are calculated considering only one chemical species. This aspect has not been addressed in the context of simultaneous measurements of fat and  $T_2^*$ .

Finally, reference values are needed to confirm the results of the fat fraction and  $T2^*$  obtained in mice. The biopsy will be a direct way to measure the fat fraction. Another way to perform this measurement may be to acquire the spectra with different echo time to make it independent of the relaxation time  $T2$ .





# Bibliography

- [1] World Health Organisation: Obesity and overweight. Fact sheet No. 311, Updated January 2015. <http://www.who.int/mediacentre/factsheets/fs311/en/> Accessed 03 Aug 2015
- [2] *Diabetes and Cardiovascular Disease: Integrating Science and Clinical Medicine*. Lippincott Williams & Wilkins, 2004.
- [3] G. Gambarota, R. L. Janiczek, R. V. Mulkern, and R. D. Newbould, “An NMR Phantom Mimicking Intramyocellular (IMCL) and Extramyocellular Lipids (EMCL),” *Appl. Magn. Reson.*, vol. 43, no. 3, pp. 451–457, 2012.
- [4] C. Boesch, J. Slotboom, H. Hoppeler, and R. Kreis, “In vivo determination of intramyocellular lipids in human muscle by means of localized  $^1\text{H}$ -MR-spectroscopy.,” *Magn. Reson. Med.*, vol. 37, no. 4, pp. 484–93, Apr. 1997.
- [5] A. Karatopis, O. Benekos, E. Efstathopoulos, I. Kandarakis, and N. Kelekis, “ $^1\text{H}$  MRS and MRSI: analysis of acquisition parameters and improvement of various clinical applications,” in *2006 IEEE Nuclear Science Symposium Conference Record*, 2006, vol. 4, pp. 2025–2028.
- [6] A. Karatopis, O. Benekos, E. Efstathopoulos, I. Valaisb, I. Kandarakis, N. Kelekis, “Molecular imaging through  $^1\text{H}$  MRS and MRSI in everyday routine: improvements in various clinical applications and parameter optimization of spectroscopic imaging sequences,” *Nucl. Instrum. Meth. A*, vol. 571, no. 1–2, Feb. 2007, pp. 502–505.
- [7] A. Hakkarainen, J. Lundbom, E. K. Tuominen, M.-R. Taskinen, K. H. Pietiläinen, and N. Lundbom, “Measuring short-term liver metabolism non-invasively: postprandial and post-exercise  $^1\text{H}$  and  $^{31}\text{P}$  MR spectroscopy.,” *MAGMA*, vol. 28, no. 1, pp. 57–66, Feb. 2015.
- [8] C. P. Bernard, G. P. Liney, D. J. Manton, L. W. Turnbull, and C. M. Langton, “Comparison of fat quantification methods: a phantom study at 3.0T.,” *J. Magn. Reson. Imaging*, vol. 27, no. 1, pp. 192–7, Jan. 2008.
- [9] S. B. Reeder and C. B. Sirlin, “Quantification of Liver Fat with Magnetic Resonance Imaging,” *Magn. Reson. Imaging Clin. N. Am.*, vol. 18, no. 3, pp. 337–357, Aug. 2010.
- [10] M. Nouredin, J. Lam, M. R. Peterson, M. Middleton, G. Hamilton, T.-A. Le, R. Bettencourt, C. Changchien, D. A. Brenner, C. Sirlin, and R. Loomba, “Utility of magnetic resonance imaging versus histology for quantifying changes in liver fat in nonalcoholic fatty liver disease trials.,” *Hepatology*, vol. 58, no. 6, pp. 1930–40, Dec. 2013.
- [11] N. F. Schwenzer, F. Springer, C. Schraml, N. Stefan, J. Machann, and F. Schick, “Non-invasive assessment and quantification of liver steatosis by ultrasound, computed tomography and magnetic resonance.,” *J. Hepatol.*, vol. 51, no. 3, pp. 433–45, Sep. 2009.
- [12] M. A. Bernstein and Y. Ikezaki, “Comparison of phase-difference and complex-difference processing in phase-contrast MR angiography.,” *J. Magn. Reson. Imaging*, vol. 1, no. 2, pp. 725–729, 1991.

- [13] Y. H. Yoo, H.-S. Kim, Y. H. Lee, C.-S. Yoon, M. Y. Paek, H. Yoo, S. Kannengiesser, T.-S. Chung, H.-T. Song, J.-S. Suh, and S. Kim, “Comparison of Multi-Echo Dixon Methods with Volume Interpolated Breath-Hold Gradient Echo Magnetic Resonance Imaging in Fat-Signal Fraction Quantification of Paravertebral Muscle,” *Korean J. Radiol.*, vol. 16, no. 5, p. 1086, Jan. 2015.
- [14] B. Kastler and D. Vetter, “Comprendre l’IRM: Manuel d’auto-apprentissage.” Elsevier Masson, 2011.
- [15] Z.-P. Liang and P. C. Lauterbur, *Principles of Magnetic Resonance Imaging: A Signal Processing Perspective*, Wiley-IEEE Press, 1999.
- [16] W. T. Dixon, “Simple proton spectroscopic imaging.” *Radiology*, vol. 153, no. 1, pp. 189–94, Oct. 1984.
- [17] S. B. Reeder, Z. Wen, H. Yu, A. R. Pineda, G. E. Gold, M. Markl, and N. J. Pelc, “Multicoil Dixon chemical species separation with an iterative least-squares estimation method,” *Magn. Reson. Med.*, vol. 51, no. 1, pp. 35–45, 2004.
- [18] G. H. Glover and E. Schneider, “Three-point Dixon technique for true water/fat decomposition with B<sub>0</sub> inhomogeneity correction.” *Magn. Reson. Med.*, vol. 18, no. 2, pp. 371–383, 1991.
- [19] H. Eggers, B. Brendel, A. Duijndam, and G. Herigault, “Dual-echo Dixon imaging with flexible choice of echo times.” *Magn. Reson. Med.*, vol. 65, no. 1, pp. 96–107, Jan. 2011.
- [20] J. Berglund, H. Ahlström, L. Johansson, and J. Kullberg, “Two-point dixon method with flexible echo times,” *Magn. Reson. Med.*, vol. 65, no. 4, pp. 994–1004, Apr. 2011.
- [21] T. Perkins, “Preliminary Clinical Experience with a Multiecho 2-Point DIXON ( mDIXON ) Sequence at 3T as an Efficient Alternative for Both the SAR-intensive Acquired In- and Out-of-Phase Chemical Shift Imaging as well as for 3D Fat-suppressed T1-weighted Sequences use,” *Proc. Int. Soc. Mag. Res. Med.*, vol. 194, no. 1984, p. 2705, 2009.
- [22] Y. Wang, D. Li, E. M. Haacke, and J. J. Brown, “A three-point dixon method for water and fat separation using 2D and 3D gradient-echo techniques,” *J. Magn. Reson. Imaging*, vol. 8, no. 3, pp. 703–710, May 1998.
- [23] M. A. Bernstein, K. F. King, and X. J. Zhou, “Handbook of MRI Pulse Sequences”. Elsevier, 2004.
- [24] Q. Chen, E. Schneider, B. Aghazadeh, M. S. Weinhaus, J. Humm, and D. Ballon, “An automated iterative algorithm for water and fat decomposition in three-point Dixon magnetic resonance imaging,” *Med. Phys.*, vol. 26, no. 11, p. 2341, Nov. 1999.
- [25] S. B. Reeder, A. R. Pineda, Z. Wen, A. Shimakawa, H. Yu, J. H. Brittain, G. E. Gold, C. H. Beaulieu, and N. J. Pelc, “Iterative decomposition of water and fat with echo asymmetry and least-squares estimation (IDEAL): Application with fast spin-echo imaging,” *Magn. Reson. Med.*, vol. 54, no. 3, pp. 636–644, 2005.

- [26] H. Yu, C. a. McKenzie, A. Shimakawa, A. T. Vu, A. C. S. Brau, P. J. Beatty, A. R. Pineda, J. H. Brittain, and S. B. Reeder, "Multiecho reconstruction for simultaneous water-fat decomposition and T2\* estimation," *J. Magn. Reson. Imaging*, vol. 26, no. 4, pp. 1153–1161, 2007.
- [27] G. Hamilton, T. Yokoo, M. Bydder, I. Cruite, M. E. Schroeder, C. B. Sirlin, and M. S. Middleton, "In vivo characterization of the liver fat 1H MR spectrum," *NMR Biomed.*, vol. 24, no. 7, pp. 784–790, 2011.
- [28] H. Yu, A. Shimakawa, C. a. McKenzie, E. Brodsky, J. H. Brittain, and S. B. Reeder, "Multiecho water-fat separation and simultaneous R 2\* estimation with multifrequency fat spectrum modeling," *Magn. Reson. Med.*, vol. 60, no. 5, pp. 1122–1134, 2008.
- [29] H. Gudbjartsson and S. Patz, "The Rician distribution of noisy MRI data.," *Magn. Reson. Med.*, vol. 34, no. 6, pp. 910–4, Dec. 1995.
- [30] S. Aja-Fernandez, C. Alberola-Lopez, and C.-F. Westin, "Noise and signal estimation in magnitude MRI and Rician distributed images: a LMMSE approach.," *IEEE Trans. Image Process.*, vol. 17, no. 8, pp. 1383–98, Aug. 2008.
- [31] B. J. Soher, C. Wyatt, S. B. Reeder, and J. R. MacFall, "Noninvasive temperature mapping with MRI using chemical shift water-fat separation," *Magn. Reson. Med.*, vol. 63, no. 5, pp. 1238–1246, May 2010.
- [32] R. T. D. Peters, R. S. Hinks, and R. M. Henkelman, "Ex vivo tissue-type independence in proton-resonance frequency shift MR thermometry," *Magn. Reson. Med.*, vol. 40, no. 3, pp. 454–459, Sep. 1998.
- [33] D. Hernando, S. D. Sharma, H. Kramer, and S. B. Reeder, "On the confounding effect of temperature on chemical shift-encoded fat quantification," *Magn Reson Med*, vol. 72, no. 2, pp. 464–470, 2014.
- [34] R. Mathur-De Vre, R. Grimee, F. Parmentier, and J. Binet, "The use of agar gel as a basic reference material for calibrating relaxation times and imaging parameters.," *Magn. Reson. Med.*, vol. 2, no. 2, pp. 176–179, 1985.
- [35] P. Walker, R. A. Lerski, R. Mathur-De Vré, J. Binet, and F. Yane, "Preparation of agarose gels as reference substances for NMR relaxation time measurement. EEC Concerted Action Program.," *Magn. Reson. Imaging*, vol. 6, no. 2, pp. 215–22, Jan. .
- [36] D. Woessner and B. . Snowden, "Pulsed Nmr study of water in agar gels," *J. Colloid Interface Sci.*, vol. 34, no. 2, pp. 290–299, Oct. 1970.
- [37] G. M. Pilhofer, H.-C. Lee, M. J. McCarthy, P. S. Tong, and J. Bruce German, "Functionality of Milk Fat In Foam Formation and Stability," *J. Dairy Sci.*, vol. 77, no. 1, pp. 55–63, Jan. 1994.



- [38] Z. Ababneh, M. Haque, S. E. Maier, and R. V. Mulkern, "Dairy cream as a phantom material for biexponential diffusion decay," *Magn. Reson. Mater. Phys.*, vol. 17, no. 2, pp. 95–100, 2004.
- [39] C. Jones, A. MacKay, and B. Rutt, "Bi-exponential T2 decay in dairy cream phantoms.," *Magn. Reson. Imaging*, vol. 16, no. 1, pp. 83–5, Jan. 1998.
- [40] F. Mariette, "NMR Relaxation of Dairy Products," in *Modern Magnetic Resonance*, Netherlands, G. A. Webb, Springer, 2008, part III, pp. 1697–1701.
- [41] D. G. Mitchell, I. Kim, T. S. Chang, S. Vinitzki, P. M. Consigny, S. A. Saponaro, S. M. Ehrlich, M. D. Rifkin, and R. Rubin, "Fatty liver. Chemical shift phase-difference and suppression magnetic resonance imaging techniques in animals, phantoms, and humans.," *Invest. Radiol.*, vol. 26, no. 12, pp. 1041–52, Dec. 1991.
- [42] J. S. Chang, B. Taouli, N. Salibi, E. M. Hecht, D. G. Chin, and V. S. Lee, "Opposed-Phase MRI for Fat Quantification in Fat-Water Phantoms with 1 H MR Spectroscopy to Resolve Ambiguity of Fat or Water Dominance," *Am. J. Roentgenol.*, vol. 187, no. 1, pp. W103–W106, Jul. 2006.
- [43] M. Monziols, G. Collewet, F. Mariette, M. Kouba, and A. Davenel, "Muscle and fat quantification in MRI gradient echo images using a partial volume detection method. Application to the characterization of pig belly tissue.," *Magn. Reson. Imaging*, vol. 23, no. 6, pp. 745–55, Jul. 2005.
- [44] M. Bydder, T. Yokoo, G. Hamilton, M. S. Middleton, A. D. Chavez, J. B. Schwimmer, J. E. Lavine, and C. B. Sirlin, "Relaxation effects in the quantification of fat using gradient echo imaging," *Magn. Reson. Imaging*, vol. 26, no. 3, pp. 347–359, 2008.
- [45] Y. Gandon, D. Olivie, D. Guyader, C. Aube, F. Oberti, V. Sebillle, and Y. Deugnier, "Non-invasive assessment of hepatic iron stores by MRI," *Lancet*, vol. 363, pp. 357–362, 2004.
- [46] V. V. Chebrolu, C. D. G. Hines, H. Yu, A. R. Pineda, A. Shimakawa, C. a. McKenzie, A. Samsonov, J. H. Brittain, and S. B. Reeder, "Independent estimation of  $T_2^*$  for water and fat for improved accuracy of fat quantification," *Magn. Reson. Med.*, vol. 63, no. 4, pp. 849–857, 2010.
- [47] D. E. Horng, D. Hernando, C. D. G. Hines, and S. B. Reeder, "Comparison of  $R_2^*$  correction methods for accurate fat quantification in fatty liver," *J. Magn. Reson. Imaging*, vol. 37, no. 2, pp. 414–422, 2013.
- [48] M. R. Bashir, X. Zhong, M. D. Nickel, G. Fananapazir, S. a. R. Kannengiesser, B. Kiefer, and B. M. Dale, "Quantification of Hepatic Steatosis With a Multistep Adaptive Fitting MRI Approach: Prospective Validation Against MR Spectroscopy," *Am. J. Roentgenol.*, vol. 204, no. 2, pp. 297–306, 2015.
- [49] X. Zhong, M. D. Nickel, S. a. R. Kannengiesser, B. M. Dale, B. Kiefer, and M. R. Bashir, "Liver fat quantification using a multi-step adaptive fitting approach with multi-echo GRE imaging," *Magn. Reson. Med.*, vol. 72, no. 5, pp. 1353–1365, 2014.

- [50] R. V. Mulkern, Y. P. Hung, Z. Ababneh, S. E. Maier, A. B. Packard, M. C. Uluer, D. F. Kacher, G. Gambarota, and S. Voss, "On the strong field dependence and nonlinear response to gadolinium contrast agent of proton transverse relaxation rates in dairy cream," *Magn. Reson. Imaging*, vol. 23, no. 6, pp. 757–764, 2005.
- [51] M. L. Johns, "NMR studies of emulsions," *Curr. Opin. Colloid Interface Sci.*, vol. 14, no. 3, pp. 178–183, 2009.
- [52] M. A. Voda and J. van Duynhoven, "Characterization of food emulsions by PFG NMR," *Trends Food Sci. Technol.*, vol. 20, no. 11–12, pp. 533–543, 2009.
- [53] M. Johns and K. Hollingsworth, "Characterisation of emulsion systems using NMR and MRI," *Prog. Nucl. Magn. Reson. Spectrosc.*, vol. 50, pp. 51–70, 2007.
- [54] M. O. Hussein, C. L. Hoad, J. Wright, G. Singh, M. C. Stephenson, E. F. Cox, E. Placidi, S. E. Pritchard, C. Costigan, H. Ribeiro, E. Ciampi, A. Nandi, N. Hedges, P. Sanderson, H. P. Peters, P. Rayment, R. C. Spiller, P. a Gowland, and L. Marciani, "Fat Emulsion Intra-gastric Stability and Droplet Size Modulate Gastrointestinal Responses and Subsequent Food Intake in Young Adults.," *J. Nutr.*, vol. 45, no. 6, pp. 1170–7 2015.
- [55] L. Marciani, M. S. J. Wickham, D. Bush, R. Faulks, J. Wright, A. J. Fillery-Travis, R. C. Spiller, and P. A. Gowland, "Magnetic resonance imaging of the behaviour of oil-in-water emulsions in the gastric lumen of man," *Br. J. Nutr.*, vol. 95, no. 02, p. 331, 2007.
- [56] L. Marciani, C. Ramanathan, D. J. Tyler, P. Young, P. Manoj, M. Wickham, A. Fillery-Travis, R. C. Spiller, and P. A. Gowland, "Fat Emulsification Measured Using NMR Transverse Relaxation," *J. Magn. Reson.*, vol. 153, no. 1, pp. 1–6, 2001.
- [57] L. J. Anderson, S. Holden, B. Davis, E. Prescott, C. C. Charrier, N. H. Bunce, D. N. Firmin, B. Wonke, J. Porter, J. M. Walker, and D. J. Pennell, "Cardiovascular T2-star (T2\*) magnetic resonance for the early diagnosis of myocardial iron overload.," *Eur. Heart J.*, vol. 22, no. 23, pp. 2171–9, Dec. 2001.
- [58] C. D. G. Hines, R. Agni, C. Roen, I. Rowland, D. Hernando, E. Bultman, D. Horng, H. Yu, A. Shimakawa, J. H. Brittain, and S. B. Reeder, "Validation of MRI biomarkers of hepatic steatosis in the presence of iron overload in the ob/ob mouse," *J. Magn. Reson. Imaging*, vol. 35, no. 4, pp. 844–851, 2012.
- [59] S. Meisamy, C. D. G. Hines, G. Hamilton, C. B. Sirlin, C. a McKenzie, H. Yu, J. H. Brittain, and S. B. Reeder, "Quantification of hepatic steatosis with T1-independent, T2-corrected MR imaging with spectral modeling of fat: blinded comparison with MR spectroscopy.," *Radiology*, vol. 258, no. 3, pp. 767–775, 2011.
- [60] H. H. Hu, H.-W. Kim, K. S. Nayak, and M. I. Goran, "Comparison of fat-water MRI and single-voxel MRS in the assessment of hepatic and pancreatic fat fractions in humans.," *Obesity (Silver Spring)*, vol. 18, no. 4, pp. 841–7, 2010.

- [61] S. B. Reeder, I. Cruite, G. Hamilton, and C. B. Sirlin, "Quantitative Assessment of Liver Fat with Magnetic Resonance Imaging and Spectroscopy.," *J. Magn. Reson. Imaging*, vol. 34, no. 4, p. spcone, Oct. 2011.
- [62] T. Yokoo, M. Shiehmorteza, G. Hamilton, T. Wolfson, M. E. Schroeder, M. S. Middleton, M. Bydder, A. C. Gamst, Y. Kono, A. Kuo, H. M. Patton, S. Horgan, J. E. Lavine, J. B. Schwimmer, and C. B. Sirlin, "Estimation of hepatic proton-density fat fraction by using MR imaging at 3.0 T.," *Radiology*, vol. 258, no. 3, pp. 749–59, Mar. 2011.
- [63] H. Kim, S. E. Taksali, S. Dufour, D. Befroy, T. R. Goodman, K. F. Petersen, G. I. Shulman, S. Caprio, and R. T. Constable, "Comparative MR study of hepatic fat quantification using single-voxel proton spectroscopy, two-point dixon and three-point IDEAL.," *Magn. Reson. Med.*, vol. 59, no. 3, pp. 521–527, Mar. 2008.
- [64] H. Kawamitsu, Y. Kaji, T. Ohara, and K. Sugimura, "Feasibility of Quantitative Intrahepatic Lipid Imaging Applied to the Magnetic Resonance Dual Gradient Echo Sequence.," *Magn. Reson. Med. Sci.*, vol. 2, no. 1, pp. 47–50, Oct. 2003.
- [65] C. D. G. Hines, H. Yu, A. Shimakawa, C. A. McKenzie, T. F. Warner, J. H. Brittain, and S. B. Reeder, "Quantification of Hepatic Steatosis with 3-T MR Imaging: Validation in ob/ob Mice.," *Radiology*, vol. 254, no. 1, pp. 119–128, Jan. 2010.
- [66] X.-G. Peng, S. Ju, Y. Qin, F. Fang, X. Cui, G. Liu, Y. Ni, and G.-J. Teng, "Quantification of liver fat in mice: comparing dual-echo Dixon imaging, chemical shift imaging, and <sup>1</sup>H-MR spectroscopy.," *J. Lipid Res.*, vol. 52, no. 10, pp. 1847–55, Oct. 2011.
- [67] D. H. Johnson, S. Narayan, D. L. Wilson, and C. a. Flask, "Body composition analysis of obesity and hepatic steatosis in mice by relaxation compensated fat fraction (RCFF) MRI.," *J. Magn. Reson. Imaging*, vol. 35, no. 4, pp. 837–843, 2012.
- [68] C. D. G. Hines, R. Agni, C. Roen, I. Rowland, D. Hernando, E. Bultman, D. Horng, H. Yu, A. Shimakawa, J. H. Brittain, and S. B. Reeder, "Validation of MRI biomarkers of hepatic steatosis in the presence of iron overload in the ob/ob mouse.," *J. Magn. Reson. Imaging*, vol. 35, no. 4, pp. 844–851, Apr. 2012.
- [69] N. S. Artz, C. D. G. Hines, S. T. Brunner, R. M. Agni, J.-P. Kühn, A. Roldan-Alzate, G.-H. Chen, and S. B. Reeder, "Quantification of hepatic steatosis with dual-energy computed tomography: comparison with tissue reference standards and quantitative magnetic resonance imaging in the ob/ob mouse.," *Invest. Radiol.*, vol. 47, no. 10, pp. 603–10, Oct. 2012.
- [70] D. A. Raptis, M. A. Fischer, R. Graf, D. Nanz, A. Weber, W. Moritz, Y. Tian, C. E. Oberkofler, and P.-A. Clavien, "MRI: the new reference standard in quantifying hepatic steatosis?," *Gut*, vol. 61, no. 1, pp. 117–27, Jan. 2012.
- [71] M. Rönn, J. Kullberg, H. Karlsson, J. Berglund, F. Malmberg, J. Orberg, L. Lind, H. Ahlström, and P. M. Lind, "Bisphenol A exposure increases liver fat in juvenile fructose-fed Fischer 344 rats.," *Toxicology*, vol. 303, pp. 125–32, Jan. 2013.

- [72] X. Yin, Y. Guo, W. Li, E. Huo, Z. Zhang, J. Nicolai, R. A. Kleps, D. Hernando, A. K. Katsaggelos, R. A. Omary, and A. C. Larson, “Chemical shift MR imaging methods for the quantification of transcatheter lipiodol delivery to the liver: preclinical feasibility studies in a rodent model,” *Radiology*, vol. 263, no. 3, pp. 714–22, Jun. 2012.
- [73] J. H. Runge, P. J. Bakker, I. C. Gaemers, J. Verheij, T. B. M. Hakvoort, R. Ottenhoff, A. J. Nederveen, and J. Stoker, “Measuring liver triglyceride content in mice: non-invasive magnetic resonance methods as an alternative to histopathology,” *MAGMA*, vol. 27, no. 4, pp. 317–27, Aug. 2014.
- [74] D. L. Smith, Y. Yang, H. H. Hu, G. Zhai, and T. R. Nagy, “Measurement of interscapular brown adipose tissue of mice in differentially housed temperatures by chemical-shift-encoded water-fat MRI,” *J. Magn. Reson. Imaging*, vol. 38, no. 6, pp. 1425–33, Dec. 2013.
- [75] H. H. Hu, C. D. G. Hines, D. L. Smith, and S. B. Reeder, “Variations in T2\* and fat content of murine brown and white adipose tissues by chemical-shift MRI,” *Magn. Reson. Imaging*, vol. 30, no. 3, pp. 323–329, Apr. 2012.
- [76] J. Berglund and J. Kullberg, “Three-dimensional water/fat separation and T2\* estimation based on whole-image optimization--application in breathhold liver imaging at 1.5 T,” *Magn. Reson. Med.*, vol. 67, no. 6, pp. 1684–93, Jun. 2012.
- [77] D. Hernando, P. Kellman, J. Haldar, and Z. P. Liang, “Estimation of water/fat images, B0 field map and T2 \* map using VARPRO,” *Proc. Intl. Soc. Mag. Reson. Med.* 16, 2008
- [78] D. Hernando, J. P. Haldar, B. P. Sutton, J. Ma, P. Kellman, and Z.-P. Liang, “Joint estimation of water/fat images and field inhomogeneity map,” *Magn. Reson. Med.*, vol. 59, no. 3, pp. 571–580, Mar. 2008.
- [79] R. M. Goldstein, H. A. Zebker, and C. L. Werner, “Satellite radar interferometry: Two-dimensional phase unwrapping,” *Radio Sci.*, vol. 23, no. 4, pp. 713–720, Jul. 1988.
- [80] “ImageJ.” [Online]. Available: <http://imagej.nih.gov/ij/>. [Accessed: 10-Oct-2015].
- [81] “StackReg.” [Online]. Available: <http://bigwww.epfl.ch/thevenaz/stackreg/>. [Accessed: 10-Oct-2015].
- [82] P. Thévenaz, U. E. Ruttimann, and M. Unser, “A pyramid approach to subpixel registration based on intensity,” *IEEE Trans. Image Process.*, vol. 7, no. 1, pp. 27–41, Jan. 1998.
- [83] L. Barantin, A. Le Pape, and S. Akoka, “A new method for absolute quantitation of MRS metabolites,” *Magn. Reson. Med.*, vol. 38, pp. 179–182, 1997.
- [84] N. Michel and S. Akoka, “The application of the ERETIC method to 2D-NMR,” *J. Magn. Reson.*, vol. 168, no. 1, pp. 118–123, 2004.
- [85] M. C. Martínez-Bisbal, D. Monleon, O. Assemat, M. Piotta, J. Piquer, J. L. Llácer, and B. Celda, “Determination of metabolite concentrations in human brain tumour biopsy samples

using HR-MAS and ERETIC measurements,” *NMR Biomed.*, vol. 22, no. July 2007, pp. 199–206, 2009.

- [86] M. J. Albers, T. N. Butler, I. Rahwa, N. Bao, K. R. Keshari, M. G. Swanson, and J. Kurhanewicz, “Evaluation of the ERETIC method as an improved quantitative reference for  $^1\text{H}$  HR-MAS spectroscopy of prostate tissue,” *Magn. Reson. Med.*, vol. 61, no. 3, pp. 525–532, 2009.
- [87] F. Ziarelli, S. Viel, S. Sanchez, D. Cross, and S. Caldarelli, “Precision and sensitivity optimization of quantitative measurements in solid state NMR,” *J. Magn. Reson.*, vol. 188, no. 2, pp. 260–266, 2007.
- [88] S. Heinzer-Schweizer, N. De Zanche, M. Pavan, G. Mens, U. Sturzenegger, a. Henning, and P. Boesiger, “*In-vivo* assessment of tissue metabolite levels using  $^1\text{H}$  MRS and the Electric REference To access *In vivo* Concentrations (ERETIC) method,” *NMR Biomed.*, no. October 2008, p. n/a–n/a, 2010.
- [89] K. I. Marro, D. Lee, E. G. Shankland, C. M. Mathis, and C. E. Hayes, “Synthetic signal injection using a single radiofrequency channel,” *J. Magn. Reson. Imaging*, vol. 34, no. 6, pp. 1414–1421, 2011.
- [90] F. Franconi, C. Chapon, L. Lemaire, V. Lehmann, L. Barantin, and S. Akoka, “Quantitative MR renography using a calibrated internal signal (ERETIC),” *Magn. Reson. Imaging*, vol. 20, no. 8, pp. 587–592, 2002.
- [91] D. Lee, K. Marro, E. Shankland, and M. Mathis, “Quantitative  $^{19}\text{F}$  imaging using inductively coupled reference signal injection,” *Magn. Reson. Med.*, vol. 63, no. 3, pp. 570–573, 2010.
- [92] H. Saint-Jalmes, P.-A. Eliat, J. Bezy-Wendling, A. Bordelois, and G. Gambarota, “ViP MRI: virtual phantom magnetic resonance imaging,” *Magn. Reson. Mater. Physics, Biol. Med.*, vol. 27, no. 5, pp. 419–424, 2014.
- [93] H. H. Hu, H.-W. Kim, K. S. Nayak, and M. I. Goran, “Comparison of Fat–Water MRI and Single-voxel MRS in the Assessment of Hepatic and Pancreatic Fat Fractions in Humans,” *Obesity*, vol. 18, no. 4, pp. 841–847, 2010.
- [94] C. D. G. Hines, H. Yu, A. Shimakawa, C. a. McKenzie, J. H. Brittain, and S. B. Reeder, “ $T_1$  independent,  $T_2^*$  corrected MRI with accurate spectral modeling for quantification of fat: Validation in a fat-water-SPIO phantom,” *J. Magn. Reson. Imaging*, vol. 30, no. 5, pp. 1215–1222, 2009.
- [95] R. L. Janiczek, G. Gambarota, C. D. J. Sinclair, T. a. Yousry, J. S. Thornton, X. Golay, and R. D. Newbould, “Simultaneous  $T_2$  and lipid quantitation using IDEAL-CPMG,” *Magn. Reson. Med.*, vol. 66, no. 5, pp. 1293–1302, 2011.
- [96] D. Hernando, J. H. Kramer, and S. B. Reeder, “Multipeak fat-corrected complex  $R_2^*$  relaxometry: Theory, optimization, and clinical validation,” *Magn. Reson. Med.*, vol. 70, no. 5, pp. 1319–1331, 2013.

- [97] D. E. Kleiner, E. M. Brunt, M. Van Natta, C. Behling, M. J. Contos, O. W. Cummings, L. D. Ferrell, Y.-C. Liu, M. S. Torbenson, A. Unalp-Arida, M. Yeh, A. J. McCullough, and A. J. Sanyal, "Design and validation of a histological scoring system for nonalcoholic fatty liver disease," *Hepatology*, vol. 41, no. 6, pp. 1313–1321, 2005.
- [98] Y. Ishihara, a Calderon, H. Watanabe, K. Okamoto, Y. Suzuki, K. Kuroda, and Y. Suzuki, "A precise and fast temperature mapping using water proton chemical shift.," *Magn. Reson. Med.*, vol. 34, no. 6, pp. 814–823, 1995.
- [99] M. O'Donnell, "NMR blood flow imaging using multiecho, phase contrast sequences.," *Med. Phys.*, vol. 12, no. 1, pp. 59–64, Jan. 1985.
- [100] G. Larry Bretthorst, "Automatic phasing of MR images. Part I: Linearly varying phase," *J. Magn. Reson.*, vol. 191, pp. 184–192, 2008.
- [101] R. V. Mulkern, M. Balasubramanian, and D. Mitsouras, "On the lorentzian versus Gaussian character of time-domain spin-echo signals from the brain as sampled by means of gradient-echoes: Implications for quantitative transverse relaxation studies," *Magn. Reson. Med.*, vol. 74, no. 1, pp. 51–62, 2015.
- [102] J. Ma and F. W. Wehrli, "Method for Image-Based Measurement of the Reversible and Irreversible Contribution to the Transverse-Relaxation Rate," *J. Magn. Reson. Ser. B*, vol. 111, no. 1, pp. 61–69, Apr. 1996.



## Appendix A - IDEAL equations

The **Equation 2.21** can be generalized and rewritten as

$$s(t_n) = \left( \sum_{j=1}^M \rho_j e^{i2\pi\Delta f_j t_n} \right) e^{i2\pi\psi t_n} = (W + F e^{i2\pi\Delta f t_n}) e^{i2\pi\psi t_n} \quad (A.1)$$

where  $\Delta f_j$  is the chemical shift frequency of the  $j$ -th component respect to the water resonant frequency and  $M$  the chemical species. In this case the chemical species  $M$  are 2 (i.e. water and fat).

If the field map  $\psi(x,y)$  is known, the signal equation can be written as

$$\widehat{s}_n = s_n e^{-i2\pi\psi t_n} = \left( \sum_{i=1}^2 \rho_i e^{i2\pi\Delta f_i t_n} \right) \quad (A.2)$$

The system of complex equation in [A2] can be split in real  $\widehat{s}_n^R$  and imaginary  $\widehat{s}_n^I$  part

$$\widehat{s}_n = \widehat{s}_n^R + i\widehat{s}_n^I = \sum_{i=1}^2 (\rho_i^R c_{i,n} - \rho_i^I d_{i,n}) + i \sum_{i=1}^2 (\rho_i^R d_{i,n} + \rho_i^I c_{i,n}) \quad (A.3)$$

where  $c_{i,n} = \cos(2\pi\Delta f_i t_n)$  and  $d_{i,n} = \sin(2\pi\Delta f_i t_n)$ .

In matrix format, considering the water and fat only component, the system of equation becomes

$$\widehat{S} = A\rho \quad (A.4)$$

with

$$\widehat{S} = [s_1^R \ s_2^R \ \dots \ s_n^R \ s_1^I \ s_2^I \ \dots \ s_n^I]^T \quad (A.5)$$

$$\rho = [\rho_1^R \ \rho_1^I \ \rho_2^R \ \rho_2^I \ \dots \ \rho_M^R \ \rho_M^I]^T = [W^R \ W^I \ F^R \ F^I]^T \quad (A.6)$$

$$A = \begin{bmatrix} c_{1,1} & -d_{1,1} & c_{2,1} & -d_{2,1} & \dots & c_{M,n} & -d_{M,1} \\ c_{1,2} & -d_{1,2} & c_{2,2} & -d_{2,2} & \dots & c_{M,n} & -d_{M,2} \\ \dots & \dots & \dots & \dots & \dots & \dots & \dots \\ c_{1,N} & -d_{1,N} & c_{2,N} & -d_{2,N} & \dots & c_{M,n} & -d_{M,N} \\ d_{1,1} & c_{1,1} & d_{2,1} & c_{2,1} & \dots & d_{M,1} & c_{M,1} \\ d_{1,2} & c_{1,2} & d_{2,2} & c_{2,2} & \dots & d_{M,2} & c_{M,2} \\ \dots & \dots & \dots & \dots & \dots & \dots & \dots \\ d_{1,N} & c_{1,N} & d_{2,N} & c_{2,N} & \dots & d_{M,N} & c_{M,N} \end{bmatrix} = \begin{bmatrix} 1 & 0 & c_1^F & -d_1^F \\ 1 & 0 & c_2^F & -d_2^F \\ \dots & \dots & \dots & \dots \\ 1 & 0 & c_N^F & -d_N^F \\ 0 & 1 & d_1^F & c_1^F \\ 0 & 1 & d_2^F & c_2^F \\ \dots & \dots & \dots & \dots \\ 0 & 1 & d_N^F & c_N^F \end{bmatrix} \quad (A.7)$$

Using the pseudoinverse of the matrix  $A$ , the vector  $\widehat{\rho}$  is explicated as



$$\rho = (A^T A)^{-1} A^T \hat{S}. \quad (\text{A.8})$$

If  $\rho_i^R = \rho_i^R + \Delta\rho_i^R$ ,  $\rho_i^I = \rho_i^I + \Delta\rho_i^I$  and  $\psi = \psi + \Delta\psi$ , then the system of equation [2] turns into

$$s_n \approx \left( \sum_{i=1}^M (\rho_i + \Delta\rho_i) e^{i2\pi\Delta f_i t_n} \right) e^{i2\pi\psi t_n} e^{i2\pi\Delta\psi t_n} \quad (\text{A.9})$$

Dividing each side for  $e^{i2\pi\psi t_n}$  and considering  $\Delta\psi$  small to use the Taylor approximation

$$\widehat{s}_n^R + \widehat{s}_n^I \approx \left( \sum_{i=1}^M \left( (\rho_i^R + \Delta\rho_i^R) + i(\rho_i^I + \Delta\rho_i^I) \right) (c_{i,n} + i d_{i,n}) \right) (1 + i2\pi\Delta\psi t_n) \quad (\text{A.10})$$

The real and imaginary component can be rearranged as

$$\begin{aligned} \widehat{s}_n^R &= \widehat{s}_n^R - \sum_{i=1}^M (\rho_i^R d_{i,n} - \rho_i^I c_{i,n}) \\ &= 2\pi\Delta\psi t_n \sum_{i=1}^M (-\rho_i^R d_{i,n} - \rho_i^I c_{i,n}) + \sum_{i=1}^M (\rho_i^R c_{i,n} - \rho_i^I d_{i,n}) \end{aligned} \quad (\text{A.11})$$

$$\begin{aligned} \widehat{s}_n^I &= \widehat{s}_n^I - \sum_{i=1}^M (\rho_i^R d_{i,n} + \rho_i^I c_{i,n}) \\ &= 2\pi\Delta\psi t_n \sum_{i=1}^M (\rho_i^R c_{i,n} - \rho_i^I d_{i,n}) + \sum_{i=1}^M (\rho_i^R d_{i,n} + \rho_i^I c_{i,n}) \end{aligned} \quad (\text{A.12})$$

In matrix format, the last systems of equation become

$$\hat{\hat{S}} = B y \quad (\text{A.13})$$

with

$$\hat{\hat{S}} = [\widehat{s}_1^R \quad \widehat{s}_2^R \quad \dots \quad \widehat{s}_N^R \quad \widehat{s}_1^I \quad \widehat{s}_2^I \quad \dots \quad \widehat{s}_N^I]^T \quad (\text{A.14})$$

$$\begin{aligned} y &= [\Delta\psi \quad \Delta\rho_1^R \quad \Delta\rho_1^I \quad \Delta\rho_2^R \quad \Delta\rho_2^I \quad \dots \quad \Delta\rho_M^R \quad \Delta\rho_M^I]^T = \\ & \quad [\Delta\psi \quad \Delta W^R \quad \Delta W^I \quad \Delta F^R \quad \Delta F^I]^T \end{aligned} \quad (\text{A.15})$$

$$B = \begin{bmatrix} g_1^R & c_{1,1} & -d_{1,1} & c_{2,1} & -d_{2,1} & \cdots & c_{M,n} & -d_{M,1} \\ g_2^R & c_{1,2} & -d_{1,2} & c_{2,2} & -d_{2,2} & \cdots & c_{M,n} & -d_{M,2} \\ \cdots & \cdots & \cdots & \cdots & \cdots & \cdots & \cdots & \cdots \\ g_N^R & c_{1,N} & c_{2,N} & c_{2,N} & -d_{2,N} & \cdots & c_{M,n} & -d_{M,N} \\ g_1^I & d_{1,1} & c_{1,1} & d_{2,1} & c_{2,1} & \cdots & d_{M,1} & c_{M,1} \\ g_2^I & d_{1,2} & c_{1,2} & d_{2,2} & c_{2,2} & \cdots & d_{M,2} & c_{M,2} \\ \cdots & \cdots & \cdots & \cdots & \cdots & \cdots & \cdots & \cdots \\ g_N^I & d_{1,N} & c_{1,N} & d_{2,N} & c_{2,N} & \cdots & d_{M,N} & c_{M,N} \end{bmatrix} = \begin{bmatrix} g_1^R & 1 & 0 & c_1^F & -d_1^F \\ g_2^R & 1 & 0 & c_2^F & -d_2^F \\ \cdots & \cdots & \cdots & \cdots & \cdots \\ g_N^R & 1 & 0 & c_N^F & -d_N^F \\ g_1^I & 0 & 1 & d_1^F & c_1^F \\ g_2^I & 0 & 1 & d_2^F & c_2^F \\ \cdots & \cdots & \cdots & \cdots & \cdots \\ g_N^I & 0 & 1 & d_N^F & c_N^F \end{bmatrix} \quad (\text{A.16})$$

where

$$g_n^R = 2\pi t_n \sum_{i=1}^M (-\rho_i^R d_{i,n} - \rho_i^I c_{i,n}) = 2\pi t_n (-W^I - F^R d_n - F^I c_n) \quad (\text{A.17})$$

and

$$g_n^I = 2\pi t_n \sum_{i=1}^M (\rho_i^R c_{i,n} - \rho_i^I d_{i,n}) = 2\pi t_n (W^R + F^R c_n - F^I d_n) \quad (\text{A.18})$$

The estimation of  $y$  can be determined as

$$y = (B^T B)^{-1} B^T \hat{S} \quad (\text{A.19})$$

which allows the estimation of  $\Delta\psi$ ,  $\Delta W^R$ ,  $\Delta W^I$ ,  $\Delta F^R$  and  $\Delta F^I$ .



## Appendix B – IDEAL dual T<sub>2</sub>\*

In chapter III, the existence of algorithms which calculate fat fraction using two T<sub>2</sub><sup>\*</sup>, was touched on. One of the “dual T<sub>2</sub><sup>\*</sup> methods” was presented in 2010 by Chebrolu et al. [46] and include in the signal equation a T<sub>2</sub><sup>\*</sup> for water and a T<sub>2</sub><sup>\*</sup> for fat. The signal equation was

$$s(t_n) = \left( W e^{-t_n/T_{2,W}^*} + F e^{-t_n/T_{2,F}^*} \sum_{i=1}^7 \alpha_i e^{i2\pi\Delta f_i t_n} \right) \quad (\text{B.1})$$

where  $t_n$  represents the time wherein the image is acquired (the TE),  $s$  the signal,  $W$  and  $F$  the water and fat component, respectively,  $T_{2,W}^*$  and  $T_{2,F}^*$  the relaxation time for water and fat, respectively,  $\alpha_i$  is the relative area underlying the  $i$ -th fat peak ( $\sum_{i=1}^7 \alpha_i = 1$ ),  $\Delta f_i$  the frequency shift of the  $i$ -th fat peak respect to the water one and  $\psi$  the magnetic field inhomogeneity (or field map). The algorithm works, following the steps described in **Figure B.1**.

$$s(t_n) = (W e^{-t_n/T_{2,W}^*} + F e^{-t_n/T_{2,F}^*} \sum_{i=1}^7 \alpha_i e^{i2\pi\Delta f_i t_n}) e^{i2\pi\psi t_n}$$

- $t_n = nth$  echo time
- $W =$  Water component
- $F =$  Fat component
- $T_{2,W}^* =$  Water relaxation time
- $T_{2,F}^* =$  Fat relaxation time
- $\Delta f_i =$   $i$ th Chemical shift frequency
- $\alpha_i =$  Relative area under the  $i$ th fat peak
- $\psi =$  Magnetic field inhomogeneity

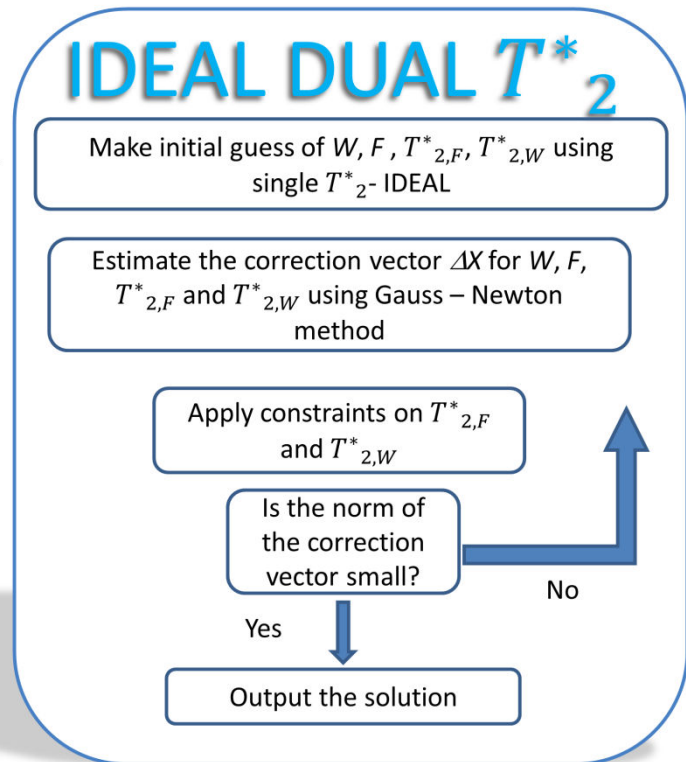


**Figure B2.1:** Scheme of the dual T<sub>2</sub><sup>\*</sup> algorithm proposed by Chebrolu et al. It is an iterative algorithm which stops when the error on the norm of the correction vector  $\Delta X$  is small (e.g. 0.1% of the magnitude). The output of the current algorithm are fat fraction, field map and T<sub>2</sub><sup>\*</sup> map for water and fat.

The algorithm works with a minimum of four complex images. A script which reproduces the dual  $T_2^*$  method was implemented in Matlab. The script to generate numerical phantoms (described in Chapter 2) was used for two purposes:

- to validate the dual  $T_2^*$  method script: this validation was necessary to ensure that no errors were present in the dual  $T_2^*$  method script;
- to investigate the performances of the dual  $T_2^*$  method (as a function of SNR).

The dual  $T_2^*$  method script was tested using infinite SNR and with different fat fractions and  $T_2^*$  values. In **Figure B.2** the output of dual  $T_2^*$  method is illustrated. In output the values found for  $T_{2,W}^*$ ,  $T_{2,F}^*$ , fat fraction and  $\psi$  are equivalent to the ground truth.

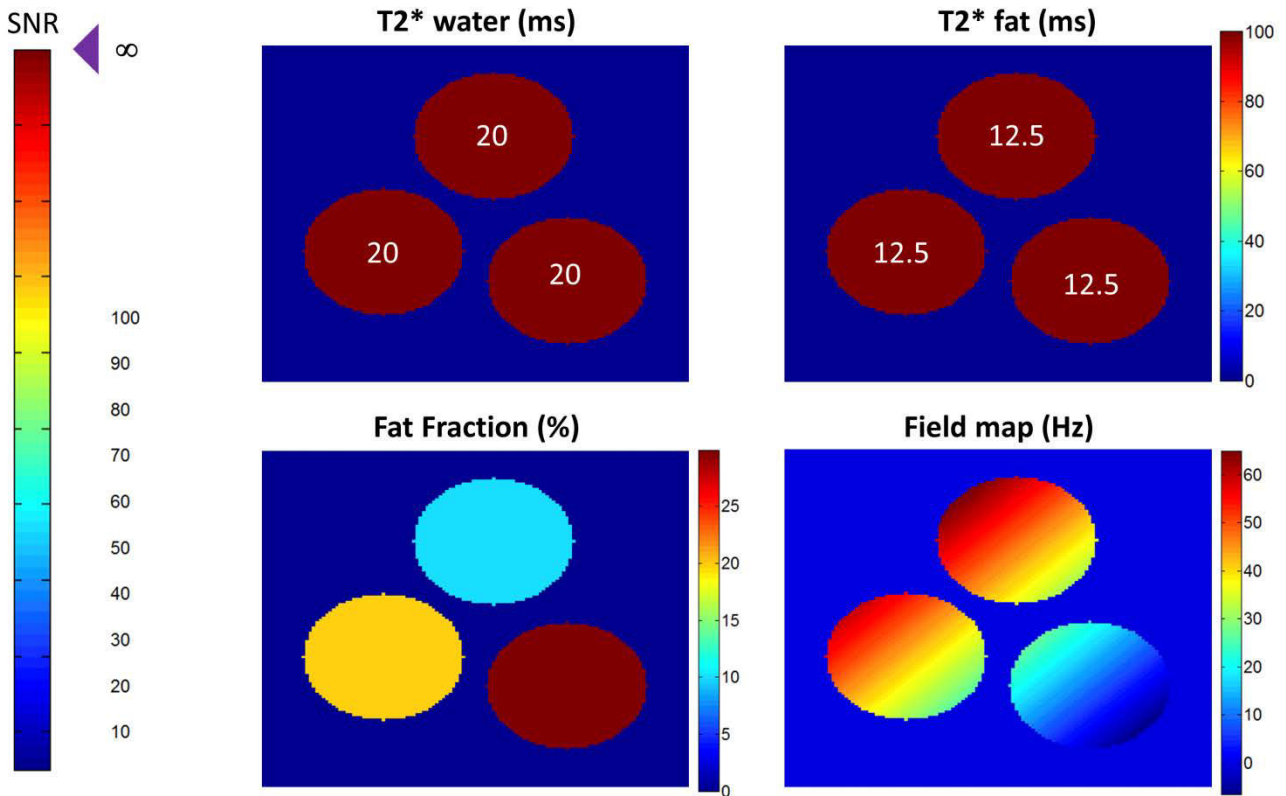


**Figure B.2:** Output of the dual  $T_2^*$  method. The  $T_2^*$  of water and fat, the fat fraction map are illustrated. The simulations were performed at infinite SNR.

The following simulations were performed adding noise to the signal **Equation B.1**. In **Figure B.3**, the output of the dual  $T_2^*$  method is illustrated. The images in input were generated with an SNR equal to 100. The  $T_2^*$  map relative to the fat is very noisy. On the field map, some sparse pixels miscalculate the values. The  $T_2^*$  map relative to water and fat fraction map are well calculated.

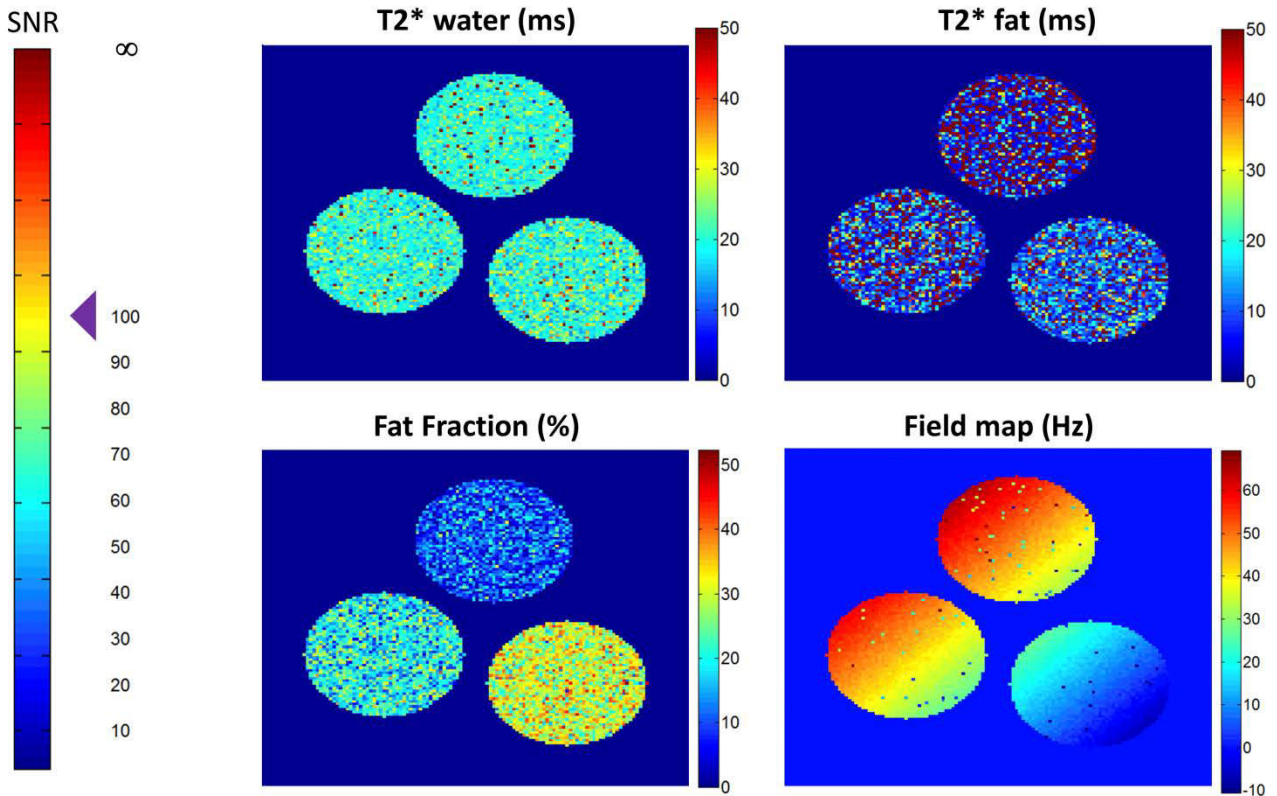


**Figure B.3:** Output of the dual  $T_2^*$  method. The  $T_2^*$  of water and fat, the fat fraction map are illustrated. The simulations were performed at SNR equal to 100.

In **Figure B.4**, the output of the dual  $T_2^*$  method is illustrated using an SNR equal to 50. Both the  $T_2^*$  maps are very noisy as the fat fraction map. From the simulations, it was outlined that the dual  $T_2^*$  method is not appropriate for MR experiment. The reason is due to the output showed above: since it is not robust at SNR comparable to the real ones, the algorithm is worthless. In the article of Horng et al. [47] the algorithm was used on patient data and the output of IDEAL algorithm was compared to the ones of the dual  $T_2^*$  method. The conclusion was that the IDEAL algorithm is more robust than the dual  $T_2^*$  method at SNR reached in clinical scenario.

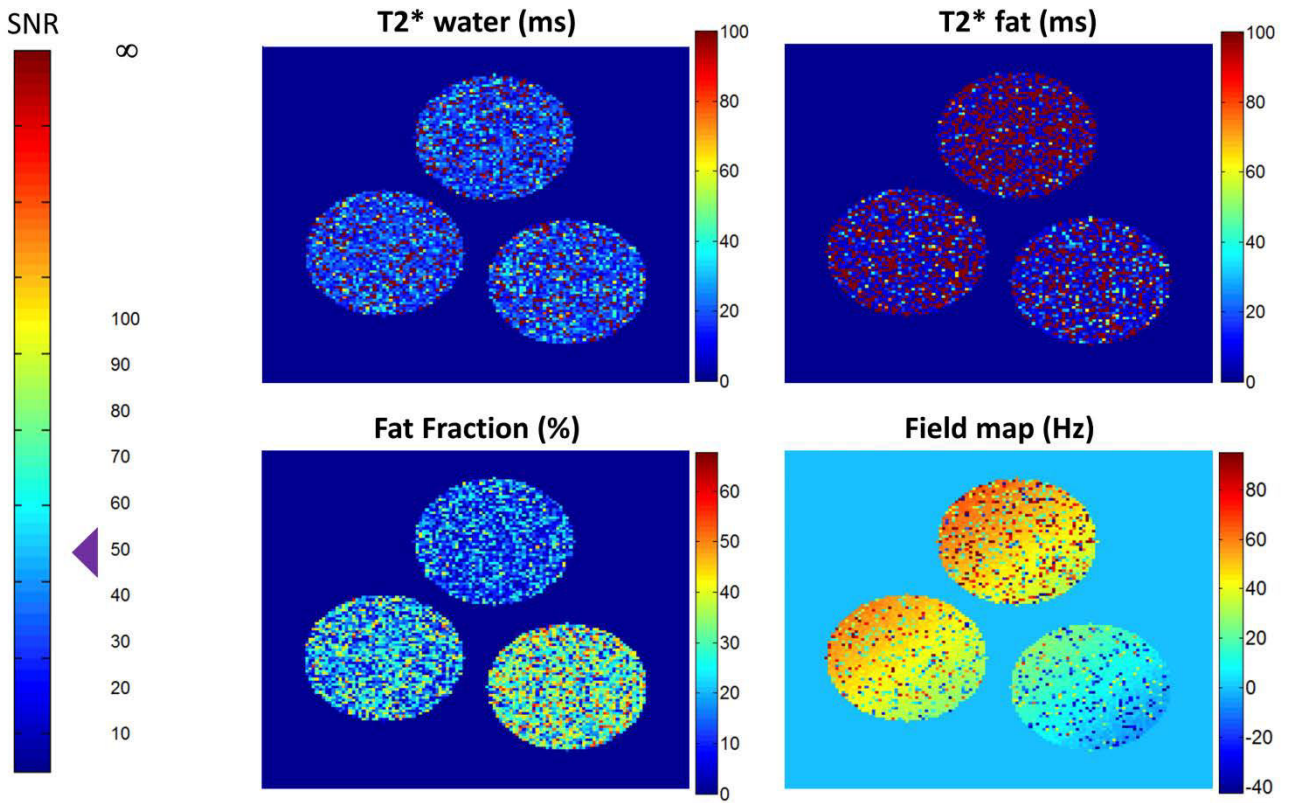


**Figure B.4:** Output of the dual  $T_2^*$  method. The  $T_2^*$  maps for water and fat, the fat fraction and field maps are illustrated. The simulations were performed at SNR equal to 50.







## Appendix C - Goldstein's algorithm (branch-cut algorithm)

A script in MATLAB which reproduces the Goldstein's algorithm [79] for unwrapping the phase was added to the IDEAL algorithm. This method is called branch-cut algorithm as well and it operates to find the pixels where the phase passes from a value to another one higher than a half cycle in difference. Between two or more of these pixels the algorithm builds a branch and if it finds the solution, it cuts the branch. In this paragraph the algorithm is explained more in detail.

### C.1 Explanation of the method

Consider a periodical function with values from 0 to 0.9 and suppose to have the following one-dimensional sequence:

... 0.0    0.2    0.5    0.6    0.6    0.7    0.9    0.1    0.4    0.5 ...


It is straightforward to understand that for having the increasing trend, a unit should be added to the last three values in way to reach:

... 0.0    0.2    0.5    0.6    0.6    0.7    0.9    1.1    1.4    1.5 ...

Consider now this following situation

0.0	0.2	0.1	0.1
0.1	0.0	0.2	0.2
0.8	0.7	0.4	0.3
0.8	0.6	0.6	0.5

The difference between the second and the third element of the first two columns is higher than a half cycle. Suppose to consider this rule, hence the matrix could be changed from top to bottom in this way:

	0.0	0.2	0.1	0.1
	0.1	0.0	0.2	0.2
	-0.2	-0.3	-0.6	-0.7
	-0.2	-0.4	-0.4	-0.5

The values of the first two columns are consistent now, but the values on the other two columns do not; in fact the second and the third element on the third and fourth columns don't respect the half cycle rule. If the matrix is scanned vertically on the third and the fourth columns

0.0	0.2	0.1	0.1
0.1	0.0	0.2	0.2
-0.2	-0.3	0.4	0.3
-0.2	-0.4	0.6	0.5

The columns respect the half cycle rule but the rows don't. This means that the algorithm for find the good trend is more complicated in the 2-D situations than in 1-D. The Goldstein's algorithm is based on the research of particular element named residue. Consider the central 4-element square of the initial matrix and the clockwise difference of value:

$$\begin{array}{ccc}
 0.0 & \rightarrow & 0.2 \\
 \uparrow & & \downarrow \\
 0.7 & \leftarrow & 0.4
 \end{array}$$

If the half cycle rule should be respected, the addition of a unit is necessary. A number is put inside this square to indicate the number of cycles added

$$\begin{array}{ccc}
 0.0 & \rightarrow & 0.2 \\
 \uparrow & 1 & \downarrow \\
 0.7 & \leftarrow & 0.4
 \end{array}$$

This number is called residue. The research of the residue on the initial matrix is done

0.0	0.2	0.1	0.1
	0	0	0
0.1	0.0	0.2	0.2
	0	1	0
0.8	0.7	0.4	0.3
	0	0	0
0.8	0.6	0.6	0.5

The sum of the cycles on the same square could be 0, so the residue is 0 as well. A matrix 3x3 is created for finding residues; if they aren't found, the dimension of the matrix increases of 2. If it is found, the matrix is placed with the center in the residue. From here, the matrix will search other residues: if the residues have the same sign, the matrix 3x3 shifts on the new residue; else a cut is placed between them and designed "uncharged". When all cuts are placed, the phase differences are integrated in way to not cross any of the cuts. When the phase estimate is obtained, a new estimate is calculated for every neighbor on the same side respect to the cut. If the residues are very dense, the algorithm could not be able to calculate the phase.

## C.2 How to use the branch-cut algorithm in IDEAL algorithm

Before entering in the IDEAL part, the phases of two echoes of the global sequence are subtracted. The branch-cut algorithm works on this difference. The user can choose the point where the algorithm begins to work (**Figure C.1**). As output of the algorithm, there are the "residue map", "the branch-cut map" and the "phase unwrapped". The phase unwrapped is used as initial estimation of the field map which IDEAL adopts. In **Figure C.2** the maps created with the brunch-cut algorithm applied on the phase in **Figure C.1** are displayed.

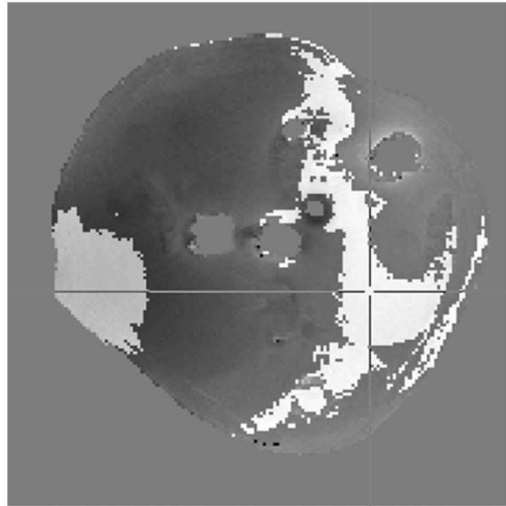


**Figure C.1:** The branch-cut algorithm provides a phase map where a cursor indicates the point to choose. The algorithm begins to work from the chosen point.

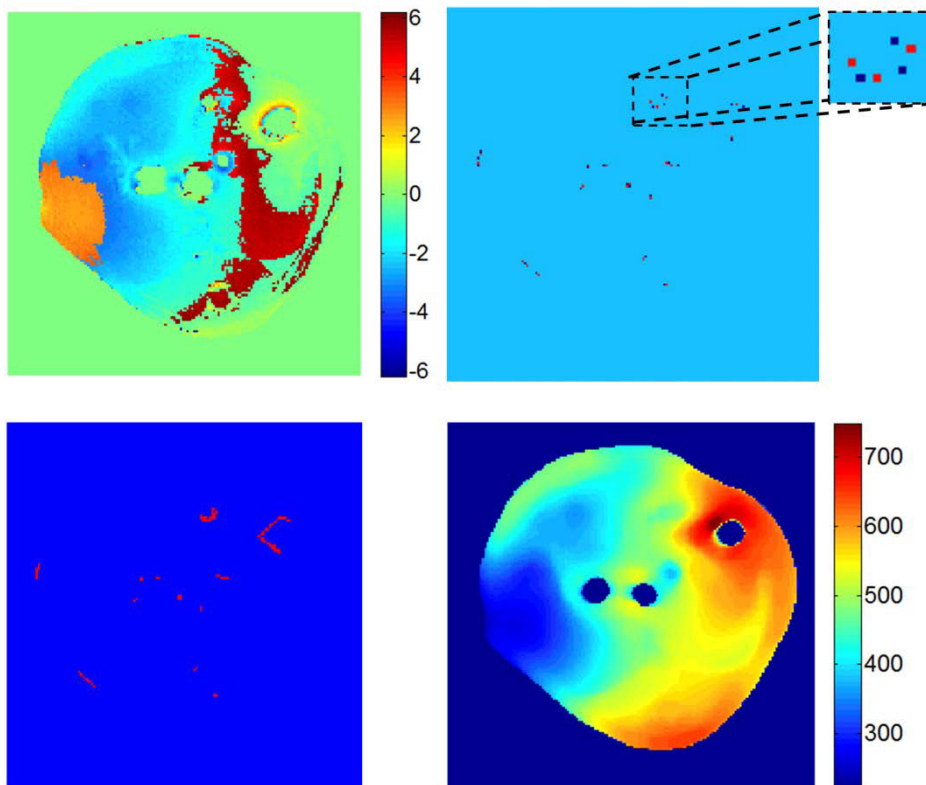


**Figure C.2:** Explication of the branch cut algorithm. a) phase of the signal, b) residues found c) cut applied on the image d) field map calculated from the phase corrections after using the branch-cut algorithm





## **Appendix D**

**Article accepted in "Magnetic Resonance Imaging"**





## **Fat ViP MRI: Virtual Phantom Magnetic Resonance Imaging of water-fat systems**

Roberto Salvati<sup>1,2</sup>, Eric Hitti<sup>1,2</sup>, Jean-Jacques Bellanger<sup>1,2</sup>, Hervé Saint-Jalmes<sup>1,2,3</sup> and Giulio Gambarota<sup>1,2</sup>

<sup>1</sup> INSERM, UMR 1099, Rennes, F-35000, France

<sup>2</sup> Université de Rennes 1, LTSI, Rennes, F-35000, France

<sup>3</sup> CRLCC, Centre Eugène Marquis, Rennes, F-35000, France

### **Running Head: Fat ViP MRI**

Corresponding author:

Roberto Salvati

INSERM, U1099

Université de Rennes 1, LTSI

35043 Rennes, France

tel: 02 23 23 48 49

email: roberto.salvati@univ-rennes1.fr

**Word count:** 3185

**Number of figures and tables:** 7 figures and 1 table

**Number of references:** 28

**Keywords:** MRI, Virtual Phantom, ViP MRI, IDEAL, fat quantification, phase map.

## Abstract

**Object:** Virtual Phantom Magnetic Resonance Imaging (ViP MRI) is a method to generate reference signals on MR images, using external radiofrequency (RF) signals. The aim of this study was to assess the feasibility of ViP MRI to generate complex-data images of phantoms mimicking water-fat systems.

**Materials and Methods:** Various numerical phantoms with a given fat fraction,  $T_2^*$  and field map were designed. The k-space of numerical phantoms was converted into RF signals to generate virtual phantoms. MRI experiments were performed at 4.7 T using a multi-gradient-echo sequence on virtual and physical phantoms. The data acquisition of virtual and physical phantoms was simultaneous. Decomposition of the water and fat signals was performed using a complex-based water-fat separation algorithm.

**Results:** Overall, a good agreement was observed between the fat fraction,  $T_2^*$  and phase map values of the virtual and numerical phantoms. In particular, fat fractions of  $10.5 \pm 0.1$  (vs 10% of the numerical phantom),  $20.3 \pm 0.1$  (vs 20%) and  $30.4 \pm 0.1$  (vs 30%) were obtained in virtual phantoms.

**Conclusion:** The ViP MRI method allows for generating imaging phantoms that i) mimic water-fat systems and ii) can be analyzed with water-fat decomposition algorithms based on complex data.

---

## Introduction

Virtual Phantom Magnetic Resonance Imaging (ViP MRI) is a method to generate reference signals on MR images, without using physical objects [1]. This method represents the extension of the 'Electronic REference To access In vivo Concentrations' (ERETIC) method [2], largely used in spectroscopy [3-7], to MRI. ViP MRI works as follows: first, a numerical MRI phantom is designed and its k-space representation is calculated; then, the k-space lines are entered into a waveform generator that converts the k-space lines into radiofrequency (RF) signals (the ViP signal); lastly, the ViP signal is transmitted to the MRI scanner by an RF coil (the ViP coil). The MRI scanner acquires the ViP signal simultaneously with the signal from the object of interest and, as a result, an MR image of the object of interest and the virtual phantom is obtained.

As a first validation of the ViP MRI method, an analysis of the MR magnitude images of virtual phantoms was performed, in order to test ViP signal reliability and stability [1]. On the other hand, MR images are intrinsically complex data with a real and imaginary part or, equivalently, with a magnitude and phase. In the study that introduced the ViP MRI method, no investigation concerning the MR phase images originating from the virtual phantom was conducted. It is well known that the phase is more sensitive than the magnitude to experimental bias/misadjustments, especially in scenarios where timings play an important role. The ViP method relies on the synchronization between the ViP k-space signal and the receiver acquisition window of the MRI scanner. Thus, it is mandatory to test experimentally whether it is possible to generate a ViP MR image with a given magnitude as well as with a given phase. In other words, can the ViP MRI method be used to generate reference signals with both a known magnitude and phase?

The magnitude and phase information of the MR images is exploited in complex-based water-fat separation algorithms. [8]. To apply the ViP MRI method to fat quantification (Fat ViP MRI), it is necessary to generate a ViP signal that represents multiple chemical species, with each species being characterized by an amplitude, a chemical shift and a  $T_2^*$  relaxation time. In the previous work on the ViP MRI method, only signals of one chemical species (water) were tested, in order to generate reference signals mimicking agar gel signals. In the current work, we sought to employ the ViP MRI method to generate reference signals similar to those of physical phantoms, such as fat emulsions, that contain two chemical species (water and fat).

Thus, the overall aim of the current study was to apply the ViP MRI method to water-fat decomposition algorithms that are based on complex-data image analysis. To this aim, it was necessary to assess the feasibility of generating: i) reference signals with both a known magnitude

and phase and ii) reference signals from two chemical species, each with a given chemical shift, amplitude and  $T_2^*$  relaxation time, so to mimic a water-fat system.

MRI experiments were performed using a multi-gradient-echo sequence on virtual and physical phantoms. Decomposition of the water and fat signals was conducted using the magnitude and phase images with a complex-based water-fat separation algorithm.

## Materials and methods

### ViP MRI method

The scheme of the Fat ViP MRI method is illustrated in Figure 1.

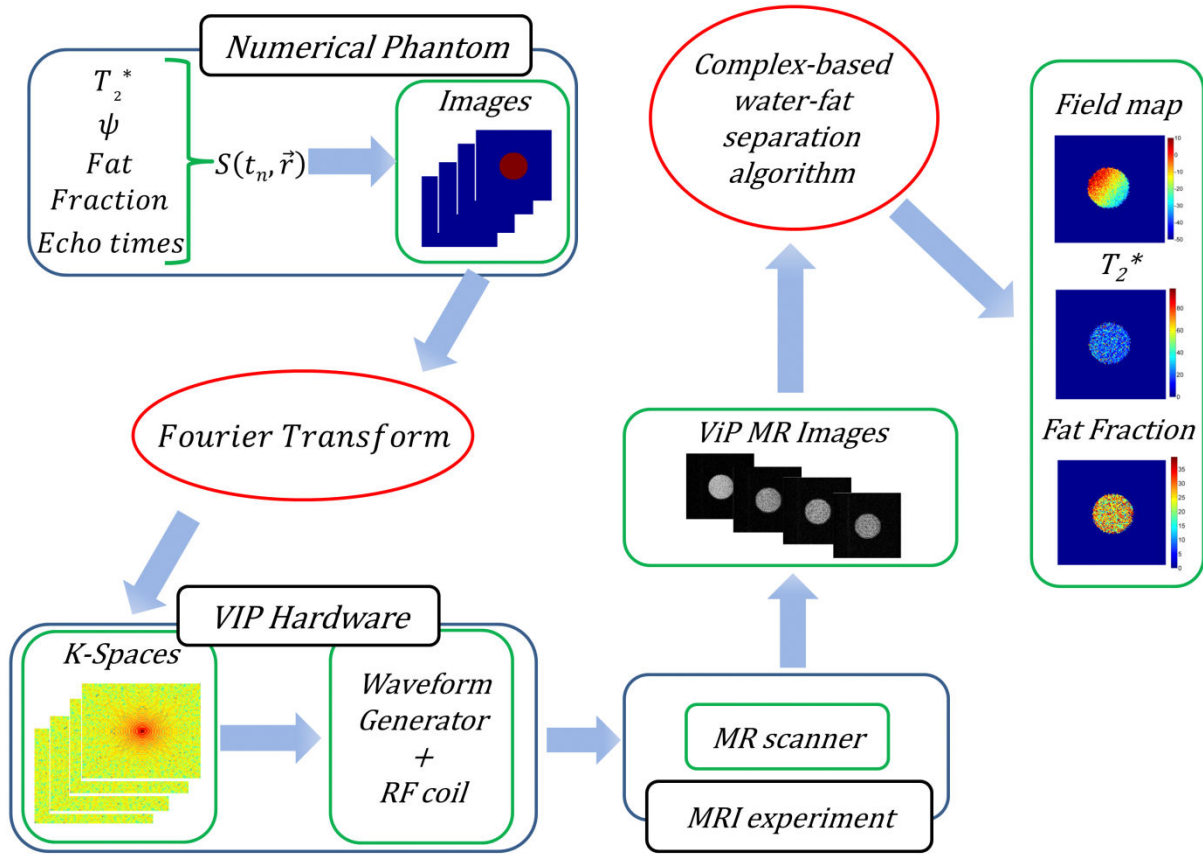


**Figure 1.** Scheme of the Virtual Phantom (ViP) MRI method applied to a complex-based water-fat separation algorithm.

A program in Matlab (MathWorks, Natick, MA, USA) that allows for simulation of MR signals was elaborated with the following signal model [9]:

$$S(t_n, \vec{r}) = \left[ \rho_W(\vec{r}) + \rho_F(\vec{r}) \sum_{i=1}^7 \alpha_i e^{i2\pi\Delta f_i t_n} \right] e^{i2\pi\psi(\vec{r})t_n} e^{-t_n/T_2^*(\vec{r})}$$

where  $S$  is the signal,  $t_n$  represents the  $n$ -th echo time,  $\vec{r}$  the spatial position,  $\rho_W$  and  $\rho_F$  the amplitude of the water and the fat signal, respectively,  $T_2^*$  the transverse relaxation time,  $\psi$  the magnetic field inhomogeneity,  $\Delta f_i$  the frequency shift of the  $i$ -th fat peak with respect to the water peak and  $\alpha_i$  the relative fat signal amplitude of the  $i$ -th peak ( $\sum_{i=1}^7 \alpha_i = 1$ ). The values of  $\Delta f_i$  and  $\alpha_i$  were taken from literature [10]. The fat fraction is defined as  $\rho_F/(\rho_F + \rho_W)$ . This program was

designed to generate images of disk-shaped phantoms of a given radius, where the signal intensity of the phantom is given by the aforementioned equation. Thus, disk-shaped numerical phantoms with a given fat fraction and  $T_2^*$  can be generated and a field map of arbitrary shape can be integrated into the image by using the  $\psi(\vec{r})$  field inhomogeneity parameter. As indicated in the scheme of Figure 1, the numerical phantom is then converted to its k-space representation, with the k-space center normalized to the value of 1. The k-space representation (amplitude and phase) is used as input to the waveform generator (Redstone, Tecmag Inc., Houston TX, USA). A homemade 15mm diameter RF coil (the ViP coil) was connected to the waveform generator and positioned inside the scanner bore. The waveform generator and the ViP RF coil constituted the ViP hardware (Figure 1).

The k-space lines, in form of a radiofrequency signal (ViP signal), were transmitted to the MR scanner by the ViP coil to generate MR images of the virtual phantom. The RF unblinking signal from the MR scanner was used to synchronize the waveform generator with the analog-to-digital converter of the MR scanner. In each experiment, the waveform transmitter gain was adjusted to obtain a range of values of the ViP signal intensity similar to that obtained from physical phantoms. The MR scanner receiver coil recorded the ViP k-space signal, played line-by-line, simultaneously with the signal from the physical phantom. The ViP signal was sent to the scanner bore with the same carrier frequency of the MR scanner (200MHz).

Three different scenarios were investigated. In all cases, four multi-echo images ( $t_n = 1.5, 4, 6.5$  and  $9\text{ms}$ ) of matrix size equal to  $128 \times 128$  were generated, with a  $T_2^*$  relaxation time of water and fat equal to  $20\text{ms}$ . For each scenario, specific numerical phantoms were created and served as an input to the ViP hardware.

In the first study, a disk-shaped numerical phantom of 24-pixel radius, with a fat fraction equal to 20% was generated. In the signal equation of this numerical phantom, a field map in the form of a plane with slope of  $45^\circ$  was considered. This numerical phantom was used to investigate the overall aim of the current work, that is, to test the feasibility of the ViP MRI method to generate complex-data images of phantoms mimicking water-fat systems.

In the second study, a phantom with a radius (48-pixels) larger than the first phantom was generated in order to achieve a better visualization of the field map. The 48-pixel radius phantom covered most of the field of view (FOV) of the  $128 \times 128$  image. This phantom was used to test the feasibility of reproducing field maps of different shapes. In particular, two field maps were simulated: a field map in the form of a plane (slope equal to  $45^\circ$ ) and a field map in the form of a 2D parabola with vertex in the center of the matrix.

In the third study, the numerical phantom consisted of three small disk-shaped phantoms. These three phantoms were located at the borders of the FOV so that they could be used in a real case scenario, where the object of interest is typically located in the center of the image and the reference phantom at the borders of the FOV. These three phantoms were generated with different fat fractions (10%, 20% and 30%). In this third experiment, a physical phantom (diary cream) was also positioned in the scanner bore and MR images of the virtual and physical phantom were simultaneously acquired.



### ***MRI experiments***

MRI experiments were performed on a 4.7T MR scanner (47/40 Biospec, Bruker, Wissembourg, France) using an RF volume coil (72mm inner-diameter) as a transmitter/receiver. In all measurements, a multi-gradient-echo sequence was used with dwell time =  $6.6\mu\text{s}$ , matrix size =  $128 \times 128$ , repetition time (TR) = 100ms and the same echo times used for generating the numerical phantoms (TE = 1.5, 4, 6.5 and 9ms). In one experiment (the third scenario) a physical phantom was positioned in the MRI scanner bore and the following pulse-sequence parameters were modified: TR = 500ms, FOV = 4cm, slice thickness = 4mm and flip angle =  $40^\circ$ . The physical phantom was a 15-ml cylindrical tube filled with dairy cream, a readily accessible substance that was used here as reference of a water/fat system.

Data analysis was performed with a homemade script in Matlab, which implements the IDEAL algorithm for decomposition of the water and fat signals using complex images. The images of the numerical phantom (that is, the images generated by the program in Matlab that allows for simulating MR signals) and the images the virtual and physical phantoms (that is, the MR images acquired with the MRI scanner) were processed with IDEAL to obtain pixel-by-pixel maps of fat fraction,  $T_2^*$  and field inhomogeneity.

## Results

### *First study*

Multi-gradient-echo magnitude images of a virtual phantom (24-pixel radius) acquired at four echo times are shown in Figure 2.

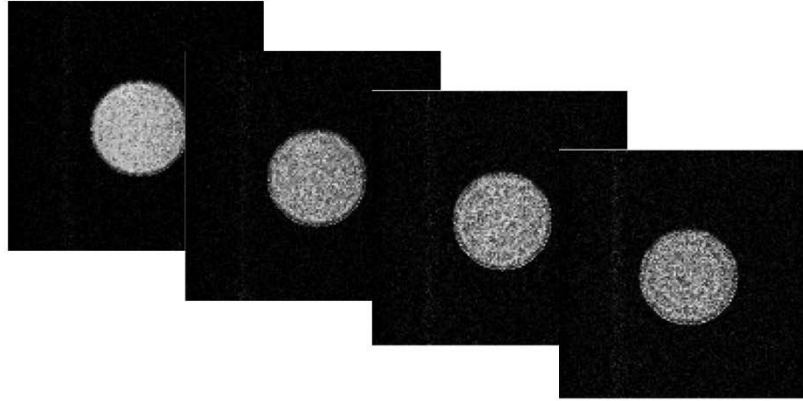


**Figure 2.** Multi-gradient-echo images of a disk-shaped virtual phantom acquired at 4 echo times (1.5, 4, 6.5 and 9ms). This virtual phantom was designed to mimic a water-fat system, with a fat fraction equal to 20% and a  $T_2^* = 20\text{ms}$ .

This virtual phantom was designed to mimic two chemical species (water and 20% fat), with a value of  $T_2^* = 20\text{ms}$  and a planar field map. Complex images were analyzed with the water-fat separation algorithm and in Figure 3, the output for the numerical and virtual phantom is shown. Data processing of the numerical phantom (top row) yielded a value of  $T_2^*$  and fat fraction equal to 20ms and 20%, respectively, and a planar field map. Data processing of the MR images of the virtual phantom (bottom row) yielded a value of  $T_2^*$  and fat fraction equal to  $23.7 \pm 0.5\text{ms}$  and  $21.9 \pm 0.2\%$ , respectively. The reconstructed field map of the virtual phantom well reproduced the plane-like shape of the numerical field map.

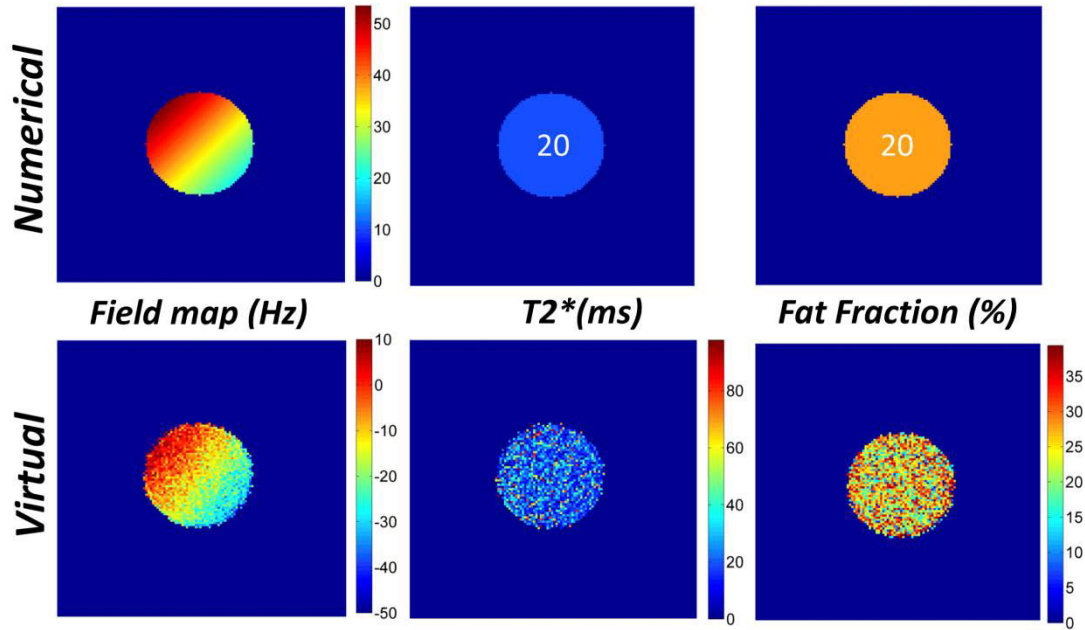


**Figure 3.** The output of water-fat separation algorithm for a numerical (top row) and virtual (bottom row) phantom. The virtual phantom shown here is the same as the one of Figure 2. The output of its corresponding numerical phantom is illustrated here as a reference. The planar field map (first column) of the numerical phantom is well reproduced by the virtual phantom. A good agreement between the  $T_2^*$  (second column) and fat fraction (third column) maps of the numerical and virtual phantom is also noticeable.

### Second study

In order to achieve a better visualization of the field maps, a large disk-shaped phantom (48-pixel radius) was generated and two experiments were performed, with field maps of two different shapes (planar and parabolic). Artifacts in the form of lines were noticeable in the field maps of the virtual phantoms (Figure 4, bottom); in particular, these artifacts were more visible in the planar field map (Figure 4, bottom left). Overall, the planar field map of the virtual phantom (Figure 4, bottom row, left) was similar to that of the numerical phantom (Figure 4, top row, left). The values of the virtual phantom field map, evaluated along the direction of the steepest descent of the plane, displayed an excellent linearity (coefficient of determination  $r^2 = 0.990$ ). The slope coefficient was  $1.096 \pm 0.014$  Hz/pixel vs 1 Hz/pixel for the numerical phantom. The range of field values was  $\sim 70$ Hz vs 67Hz for the numerical phantom. A good agreement was also observed between the parabolic field map of the virtual phantom (Figure 4, bottom row, right) and that of the numerical phantom (Figure 4, top row, right). The field map values were evaluated along an image profile corresponding to the intersection with a plane that contains the axis of symmetry of the parabola. The quadratic fit applied to the virtual phantom data yielded the quadratic coefficient value of  $0.049 \pm 0.001$  Hz/pixel

vs 0.05 Hz/pixel in the numerical phantom, with coefficient of determination  $r^2 = 0.986$ . The range of field map values in the virtual phantom was  $\sim 120\text{Hz}$  vs  $115\text{Hz}$  in the numerical phantom.

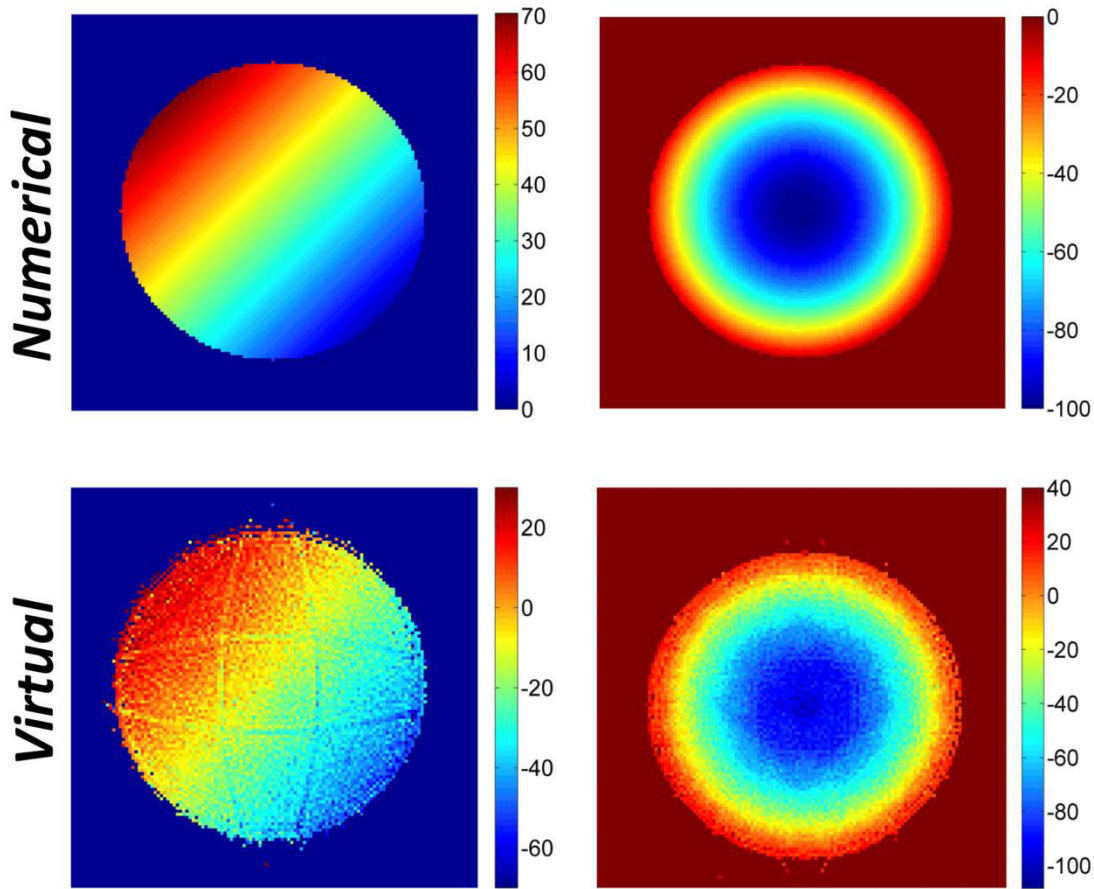


**Figure 4.** Example of two field maps (planar, left column; parabolic, right column) obtained with the ViP MRI method. As a reference, the field maps the numerical phantom are also illustrated (top row). The fields maps calculated from the MR images of the virtual phantom (bottom row) are in good agreement with those of the corresponding numerical phantom (top row).

### Third study

Figure 5 shows the results of the experiment performed on a physical phantom containing dairy cream and three virtual phantoms. Similarly to the previous experiments, the water-fat separation algorithm was applied to multi-gradient-echo images acquired at four TEs. In the numerical phantom, the reconstruction yielded a value of  $T_2^* = 20\text{ms}$ , fat fraction equal to 10, 20 and 30% and a constant-value field map (Figure 5, top row). Similar values were obtained for the  $T_2^*$ , fat fraction and field maps of the virtual phantoms (Figure 5, bottom row). In Table 1, the values of  $T_2^*$  and fat fraction relative to the physical and virtual phantoms are shown. Overall, an excellent agreement between the fat fraction values of the virtual and numerical phantoms was observed. The  $T_2^*$  values

of the virtual phantoms were similar to that of the numerical phantom ( $T_2^* = 20\text{ms}$ ), with the exception of the 20% fat-fraction virtual phantom.

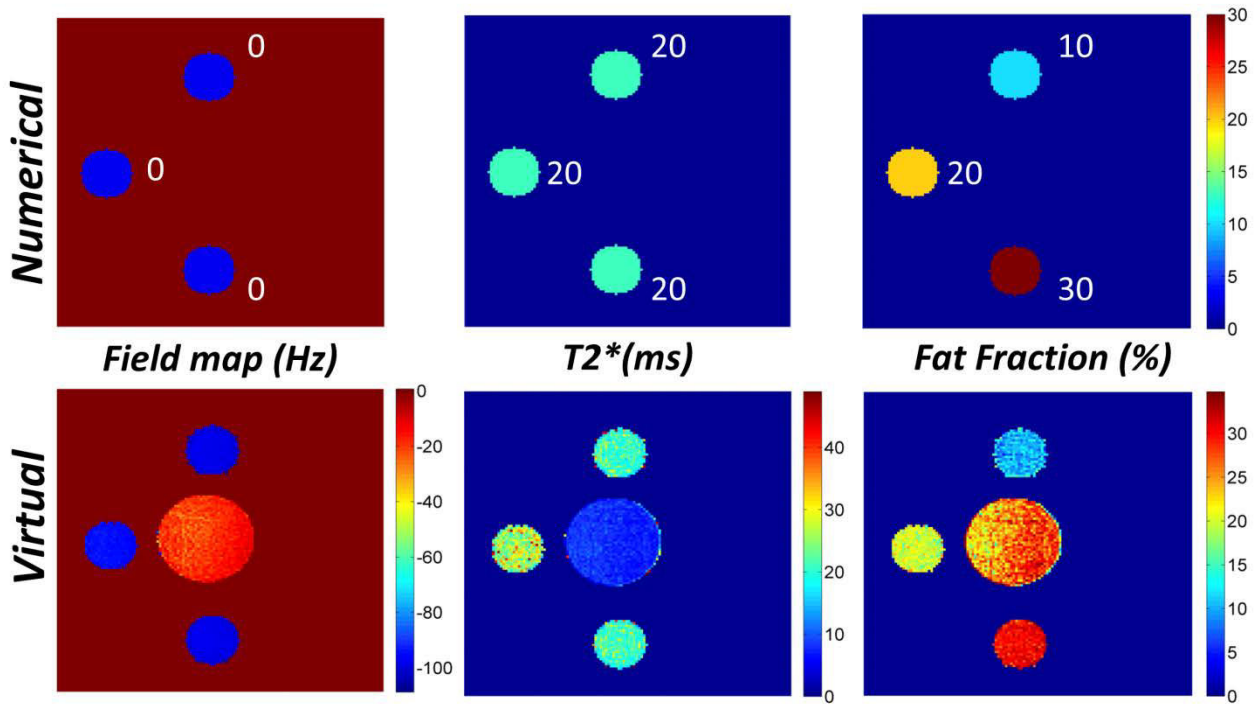


**Figure 5.** The output of the water-fat separation algorithm of the numerical (top row) and virtual + physical phantoms (bottom row). The physical phantom is a 15-ml cylindrical tube filled with dairy cream, positioned in the center of the field of view. The three virtual phantoms, located around the physical phantom, are designed with a  $T_2^* = 20\text{ms}$  and different fat fractions (10%, 20% and 30%). A good agreement between the numerical and virtual phantom is observable.

To determine the origin of the artifacts observed in Figure 4, where four lines crossing the field maps were noticeable, an additional investigation was performed. The results of the MR experiments and simulations are illustrated with magnitude images in Figure 6. A large disk-shaped phantom was designed. As in all previous experiments, the numerical phantom was generated in 32 bits (Figure 6, left). A ViP MR experiment was performed using this numerical phantom and artifacts similar to those of the field maps of Figure 4 were observed (Figure 6, center). The k-space of the numerical phantom was then discretized to different bit values and, for each discretization value, a simulated image was generated by Fourier transform of this k-space. When the k-space of the numerical phantom was discretized to 7 bits, the corresponding image (Figure 6, right) displayed artifacts similar to those of the ViP MR image acquired on the scanner (Figure 6, center).

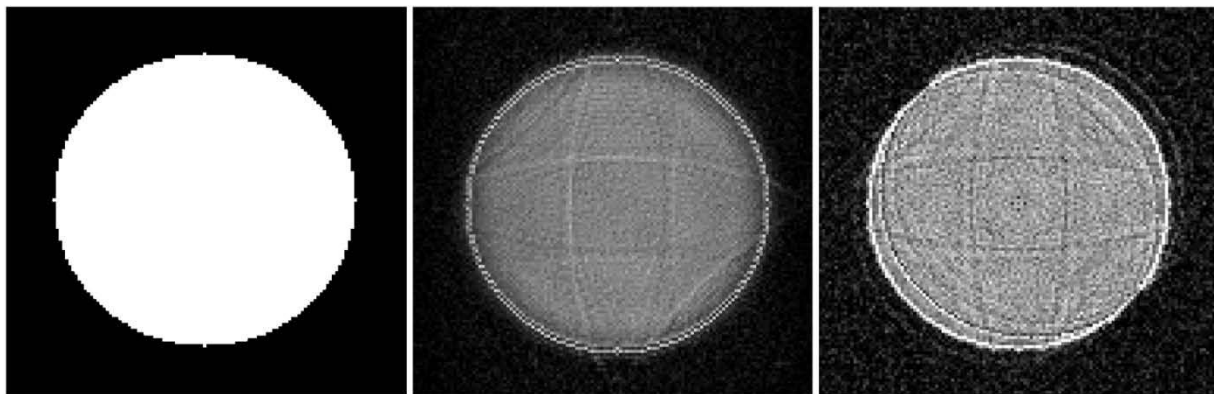


**Figure 6.** The effect of the  $k$ -space discretization on magnitude images in a large disk-shaped phantom. The 32-bit to 7-bit numerical phantom (left) and the ViP MR image, generated using the 32-bit numerical phantom (right), are shown. The 7-bit discretization of the numerical  $k$ -space yields the same artifacts as those observed in the ViP MR image. The discretization of the ViP  $k$ -space occurs in the waveform generator.

---

## Discussion

The application of the ViP MRI method to water-fat signal decomposition using complex images was here investigated. First, the results of the current study indicate that ViP MRI allows for generating reference signals (i.e., imaging phantoms) with a well-defined magnitude and phase. It should be noted that in the previous validation study of the ViP MRI method only the magnitude of the signal was investigated [1]. In the current study, different phase-map patterns were tested and an excellent agreement between the simulated and experimental phase maps was observed.

Secondly, it was shown here the ViP MRI method is not restricted to mimicking a single chemical species: various virtual phantoms were designed to mimic phantoms such as fat emulsions, which contain two chemical species (water and fat). MR images of virtual phantoms with different fat percentages were acquired. A good agreement was observed between the simulated and experimental fat fraction values, that is, between the fat fraction values of the numerical and virtual phantoms. In a previous study, the ViP MRI method was employed to mimic agar gel signals. Since the beginning of MRI, agar gels have been extensively investigated (and then used over the years) to provide reference signals in MR experiments [11-12]. On the other hand, agar gels cannot reproduce signals originating from tissues containing both water and fat components, so other phantoms are employed for mimicking this scenario. Emulsions composed of oil and water [13-14] and dairy creams [15-17] are among the most commonly-employed reference phantoms for mimicking water/fat systems or, in general, two-compartment models. The Fat ViP MRI method could be of interest for replacing these physical phantoms when performing an MR experiment.

Given the growing interest in the simultaneous measurement of fat content and  $T_2^*$  relaxation time, the transverse relaxation decay was also included into the signal model [9]. As matter of fact, both fat content and  $T_2^*$  are useful biomarkers, in particular with respect to liver pathologies: a fat content greater than 5% is indicative of liver steatosis [18] and  $T_2^*$  values can be used to determine liver iron overload [19]. As a result, in the last decade there has been a substantial development of MR quantitative approaches for simultaneous fat and  $T_2^*$  quantification. In this context, reference phantoms that simulate water-fat systems, including  $T_2^*$  relaxation effects, could be useful for development, testing and improvement of novel signal decomposition algorithms [20-22].

All MRI experiments were performed using a multi-gradient-echo sequence and data analysis was conducted with a complex-based water-fat separation algorithm. In particular, numerical phantoms were generated at four echo-time values, four multi-gradient-echo images were acquired on the MR scanner and used for water-fat separation algorithm.. However it should be noted that the Fat ViP

MRI method as proposed here has no limitation with respect to the number of echoes, that is, it can be directly extended to include a higher number of echoes. With an increased number of echoes, for instance, the estimation of  $T_2^*$  can be also improved [9].

Virtual phantoms that covered a large part of the FOV were generated to aid in the visualization and quantification of the phase maps. These ViP MR images displayed an unusual and unexpected artifact. Different hypotheses were considered. The most appropriate one was that the origin of this artifact was related to the discretization of the ViP k-space signal that was sent into the MRI scanner by the waveform generator. To test the validity of this hypothesis, a numerical phantom was generated in 32 bits and its k-space was converted to lower number-of-bit representations. The image obtained by the Fourier transform of the 7-bit k-space displayed the same artifact as the image of the virtual phantom acquired by the MR scanner. Thus, the origin of the artifact is to be found in the limited dynamic range of the waveform generator. In phantom of smaller size (such as the single disk-shaped phantom show in Figure 3), this artifact was not present, as the total signal did not reach the levels that would result in this k-space discretization problem. As a consequence, this type of artifact would not occur in a typical application of the ViP MRI method, since usually the dimensions of the reference phantoms are much smaller than the FOV of the image.

One of the main results of the current study is the excellent agreement between the simulated and experimental phase maps (Figure 4). The ability to generate virtual phantoms with a given phase, so to provide a phase reference value on an MR image, might be of interest not only to the water-fat decomposition techniques, but also to other techniques that exploit the phase information of the MR images [23-26]. It should be also noted that one interesting feature of the ViP method is that the ViP signal is transparent to the spatial encoding. Thus with a fixed matrix size, when changing the dimension of the FOV the virtual phantom keeps the same position and shape. This might be useful in real case scenario, where the FOV need to be adjusted to the patient size. Furthermore, the ViP method as proposed here can be applied to other chemical-shift encoded MRI scenarios, such the three species system water-fat-silicone.

To date, only a handful of studies have been focussed on the development of reference signals in imaging [1, 27-28]. The main difference between ViP MRI [1] and previously proposed approaches [27-28] is that in ViP MRI no hardware or software components of the MR scanner (with the exception of a trigger signal) are used for generating the signal of the virtual phantom. Thus ViP MRI can be performed on MRI scanners of different types and vendors, since the ViP hardware/software is a self-contained unit, independent of the MRI scanner hardware/software.



## References

- [1] Saint-Jalmes H, Eliat PA, Bezy-Wendling J, Bordelois A, Gambarota G. ViP MRI: virtual phantom magnetic resonance imaging. *Magn Reson Mater Phys* 2013;27:419-24.
- [2] Barantin L, Le Pape A, Akoka S. A new method for absolute quantitation of MRS metabolites. *Magn Reson Med* 1997;38:179-82.
- [3] Michel N, Akoka S. The application of the ERETIC method to 2D-NMR. *J Magn Reson* 2004;168:118-23.
- [4] Martinez-Bisbal MC, Monleon D, Assemat O, Piotto M, Piquer J, Llacer JL, et al. Determination of metabolite concentrations in human brain tumour biopsy samples using HR-MAS and ERETIC measurements. *NMR Biomed* 2009;22:199-206.
- [5] Albers MJ, Butler TN, Rahwa I, Bao N, Keshari KR, Swanson MG, et al. Evaluation of the ERETIC method as an improved quantitative reference for <sup>1</sup>H HR-MAS spectroscopy of prostate tissue. *Magn Reson Med* 2009;61:525-32.
- [6] Ziarelli F, Viel S, Sanchez S, Cross D, Caldarelli S. Precision and sensitivity optimization of quantitative measurements in solid state NMR. *J Magn Reson* 2007;188:260-6.
- [7] Heinzer-Schweiser S, De Zanche N, Pavan M, Mens G, Sturzenegger U, Henning A, et al. In-vivo assessment of tissue metabolite levels using <sup>1</sup>H MRS and the Electric REference To access In vivo Concentration (ERETIC) method. *NMR Biomed* 2010;23:406-13.
- [8] Reeder SB, Wen Z, Yu H, Pineda AR, Gold GE, Markl M, et al. Multicoil Dixon chemical species separation with an iterative least-squares estimation method. *Magn Reson Med* 2004;51:35-45.
- [9] Hernando D, Kramer H, Reeder SB. Multiplex fat-corrected complex  $R_2^*$  relaxometry: theory, optimization and clinical validation. *Magn Reson Med* 2013;70:1319–31.
- [10] Hamilton G, Yokoo T, Bydder M, Cruite I, Schroeder ME, Sirlin CB, et al. In vivo characterization of the liver fat <sup>1</sup>H MR spectrum. *NMR Biomed* 2011;24(7):784–90.
- [11] Mathur-De Vre R, Grimee R, Parmentier F, Binet J. The use of agar gel as a basic reference material for calibrating relaxation times and imaging parameters. *Magn Reson Med* 1985;2:176–9.
- [12] Walker P, Lerski RA, Mathur-De Vre R, Binet J, Yane F. Preparation of agarose gels as reference substances for NMR relaxation time measurement. *Magn. Reson. Imaging* 1988;6:215–22.
- [13] Hu HH, Kim HW, Nayak KS, Goran MI. Comparison of Fat–Water MRI and Single-voxel MRS in the Assessment of Hepatic and Pancreatic Fat Fractions in Humans. *Obesity* 2010;18:841–7.
- [14] Hines CD, Yu H, Shimakawa A, McKenzie C.A, Brittain JH, Reeder SB. T1 independent, T<sub>2</sub>\* corrected MRI with accurate spectral modeling for quantification of fat: Validation in a fat-water-SPIO phantom. *J Magn Reson Imaging* 2009;30:1215–22.
- [15] Jones C, MacKay C, Rutt B. Bi-Exponential T<sub>2</sub> Decay in Dairy Cream Phantoms. *Magn Reson Imaging* 1998;16:83–5.

- [16] Ababneh Z, Haque M, Maier SE, Mulkern RV. Dairy cream as a phantom material for biexponential diffusion decay. *Magn Reson Mater Phys* 2004;17:95-100.
- [17] Janiczek RL, Gambarota G, Sinclair CD, Yousry TA, Thornton JS, Golay X, et al. Simultaneous  $T_2$  and lipid quantitation using IDEAL-CPMG. *Magn Reson Med* 2011;66(5):1293-302.
- [18] Kleiner DE, Brunt EM, Van Natta M, Behling C, Contos MJ, Cummings OW, et al. Design and validation of a histological scoring system for nonalcoholic fatty liver disease. *Hepatology* 2005; 41:1313–21.
- [19] Gandon Y, Olivie D, Guyader D, Aubé C, Oberti F, Sebille V, et al. Non-invasive assessment of hepatic iron stores by MRI. *Lancet* 2004;363(9406):357-62.
- [20] Bydder M, Yokoo T, Hamilton G, Middleton MS, Chavez AD, Schwimmer JB, et al. Relaxation effects in the quantification of fat using gradient echo imaging. *Magn Reson Imaging* 2008; 26(3):347-59.
- [21] Zhong X, Nickel MD, Kannengiesser SA, Dale BM, Kiefer B, Bashir MR. Liver fat quantification using a multi-step adaptive fitting approach with multi-echo GRE imaging. *Magn Reson Med* 2014; 72(5):1353-65.
- [22] Chebrolu VV, Hines CDG, Yu H, Pineda AR, Shimakawa A, MacKenzie CA, et al. Independent estimation of  $T_2^*$  for water and fat for improved accuracy of fat quantification. *Magn Reson Med* 2010; 63: 849-57.
- [23] Ishihara Y, Calderon A, Watanabe H, Okamoto K, Suzuki Y, Kuroda K, et al. A precise and fast temperature mapping using water proton chemical shift. *Magn Reson Med* 1995;34:814–23.
- [24] O'Donnell M. NMR blood flow imaging using multiecho, phase contrast sequences. *Med Phys* 1985;12(1):59-64.
- [25] Bernstein MA, Ikezaki Y. Comparison of phase-difference and complex-difference processing in phase-contrast MR angiography. *J Magn Reson Imaging* 1991;1(6):725-9.
- [26] Bretthorst LG. Automatic phasing of MR images. Part I: linearly varying phase. *J Magn Reson* 2008;191(2):184-92.
- [27] Franconi F, Chapon C, Lemaire L, Lehmann V, Barantin L, Akoka S. Quantitative MR renography using a calibrated internal signal (ERETIC). *Magn Reson Imaging* 2002;20(8):587-92.
- [28] Lee D, Marro K, Shankland E, Mathis M. Quantitative  $^{19}\text{F}$  imaging using inductively coupled reference signal injection. *Magn Reson Med* 2010;63(3):570-3.



## **Appendix E**

**Article accepted in “Applied Magnetic Resonance”**



# MRI-Based Direct Measurements of the T2\* Transverse Relaxation Time of Water and Lipid Protons in Water–Lipid Mixtures

Roberto Salvati<sup>1,2</sup> · Giulio Gambarota<sup>1,2</sup>

Received: 4 August 2015  
© Springer-Verlag Wien 2015

**Abstract** Magnetic resonance imaging (MRI) has emerged as the method of choice for in vivo quantification of lipids. The MRI methods originally proposed for lipid quantification did not take into account for the loss of signal due to T2\*. In the last decade, a number of algorithms has been introduced for the T2\* correction. These algorithms assumed that the T2\* of the water protons (T2<sub>w</sub>\*) is the same as the T2\* of lipid protons (T2<sub>L</sub>\*). More recent algorithms have proposed a more sophisticated model (dual T2\* correction), which consider different values for T2<sub>w</sub>\* and T2<sub>L</sub>\*. However, no reference values exist for validating the values of T2<sub>w</sub>\* and T2<sub>L</sub>\* obtained by these algorithms in tissues or phantoms where water and lipid protons co-exist. In the current work, we propose a direct measurement of T2<sub>w</sub>\* and T2<sub>L</sub>\* in phantoms consisting of water–lipid mixtures. MR multi-gradient-echo images were acquired with a low receiver bandwidth/pixel with the aim of separating the water and lipid signals. In all phantoms, T2<sub>L</sub>\* (range 7.6–10.7 ms) was significantly shorter than T2<sub>w</sub>\* (range 48.9–57.4 ms). The proposed method provides the ground truth values of T2<sub>w</sub>\* and T2<sub>L</sub>\* for development, validation, and optimization of lipid quantification methods based on dual T2\* correction.

## 1 Introduction

In the last decade, there has been an exceptional effort by the bioimaging scientific community in developing methods for the quantification of lipids in vivo. These methodological developments have been fuelled by the worldwide problem of obesity, which is currently at epidemic proportions with more than 1.3 billion adults

---

✉ Roberto Salvati  
roberto.salvati@univ-rennes1.fr

<sup>1</sup> Present Address: UMR 1099, INSERM, 35000 Rennes, France

<sup>2</sup> Université de Rennes 1, LTSI, 35000 Rennes, France

overweight and over 600 million adults obese [1]. Nowadays, obesity is causing an increasing morbidity and mortality connected with diseases such as type 2 diabetes, dyslipidemia, and non-alcoholic fatty liver disease [2]. Among the different approaches for the quantification of lipids, magnetic resonance imaging (MRI) has emerged as the method of choice. The main advantages of MRI versus other established techniques—such as biopsies and computed tomography (CT)—are that MRI is not invasive and does not use ionizing radiation, so repeated measurements can be safely performed in longitudinal studies.

In general, MRI methods for lipid quantification are based on the principle of chemical shift imaging [3]. In other words, these MRI methods exploit the fact that water protons precess at a different frequency than lipid protons, the difference (i.e., the chemical shift) being 3.5 parts-per-million (ppm). Thus, in gradient echo sequences, the water and lipid protons are in phase with each other at certain echo times ( $TE = 0, 1.4, 2.8$  ms at 4.7 T, for example) whereas at other  $TE$ s ( $TE = 0.7, 2.1, 3.5$  ms at 4.7 T) the water and lipid protons are  $180^\circ$  out of phase with each other. In one of the first methods proposed for lipid quantification (the Dixon's method [3]), the lipid content was obtained using the “in-phase” and “out-of-phase” MR images.

MRI methods for lipid quantification have been steadily improved over the years to yield a more accurate measurement of lipid content, with literally hundreds of studies performed worldwide. Among the major improvements, the correction for the loss of signal due to transverse relaxation decay ( $T2^*$ ) is of particular relevance. As matter of fact, the Dixon's method as originally proposed did not take into account for the loss of signal due to  $T2^*$  decay when measuring the lipid content with gradient echo images. With the aim of correcting the measure of the lipid content for  $T2^*$  decay, a number of algorithms were introduced over the years. Nevertheless, these algorithms assumed that the  $T2^*$  of the water protons is the same as the  $T2^*$  of lipid protons; thus, these methods are typically referred to as ‘single  $T2^*$ ’ correction methods [4]. It should be noted that these correction methods also allow for the quantification of  $T2^*$ , and thus, they provide an additional biomarker of interest in clinical settings. Specifically, the knowledge of  $T2^*$  is important in the case of liver pathologies, for assessing liver iron overload [5].

Very recently, a handful of studies have proposed a further refinement of the model for lipid quantification [6–10]. The main idea is the following: since the  $T2^*$  of the water protons might differ from the  $T2^*$  of lipid protons, a more appropriate correction algorithm should include two separate  $T2^*$  values, one for the water protons ( $T2_w^*$ ) and the other for the lipid protons ( $T2_L^*$ ). These methods are typically referred to as ‘dual  $T2^*$ ’ correction methods. However, as pointed out by the same authors, the performance of dual  $T2^*$  models ‘remains controversial,’ since it increases the model instability related to the higher number of degrees of freedom [8, 9].

Furthermore, the problem with dual  $T2^*$  methods is exacerbated by the fact that there are no reference values for the  $T2^*$  of water protons and  $T2^*$  of lipid protons. In other words, dual  $T2^*$  methods provide in output: i) the value of lipid content, which can be compared with a reference value obtained by other techniques, and ii)

the value of  $T2_w^*$  and  $T2_L^*$ , which however cannot be compared to any reference value. It is straightforward to measure with a gradient echo sequence the  $T2^*$  of a single chemical species (water in tissue, for instance), when no other chemical species are present. However, when two chemical species (water and lipid, for instance) co-exist in the same pixel, as in the case of liver tissue, a basic multi-gradient echo approach does not allow for measuring the  $T2^*$  of each chemical species. As a consequence, no ground truth value is available to test and validate the dual  $T2^*$  correction methods.

Motivated by these recent developments of dual  $T2^*$  methods and by the challenges involved in validating these methods, we sought a direct measure of  $T2_w^*$  and  $T2_L^*$ , with the aim of providing ground truth values in phantoms. These measurements may be of importance for developing, optimizing, and testing dual  $T2^*$  methods for quantification of lipid content and  $T2^*$  values.

## 2 Materials and Methods

### 2.1 Theory

The MR signal of a water–lipid system can be modeled as follows:

$$S(t_n) = \left[ \rho_W + \rho_L \sum_{i=1}^7 \alpha_i e^{i2\pi\Delta f_i t_n} \right] e^{i2\pi\psi t_n} e^{-t_n/T2^*},$$

where  $S$  is the signal,  $t_n$  the  $n$ th echo time,  $\rho_W$  and  $\rho_L$  the amplitudes of the water and the lipid signal, respectively,  $T2^*$  the transverse relaxation time,  $\psi$  the magnetic field inhomogeneity,  $\Delta f_i$  the frequency shift of the  $i$ th lipid peak with respect to the water peak, and  $\alpha_i$  is the relative lipid signal amplitude of the  $i$ th peak ( $\sum_{i=1}^7 \alpha_i = 1$ ). It should be noted that  $\rho_W$ ,  $\rho_L$ ,  $T2^*$ , and  $\psi$  are functions of the spatial position, i.e., may have a different value in different pixels of the image. The lipid content is defined as  $\rho_L/(\rho_L + \rho_W)$ . This model represents a ‘single  $T2^*$ ’ correction model since a common value of  $T2^*$  for water and lipid is considered. In more recent studies, a more sophisticated model, where the  $T2^*$  of water and lipid protons have different values, has been proposed:

$$S(t_n) = \left[ \rho_W e^{-t_n/T2_w^*} + \rho_L e^{-t_n/T2_L^*} \sum_{i=1}^7 \alpha_i e^{i2\pi\Delta f_i t_n} \right] e^{i2\pi\psi t_n},$$

where  $T2_w^*$  and  $T2_L^*$  are the transverse relaxation time of the water and lipid signal, respectively.

### 2.2 Magnetic Resonance Imaging

Magnetic resonance imaging experiments were performed on a 4.7 T horizontal-bore MR scanner (47/40 Biospec, Bruker, Wissembourg, France) using a volume coil (72 mm inner-diameter) as a transmitter/receiver. Three phantoms were



prepared with dairy creams (full, light, and light thick cream) that were bought at a local grocery shop. Each dairy cream was poured into a 15-ml tube.

To calculate the  $T2^*$  of water protons and  $T2^*$  of lipid protons by a direct measurement, MR images were acquired with a low receiver bandwidth/pixel to separate water and lipid signals along frequency encoding direction. Four multi-gradient echo sequences were acquired with the following parameters: 10 echoes, echo spacing = 13.3 ms, repetition time (TR) = 280 ms, flip angle =  $25^\circ$ , matrix size =  $256 \times 256$ , field of view (FOV) =  $4.3 \times 4.3 \text{ cm}^2$ , and receiver bandwidth (BW) = 35 kHz. Each sequence was acquired with a different value of the first echo time (TE = 6.1, 8.1, 10.1, and 12.1 ms, respectively). This would result into an off-set of the sampling echoes, i.e., four shifted multi-gradient echo sequences. The data were combined together to generate a single relaxation decay curve. The goal of combining the data from four shifted multi-gradient echo sequences was to obtain a finer sampling of the relaxation decay curve, in order to improve the  $T2^*$  measurement.

Additional measurements were also performed to measure lipid content and  $T2^*$ , using an established MRI protocol for lipid quantification. MR images were acquired with a multi-gradient echo sequence. Imaging parameter were 10 echoes, first TE = 1.5 ms, echo spacing = 2.5 ms, TR = 30 ms, flip angle =  $5^\circ$ , matrix size =  $128 \times 128$ , FOV =  $4 \times 4 \text{ cm}^2$ , and BW = 140 kHz.

### 2.3 Data Analysis

The curve fitting of data acquired with a low receiver bandwidth was performed to obtain the  $T2^*$  of water protons and  $T2^*$  of lipid protons. For each phantom, three regions of interest (ROIs) were drawn to include separately the signal from water, lipid, and water + lipid. The  $T2^*$  relaxation time values of water, lipid, and water + lipid were calculated by fitting the signal from magnitude images at 40 TEs to a monoexponential function. The curve fitting routine of Matlab (Mathworks, Natick, MA, USA) was employed. Mean and standard deviation values of  $T2^*$  were obtained in water-only, lipid-only, and water + lipid regions of interest. For each curve fitting, the coefficient of determination  $r^2$  was also calculated to assess the goodness of the data fitting.

A somewhat more elaborated data analysis was necessary to determine the lipid content and  $T2^*$  values. A homemade script in Matlab, which implements the single  $T2^*$  IDEAL algorithm for decomposition of the water and lipid signals, was developed [4, 11, 12]. It should be noted that the IDEAL algorithm requires in input complex-valued images. Thus, raw data were reconstructed on the MR console as real and imaginary images and transferred to a separate workstation for the IDEAL decomposition analysis. Pixel-by-pixel maps of lipid content and  $T2^*$  were generated. Three and 10 echoes were used for lipid content and  $T2^*$  measurements, respectively.

## 3 Results

In Fig. 1, the MR image of the three phantoms acquired at the first echo (6.1 ms) of a multi-gradient echo sequence is shown. A shift of five pixels between the water and lipid signals along the frequency encoding direction is noticeable. This shift can

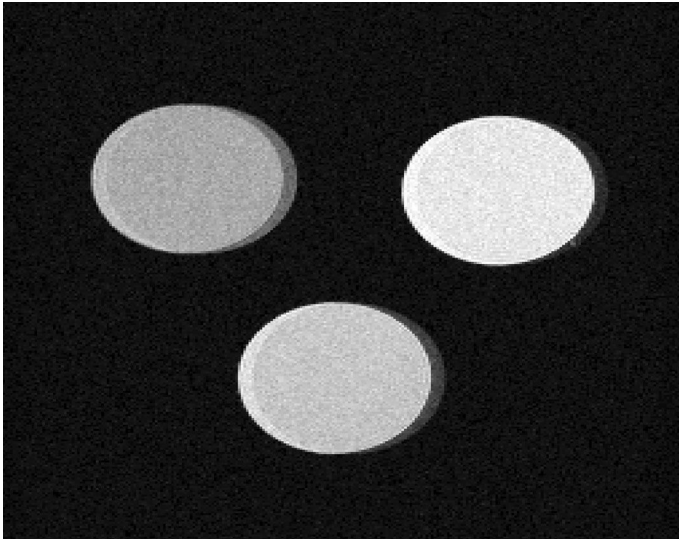


**Fig. 1** MR gradient echo image of the three water–lipid phantoms: full dairy cream (*left*), light dairy cream (*right*), and thick light dairy cream (*bottom*). A chemical shift artifact can be observed along the left–right frequency encoding direction. The receiver bandwidth value was purposely chosen to generate this artifact, in order to detect separately the signal of water and lipid protons

be ascribed to the low receiver bandwidth/pixel and the measured value of five pixels is in agreement with the expected theoretical value of 5.1. In Fig. 2, a detail of Fig. 1 is displayed. Specifically, the MR image of the phantom containing full cream is illustrated. To help the visualization of the separate signals two circles—one for highlighting the water signal (in red) and the second for the lipid signal (in blue)—are drawn. The intersection between these two circles represents the signal originating from water + lipid protons (in purple). The values of the signal calculated in water-only and lipid-only areas of the full cream are plotted as a function of the echo time in Fig. 3. It can be noticed that the lipid signal decays faster than the water signal. The values of T2\* found in lipid-only and water-only regions were  $10.7 \pm 0.8$  and  $57.1 \pm 1.0$  ms, respectively. The values of the signal calculated in the water + lipid area of the full cream are plotted as a function of the echo time in Fig. 4. At short TEs, a scatter of the data points around the curve fitting is noticeable. At longer TEs, this scatter virtually disappears. The value of T2\* found in the water + lipid region was  $57.7 \pm 6.6$  ms.

In Table 1, the results of T2\* measurements for full, light, and light thick cream are shown. In all phantoms, the T2\*s of lipid protons were significantly lower than the T2\*s of water protons. The value of T2\* of water protons in light thick cream was significantly lower than those found in full and light cream. The coefficients of determination relative to the data fitting of the water signal were equal or higher than 0.998. Lower coefficients of determination were found for the lipid signal.

In Fig. 5, the output of the single T2\* IDEAL algorithm—the lipid content (left) and T2\* (right) maps—is displayed. The mean and standard deviation values of lipid content and T2\* were calculated with 15-pixel radius ROIs on each phantom.

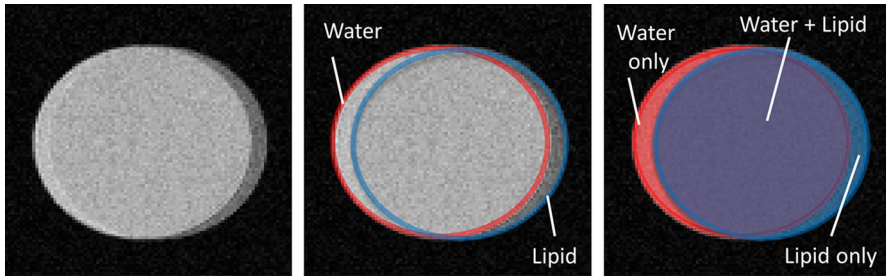


**Fig. 2** Zoom-in of the full dairy cream phantom, which is shown in Fig. 1. In the *center* and *right panel*, two *circles* are drawn on the MR images in order to aid visualization of the separate signal of water and lipid protons

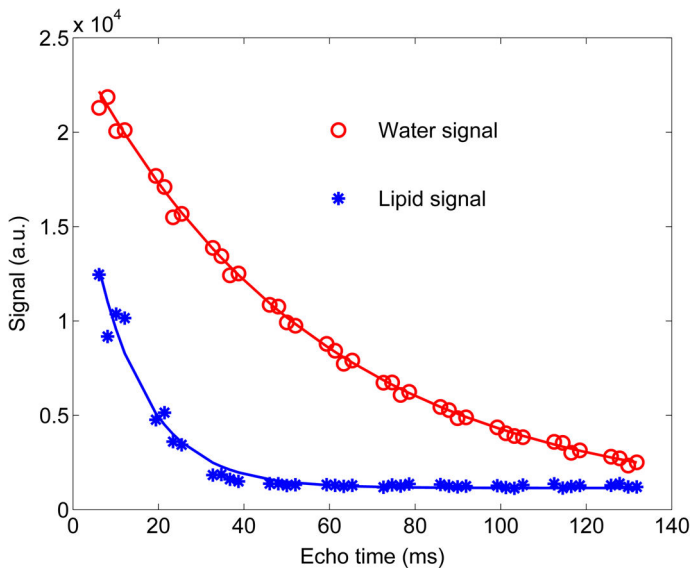


**Fig. 3**  $T_2^*$  relaxation decay of water (symbol 'O') and lipid (symbol '\*') protons in full cream. The *continuous lines* indicate the curve fitting calculated on the water and lipid signals using the monoexponential function. The water signal ( $T_{2_w}^* = 57.1 \pm 1.0$  ms) decays slower than the lipid signal ( $T_{2_L}^* = 10.7 \pm 0.8$  ms)

The values of  $T_2^*$  of full, light, and light thick cream were  $36.4 \pm 2.0$ ,  $54.2 \pm 3.5$ , and  $40.7 \pm 1.9$  ms, respectively. The values of lipid content of full, light, and light thick cream were  $41.2 \pm 2.0$ ,  $18.9 \pm 2.8$ , and  $22.6 \pm 2.7$  %, respectively.

## 4 Discussion

In the current study, a direct measure of the  $T_2^*$  of water protons and the  $T_2^*$  of lipid protons was achieved in dairy cream phantoms, which were chosen here as a model of water–lipid mixtures [13, 14]. Thus, the low-receiver bandwidth

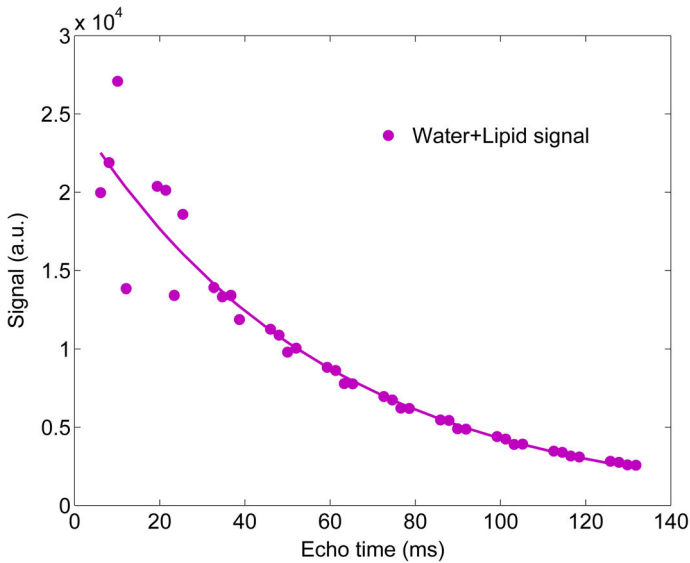


**Fig. 4** T2\* relaxation decay of water + lipid signal in full cream. The *continuous lines* indicate the curve fitting calculated on the water + lipid signal using the monoexponential function. At short TEs, the monoexponential model poorly reproduces the experimental data

**Table 1** Values of T2\* (mean  $\pm$  standard deviation) measured in water-only, lipid-only and water + lipid regions selected on the three phantoms

Phantom	Water T2* (ms)	Lipid T2* (ms)	Water + lipid T2* (ms)
Full cream	57.1 $\pm$ 1.0 [0.998]	10.7 $\pm$ 0.8 [0.992]	56.7 $\pm$ 6.6 [0.924]
Light cream	57.4 $\pm$ 0.9 [0.998]	7.6 $\pm$ 0.9 [0.984]	54.5 $\pm$ 0.8 [0.999]
Light cream (thick)	48.9 $\pm$ 0.7 [0.999]	10.3 $\pm$ 1.5 [0.966]	47.1 $\pm$ 0.9 [0.998]

Below each value of T2\*, the coefficient of determination of the curve fitting is indicated in square brackets

approach—as proposed in the current study—represents a fast and effective method for an unequivocal measurement of T2<sub>w</sub>\* and T2<sub>L</sub>\*.

The knowledge of T2<sub>w</sub>\* and T2<sub>L</sub>\* may prove of value for developing, testing, and optimizing lipid quantification algorithms. As a matter of fact, novel algorithms for lipid quantification have been recently proposed with a dual T2\* correction model. However, while the value of the lipid content (obtained by these algorithms) can be compared to a reference value obtained with other techniques, this is not the case for T2<sub>w</sub>\* and T2<sub>L</sub>\*. In other words, the value of T2<sub>w</sub>\* and T2<sub>L</sub>\* obtained by these algorithms cannot be compared to any reference value. In the current study, we propose the low-receiver bandwidth approach to directly measure T2<sub>w</sub>\* and T2<sub>L</sub>\* in phantoms so to provide the ground truth values of T2<sub>w</sub>\* and T2<sub>L</sub>. As a result, T2<sub>w</sub>\* and T2<sub>L</sub>\* values obtained by the algorithms can be validated versus ground truth values.

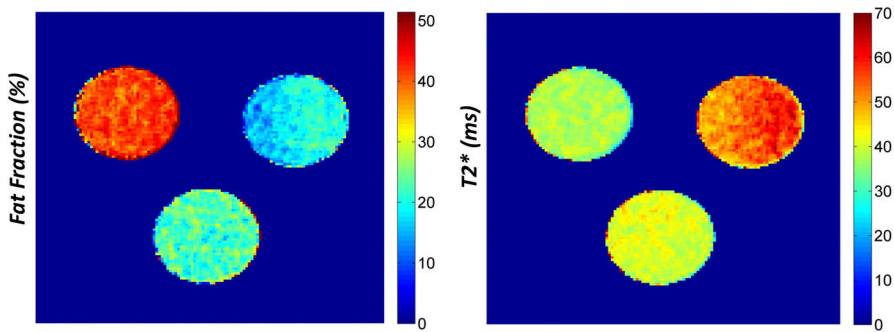


**Fig. 5** Single  $T2^*$  IDEAL reconstruction output for the full dairy cream (*left*), light dairy cream (*right*), and thick light dairy cream (*bottom*). The pixel-by-pixel maps of lipid content (*left*) and  $T2^*$  values (*right*) are shown

To the best of our knowledge, no reference values exist for  $T2_w^*$  and  $T2_L^*$  in tissues (such as liver for example) where the water and lipid proton pools share the same microenvironment. It is needless to say that it is straightforward to perform measurements of  $T2_w^*$  and  $T2_L^*$  in tissues such as subcutaneous adipose tissue and gray/white matter, where only one of these two proton pools is present. At this stage, the low-receiver bandwidth approach for direct measure of  $T2_w^*$  and  $T2_L^*$ , where the water and lipid proton pools share the same microenvironment, does not appear feasible for tissue measurements *in vivo*. Nevertheless, the reference values observed in phantoms are of interest for algorithm validation and the ability to measure  $T2_w^*$  and  $T2_L^*$  in phantoms certainly represents an important step towards the development of robust dual  $T2^*$  algorithms. Indeed, as indicated also in the literature, current dual  $T2^*$  algorithms methods still suffer from instability and poor noise performances [8–10].

With respect to the results obtained in the current study, it is noteworthy that the values of  $T2^*$  calculated by the IDEAL algorithm decrease with the increasing of cream thickness ( $T2^*$  light cream =  $54.2 \pm 3.5$  ms vs.  $T2^*$  of light thick cream =  $40.7 \pm 1.9$  ms) and lipid fraction ( $T2^*$  light cream =  $54.2 \pm 3.5$  ms vs.  $T2^*$  of full cream =  $36.4 \pm 1.6$  ms). The values of  $T2^*$  (of water and water + lipid) obtained by the low-receiver bandwidth approach also decrease with the increasing of cream thickness (Table 1). Overall, the  $T2^*$  values determined with the low-receiver bandwidth approach show that in all phantoms the  $T2^*$  relaxation time of the lipid protons is significantly shorter than that of water protons (Table 1). In light cream, the value of  $T2^*$  found by the low-receiver bandwidth approach in the water + lipid region is in excellent agreement with the value of  $T2^*$  calculated by IDEAL algorithm.

Within the context of lipid quantification *in vivo*, it is important to notice that worldwide obesity has more than doubled since 1980, and nowadays, it represents an important burden to the economy and the health care system. Because of the high clinical interest of lipid quantification, MRI vendors have installed on the MRI scanners novel algorithms that allow for a real-time calculation of the lipid content

[8, 9, 11]. So, at the end of the MRI examination, physicians have access to images of lipid content, that is, pixel-by-pixel maps of lipid content in a chosen anatomical area. Thus, a paradigm shift is currently taking place: for investigations of certain pathologies, the relevant output of an MRI examination is not anymore a T1- or T2-weighted image, but a quantitative map of a biomarker. The physicians at the end of the MRI acquisition will base their diagnosis on these quantitative maps. For instance, liver is one of the main organs of interest for lipid quantification: lipid content greater than 5 % is indicative of liver steatosis, and the T2\* values can be used to determine liver iron overload. An example of pixel-by-pixel maps of lipid content and T2\* values, similar to those generated on clinical MRI scanners, was obtained in the current study using the single T2\* IDEAL algorithm.

The water–lipid mixture models are of interest to a wide range of scientific disciplines, e.g., clinical research, colloid science, and food industry [15–17]. For instance, in food science, the knowledge of the mixture physico-chemical properties is essential for the development of food products. These products include water–lipid mixtures consisting of oil droplets dispersed in an aqueous phase (the so-called oil-in-water food emulsion: milk, dairy cream, mayonnaise...) and water–lipid mixtures consisting of water droplets dispersed in an oil phase (the so-called water-in-oil food emulsion: butter, margarine...). In this context, the application of MR techniques to investigations of water–lipid mixtures is not novel. Many NMR studies have been performed on water–lipid mixtures [15–17], but less attention has been paid to quantitative MRI [18–20]. The ability to directly measure the T2\* relaxation time of the water proton pool and the T2\* relaxation time of the lipid proton pool may prove of value also for investigating the basic relaxation mechanisms in water–lipid mixtures. For instance, in emulsion that have been generated in a well-controlled environment, detailed measurements of T2\* as a function of the lipid content can provide insight into the relaxation mechanisms and/or structural properties of water–lipid mixtures.

To conclude, direct T2\* measurements of water and lipid protons are of interest as they provide reference values for T2\*. In the current study, we showed that the low-receiver bandwidth approach represents a fast and effective method for direct measurements of T2<sub>w</sub>\* and T2<sub>L</sub>\*. Within the context of the lipid quantification in vivo, these reference values of T2<sub>w</sub>\* and T2<sub>L</sub>\* may be of interest for development, validation, and optimization of lipid quantification methods based on dual T2\* correction.

## References

1. World Health Organisation: Obesity and overweight. Fact sheet No. 311, Updated January 2015. <http://www.who.int/mediacentre/factsheets/fs311/en/> Accessed 03 Aug 2015
2. A. Must, J. Spadano, E.H. Coakley, A.E. Field, G. Colditz, W.H. Dietz, *JAMA* **282**, 1523 (1999)
3. W.T. Dixon, *Radiology* **153**, 189 (1984)
4. H. Yu, C.A. McKenzie, A. Shimakawa, A.T. Vu, A.C.S. Brau, P.J. Beatty, A.R. Pineda, J.H. Brittain, S.B. Reeder, *J. Magn. Reson. Imaging* **26**, 1153 (2007)

5. Y. Gandon, D. Olivíé, D. Guyader, C. Aubé, F. Oberti, V. Seville, Y. Deugnier, *Lancet* **363**, 357 (2004)
6. V.V. Chebrolov, C.D. Hines, H. Yu, A.R. Pineda, A. Shimakawa, C.A. McKenzie, A. Samsonov, J.M. Brittain, S.B. Reeder, *Magn. Reson. Med.* **63**, 849 (2010)
7. M. Bydder, T. Yokoo, G. Hamilton, M.S. Middleton, A.D. Chavez, J.B. Schwimmer, J.E. Lavine, C.B. Sirlin, *Magn. Reson. Imaging* **26**, 347 (2008)
8. M.R. Bashir, X. Zhong, M.D. Nickel, G. Fananapazir, S.A.R. Kannengiesser, B. Kiefer, B.M. Dale, *Am. J. Roentgenol.* **204**, 297 (2015)
9. X. Zhong, M.D. Nickel, S.A.R. Kannengiesser, B.M. Dale, B. Kiefer, M.R. Bashir, *Magn. Reson. Med.* **72**, 1353 (2014)
10. D.E. Horg, D. Hernando, C.D.G. Hines, S.B. Reeder, *J. Magn. Reson.* **37**, 414 (2013)
11. S.B. Reeder, Z. Wen, H. Yu, A.R. Pineda, G.E. Gold, M. Markl, N.J. Pelc, *Magn. Reson. Med.* **51**, 35 (2004)
12. S.B. Reeder, A.R. Pineda, Z. Wen, A. Shimakawa, H. Yu, J.H. Brittain, G.E. Gold, C.H. Beaulieu, N.J. Pelc, *Magn. Reson. Med.* **54**, 625 (2005)
13. R.V. Mulkern, Y.P. Hung, Z. Ababneh, S.E. Maier, A.B. Packard, M.C. Uluer, D.F. Kacher, G. Gambarota, S. Voss, *Magn. Reson. Imaging* **23**, 757 (2005)
14. G. Gambarota, R.L. Janiczek, R.V. Mulkern, R.D. Newbould, *Appl. Magn. Reson.* **43**, 451 (2012)
15. M.L. Johns, K.G. Hollingsworth, *Prog. Nucl. Magn. Reson. Spectrosc.* **50**, 51 (2007)
16. M.L. Johns, *Curr. Opin. Colloid Interface Sci.* **14**, 178 (2009)
17. M.A. Voda, J. van Duynhoven, *Trends Food Sci. Technol.* **20**, 533 (2009)
18. M.O. Hussein, C.L. Hoad, J. Wright, G. Singh, M.C. Stephenson, E.F. Cox, E. Placidi, S.E. Pritchard, C. Costigan, H. Ribeiro, E. Ciampi, A. Nandi, N. Hedges, P. Sanderson, H.P. Peters, P. Rayment, R.C. Spiller, P.A. Gowland, L. Marciani, *J. Nutr.* **145**, 1170 (2015)
19. L. Marciani, M.S. Wickham, D. Bush, R. Faulks, J. Wright, A.J. Fillery-Travis, R.C. Spiller, P.A. Gowland, *Br. J. Nutr.* **95**, 331 (2006)
20. L. Marciani, C. Ramanathan, D.J. Tyler, P. Young, P. Manoj, M. Wickham, A. Fillery-Travis, R.C. Spiller, P.A. Gowland, *J. Magn. Reson.* **153**, 1 (2001)

## **Summary**

Obesity is associated with increased morbidity and mortality linked to many diseases, including type 2 diabetes, hypertension and disease nonalcoholic fatty liver. Recently,  $^1\text{H}$  magnetic resonance imaging (MRI) has emerged as the method of choice for non-invasive fat quantification.

In this thesis, MRI methodologies were investigated for *in vitro* (MR phantoms) and *in vivo* (mice) measurements on a 4.7T preclinical scanner. Two algorithms of fat quantifications – the Dixon's method and IDEAL algorithm – were considered. The performances of the IDEAL algorithm were analyzed as a function of tissue proprieties ( $T2^*$ , fat fraction and fat spectral model), MRI acquisition parameters (echo times, number of echoes) and experimental parameters (SNR and field map). In phantoms, the standard approach of single- $T2^*$  IDEAL showed some limitations that could be overcome by optimizing the number of echoes. A novel method to determine the ground truth values of  $T2^*$  of water and  $T2^*$  of fat was here proposed.

For *in vivo* measurements, different analyses were performed using the IDEAL algorithm in liver and muscle. Statistical analysis on ROI measurements showed that the optimal choice of the number of echoes was equal to three for fat quantification and six or more for  $T2^*$  quantification. The fat fraction values, calculated with IDEAL algorithm, were statistically similar to the values obtained with Dixon's method.

Finally, a method for generating reference signals mimicking fat-water systems (Fat Virtual Phantom MRI), without using physical objects, was proposed. These virtual phantoms, which display realistic noise characteristics, represent an attractive alternative to physical phantoms for providing a reference signal in MRI measurements.

---

## **Résumé**

L'obésité est associée à une augmentation de la morbidité et de la mortalité liée à de nombreuses maladies, y compris le diabète de type 2, l'hypertension et des pathologies hépatiques menant à une surcharge lipidique d'origine non alcoolique.

Récemment, l'imagerie par résonance magnétique (IRM) est devenue la méthode de choix pour la quantification non invasive de la graisse.

Dans cette thèse, les méthodes d'IRM ont été étudiées sur un scanner préclinique de 4.7T *in vitro* (fantômes MR) et *in vivo* (souris). Deux algorithmes de quantifications de la graisse -la méthode de Dixon et l'algorithme IDEAL- ont été considérés. Les performances de l'algorithme IDEAL ont été analysées en fonction de propriétés des tissus ( $T2^*$ , fraction de graisse et la modèle spectral de la graisse), paramètres d'acquisition IRM (temps d'écho, nombre d'échos) et les paramètres expérimentaux (SNR et carte de champ). Sur les fantômes, l'approche standard single- $T2^*$  IDEAL a montré certaines limites qui pourraient être surmontées en optimisant le nombre d'échos. Une nouvelle méthode, pour déterminer les valeurs de vérité terrain pour  $T2^*$  de l'eau et pour  $T2^*$  de la graisse, a été proposée.

Pour les mesures *in vivo*, différentes analyses ont été effectuées en utilisant l'algorithme IDEAL sur le foie et les muscles. L'analyse statistique sur les mesures de ROI a montré que le choix optimal du nombre d'échos est égal à trois pour la quantification de la graisse et six ou plus pour la quantification du  $T2^*$ . Les valeurs de la fraction de graisse, calculées avec l'algorithme IDEAL, étaient statistiquement comparables aux valeurs obtenues avec la méthode de Dixon.

Enfin, un procédé pour générer des signaux de référence mimant les systèmes eau-graisse (Fat Virtual Phantom MRI), sans l'aide d'objets physiques, a été proposé. Ces fantômes virtuels, qui présentent des caractéristiques de bruit réalistes, représentent une alternative intéressante aux fantômes physiques pour fournir un signal de référence dans les mesures IRM.